Synthesis of Strained Metal Nanocrystal Architectures for Energy Conversion Electrocatalysis

Author: Brian Thomas Sneed

Boston College

The Graduate School of Arts and Sciences

Department of Chemistry

"SYNTHESIS OF STRAINED METAL NANOCRYSTAL ARCHITECTURES FOR ENERGY CONVERSION ELECTROCATALYSIS"

a dissertation

by

BRIAN T. SNEED

submitted in partial fulfillment of the requirements for the degree of

Doctor of Philosophy

May 2015

For my brother, Luke.

"There is nothing like looking, if you want to find something. You certainly usually find something, if you look, but it is not always quite the something you were after."

- J. R. R. Tolkien

"Synthesis of Strained Metal Nanocrystal Architectures for Energy Conversion Electrocatalysis"

Brian T. Sneed, Chia-Kuang Tsung

ABSTRACT

In order to understand the lattice strain effect and its relationship to size, shape, composition, and catalytic performance, novel well-defined nanocrystal archetypes were designed and synthesized by taking advantage of wet chemical, seed-mediated (mild) reduction routes developed by our lab. First, the current synthesis challenges are addressed in creating smaller monometallic shape-controlled metal nanocrystals, and novel cuboctopods via a hybrid nanoparticle stabilizer. A look at the relationship between lattice strain and morphology is then shown in a single-component system, where still new features have been observed for the first time by the traditional technique of powder x-ray diffraction. Synthesis methods for differently strained Pd surfaces are described and catalysis by these surfaces is discussed. Finally, studies of the synthesis, characterization, electrocatalytic activity, and restructuring of novel and more sophisticated strained architectures are presented: core-island-shell nanocrystals, phase-segregated nanoboxes, island nanoframeworks, and core-sandwich-shell nanoparticles. Lattice strain and composition effects were studied in carbon monoxide, small alcohol, and formic acid electrocatalytic oxidations as well as in oxygen reduction, the latter of which, governs the commercial viability of automotive fuel cells, a sustainable energy and zero-emission technology. Here it is demonstrated how a tunable thickness of Ni sandwich layers can be used to improve catalytic performance by increasing lattice strain on the Pt surface. The sandwich archetype offers a new platform for the investigation of lattice strain and could be a promising, industrially relevant, catalyst design concept, to

help address the need for a more sustainable energy future. The results help paint a new picture of catalysis by metal nanocrystals; one which brings lattice strain to the forefront of the discussion, as an important parameter for further study and for use in developing higher-performing catalysts.

TABLE OF CONTENTS

ACKNOWLEDGMENT

I want to first and foremost acknowledge my advisor Frank Tsung, and my post-doctoral mentor, Chun-Hong Kuo, who I learned much from. I am grateful to Professors Wang, Mohanty, and Davidovits on the committee for taking time out of their busy lives for this dissertation. I would like to thank the ACS journals, JACS and ACS Nano, as well as ChemSusChem and Phys. Rev. B for the publications I have authored or co-authored, and for the material from which much appears in this dissertation verbatim. I thank my labmates, current and former, for both their help with experiments and the conducive atmosphere that they bring to the group for good research. Allison Young has been incredibly helpful to me, as well as, former undergraduate Casey Brodsky, and current undergraduate Matthew Golden. I must also thank a former graduate exchange student, Daniel Jalalpoor. I thank all of our collaborators around the world: Prof. Xing Yi Ling, Prof. Franklin Tao, Prof. Paolo Scardi, Prof. Yong Wang, Matthew Suchomel, Weixin Huang, Ying Jiang, Yejing Lui, Hiang K. Lee, Alberto Leonardi, and Luca Gelisio. I thank our local TEM manager, Greg McMahon, and those at JEOL, Natasha Erdman and Masateru Shibata. I thank the Wang and Wilson groups, the Physics Dept., and the Chemistry Dept. staff for their continued efforts in support of our work. I thank Boston College for the funding of these projects, as well as, the awards that were given in support of my efforts here. I thank my family, and my parents especially, for their support. I thank my doctors, nurses, and the numerous friends and support groups, for their efforts in getting me to this point, my 10^{th} year in remission of leukemia. I thank Yunan Zheng, who has been my rock of support these last five years, and who continues

to provide so much encouragement and meaning in my life. I thank the many friends I have made here in Boston, for catalyzing many fun escapes from exhaustive times of research. Thank you all for your support.

LIST OF FIGURES

PROJECT INCEPTION

The initial goal of the project was to develop and extend methods for the shape-controlled synthesis of late transition metal nanoparticles, such as Pd, to others in the group, mainly Rh, followed by Ni. This was mostly driven by the fact that there was little work present in the literature on the subject, and the few pioneering examples that existed, evidenced poor regularity and reproducibility in the final structures. In addition, better control was sought for these materials because of their intrinsic activity for a variety of industrially relevant chemical transformations. After attempting to produce shape-controlled monometallic nanoparticles of these metals, it quickly became apparent the reasons for their vacancy in the literature: the low reduction potentials and high surface energy of Rh and Ni compared to more noble metals such as Pd, Pt, Ag, and Au, made them significantly more difficult to reduce and to control their surfaces. Another challenge was confronted in restricting our scope to 'greener' chemical routes (aqueous phase, low temperature, ionic surfactants as capping agents), rather than relying on high temperature and organic solvents, which was standard up to that point in time for these materials. The challenges were overcome via aqueous, seed-mediated overgrowth with cationic surfactants, adapting procedures for shaped Pd nanoparticles to be used as substrates, and by taking advantage of different shaping and reducing agents, such as iodide and hydrazine, respectively. The different interfaces generated, combined with recent interest in the field, naturally resulted in a focus on the topic of lattice strain effects. It should be noted that a combination of *ab initio* design targets, insight from the

literature, trial and error screening of synthesis conditions, as well as adaptation and re-optimization of procedures ultimately led to the new materials and scientific discoveries that follow.

1.0 BACKGROUND INFORMATION

The importance of lattice strain as a fundamental topic of research has quickly gained momentum in recent years as scientists investigated its significant impact on the surface electronic structure and catalytic properties of nanomaterials. Furthermore, researchers have begun to tell a more complete story of catalysis from a perspective which brings this new concept to the forefront of the discussion. The nano-'realm' makes the effects of lattice strain, active on the same spatial dimensions, more pronounced, especially in catalysis. In part, this field opened up because of the achievements that were made in the synthesis of more sophisticated metal nanoparticles from an ever-expanding library of methodologies. Developing rational synthesis methods for metal nanoparticles with well-defined strained architectures is a worthy goal that will have considerable impact in the search for catalysts which can help to achieve a more sustainable energy future. My work has contributed to this area and I have developed many novel lattice-strained metal nanoparticle archetypes. This introductory chapter broadly describes nanoparticle synthesis and applications leading up to the current work. The principles of nanoparticle synthesis are described, followed by a survey of their applications. Included in this discussion are the emerging design strategies for the state-of-the-art fuel cell

electrocatalysts and the restructuring of nanoparticles under different reaction conditions. The final introductory section provides background on the concept of lattice strain and will give a short review of the relevant recent literature in the field as it pertains to this direction. This introduction will not cover these topics exhaustively, and as such, is meant to simply set the stage for the results and discuss and to place the work in broader context. *If the reader is already familiar with these topics, it is strongly suggested to skip the introductory material and to begin reading from the results section instead.*

1.1 Metal Nanoparticles

The first human-made metal nanoparticles were created by artisans in ancient times. Colloidal gold solutions were even consumed during the middle ages for medicinal purposes. Faraday reported the production of colloidal gold solutions from the reduction of chloride precursors in the 1800s, and chemists today are still using variations of this general procedure to synthesize metal nanoparticles. Noble metal nanoparticles are useful due to their unique optical properties, however, most late transition metal nanoparticles find their major application in heterogeneous catalysis. There are other important types of nanoparticle materials, such as semiconductor quantum dots, however, this is beyond the scope of the thesis, which focuses on metallic nanoparticles, and they will not be discussed here.

1.1.1 Nucleation and Growth of Metal Nanoparticles

In general, the nucleation and growth of metal nanoparticles in solution by reduction of ionic metal precursors can be described using the classical LaMer approach and plot (Figure 1a).[1] As zero-valent metal atoms and clusters are produced in solution from the reduction reaction, they are consumed by the reverse oxidation/dissolution reaction in equilibrium. Homogenous nucleation can occur when the concentration of these monomers (clusters of atoms) is high enough such that the diffusion rate between monomers is large relative to the rate of dissolution. A fraction of these monomers merge to form larger, more stable nuclei, overcoming the energy barrier associated with creating the new interface. Once a solution reaches this critical supersaturation, homogeneous nucleation occurs, depleting the concentration of monomers, and so the nucleation event ceases due to larger diffusion distances, while a period of growth of these preformed nuclei or seeds into larger particles follows. The growth will continue at the expense of additional monomer concentration so that it slows and decays with time. There can be sacrificial dissolution of smaller particles at the expense of growing larger crystals. This process is referred to as Ostwald ripening. The dependence of the size of the nuclei on the nucleation event is generally ascribed to the two competing factors of surface energy and lattice energy (Figure 1b).[2] Assuming a spherical nucleus is formed because spheres have the lowest surface area to volume ratios (minimizing surface energy), the free energy of nucleation, ΔG_{nuc}, is given by the relation:

$$\Delta G_{nuc} = \frac{4}{3}\pi r^3 \Delta G_v + 4\pi r^2 \gamma$$

where, r is the radius of the nucleus, ΔG_v is the energy difference between the metal lattice and solvent phases per unit volume, and γ is the surface tension. Introduction of a new surface, or a new interface in solution, is always energetically less favorable and positive as the solvent molecules have to be driven back to generate the surface, whereas decreasing of the surface area to volume ratio (nanoparticle growth into bulk materials) will always be energetically favorable and negative because this stabilizes the lattice energy of the crystal. The surface area term goes by the square of the radius, while the volume term goes by the cube of the radius. This leads to a crossover to spontaneous nucleation at a size of particle with critical radius, r_c. This means that nuclei below the critical radius are more likely to be redissolved, while those at or beyond the critical radius, are stable, and continue to grow.

Heterogeneous nucleation takes place when a surface is already present, effectively lowering the barrier and serving as a pre-formed seed (substrate) for the overgrowth process. The overgrowth of one material on another can be divided into the three general classes based on the growth mode: Volmer—Weber type island growth, Frank—van der Merwe monolayer film growth, or Stranski-Kastanov mixed island and monolayer film growth (Figure 2).[3] The growth modes begin with single atom or cluster deposition. Then, based on the bonding differences between atoms in the two materials and the degree of lattice mismatch, different modes of growth result. In island growth, the first deposited atoms and clusters serve as seed sites for further growth. This generally occurs when the interaction between atoms in the growing layers are stronger than their interaction with substrate layers. In monolayer film growth, atoms will deposit, diffuse,

and pack together on the substrate until a complete film is established before the next layer grows. Typically this occurs when the overgrowing material has a strong interaction with the substrate atoms. Mixed growth can result as an intermediate type between these two general deposition modes, where there is no clear preference in chemical bonding.

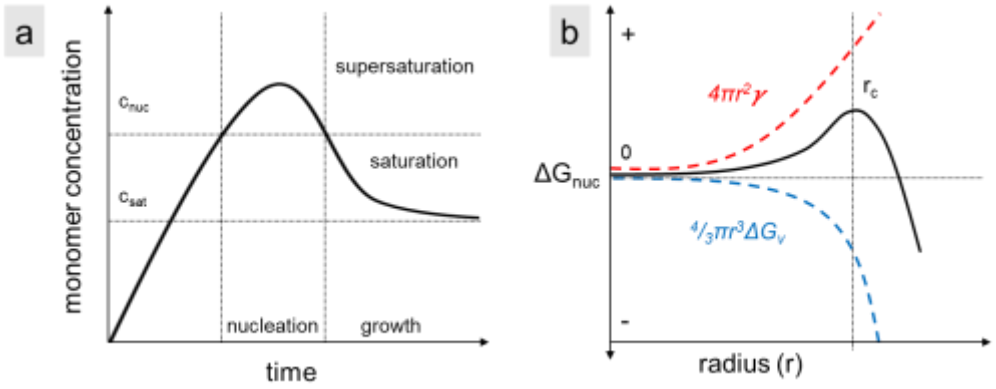

Figure 1. La Mer plot (a) for nucleation and growth of metal nanoparticles and plot (b) of change in free energy versus particle radius with dependence on surface area and volume (lattice energy) terms.

1.1.2 Stabilizers: Capping Agents, Surfactants, Polymers, Ligands, and Solvents

When nanoparticle nucleation and growth occurs in solution, the particles will aggregate to form micro-sized agglomerations, and precipitate out as bulk materials, to reduce surface energy, unless they stabilized by some form of capping agent molecules. Typically these molecules are refered to as capping agents, but the terms stabilizer and ligand are often used to describe the same beneficial effect. For example, it is well known that citric acid can keep gold nanoparticles dispersed for long periods of time in aqueous

solutions. This is accomplished by the carboxylate groups in the molecules. By their interaction with the metal atoms as ligands, they create an electric charged double layer around the metal nanoparticles, shielding them from other particles also covered, in this case, by citrate via electrostatic repulsions (Figure 3). Energetically, if the separation distance was small enough, the particles could overcome this repulsion through a merger of the anionic layers and aggregate, however, the barrier for this is normally too high if the ligands are present in high enough concentration in solution, and only excessive force can destabilize or cause the particles to agglomerate (such as centrifugation at high enough speeds). The potential energy well at separation distance just before the repulsion distance is optimum, where the double-layers between two particles can both be balanced by solvent or a positively charged cation layer in between, facilitating self-assembly, but keeping the particles separated. Metal nanoparticles have partially positively charged surfaces due to the large number of dangling bonds from undercoordination at the surface, placing more electron density in the core of the structures. These Coulomb forces are responsible for the stabilization of nanoparticles in solution. The repulsions prevent both precipitation and agglomeration of the particles over time. In the example above, citrate, having negative charge, is balanced by the partial positive charge of the metal surface, however, the reverse situation can operate where surface charge is negative, as in metal-oxides in solution; the particles here will terminate with a negative charge from oxygen, which could then be balanced by positively charged ions.

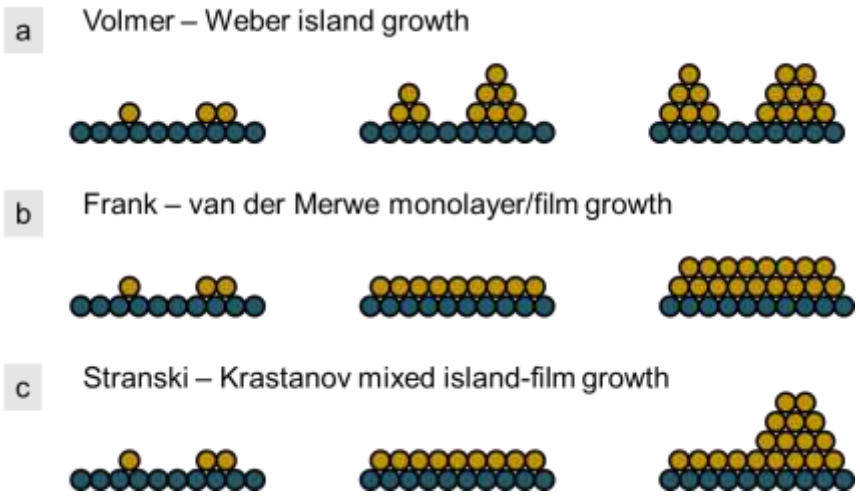

Figure 2. Growth modes for deposition of materials: a) Volmer-Weber island growth, b) Frank-van der Merwe monolayer film growth, and c) Stranksi-Krastanov mixed island/film growth.

The self-assembly of surfactant molecules is based on this same concept. Surfactants make effective nanoparticle stabilizers, and play a crucial role in the growth of metal nanoparticles, as they self-assemble into highly ordered structures in solution: micelles, double-layered micelles, rods and cylinders, etc. Speculation of the role of such surfactants as CTAB (cetyltrimethylammonium bromide) in nanoparticle synthesis continues. In a recent work by Liz Marzan et al., CTAB was found to play one of the most important roles in conjunction with Ag adatoms in the popular synthesis of Au nanorods.[4] It is believed that the quaternary ammonium positively charged head groups, balanced by halides and terminated by a long hydrocarbon tail, creates a double-layer around nanoparticle surfaces, where the halides prefer to bind to the metal surface,

followed by the head groups and non-polar tails, this is then followed by a mirrored 2nd layer of surfactant. The ammonium/bromide ion pairs near the surface were found to complex with silver ions at specific surface sites, and this controlled the assymetric particle growth in two opposite directions, based on the lowest energy supramolecular structure having two of these sites unoccupied. It is clear from this example that we are only just beginning to understand growth of simpler nanoparticles, such as Au nanorods, at the molecular level, and there is still much to be learned regarding the growth mechanisms of shaped nanocrystals.

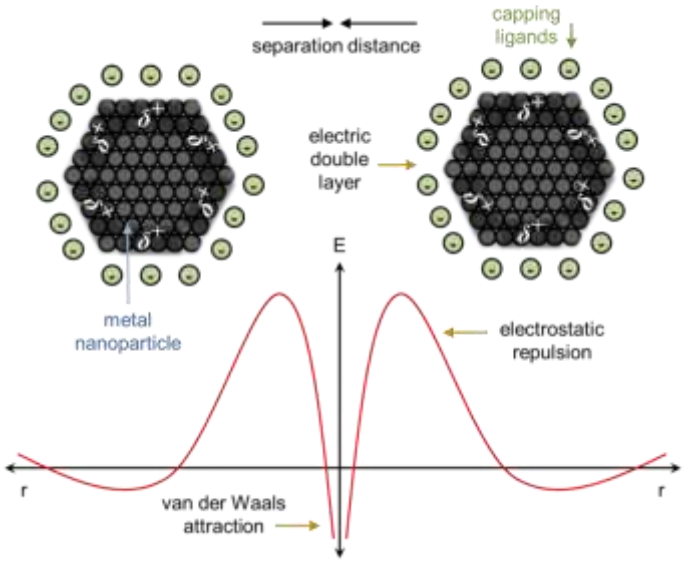

Figure 3. Stabilization of nanoparticles in solution by electrostatic repulsion.

In addition to micelle forming surfactants, polymers are often used as nanoparticle stabilizers, however, the supramolecular structure these polymers form around nanoparticles is not definitively known. It is generally believed they randomly envelope

nanoparticles through metal binding functional groups and van der Waals forces. Perhaps the most prevalent polymer in nanoparticle synthesis is polyvinylpyrrolidone (PVP). PVP is a popular choice in poly-ol methods, where metal ions are reduced through the solvent alcohol, usually ethanol, and assisted by the polymer. Neutral solvent molecules can also have characteristics much like surfactants. Oleylamine and dimethylformamide (DMF), for example, are also used heavily in the synthesis of non-precious metal-containing nanocrystals, where stability in aqueous environments is an issue. These solvents also contain metal-binding nitrogen moieties, which serve to stabilize the nanoparticles by strong dipole forces, rather than by charged surfactant layers. There are some groups promoting nanoparticle synthesis using organic solvents as capping-agent-free methods,[5] however, the particles are stabilized by the solvent molecules and thus still require cleaning because of different conditions for the catalysis application. Additionally these methods require the particles be loaded onto a support immediately after synthesis, as they agglomerate quickly.

1.1.3 Reducing Agents and Size Control

Conventionally, hydrogen gas was used to reduce metal ions to form nanoparticles, however, there are a number of alternative reducing agents that can accomplish the task with more control of structure. There are strong and milder approaches, each with their own advantages and disadvantages. Generally, strong reducing agents such as sodium borohydride and hydrazine are used when the desired nanoparticle size is small. This is because strong reducing agents create a rapid nucleation event, consuming most of the

monomers so that little growth occurs afterwards. Weak reducing agents create larger nanocrystals in general because the nucleation event is slower to proceed, so that mainly growth of relatively few nuclei occurs. Typically this makes mild reducing agents the perfect selection for overgrowth in seed-mediated synthesis, where further nucleation should be avoided. Organic anti-oxidants are primarily chosen for this purpose. Mainly ascorbic acid, citric acid, and glucose are employed, though almost any anti-oxidant molecule from biological systems can be chosen. The reduction potential of metals governs their ease of reduction, and reducing agents should be selected appropriately. However, it should be noted that the size and shape of the resulting nanoparticles will depend mostly on the intrinsic properties of the element being reduced. This is evident by a study done by Sanchez et al., where the temperature, capping agent, reductant identity, and their respective concentrations were held constant while different metal nanoparticles were synthesized.[6] Different sizes, morphologies, and ordering of nanoparticles were observed, and though some trends were discovered, each different metal system seemed to retain its own unique characteristics. Specifically the 3rd row late transition metal nanoparticles of Ir, Pt, and Au tended to exhibit more long-range ordered structures, while the 2nd row analogues of Rh, Pd, and Ag showed more particle twinning and more complex faceting. Trends in size were ambiguous as Pd and Au particles tended to be larger. Though this was not discussed, the reason they behave similarly is likely due to the periodic table "diagonal" relationship where going down and across the column and period, respectively, has a canceling effect; the smaller atomic size due to electronegativity increase is negated by the added shell of electron shielding of heavier

elements (much like the step-wise boundary between metals and non-metals gives rise to the intrinsic semiconductors). Once a reducing agent is selected, size can be controlled within a range of nm by changing the concentration of the reducing agent, which changes the rates of nucleation and growth. Typically, adding more reducing agent will reduce the size by causing a more rapid nucleation event and shortened growth period. Decreasing the reducing agent concentration will result in larger particles conversely. There is a similar trend on size for changes in the concentration of precursors and capping agents, as they both will have an effect on nucleation and growth rates, but this is generally exploited less as the effect is more subtle. Alternatively, the use of carbon monoxide for size confinement of nanoparticles has been demonstrated recently, by either gas bubbling, or introduction of transition metal-carbonyls as the source.[7-9]

1.1.4 Shaping Agents and Control of Shape

Morphology is a commonly sought after characteristic of nanocrystals, especially when coupled to property maps of surface strain and chemical composition. This information is critical to many research fields and is particularly important for understanding catalytic reactivity. Since the first classical demonstrations of shape-controlled metal nanocrystals, perhaps best displayed by El-Sayed et al.,[10] scientists have been exploring new ways to better control the shape of metal nanoparticles. Perhaps one of the most impressive accomplishments was demonstrated by the Huang group in 2008 as they were able to create size and shape control of the Au system in making cubes, truncated cubes, cuboctahedra, truncated octahedra, rhombic dodecahedra, and octahedra

by adjusting the amount of reducing agent, ascorbic acid, in a multistep reaction.[11] Shortly after, Niu et al. were able to accomplish a similar feat for Pd nanoparticles in 2010.[12] There are of course other excellent examples, however, these two studies are most important for shaped nanocrystal synthesis, as they are the first to display shape evolution of radically different structures at relatively small sizes (under 100 nm) with only slight changes to the reaction parameters. Additionally, both of these seed-mediated synthesis methodologies utilize similar cationic quaternary ammonium surfactants, halide shaping additives, and the same mild reducing, ascorbic acid in an aqueous system at low temperature. This is remarkable considering the similarities between the approaches seem to be effective for two different metals. These works, serving as benchmarks for the field, have put forward some general guidelines for shape control of metal nanocrystals that I have since taken advantage of in my work. By adapting Niu's method, examples of shape-controlled Pd nanocrystals (the primary substrates for the following work) are shown in Figure 4.

The control of shape in epitaxial overgrowth in these cases, either homo-epitaxial for monometallic nanocrystals, or hetero-epitaxial for bimetallic particles, arises primarily due to differences in the thermodynamic surface energy of the different crystal facets. The Gibbs-Wulff polyhedron is arrived at for face-centered-cubic (fcc) metals as it balances the competing factors for lowest surface energy facets (low-index surfaces) that most closely resemble a spherical shape (lowest surface to volume ratio). The Wulff polyhedron is a cuboctahedron with a combination of (111), (100), and (110) facets. The ordering of surface energies for these thermodynamically most stable facets is (111) <

(100) < (110) for fcc crystals. These ordering tendencies follow the close-packedness of the surface geometry, with (111) being the most close-packed surface, and (110) being the most open. High-index facets are essentially different combinations of low-index steps and terraces. Despite the (111) surface being the most favorable, the vertices and edges that would be produced from an octahedron (or tetrahedron) containing only (111) facets have a large number of highly undercoordinated, high-energy, dangling or exposed atoms. For this reason, the structure is truncated to reveal (100) and (110) surfaces at corners and edges, respectively. Therefore, the goal has been to find ways to manipulate these relative energy differences of surfaces to produce polyhedra that deviate from the Wulff construction through the preferential adsorption of molecules on certain crystallographic faces during growth. Particles with high-index-facets, anisotropy, and twinning can also be produced through changes to reaction parameters, such as temperature, modulating the reduction and growth rates (kinetic control) of different facets. There are many reviews that discuss the use of molecular adsorbates for this purpose and can be consulted, perhaps best described by Sau and Chen.[13,14] These studies were the basis for the use of the heavier halide anions (Br-, I-) for production of cubic Pd, Rh, and Pt (100)-terminated nanocrystals. Octahedra terminated by (111) surfaces can be obtained by the use of citrate, gases, such as CO and O_2, were bubbled into growth solutions also to control shape (and size). The vast library of small molecules available to chemists is still being explored for this purpose, however, the real challenge of future research lies in decoupling the diverse range of effects such molecules have on synthesis: surface energy of facets, facet growth kinetics, reduction rates,

diffusion rates, deposition rates, changes to reduction potentials by the ligands of metal precursor complexes, and changes caused by different surfactants, reducing agents, and concentrations thereof.

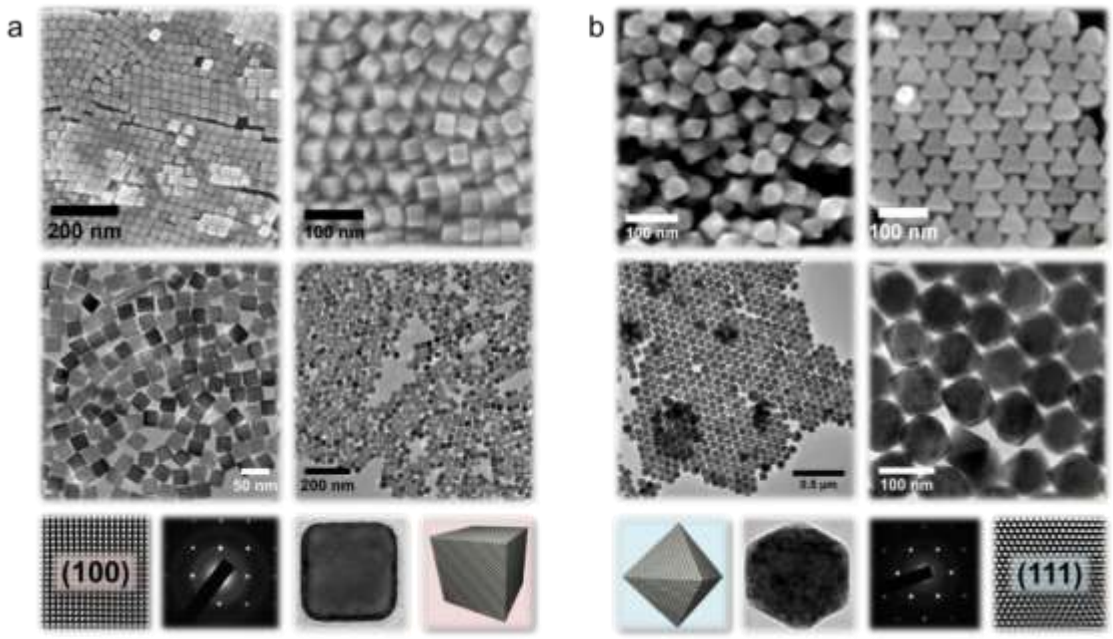

Figure 4. Examples of shape-controlled metal nanocrystals produced by our group. Shown are models and electron microscope images of Pd cubes in (a) and Pd octahedra in (b).

1.1.5 Multimetallic Nanocrystals and Composition Control

The design of multimetallic nanoparticles arose as a way to combine the benefits of different metals for the purpose of catalysis, without retaining their disadvantages. Core-shell metal nanoparticles are heterostructures consisting of a metal core with a different metal shell, whereas alloy nanoparticles contain two metals distributed in a single

particle. There are three main benefits that these types of bimetallic nanoparticles have over the monometallics: 1) a second metal can introduce added stability by preventing particle aggregation and by increasing thermal stability, 2) incorporating an inexpensive metal into a noble metal nanoparticle can greatly reduce catalyst cost by conserving the use of precious metals, and 3) perhaps most importantly, a second metal can modify the structural and electronic properties of a nanoparticle leading to sometimes orders of magnitude enhancement in catalytic activity.

Two common methods for synthesizing multimetallic nanoparticles are co-reduction and seed-mediated growth, creating alloy nanoparticles and core-shell nanoparticles, respectively. The reduction potentials of the metal precursors play a crucial role in both the alloying and growing of epitaxial shells of different materials. Non-precious metals such as Co and Ni have low reduction potentials, and generally this requires higher temperatures and stronger reducing agents. However, these metals have been found to be taken up into particles in their co-reduction with Pt ions to make alloy nanoparticles, despite large differences in reduction potential. The slow reduction rates in low temperature aqueous solution and use of cationic surfactant has been a successful way to produce core-shell bimetallic nanoparticles.

Ray Schaak's group is one of the leaders in the field of creation and conversion of inorganic nanoparticles into novel materials. His work popularizes the extension of the concept of "total synthesis of molecules," analogous to the goals of organic chemistry, to inorganic materials, where chemical selectivity and functionality can all be tuned in nanoscale materials by stepwise synthesis. In a review by M. Buck, the different

emerging chemical conversion pathways are discussed.[15] Once inorganic nanoparticles are formed, they can be converted through: oxidation, reduction, addition, elimination, ion exchange, diffusion (Kirkendall), replacement (Galvanic), and coupling reactions. Alloys, intermetallic alloys, metal-chalcogenides, and metal-phosphides are the product compositions accessed through these processes, in addition to structure changes, such as in the formation of hollow nanoparticles.

1.1.6 Restructuring of Metal Nanoparticle Surfaces

An important parameter that governs such compositional changes and restructuring in metal nanoparticles is metal segregation energy.[16-19] Large tables can be formulated that allow for predictive maps of stable configurations. The segregation energy is correlated to fundamental properties such as atomic size, cohesive energy, vapor pressure, and surface energy. Atomic size and cohesive energy were found to be the most useful in predicting preferences, where smaller atoms with more cohesive energy nearly always having a preference for the core.[17] Though these preferences in core-shell structures are good for a first guess, these properties can change due to surrounding chemical environments. This was studied for bimetallic systems of Pd, Rh, and Pt by Tao et al.[20] They saw metal diffusion leading to restructuring of nanoparticles (different core-shell preferences) due to either oxidative or reducing gas environments. They found that this most likely was driven by heats of formation of oxides and the surface energy of the different metals.

Metal nanoparticle restructuring similarly occurs during heterogeneous catalysis and electrocatalysis due to the harsh conditions the particles can be exposed to for extended periods of time, for example, in fuel cell electrocatalysis electrolyte solutions. Pourbaix diagrams show the stability of metals under different potentials and pH values in aqueous solutions.[21] Metals are shown here to be stable, completely or partially dissolved, or passivated by hydrides or hydroxides depending on their nobility. The leaching of non-precious metals in Pt alloys and degradation of fuel cell catalyst materials is well-known to the field. There is a relationship of this leaching to the size of the particles, where generally smaller sizes are more stable. They tend not to leach as much non-precious metal and so have less tendency to form porous structures.[22] Below approximately ~10-12 nm there was a significant drop in the observance of porous alloyed PtNi nanoparticles after potential cycling in the oxygen reduction reaction catalysis conditions. Further studies of metal migration, leaching, and restructuring of nanoparticles relating to the development of the state-of-the-art fuel cell electrocatalysts is discussed in the following section.

1.2 Applications of Metal Nanoparticles

The major application of metal nanoparticles is in heterogeneous catalysis. Technologies such as fuel cells and metal-air batteries rely on metal nanoparticle electrocatalysts.[23] Fuel cells and metal-air batteries are currently being researched as power sources for a variety of electronic devices including, cars, laptops, PDAs, and small machinery. Applications relating to surface plasmon resonance for Au and Ag

nanoparticles include plasmon-enhanced catalysis, surface-plasmon enhanced Raman spectroscopy, sensing, biological applications such as drug delivery and phototherapy (laser liposuction, targeted cell death), and in displays.[24] A brief survey of applications in heterogeneous catalysis and plasmonics, is given, followed by a more detailed description of the development of the current fuel cell electrocatalyst design.

1.2.1 Localized Surface Plasmon Resonance

Localized surface plasmon resonance (SPR) is a phenomenon that is especially prevalent with the coinage metals. Nanoparticles of Au and Ag absorb and scatter light strongly in the visible wavelengths. This is due primarily to SPR, which is a collective resonant oscillation of electrons with the frequency of the incident electromagnetic waves (Figure 5). The absorption and scattering (extinction) spectrum of Au nanoparticles produces a band from plasmon modes dependent on the nanoparticle size, shape, and anistropy. In the case of Au, this results in a broad range of colors for differently sized nanoparticles. From a few nanometers in diameter up to over a hundred nanometers the Au particle solutions will scatter from red to purple and blue light. The metal-solvent interface also plays an important role in the position and different modes of plasmon resonance bands. The localized plasmon resonance of these nanoparticles makes them ideal substrates in surface-enhanced Raman spectroscopy (SERS) of Raman-sensitive molecules. Further applications are in plasmon-enhanced catalysis. Gold nanoparticles are being studied as potential catalysts for solar steam generation. Hot electrons generated by irradiating gold nanoparticles with light can raise the local temperature

around nanoparticles, so as to generate steam.[25,26] This effect has been demonstrated to be potentially useful in liposuction, where nanoparticle solutions would be injected into fatty tissues in the human body and irradiated with lasers.[27] The raised temperature caused by the plasmon-heating can rupture and destroy fat cells which can then be removed via traditional liposuction. Metal nanoparticles such as Ag and Au are often cocatalysts in semiconductor photo-catalyzed reactions and photovoltaic devices.[28-30] Additionally, studies have revealed that different mechanistic pathways can be activated for composite structures of plasmonic nanoparticles on semiconducting nanoparticles, where the locations of electrons and holes injected to and from the gold nanoparticle can be spatially resolved.[31]

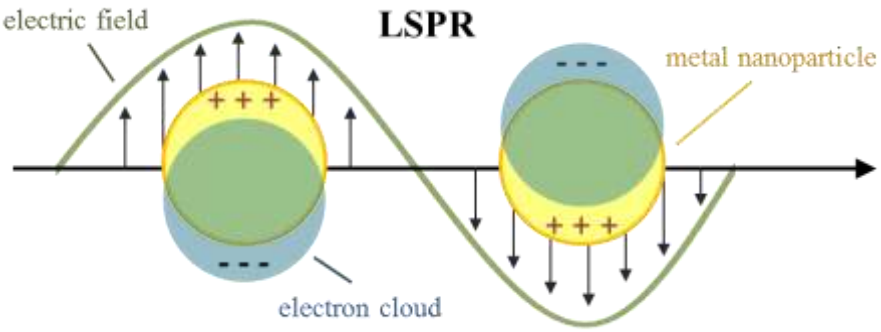

Figure 5. Schematic illustration of localized surface plasmon resonance.

1.2.2 Heterogeneous Catalysis on Metal Surfaces

Catalytic processes contribute in some way to more than one third of global GDP, and heterogeneous catalysis on metal surfaces constitutes a large portion of this industry,

facilitating the chemical production of common products, e.g. ammonia, hydrogen from steam reforming of natural gas, and reduced CO emissions in automotive exhaust.[32] Most catalytic systems research trends toward being heterogeneous, as there is considerable incentive in lowering costs associated with the separation of a catalyst within the same phase as the reactants and products, by using a solid (or tethered) catalyst. Heterogeneous catalysis by metal nanoparticles is critical for the prosperity of human civilization and future sustainability, and has thus been the subject of extensive research in recent years. Sabatier established the idea of a generalized 'goldilocks'-type relation for catalysis on different transition metals, where higher rates of reaction are observed for intermediate binding strength or intermediate numbers of d-electrons (nobility) moving across the transition metal block, shown schematically in Figure 6.[33]

A new trend towards developing improved heterogeneous catalysts is to generate atomic-level control of the nanostructures in order to further fine-tune their surface electronic structure. Several mechanisms have been proposed to control the surface electronic structures as there are four main factors which determine catalytic activity through modification of the structure: size, shape, composition, and metal-metal interface. Each of these factors is controlled during synthesis. The nanoscale-architectural control of the interface between two metals or and metal and metal oxide can be used to tune the electronic structure of the active sites. Significant enhancement of transition metal catalysts can be achieved by tuning the geometric and electronic structure because these characteristic properties determine the d-band center, which affects the sorption behavior of molecules on the metal surface. The mechanism of electronic

perturbation of a material by a second component, most often denoted as ligand effects or charge redistribution, alters the metal surface through direct electronic interactions between the different metal atoms. The ensemble effect, involves the symmetrical arrangement of surface atoms which can change the availability of specific active sites in multimetallic surfaces.

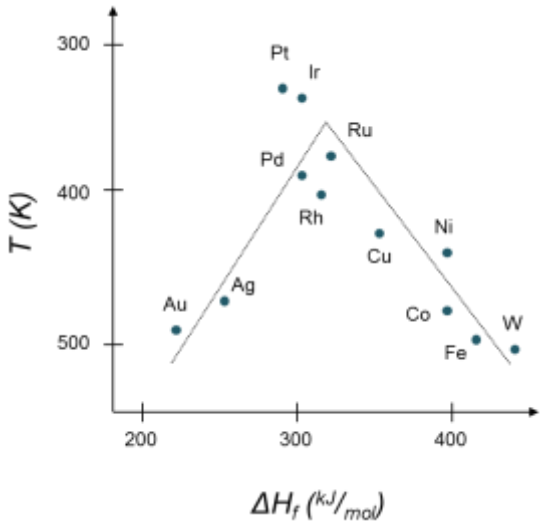

Figure 6. Example of the Sabatier principle in decomposition of formic acid on transition metal surfaces (Reference 30). The highest rates (at lowest temperature) are observed for intermediate values of ΔH_f (rates held constant, so that T is used as the y-axis). The most noble and least noble metals have the lowest rates.

The size and shape of nanostructures influences their catalytic behavior through the adjustment of the number and geometric structure of the active sites. The surface area of a batch of particles increases as the size decreases, and the percentage of under-coordinated metal atoms at edges and vertices of nanoparticles is also inversely

proportional to the particle size. These metal sites have a large number of dangling bonds which can make them more reactive. The degree of close-packing of atoms on the surfaces of different crystal facets similarly affects sorption characteristics. A great effort has been made to understand morphology-dependent catalysis,[34-40] however, it is not a straightforward process to assess as the actual arrangement of atoms within shaped nanocrystals is more complex than the traditional polyhedral model crystals envisaged. Edges and corners can have varying degrees of truncation, and in addition, compressed or expanded atomic arrangements arise from the high energy of the under-coordinated atoms at the surfaces, edges, and vertices due to anistropy. It is important to resolve these non-idealized atom arrangements, as the surface electronic structure directly influences the binding energies of adsorbates, intermediates, and products along reaction pathways on catalytic surfaces.[41-45]

1.2.3 Development of Metal Nanoparticle Fuel Cell Electrocatalysts

There has been a growing interest in the preparation of shaped binary and ternary metal nanoparticles (NPs) comprising non-precious metals (M) as they achieve better activity, stability, and efficiency as electrocatalysts for energy conversion chemistry.[23,46-52] In particular, such shaped M-Pt NP oxygen reduction electrocatalysts could advance the commercial viability of automotive hydrogen fuel cells (Figure 7a,b).[53] In the last three years alone, several record-breaking oxygen reduction nanoparticle electrocatalysts that have surpassed the DOE targets have been developed separately by various groups. Strasser's group and Xia's group have both been able to synthesize Pt-Ni alloy

nanooctahedra (~10 nm in diameter) by different pathways,[54,55] and Yang's group has developed rhombic-dodecahedral Pt-Ni nanoframes, the current record holder.[56]

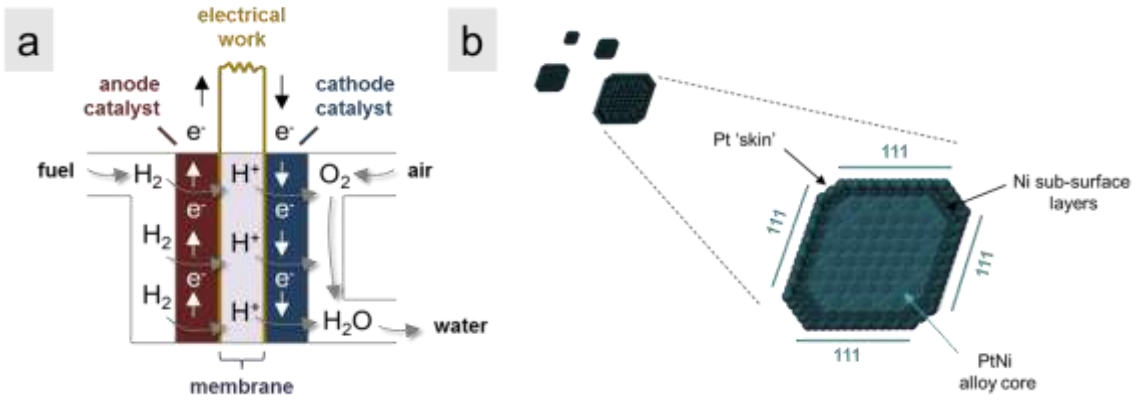

Figure 7. Hydrogen fuel cell schematic (a) and model (b) of the state-of-the-art fuel cell electrocatalyst where octahedral nanocrystals of Pt-surface-enriched layers and Ni sub-surface-enriched layers form over a PtNi alloy core in operating conditions.

The superior performance of shaped M-Pt NPs merits their study, but the many factors that influence catalytic behavior in these complex systems (ligand, ensemble, geometric, and strain effects) are difficult to parse out.[57] Often it remains that the most active and stable structures for these catalysts are composed of layers of Pt atoms above an M-Pt core, so the target structure is re-envisioned as a core-shell NP architecture.[53,58] In addition, it is shown that thin M-sandwich layers can exist due to restructuring during the reactions, and indeed there is experimental and theoretical work which discusses the stability of various Pt-M-Pt sandwich and multilayered Pt-skin structures.[59-61] The afore mentioned M-Pt NP surfaces reconstruct to the Pt-skin motif due to dealloying (leaching)

of the non-precious component from the surface during potential cycling in acidic conditions.[62,63] Recent work predicts M-Pt NPs comprising a Pd-Ni core and Pt-shell to be more stable and highly active electrocatalysts for oxygen reduction. All of this information suggests the investigation of core-shell and multi-shelled M-Pt nanoarchitectures to be a promising direction for fundamental catalysis research.

1.3 Lattice Strain

The lattice strain phenomenon that arises from metal-metal interfaces has been known for many decades, but has only recently been investigated at nanoscales due to the recent growth of nanoscience. Many important discoveries have been made regarding the prevalent nature of lattice strain, primarily dealing with its effects on the reactivity of metal nanocrystal electrocatalysts.[57,64] Lattice strain is arguably one of the most significant factors to be controlled in tuning catalytic performance of nanocrystals, as its impact can be felt at the catalyst surface, even with the source of strain being buried several atomic layers deep in a nanostructure. This demands a new paradigm for studies of structure and catalysis at the nanoscale, one that could offer a much more complete mechanistic understanding, albeit with the added complexity of introducing another parameter for optimization. Lattice strain alters the atomic arrangement (and d-band) of nanoparticles, which in turn produces different adsorbate binding behaviors. Tuning the strain near the surface can be used to promote specific catalytic pathways, for example, in promoting direct versus indirect reaction pathways in formic acid oxidation. Improved

fuel cell electrocatalysis will be tied to the future development of this field as a more sustainable energy conversion, zero-emission technology.

Generally defined, lattice strain is a measure of the deformation (or distortion) of a lattice caused by stress (or tension) at the interface between phases causing displacement of atoms in the lattice, resulting in compression or expansion away from the bulk (original) lattice parameters (Figure 8). Depending on the source, the effects of strain propagate throughout the crystal, but decay further away from the source due to relaxation. This has a dramatic impact on the local properties of the metal surface, providing the source of strain is within a few nanometers. Lattice strain is generated by and dependent on the degree of lattice mismatch between metals in multimetallic alloy and core-shell nanoparticle structures, by particle twinning, and by size and shape effects. The lattice mismatch between metals in bimetallic nanoparticles is given by:

$$\frac{(core_a - shell_a)}{core_a} \, x \, 100\ \%$$

where $core_a$ and $shell_a$ represent the lattice constants of the core and shell metals, respectively. Alternatively, lattice percent different can also be used and is given by:

$$\frac{(core_a - shell_a)}{(core_a + shell_a)/2} \, x \, 100\ \%$$

When the mismatch is very large, epitaxial growth can still occur, but defects, such as edge dislocations, result in order to minimize the energy around such a highly strained interface. The average displacement due to lattice strain can then be defined as the real percent difference from bulk metal parameters, determined experimentally using

diffraction data and Vegard's law. This can be done for alloy and core-shell structures, however a displacement gradient away from the source means that an accurate measurement of strain of surface atoms has to be calculated differently or determined indirectly by other means (indirectly from electronic structure by X-ray photoelectron spectroscopy, or by accounting for strain released by defects). There has been little attention paid to shape as a source of strain, so it will not be reviewed here in this section. However, we have begun to study the shape-strain relationship in detail in our work. This will be discussed in great detail in the results and discussion section. A review of studies of strain due to other sources is given, followed by the implications for catalysis.

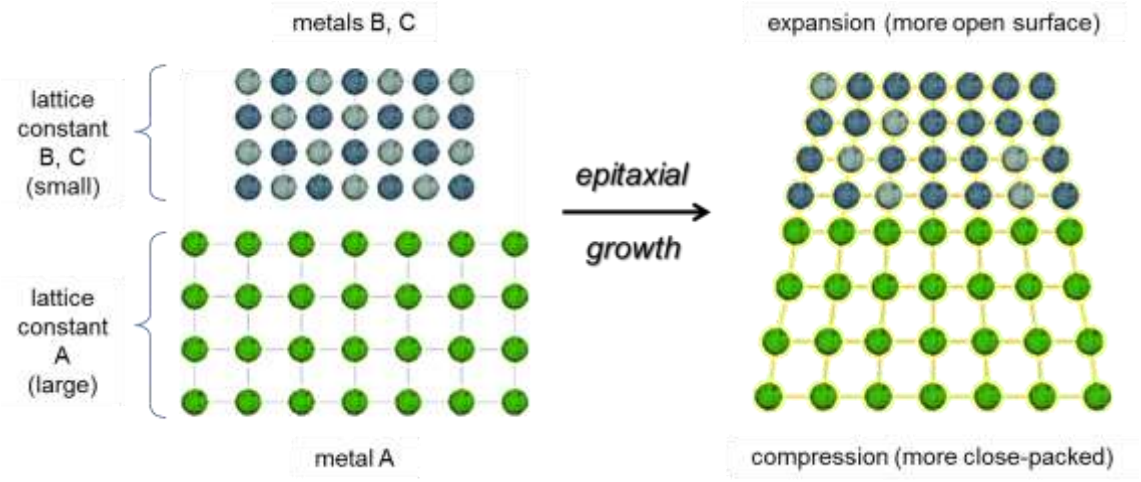

Figure 8. Generic model of strain for core-shell structures

1.3.1 Strain Due to Size

The relationship of increased strain for decreasing nanoparticle size is perhaps best understood through observation of the shifting and broadening of x-ray diffraction peaks

of nanocrystalline powders consisting of particles approaching a few nanometers in diameter. The Scherrer relationship gives quick estimates of size based on this trend. The broadening of peaks is due to both the increased number of diffracting crystallite domains and the effects of an increased percentage of surface area, whereas, shifts in the peaks account for the contraction of the nanoparticle ensemble. The increase of the surface area to volume ratio gives rise to higher dependence on the effects of surface tension, which results in expansion and compression of the atomic arrangement to minimize the energetics of the system as discussed in the section on nanoparticle synthesis. The dependence of strain on particle size, where smaller particles contract to a higher degree to lower surface area, can be modeled by the Gibbs-Thompson equation.[65,66] For single component nanoparticle systems, the linear strain gradient from the core to the surface can be expressed as an exponential function:

$$\Delta a_n = \Delta a_{max} e^{\frac{-(m-n)a_{bulk}}{\kappa}} \; ; \; (0 < n \leq m)$$

where a_n is the atomic displacement (lattice parameter) of the nth atom from the origin (center of a chain of atoms from core to surface), $n = 0$ is the origin, a_{max} is the maximum value of the relaxation (contraction) at the surface (maximum lattice parameter), a_{bulk} is the bulk parameter, κ is the relaxation length, and m is the total number of atoms in the linear chain of both directions from the origin, toward core and surface.[65,67] It could be assumed that having a smaller size causes some compression and expansion of atoms (to become more close-packed on the surface, but still fill a larger, more spherical volume), reducing the surface area (and surface energy), where the average total displacement

would tend to be more compressive versus the bulk (relaxation of surface atoms winning out over expansion); however, this is complicated by capping ligands, particle shape, impurities in the metal matrix, metal identity (3d vs. 4d vs. 5d metals), and oxidation state, the latter of which is coupled to the size as well, so that this assumption may not generally hold true. For example, Sanchez et al found net expansion of the lattice parameters of nanoparticles below 10 nm of Ag, Pd, and Rh, (4d metals) whereas the heavier elements Au and Pt (5d) were compressed.[6] Iridium was found to have similar constants to the bulk. Relativistic effects for the 5d metals and d-orbital overlap were reasoned to be the source for these deviations in expected behavior. However, earlier work reports both expansion and compression of Pd nanoparticle lattices, presumably dependent on the presence of impurities adsorbed into or onto the Pd surfaces, such as hydrogen and oxygen.[68] Metal oxide and carbide compounds have also been found to have contracted parameters.[69] While contraction is perhaps a fair expectation, it must be emphasized for catalysis applications, the surface and core of particles experience different degrees of both tensile and compressive strain which may have a canceling effect. Determining the real strain at the surface of particles is still challenging and is being addressed by our collaborators. Because of the current limitations toward experimentally sampling nanoparticle surfaces specifically at global scales, development of theory in combination with experimental diffraction is believed to bring about significant progress in this regard.

1.3.2 Twinned Crystals

Twinned nanoparticle morphologies commonly encountered, such as twinned decahedra (the ever popular Au nanorods are essentially elongated twinned decahedra) and icosahedra of face-centered cubic (FCC) crystal structures possess multiple twinned crystal boundaries. Each of these important examples is made up of (111)-terminated tetrahedra which meet along faces to form a polycrystalline nanoparticle. For instance, an icosahedron has 20 faces, 30 edges, and 12 vertices from 20 tetrahedral subunits. Related in structure to the icosahedron, the twinned decahedron has 10 faces made from 5 tetrahedral subunits, with 15 edges and 7 vertices. Since these twinned structures do not perfectly fill the volume the atoms would normally occupy, strained structures result, with the majority of the displacement occurring along the boundaries of the tetrahedral subunits. There are some examples of catalysis by twinned icosahedral nanoparticles. Others have looked at the strain gradient in decahedral nanocrystals through computational studies.[70] Wu et al attributed higher activity of oxygen reduction catalytic activity of Pt_3Ni nanoicosahedra to strain effects along edges of the structure,[71] further supported by strain maps generated from molecular dynamics modeling. Lv et al also found higher activity for Pd icosahedra compared to other shapes and ascribed this to defects at the twinned boundaries resulting from the strain.[72]

1.3.3 Alloy Nanoparticles

Bimetallic alloy nanoparticles have been heavily studied for their improved performance in catalysis applications.[49,50,54,55,73-82] Alloy nanoparticles also experience

lattice strain, however, this is seldom discussed as an active participant in the catalysis mechanisms. Each metal in an alloy is displaced from its normal, bulk positioning, and this resulting in different electronic structure. That is to say, atoms of an alloy may not behave the same as atoms in monometallic bulk, because of lattice strain, in addition to charge transfer from the secondary metal, and multi-atom sites (ligand and ensemble effects). Changes in the composition of alloys coincide with changes in the degree of strain. Due to this, many works may invoke ensemble or ligand effects (composition) for improved performance, when lattice strain could be operative as well. The determination of surface strain displacement of alloy nanoparticles is discussed in the results section, however, it is duly noted that metal segregation of one metal over another in nanoparticle systems is common, and should also be accounted for in future studies.

1.3.4 Core-Shell Nanoparticles

Mismatching lattices at the interface between differing metal phases results in an atomic rearrangement. The crystal can either leave the misfit (creation of defects), to create a highly strained boundary, or it can distribute the strain through oriented alignment of the crystal domains. This can be accomplished in epitaxial growth of one metal on another. The displacement of atoms near the interface exists over several atomic layers surrounding the interface. In real systems, a combination of both epitaxy, and release of strain through defects will be present. The degree of the displacement, defect density, and range of the gradient in lattice parameters will depend on the lattice mismatch (identity of metals). The decay of strain versus the distance away from the

interface follows an exponential curve, similar to the function given in the section on size, but made more complex because of added interface (metal-metal interface and surface). An example of this curve versus the number of monolayers of Pt on Cu(111) was shown by Strasser and co-workers using lattice parameters measured from electron diffraction patterns.[63] Significant values of the average strain (between 1 and 2%) were observed, even beyond a dozen monolayers for this system. The lattice mismatch for Pt and Cu is relatively large at ~8 %, yet their study highlights the importance of the strain effect. They found enhancement of the ORR activities of CuPt-Pt dealloyed core-shell nanostructures trended with increased compressive strain on Pt monolayers by the Pt-Cu core. Zhu observed a similar effect for Pt-Fe alloy nanoparticles,[83] and Wang also quantified the relationship between increased activity and decreasing Pt-Pt bond distance in Pd-Pt core-shell nanoparticles.[84] Montes de Oca studied the Pd shell thickness on Au cores and showed a dependence in strain versus the CO oxidation potential.[85] Other core-shell nanoparticle architectures have been studied also showing similar improved catalytic behavior for this structure type by tuning strain on the active surface.[58,86-88]

1.3.5 Limitations and Concerns for Catalysis

By carefully tuning the degree of lattice strain in a nanoparticle, the sorption energies of molecules can be optimized for a particular chemical reaction. This can be explained by a change in the d-band center of a metal nanoparticle as a result of lattice distortion generated from strain.[89,90] This depends on the element of interest, however, in general, expansive strain causes a reduction in orbital overlap, narrowing the d-band and raising

the d-band center; whereas compressive strain increases overlap, widening the d-band and lowering the d-band center. The altered d-band affects the molecule sorption energies, altering the catalytic activity.[91,92] Core-level electron binding energy shifts due to strain have also been studied.[93,94]

For some late transition metals as matrix elements, the d-band model is quite reliable for predicting catalytic activity. However, as a general descriptor it is still up for debate.[95,96] This is likely because of the inherent complexity of different reactions on metal surfaces, where many different binding species may compete for the main role in the rate of reaction. Not surprisingly, there are exceptions even for Pt. It has been observed in specific cases that both expansion and compression of surface atoms of Pt via lattice strain from sub-surface metals can lead to similar shifts in the d-band center, resulting in improved catalytic activity for both situations.[57] This was the case for Ag and Cu subsurface layers, where Cu compressed the Pt surface, and conversely, Ag expanded the Pt surface. It was reasoned that this discrepancy could be due to the differences in d-orbital overlap resulting from the 3d and 4d metals to the 5d metal.

The release of strain through defects will lessen the strain effect on catalysis by helping to relax the structure. Several mechanisms of strain release in nanosystems have been studied. One such case was examined by Wang et al, where a nearly ~40° reversible flip in the unit cell of Ni was observed when Ni nanowires were bent.[97] In another work by Bhattarai, defect generation at the interface of Au-Pd nanoparticles was studied by electron microscopy.[98] They found that Shockley partial dislocations, stacking faults, and misfit dislocations resulted in a more relaxed structure (lattice mismatch of ~5%) after

the synthesis. They also showed that Au diffused into the growing Pd shell to further accommodate the strained shell. A similar finding was revealed by Kwon et al for heterogeneous overgrowth of Au on PtCo alloy seeds in the synthesis of dumbbell structures, where they found many slipping plane defects in the Au layers near the interface.[99] The limitation for the strain effect in catalysis (strain release by defect generation and poor predictability) suggested by these studies could diminish its importance, but it can be argued as well that there is not yet enough understanding and fundamental research of this topic to draw such a conclusion, as the real limits of the strain effect have not been elucidated yet.

2.0 METHODS

2.1 Chemicals

Palladium (II) chloride ($PdCl_2$, 99%), gold (III) chloride trihydrate ($AuCl_3•H_2O$, 50% Au by wt.), rhodium (III) chloride hydrate ($RhCl_3•nH_2O$, 40% Rh by wt.), nickel (II) chloride hexahydrate ($NiCl_2•6H_2O$, 99%), potassium tetrachloroplatinate (II) (K_2PtCl_4, 99%), copper (II) chloride ($CuCl_2$, 97%), sodium iodide (NaI, 99.5%), sodium bromide (NaBr, 99%), sodium chloride (NaCl, 99.5%), sodium citrate dihydrate ($Na_3C_6H_5O_7•2H_2O$, 99.5%), L-ascorbic acid ($C_6H_8O_6$, 99%), hydrochloric acid (HCl, 37% by vol. in water), hydroxylamine hydrochloride ($NH_2OH•HCl$, 98%), perchloric acid ($HClO_4$, 70% by vol. in water), formic acid (HCOOH, 95%), potassium hydroxide (KOH, 99%), were all obtained from Sigma-Aldrich. Polydiallyldimethylammonium

chloride (PDADMAC, MW. avg. 150,000, 20 wt. % in water) was obtained from Aldrich. Cetyltrimethylammonium chloride (CTAC, 95%), and polyvinylpyrrolidone (PVP, MW. avg. 40,000, 99%) were obtained from TCI America. Hydrazine monohydrate ($H_2NNH_2 \cdot H_2O$, 98%) was obtained from Alfa Aesar. Sodium tetrachloropalladate (II) (Na_2PdCl_4, 99%) was obtained from Strem Chemicals. Cetyltrimethylammonium bromide (CTAB, 99%) was obtained from CalBioChem. Sulfuric acid (H_2SO_4, 95%) and sodium hydroxide (NaOH, 97%) were obtained from BDH. Sodium borohydride ($NaBH_4$, 99%) was obtained from Fluka. Iron (III) chloride ($FeCl_3$, 98%) and methanol (CH_3OH, 99.8%) were obtained from Acros. Nitrogen, oxygen, and carbon monoxide were all obtained from Airgas. The acidic Au and Pd metal precursors were prepared by dissolving the chloride salts in dilute HCl. The mixtures were gently heated for 1 hour to ensure complete dissolution. Deionized water (DI H_2O, 18.2 Ω) was used in all experiments.

2.2 Synthesis of Pd Nanocrystals

Synthesis procedures for differently shaped Pd nanocrystals were developed in lab and are described in detail below. The preparation of Au nanocrystals could be accomplished by following procedures from the literature.[11,100] Since no changes to the procedures were made in the synthesis of Au substrates, they are not described here, but can be found in the referenced publications.

2.2.1 Pd Cubes

Palladium nanocubes of different sizes exposing (100) facets were synthesized by adapting procedures from the literature or developing them in our lab. The Pd cubes can be synthesized using different capping agents. The commonalities between the procedures are that bromide or iodide ions must be present to bind the (100) facets in the aqueous growth solutions, and that ascorbic acid is always used as the reducing agent.

For ~30 nm Pd nanocubes capped by CTAB, a procedure developed by Niu et al. was modified.[12] The adapted procedure for Pd nanocubes was heavily utilized later in much of our group's following work.[101-106] The original procedure was altered by adding 200 μL of 0.1 M sodium iodide to the solution prior to reduction. The details of the procedure are given below. First, to a 20 mL scintillation vial was added 0.05 g of CTAB surfactant. Then 9.3 mL of DI water was added and the solution was sonicated to dissolve the CTAB (or heated briefly with an air gun). To this solution was then added 0.500 mL of 0.01 M H_2PdCl_4, which was prepared previously by adding a diluted HCl solution to $PdCl_2$ salt. Next, 0.200 mL of aqueous 0.1 M NaI was added and the solution color changed from a bright orange to a deep reddish brown. This indicated the incorporation of iodide ions into the precursor complex. A stir bar was added and the vial was then placed in an oil bath set to 95°C and a stir rate of 200 RPM. The bath was allowed to equilibrate for approximately five minutes before a rapid injection of the reducing agent to the solution. For this, a 0.200 mL aliquot of 0.04 M ascorbic acid was used. The vial remained in the bath for approximately 30 minutes or until the solution color changed from the dark reddish brown to a green-tinted transparent brown. The

color change indicated the formation of the Pd nanoparticles and the disappearance of the metal precursor. The solution was then allowed to cool, the stir bar was removed, and then the particles were collected via centrifugation at 8000 RPM. The reaction was scaled up by repeating this process for 7 other solutions and redispersing the collection of 8 batches in 10 mL of DI water for later use.

For ~15 nm Pd nanocubes capped by PVP, a procedure developed by Jin et al. was adapted for use.[107] This procedure gave the most uniformly shaped cubes with smallest variation in size, and so was used in the lattice strain HRXRD study. Briefly, 600 mg of KBr, 105 mg of PVP, and 60 mg of ascorbic acid were dissolved in a total volume of 8.0 mL of DI water in a 20 mL scintillation vial. An oil bath was set to 100°C and the vial was placed in the bath with a stir bar to stir at 500 RPM. While the bath was equilibrating, a solution of 57 mg Na_2PdCl_4 dissolved in 3.0 mL of DI water was prepared. The second solution was injected into the first approximately 10 minutes after it was placed in the bath. The vial was then capped and the solution was removed 3 hours later. The colloid was collected via centrifugation at 8000 RPM. The particles were rinsed and redispersed in DI water twice after this to prepare them for XRD and TEM analysis.

For ~9 nm Pd nanocubes, PDADMAC was utilized as the stabilizer. This procedure was developed in our lab by substituting PDADMAC for CTAB in the previously adapted CTAB-capped Pd cube procedure (iodide ions present). Specifically, 0.050 mL of PDADMAC solution was mixed in 10 mL of water. Then 0.500 mL of 0.01 M H_2PdCl_4 and 0.200 mL of NaI were added and the solution was gently mixed. The color

changed from a light yellow to a deep red indicating the ligand exchange in metal precursor complex. The solution was then heated in an oil bath set to 95°C for 5 minutes, uncapped, and stirred at 200 RPM. After the temperature equilibrated, 0.200 mL of 0.04 M ascorbic acid was rapidly injected and the reaction continued for 30 minutes or until the disappearance of the dark red color to form a brown-colored transparent solution. The solution was then removed from heat, allowed to cool, and the particles were collected via centrifugation at 12,000 RPM and by adding an equal volume of acetone to disrupt the polymer stabilization. The nanoparticles were redispersed in 1.25 mL DI water for later use as substrates for the cuboctopod growth in PDADMAC solution.

The cationic polymer PDADMAC could also be used to make larger cubes by using CTAB in a mixed stabilizer system. Briefly, a solution was prepared similarly except with 0.05 g of CTAB being added after the PDADMAC addition. The size of particles fell between the two monostabilizer methods at approximately 20 nm, yet the distribution of size was much greater and so the synthesis was not as useful in experiments going forward.

Prior to the PDADMAC synthesis of small 9 nm Pd cubes, we developed a seed-mediated route to CTAB-capped ~12 nm Pd cubes.[101,102,104,105] These CTAB-capped cubes were utilized for the Rh and Ni overgrowth studies, where smaller bimetallic and trimetallic particles were synthesized. A fresh solution of 0.02 M $NaBH_4$ was prepared and placed in an ice bath for future use. Then 9.3 mL of DI water was added to 0.05 g of CTAB in a 20 mL scintillation vial and sonicated to dissolve. Then 0.250 mL of 0.01 M H_2PdCl_4 was added to the solution and it was gently shaken. A stir bar was added to this

solution and the vial was placed on a stir plate to stir at room temperature. The solution was stirred until a vortex was established and 0.450 mL of the chilled sodium borohydride solution was injected rapidly. The reaction was allowed to proceed for 1 hour before these Pd seeds were used in the next step. A separate vial was prepared with 0.05 g of CTAB and 9.3 mL of DI water. The mixture was sonicated to dissolve CTAB and 0.500 mL of 0.01 M H_2PdCl_4 was added. Then 0.050 mL of 0.1 M sodium iodide was added and the solution was placed in an oil or water bath set to 60°C with a stir bar stirring at a rate of 200 RPM. After 5 minutes, 0.050 mL of the previously prepared Pd seed solution was added, which was then followed directly by an injection of 0.100 mL of 0.04 M ascorbic acid. The solution was left to heat for 2 hours at this temperature and then removed from heat, cooled, and centrifuged at 14000 RPM to collect the nanoparticles. These were then scaled up in the same manner as the 30 nm Pd cubes for later use as substrates.

2.2.2 Pd Octahedra

Octahedral Pd nanocrystals exposing a majority of (111) crystal facets were synthesized in three different sizes using CTAB and PDADMAC as capping agents. For ~60 nm octahedra, the procedure by Niu et al.[12] was modified.[104] First, 8 batches of ~30 nm Pd nanocubes were synthesized as described above, except that 0.030 mL of 0.1 M NaI was used in each reaction, and the colloids were combined and redispersed in 10 mL as a seed solution for the overgrowth step. Then 0.36 g of CTAB and 10 mL of DI water were sonicated in a 20 mL scintillation until the surfactant was dissolved. Next, 0.250

mL of 0.01 M H_2PdCl_4 and 0.050 mL of 1 mM sodium iodide were added and the vial was placed into an oil bath set to 30°C with a stir bar to stir at 200 RPM. After 5 minutes, 0.080 mL of the previously prepared Pd cube solution was added to the growth solution, followed by 0.250 mL of 0.04 M ascorbic acid. The reaction was allowed to proceed for 40 hours before removal and collection of the nanoparticle by centrifugation at 6000 RPM. Eight reactions were done in this fashion and the colloids were collected and redispersed in 5 mL DI water for later use.

Octahedral CTAB-capped Pd nanocrystals ~30 nm on edge were synthesized by a 3-step seed-mediated approach.[101,102,105] A concentrated ~12 nm Pd cube solution containing 8 batches was first synthesized as described above. Then 0.36 g of CTAB was added to 10 mL of DI water and this was then sonicated to dissolve the surfactant. Next, 0.250 mL of 0.01 M H_2PdCl_4 was added followed by 0.050 mL of 1 mM sodium iodide. A stir bar was then added to the scintillation vial containing this solution and the vial was placed in an oil bath set to 30°C. After 5 minutes, 0.200 mL of the previously prepared concentrated ~12 nm Pd cube solution was added followed by 0.250 mL of 0.04 M ascorbic acid, and the reaction was allowed to proceed for 40 hours before removing and collecting the particles via centrifugation at 9000 RPM. The reactions again were scaled up by running 8 reactions and combining the precipitates together and redispersing in DI water to a volume of 5 mL.

Smaller, ~16 nm Pd octahedra capped by PDADMAC were prepared in one step. First, 60 mg of ascorbic acid was put into a 20 mL scintillation vial containing 7.0 mL of DI water and 1.0 mL of PDADMAC solution. A stir bar was added the vial was placed

on a stir plate to stir. Meanwhile, 57 mg of Na_2PdCl_4 was dissolved in 3.0 mL of water in a separate vial. The solution containing PDADMAC and ascorbic acid was then moved to an oil bath set to 65°C stirring at rate of 200 RPM. After a 5 minute equilibration period, the Pd precursor solution was injected into the heated solution containing the polymer stabilizer and reducing agent, and this solution was then capped and allowed to stir at this temperature for 2 hours. The vial was then removed from heat to cool. A 1 mL aliquot of this concentrated solution was then diluted in 50/50 acetone/water solution up to a total volume of 10 mL. This solution was then centrifuged and the precipitate was then collected and rinsed twice more in the same manner in preparation for TEM and SEM analysis.

2.2.3 Pd Cuboctopods

Palladium cuboctopods capped by PDADMAC were synthesized by a 2 step seed-mediated approach. First ~9 nm PDADMAC-capped Pd nanocubes were synthesized as described above for use as seeds. One batch of these cubes was synthesized, collected, and redispersed in 1.25 mL and set aside. In a 20 mL scintillation vial, 0.365 mL of PDADMAC solution was added to 10 mL of DI water. Then 0.250 mL of 0.01 M H_2PdCl_4 and 0.050 mL of 1 mM NaI solution were added while stirring with a stir bar. This solution was then placed in an oil bath set to 30°C with a stir rate of 200 RPM for 5 minutes. After this time, 0.200 mL of the Pd cube solution was added and this was followed by 0.250 mL of 0.04 M ascorbic acid. The reaction was allowed to proceed for 2 hours before removal and centrifugation at 10,000 RPM. The particles were rinsed

with DI water and precipitated in the same manner twice for characterization. Products without noticeably different morphology could also be prepared with the same molar amount of bromide ions instead of iodide ions in the overgrowth solution.

2.3 Synthesis of Rh Bimetallic Nanoparticles

Overgrowth of Rh with control of thickness on differently sized and shaped Pd and Au nanocrystal substrates was performed via a two-step procedure using CTAB surfactant and ascorbic acid as the reducing agent.[104] As-synthesized Pd-Rh core-island-shell nanoparticles could then be transformed into nanoboxes and nanoframeworks through different redox pathways.[102,104] Yolk-shell Au-Rh nanoparticles could additionally be generated similarly via acid etching of a Pd interlayer.[102]

2.3.1 Pd-Rh and Au-Rh Core-Island-Shell Nanoparticles

A Pd substrate solution containing either 30 nm cubes, 60 nm octahedra, or 12 nm cubes capped by CTAB was first synthesized according to the previously described procedures (8 batches concentrated together and redispersed in 5 or 10 mL of DI water to give a nominal Pd atom concentration of ~ 4.0 mM). Then 9.3 mL of DI water and 0.05 g of CTAB were added to a 20 mL scintillation vial and sonicated to dissolve the surfactant. Depending on the desired shell thickness, 0.100, 0.200, or 0.500 mL of 0.01 M $RhCl_3$ (1, 2, or 5 μmol Rh ions, respecitively) was then added to this solution. Next, 0.500 mL of the Pd substrate solution was added (in the case of Pd octahedra, 12 nm Pd cubes, and both cubic and octahedral Au substrates, 0.025 mL of 0.01 M sodium iodide

was added at this time to promote the Rh overgrowth). The vial was then moved to an oil bath set to 95°C with stirring at a rate of 200 RPM. After 5 minutes, 0.500 mL of 0.04 M ascorbic acid was injected and the reaction was allowed to proceed for 30 minutes. The reaction was then removed from heat to cool, and the particles were collected via centrifugation at 7000 RPM.

To form Au-Rh yolk-shell nanoparticles, cubic Au-Pd core-shell nanoparticles were first synthesized following a procedure developed by our lab.[101] Then, 0.500 mL of the 1 mL solution containing the Au-Pd cubes collected from this reaction was used in place of the Pd/Au substrates described above in the overgrowth of Rh. This generated trimetallic Au-Pd-Rh core-shell-island-shell nanoparticles. The nanoparticles were collected similarly and then redispersed in a solution containing 0.05 g CTAB, 10 mL of DI water, and an acid etchant (0.500 mL 0.01 M HCl). This solution was then transferred to a 50 mL pressure vessel that was sealed and placed in an oven set to 110°C to react for 48 hours to ensure complete etching of the Pd interlayer. The particles were collected again via centrifugation and rinsed for TEM characterization.

2.3.2 Pd-Rh Phase-Segregated Nanoboxes

Bimetallic Pd-Rh phase-segregated nanoboxes were synthesized by continued heating of the Pd-Rh core-island-shell reaction solution. First, core-island-shell nanoparticles with 2 μmol of Rh overgrowth were synthesized and removed from heat. The original reaction solution was then poured into a 50 mL pressure vessel which was sealed and placed into an oven set to 110°C. The vessel was left at the elevated temperature in the

oven for 48 hours before removing for cooling. The particles were then collected via centrifugation and rinsed in the same manner as was done for the core-shell structures. Using more or less metal precursor in the overgrowth step resulted in either incomplete nanobox formation, or over-etching; both were likely due to the metal precursor acting as a Lewis acid and the stability of the structure in these conditions being dependent on the pH of the solution.

2.3.3 Rh Island Nanoframeworks

Porous Rh island-nanoframeworks were synthesized in a similar fashion as the Pd-Rh nanoboxes, but with the following exceptions: 1) the original reaction solution was centrifuged once and the particles were collected and redispersed prior to the post-synthesis heat treatment, and 2) an etchant was added in the form of 0.500 mL of dilute, 0.01 M HCl, or aqueous $FeCl_3$ could be used alternatively. The washing of the original solution was done to remove any excess and unreacted reducing agent to promote the etching process. In this case, different sizes of hollow Rh structures could be generated by tuning the Rh precursor amount in the overgrowth step.

2.4 Synthesis of Core-Sandwich-Shell Nanoparticles

The novel shaped core-sandwich-shell nanoparticle archetype was synthesized by applying the CTAB-capped cubic or octahedral Pd nanocrystals as substrates for stepwise Ni and Pt reduction by hydrazine in aqueous solution.[105] Quaternary metal nanoparticles were synthesized by using Au-Pd cubes as substrates for the Ni-Pt overgrowth.[105]

2.4.1 Pd-Ni-Pt Cubes and Octahedra

Palladium substrates that were CTAB-capped were first prepared according to previously described procedures. Then 0.05 g of CTAB was combined with 10 mL of DI water in a 20 mL scintillation vial. The vial was sonicated to dissolve the surfactant. Next, 0.500 mL of Pd substrate solution (30 nm cubes, 30 nm octahedra, or 12 nm cubes) was added followed by an amount of Ni precursor (0.01 M $NiCl_2$). For ~2.5 nm or ~4.1 nm Ni sandwich layers, 0.100 mL or 0.200 mL, were added, respectively. Increasing the Ni precursor amount further (in excess of 0.200 mL) reduced the uniformity in the coating as the larger Ni domains become magnetic and start to agglomerate and precipitate out of the growth solution as visibly suspended black specks. After this, 0.500 mL of ~1.0 M hydrazine was added to the solution, and the vial was capped, vortexed, and placed in an oil (or water) bath set to 50°C, without stirring. A color change from light brown to gray indicated the reduction of Ni after approximately an hour and 0.50 mL (or 0.100 mL for thicker shells) of 0.01 M K_2PtCl_4 was then injected and the vial resealed and placed back into the bath for an additional 30 minutes. The solution became darker again and the reaction was removed from heat and the particles were collected via centrifugation at 4000 RPM.

2.4.2 Pd-Pt Cubes

The cubic Pd-Pt nanoparticles were synthesized from ~30 nm Pd cubes following the same procedure as for Pd-Ni-Pt nanoparticles, but with the following modifications: 1)

0.200 mL of 0.04 M ascorbic acid replaced hydrazine as the reducing agent, 2) No Ni ions were added, and 3) 0.250 mL of 0.01 M K_2PtCl_4 was used for the Pt overgrowth.

2.4.3 Cubic Au-Pd-Ni-Pt Quaternary Metal Nanoparticles

The Au-Pd cubic cores were first synthesized according to our previously published procedure,[101] with modifications, and used as substrates in the overgrowth of Ni and Pt (0.500 mL of the Au-Pd cube solution from one reaction concentrated in 1 mL). The procedure was modified by scaling up the reaction 10 times and using a 250 mL beaker instead of a scintillation vial. Notably the quality of the substrates was increased by this method, which is normally not the case in nanoparticle synthesis.

2.5 Materials Characterization

The materials were characterized by electron microscopy, x-ray diffraction, and spectroscopy techniques. The preparation of materials for characterization and a description of the principles of the different characterization techniques are given in this section.

2.5.1 Transmission Electron Microscopy (TEM)

The operating principles of transmission electron microscopy are nearly identical to optical microscopy, except that electrons are used instead of light to gain information about structure (schematic shown in Figure 9b, and Figure 10a). Because the electron acts on scales much smaller than those of the wavelengths of visible light, the resolution

of electron microscopy is far superior to optical microscopy, with the caveat that fine details can only be observed if the material interacts with electrons (primarily used for analysis of conducting and semi-conducting materials). Electrons may be transmitted through the material or scattered. The extent of scattering scales with the atomic number or heaviness of the atoms in the materials and so contrast can give information on the composition. Transmitted electrons are observed as bright regions in images, whereas electrons that are scattered do not make it to the screen and so a dark spot is observed. In the case of metal nanoparticles, they appear as dark spots in the image, while the carbon film they are supported on will be transparent. Scattered electrons and radiation generated by the many different scattering processes return much more information and this is discussed in more detail later in the chapter.

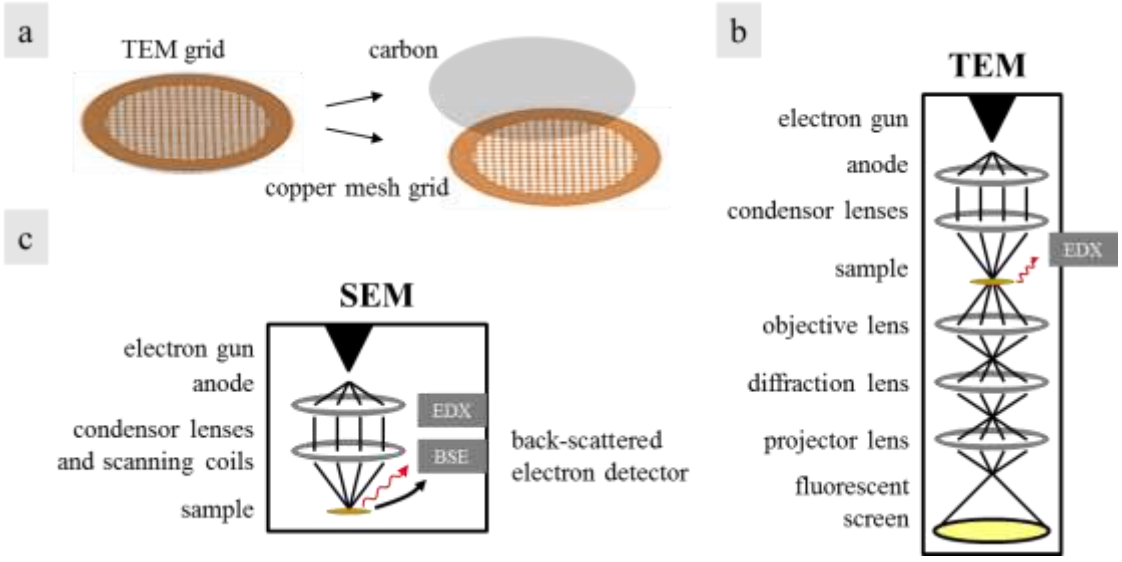

Figure 9. Illustration of a typical copper TEM sample grid (a) and schematic illustrations of TEM (b) and SEM (c).

Samples were prepared for TEM analysis by repetitive centrifugation and redispersion of nanoparticle precipitates in DI water and subsequent loading of portions of these washed and concentrated nanoparticle solutions onto thin carbon coated copper grids (Figure 9a). Typically, the final concentrated solution contained 0.100 mL of colloid, and of this total volume, 20 µL droplets were 'drop-cast' onto the grid, by placing the grid directly above a filter paper. This resulted in an even distribution of particles across the surface, which was preferred for single particle analysis. After the dropcast, the grid was picked up off the filter paper using fine tweezers, and a 2 µL droplet of sample was placed on the suspended grid and allowed to dry in air. This resulted in a ring of particles around the edge of the drying droplet, which was preferred in observing the self-assembly of many particles at once in low-magnification images. The instrument used was a JEOL JEM 2010F and was operated at 200 kV.

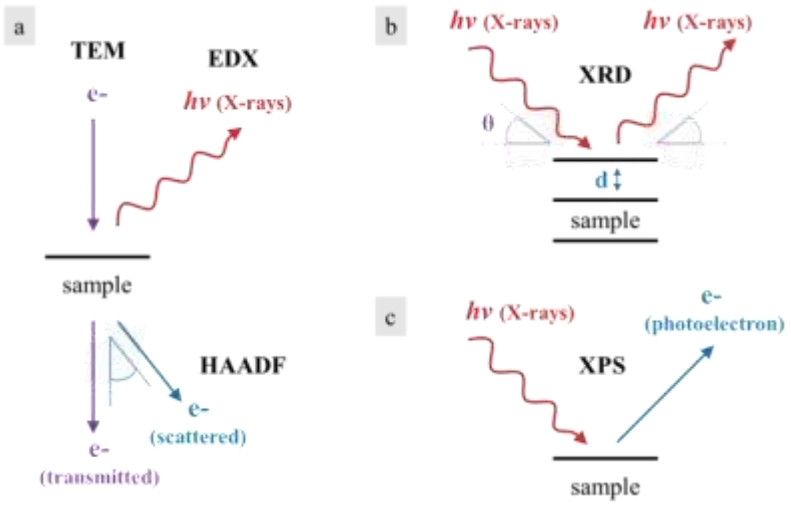

Figure 10. Schematic illustration of how electrons and x-rays are used to obtain information of structure and composition in a) TEM, b) XRD, and c) XPS.

2.5.2 Scanning Electron Microscopy (SEM)

The scanning electron microscope gives information on the 3D structure of the material, as back-scattered electrons are detected (schematic shown in Figure 10c). This is distinguished from TEM where typically transmitted electrons are observed, and the 2D cross-sections of TEM sometimes do not give enough information to guess at the overall 3D structure. The SEM images that result show bright areas for high-scattering materials, and dark regions for low-scattering elements.

Samples were prepared for scanning electron microscopy similarly to TEM, except that the particle droplets were placed on a square silicon wafer instead of the copper TEM grids. These sample supports were prepared by pre-slicing from a larger wafer. The wafers with the dried sample droplet would be placed on a piece of double-sided copper tape which was fixed to the sample holder for SEM analysis. In some instances, conductive silver glue was applied between the copper tape and the silicon wafer. This enhanced the imaging by making better contact at the interface, increasing the conductivity between the sample and sample holder. The instrument used was a JEOL JSM6340F. For the analysis of PDADMAC-capped nanoparticles, a benchtop Novascan UV cleaner and in-situ IBSS cleaner were used to clean the samples further after washing to prepare them for SEM. The instrument used for these particles was a JEOL JSM7800F.

2.5.3 High Resolution TEM (HRTEM)

Two-dimensional images of crystal lattices can be obtained at higher magnifications in TEM, and this is generally referred to as 'high-resolution' TEM or HRTEM for short. These images are a result of a combination of the diffraction, transmission, and other scattering of electrons as they interact with a crystal lattice. In order for this to occur, the particle size must not be so large that the electrons cannot penetrate the material and is related to the mean free path. There are several typical patterns that can be observed for the face-centered-cubic structure of the metals discussed. Most often encountered (and measured) are those of the low Miller index planes, for example (200), (111), and (220) d-spacings from a zone axis of [100], [110], and [111], respectively. All of the HRTEM images were acquired in our studies using the same JEOL JEM 2010F TEM operated at 200 kV at magnifications usually greater than 250,000 times. The HRTEM lattice d-spacing measurements were calibrated using those obtained for large and thin Au nanoplates as a standard.

2.5.4 High Angle Annular Dark Field TEM (HAADF)

It is possible to achieve images in TEM of scattered electrons, similar to SEM (shown schematically in Figure 10a). This is done by placing an aperture underneath the sample which blocks the transmitted beam, but allows the scattered electrons beyond a specific angle to be collected on a ring detector and converted into an image. The technique, called High Angle Annular Dark Field TEM allows for 3D images to be obtained, because of the nature of the scattered electrons. The contrast in these images depends

more-so on the scattering properties (atomic number) of the material and so can be used to more accurately confirm local composition and structure. As in SEM, the support (carbon) shows as a dark field because of low scattering and the metal nanoparticle samples are observed now as brightness due to high scattering. High resolution lattice images can also be produced in this mode, and d-spacing measurements can be obtained. The HAADF TEM images were obtained on a FEI Probe Cs Corrected Titan TEM using a Fischione HAADF detector.

2.5.5 Scanning Transmission Electron Microscopy and Energy Dispersive X-ray Spectroscopy (STEM/EDX)

Energy dispersive X-ray spectroscopy is an analytical technique that often accompanies the electron microscope. This technique determines the composition of a material based on the energy of X-rays emitted as a result of the scattering of high energy electrons in the beam (see Figure 10a). The x-rays are generated from an electronic transition which occurs due to collisions of core electrons with those from the beam. An electron collides with and transfers energy to an inner core electron. Having lost a core-level electron, one of the outer shell electrons drops in to fill the vacancy releasing an X-ray characteristic for this transition for that specific element. The different transitions that are possible are shown schematically in Figure 11. The process is rather complex and chaotic as it produces an X-ray and two electrons which may or may not collide with additional electrons, and X-rays are produced even very far away from the beam (relatively speaking) because of the chained reaction, hence the term ‘energy-dispersive’.

This makes local information of single particles difficult and the information is limited to the surfaces for objects larger than nanoscale because of the mean free path of electrons in the materials. Other more sensitive processes involving the electron beam and the sample, such as the production of Auger electrons, can also be used to gain information on the material; however, they are discussed elsewhere.

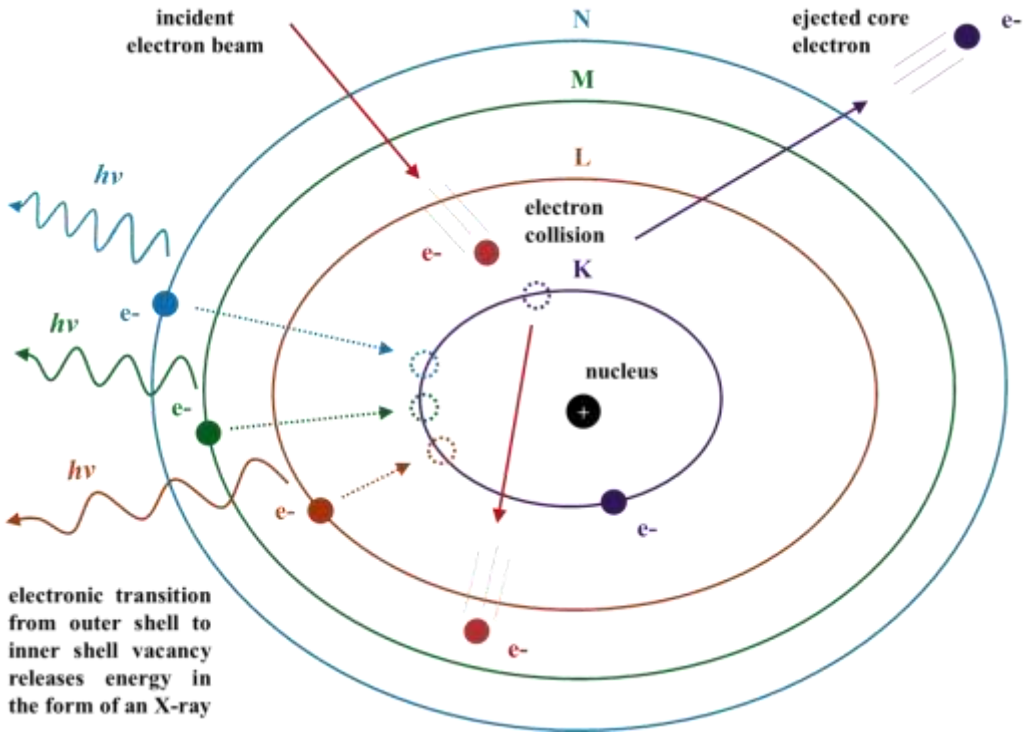

Figure 11. Schematic illustration of energy dispersive X-ray spectroscopy.

Some TEMs are equipped to scan in HAADF mode akin to SEM. If this is accompanied by EDX, a powerful characterization technique results, STEM/EDX. The point-by-point line-scanning (or full area mapping) combined with EDX, yields plots (or

maps) of elemental distributions. With aberration-corrected TEMs (accounting for the astigmatism that results from inevitable imperfections electromagnetic lenses), the resolution of this technique can reach the atomic level, providing colorful composition maps, which are extremely useful to the nanoparticle scientist.

The STEM/EDX images and composition maps for our studies were done using an FEI Probe Cs Corrected Titan STEM operated at 200 kV. The EDX maps were generated using ChemiSTEM technology with four windowless SDD detectors. The instrument utilizes a spherical condenser lens aberration corrector and X-FEG with a probe current of 0.4 nA in 0.31 nm spots and achieves resolution of 0.08 nm in addition to a highly efficient X-ray collection rate.

2.5.6 Selected Area Electron Diffraction (SAED) and Fast Fourier Transform (FFT) Pseudo-SAED for Enhanced Contrast Imaging

Electron diffraction is an extremely useful TEM technique as it can reveal the degree of crystallinity and give structural information of crystal orientation and composition. The image of diffraction is created by inserting an aperture beneath the specimen and objective lens, but before the projected image plane. If the material is crystalline, thin, and at proper orientation, a pattern in reciprocal space that is essentially an inverse of the lattice in real space is generated (Figure 12). Bright spots can be indexed according to the zone axis, and so measurements can be made between spots in units of reciprocal space (1/nm).

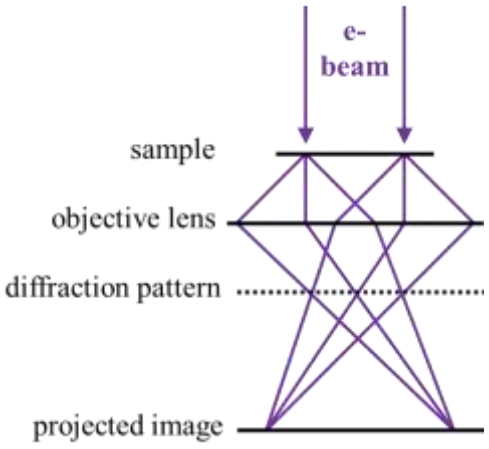

Figure 12. Schematic illustration of electron diffraction in TEM.

The Fourier transformation function can also be used to mathematically convert a 2D lattice image into a pseudo SAED pattern. This is not a 'real' electron diffraction pattern, however, it can still be used to gain similar information. This function has actually become essential to electron microscopy (beyond so many applications elsewhere), because it is so useful to do what's call "Live FFT" while acquiring the CCD image to improve the focus, correct astigmatism, and alignment, etc. In this mode a continuous pattern can be generated from the area being surveyed and so one can tune the beam with both the pattern and the image in view. This simplified pattern can also then be used to enhance the contrast of the original image, by masking the observed spots, removing the background, and performing an inverse of the Fourier transform after the image is acquired. This all is accomplished because the Fourier transformation essentially results in a 'spectrum' of the different frequencies observed, and so periodic bright and dark lines in a 2D lattice image will give a 2D spectrum (pattern) similar to SAED. For most

purposes, there is not much of an advantage in performing SAED over the FFT function, because the FFT is so rapidly and easily done in comparison. The SAED and FFT patterns allow identification of the crystal structure and orientation. The d-spacings of the materials can also be determined by indexing and measuring the distances between spots, then taking the reciprocal of these values. These measurements can then be compared to bulk spacings.

2.5.7 X-ray Diffraction (XRD)

Perhaps the most significant limitation of electron microscopy (and there are few for the technique with regard to materials science) is the low sampling rate, where it takes a great deal of time to sample a significant portion of the batch, and so one must be cautious in extending the conclusions from analysis of just a few particles to the rest of the ensemble. For this reason, electron microscopy of materials is greatly complemented by global techniques such as XRD.

In powder XRD, X-rays are typically generated by a copper K_α source with a wavelength of ~ 154.18 pm. The X-rays are directed toward the sample at different incident angles as the independent variable. The X-rays diffract from atoms in the sample and reach the detector at varying intensities dependent on the angle of the reflection (Figure 10b). This occurs because of constructive and deconstructive interference as the X-rays pass and reflect through multiple atomic planes. The Bragg condition must be met for diffraction to occur and is given by the relation:

$$n\,\lambda \;=\; 2\,d\,sin(\theta)$$

where d is the spacing between diffracting planes, θ is the angle of the reflection, n is the diffraction order, and λ is the wavelength of the incident X-ray. For face-centered-cubic systems, the d-spacing of atomic planes is related to the Miller indeces (h, k, l) by the following equation:

$$d \;= \frac{a_0}{\sqrt{(h^2 \;+\; k^2 \;+\; l^2)}}$$

where a_0 is the lattice parameter of the unit cell. The equations can be combined to index the diffraction peaks in a spectrum. It is also possible to measure the crystallite size by using the Scherrer method:

$$\tau \;= \frac{K\,\lambda}{\beta\;cos(\theta)}$$

where τ is the average size of the domains, K is a shape factor with value close to unity (typically 0.9), λ is the X-ray wavelength, β is the full line (peak) width at half the maximum intensity (FWHM), and θ is the Bragg angle. The peaks become broader as the crystallite domain size decreases to the nanoscale, because of increased contribution of lattice strain and because of a larger numbers of diffracting crystallite domains.

Since electrons in the lattice scatter X-rays and the concentration of electrons is periodic in the crystal lattice, the amplitude of scattering will be proportional to the periodicity of electrons, according to the Bloch theorem. Electron orbitals of different atoms in a crystal lattice will have some overlap, so it can be imagined that a crystal consists of one large molecular orbital, which is envisioned as a Bloch wave, since it

repeats periodically. The Schrödinger equation can then be set up for a periodic potential, and the wave function takes the form:

$$\Psi(r) = e^{ikr}\, u(r)$$

where Ψ is the Bloch wave, r is the position, k is the crystal wave vector, and u is a periodic function with the same periodicity as the crystal. This gives rise to the concept of electronic band structures of materials.

Samples were prepared for powder XRD by scaling up reactions and concentrating nanoparticle solutions in 0.100 mL of DI water. A 0.020 mL aliquot of the resulting colloid was dropcast onto a thin glass slide and allowed to dry. This was repeated until all of the solution was used. The powder XRD experiments were performed using a benchtop Bruker AXS D2 Phaser diffractometer using a copper Kα source with λ = 0.15418 nm.

2.5.8 High Resolution Synchrotron-Based XRD (HRXRD)

A synchrotron is a particle accelerator that moves electrons to relativistic speeds. The high energy electrons generated at a synchrotron ring release high energy X-ray radiation at a large flux with an extremely narrow band of wavelengths. Because of the high energy flux and narrow distribution of wavelengths, synchrotrons can be used to perform a myriad of high quality X-ray spectroscopic and diffraction experiments.

The HRXRD for our work was done at the Advanced Photon Source (APS) at Argonne National Laboratory (ANL). The data was collected at beamline 11-BM which

is the powder diffraction beamline. Samples were prepared by slowly injecting 0.020 mL of highly concentrated colloid dispersions into Kapton tubes (transparent to X-rays), ~2-3 cm in length and 0.8 mm in diameter using a microsyringe. The tubes were then left to dry in a dessicator for 48 hours before they were sealed with epoxy. The capillary was then mounted on the 11-BM spinner, operated at 4,200 RPM, which improves uniformity and statistics of the measurements. Two one-hour measurements of the same samples were acquired at room temperature to be added later. The wavelength of the synchrotron radiation was 0.0413874 nm (~30 keV), and the spectra were collected over a 2θ range of 0° to 60°, using 12 independent Si(111) detectors. The sampling step was 0.005°, and there was a counting time of 0.3 seconds per step. The detailed analysis of the HRXRD experiments and molecular dynamics (MD) simulations performed on Pd cubes was done by our collaborators at University of Trento Italy and are not discussed here. The use of the APS at ANL was supported by the U.S. Dept. of Energy Science Office of Basic Energy Sciences under contract number DE-AC02-06CH11357.

2.5.9 X-ray Photoelectron Spectroscopy (XPS)

Photoelectrons can be generated when incident light impinges on the surface of a material (Figure 10c). Because the energy of incident X-rays can be known and the kinetic energy of electrons are measured in XPS, the binding energy of electrons in the material can be obtained by the relation:

$$E_{binding} = E_{photon} - (E_{kinetic} + \phi)$$

where ϕ is the work function of the material. The number of electrons detected is plotted against the binding energy of the electrons. This information can then be used to determine the elemental composition, oxidation, and electronic states of a material. Valence electron binding energy can also be used to determine the d-band center and core-level shifts indicate changes in electronic structure. There is a caveat to this technique in that it is surface-sensitive because photoelectrons are collected only from the first few layers of the surface (up to 10 nm in most cases). This is because of collisions and the escape depth of electrons, which is related to the mean free path of electrons in the material. The XPS experiments for our study were performed by our collaborators at University of Notre Dame.

2.5.10 UV-Visible Absorption Spectroscopy (UV-Vis)

Absorption spectroscopy is particularly useful in studies of nanoparticle growth and reduction kinetics by monitoring metal concentration through the decay of the absorption bands of metal precursor complexes. It is also utilized in studies of metal nanoparticles that can interact strongly with light in the ultraviolet and visible regions. Localized surface plasmon resonance (SPR) is a phenomenon that is especially prevalent with the most noble metals. Nanoparticles of Au and Ag absorb and scatter light strongly in the visible wavelengths. This is due primarily to SPR, which is a collective resonant oscillation of electrons with the frequency of the incident electromagnetic waves (Figure 5). The absorption and scattering (extinction) spectrum of Au nanoparticles produces a band that is shaped depending on the nanoparticle size. In the case of Au, this results in a

broad range of colors for differently sized nanoparticles. From a few nanometers in diameter up to over a hundred nanometers the Au particle solutions will scatter from red to purple and blue light. Shape and the metal-solvent interface also play important roles in the position and different modes of plasmon resonance bands. Diluted nanoparticle growth solutions before and after the synthesis reactions were used directly for the UV-Visible spectroscopy experiments. The UV-Visible spectrometer utilized was an Ocean Optics ISS.

2.5.11 Surface-Enhanced Raman Spectroscopy (SERS)

The direct application of LSPR in Au and Ag nanoparticles is in surface-enhanced Raman spectroscopy (SERS). The principles of SPR allow for significantly better detection of low concentrations of Raman-active molecules and the improvement of Au nanoparticle synthesis has allowed for further enhancement of the technique by being able to tune plasmon "hot spots" on nanoparticle surfaces.

In our study, SERS is used to measure the capping of quaternary ammonium group functionalized surfactants on the surface of Au nanoparticles. This work was done by our collaborators at Nanyang Technological University of Singapore. Au nanoparticles were synthesized following a procedure in the literature.[108] First, 0.6 mL of ice-cold 0.02 M $NaBH_4$ solution was quickly injected into a mixture of 1 mL of $HAuCl_4$ (5 mM), 1.0 mL of 0.1 M trisodium citrate and 18 mL of water. After stirring for 4 hours, the solution was used as a seed solution for the overgrowth to form Au nanospheres. Under moderate stirring (1500 rpm), 5 μL of the seed solution was injected into the mixture of 500 μL of

PVP (5 wt%), 250 μL of ascorbic acid (0.1 M), 200 μL of KI (0.2M), 60 μL of $HAuCl_4$ (0.25 M) and 2 mL of water. The reaction lasted 10 min and the Au nanospheres were re-dispersed in water.

For SERS preparation, 1.0 mL of 80-nm Au nanospheres dispersed in water were centrifuged and washed with piranha solution (a mixture of H_2O_2 and H_2SO_4) twice to remove PVP capping agent and re-dispersed in 1.0 mL of water. Then 0.500 mL of Au nanosphere suspensions was added with 1.0 mL of CTAC (25 wt% in water) and PDADMAC (20 wt% in water), respectively. After four hours, the mixtures were centrifuged and the Au nanospheres were re-dispersed and washed with water. Finally, the Au nanospheres were dispersed in ethanol, before being deposited on cleaned Si substrates for SERS measurements. The substrate drop-casted with Au nanospheres was then immersed in ethanol for 1 min to remove excess unbound surfactants, and dried in nitrogen gas. SERS spectra and SERS mapping were obtained using Ramantouch microspectrometer (Nanophoton, Osaka, Japan). A 785 nm laser was used as an excitation laser. The excitation laser light was focused into a line on a sample through a cylindrical lens and an air objective lens (LU Plan Fluor 100x NA 0.9). The back-scattered Raman signal from the line illuminated site was collected with the same objective lens, and a one-dimensional Raman image (1D space and Raman spectra) was obtained with a two-dimensional image sensor (pixis 400 BR,-70°C) at once. Two-dimensional (2D) Raman spectral images were obtained by scanning the line-shaped laser focus in a single direction. The excitation laser power was 0.34 mW on the sample plane. The exposure time for each line and slit width of the spectrometer were 10 s and 50 μm

for 2D Raman imaging. The line scan mode with the resolution of y direction around 300 nm was used for x-y imaging.

2.5.12 Crystal Modeling, Imaging, and 3D-Printing Software

Digital Micrograph was the primary imaging software utilized for our work in calculating d-spacings, while ImageJ was used alternatively for particle counting statistics. OriginPro 8 was used to generate spreadsheets and to plot all of the data shown. Windows CrystalMaker was used to generate the 3D crystal models used in the synthesis schemes, and Carine Crystallography was used to simulate diffraction patterns. The 3D printing service was from Shapeways, Inc. (www.shapeways.com, Shapeways HQ, 419 Park Ave. South, Suite 900, Floor 9, New York, NY 10016, .USA). Some other programs were used to convert the crystal files into point clouds that could then be used to generate the meshes for 3D printing: primarily GoogleSketchUp and MeshLab.

2.3 Electrochemical Characterization and Catalysis

Electrochemistry can be used to characterize the surface of metal nanoparticles and to study their activity in electrocatalysis. We primarily performed cyclic voltammetry and chronoamperometry experiments in a three-electrode system to gain information on the surface of the nanoparticle catalysts. A saturated calomel reference electrode and platinum wire counter electrode were used in all experiments. A glassy carbon electrode was used as the working electrode. A rotating ring disc electrode was used for the oxygen reduction experiments. All electrodes were purchased from CH Instruments.

The potentiostat utilized was a BioLogic VSP. Typically the experiments were run in a 25 mL three-neck round bottom flask. Brief descriptions of concepts, mechanisms, and further details of electrochemistry experiments are given below.

2.3.1 Catalyst Preparation and Loading

The catalysts were rinsed a minimum of three times before loading on the glassy carbon working electrodes. An additional cleaning treatment was performed for those catalysts where iodide ions from the synthesis were bound too strongly to the surface, blocking much of the catalytic activity. For these batches, a sacrificial conformal Cu_2O coating was grown on the surface of the particles in basic solution and was subsequently removed after two steps of centrifugation and dispersion in water (Cu_2O is not stable at neutral pH and is etched away). Activity was dramatically improved by this cleaning step. For this, a procedure from the literature was modified.[109] Briefly, a solution containing DI water, concentrated nanoparticles, NaOH, NH_2OH, and $CuCl_2$, was prepared by combining solutions together at room temperature and allowed to sit for 30 minutes. The Cu_2O-coated particles were then collected via centrifugation and dispersed in methanol. The particles were then precipitated a final time and redispersed in water. We believe the initial coating displaces surface capping agents (CTAB, I-), which are removed after centrifiguation, and the sacrificial coating layer is then removed in the final rinsing step.

The glassy carbon working electrodes were polished before use by micro-alumina powder. Glassy carbon working electrodes were loaded with catalysts directly by

dropcasting 2-5 μL droplets of the concentrated nanoparticle solutions on the electrode surface and allowing them to sit in air to dry. Alternatively, catalyst nanoparticles were loaded on to a carbon powder support (Vulcan XC-72 Carbon) before dropcasting on the working electrode.

2.3.2 Cyclic Voltammetry (CV)

In a cyclic voltammetry experiment, a potential is continuously applied, swept forward, and reversed back to the starting potential, while the current is being measured. This process is repeated for a desired number of cycles. The initial potential, the potential range, and scan rate can all be adjusted. In general, positive current corresponds to oxidation reactions (electrons are transported from the surface), while negative current corresponds with reduction reactions (electrons are transported to the surface). In the electrooxidation of alcohols and formic acid at the anode, a high forward scan oxidation peak at low potential is an indicator of a good catalyst, whereas a large negative current at high potential indicates a good oxygen reduction cathode catalyst. There is a significant overpotential that is associated with most reactions that should be overcome, and so both the potential and current are important with regard to assessing a catalyst's performance.

2.3.2.1 Blank Scans

Before catalysis experiments were run, blank scans are first acquired to confirm the quality of the working electrode prior to the catalyst loading. The shape of the cyclic

voltammetry curve should be flat, rectangular, and reversible. After observing the normal shape of the blank scan, further blank scans were run after catalyst loading on the working electrode.

2.3.2.2 Hydrogen Sorption Sweeps

The blank scans of catalysts on the glassy carbon working electrode show the characteristic sorption of hydrogen and oxygen on the metal surfaces and can be used to analyze composition and faceting by voltage position of current peaks, and to determine surface area of the catalyst on the electrode by the area under the hydrogen sorption region. The cycling in the blank conditions serves also to prepare the catalyst for reactions by allowing them to equilibrate to the electrolyte and the potential sweeping conditions. The reversible oxidation and reduction of the metal surface at the high potential end of the sweeps helps to rid the surface of any remaining capping agents, though it is noted that roughening of the surface may occur during the process, which is generally termed as activation of the catalyst.

Typically, 0.5 M sulfuric or perchloric acid was prepared as the electrolyte solution for the blank scans and poured to fill a 25 mL three-neck flask for catalysis experiments in acidic media. Nitrogen was then bubbled into the solution for ~30 minutes to purge the solution of other dissolved atmospheric gases (O_2, CO_2) which are present and could interfere with the analysis. Approximately 50 cycles were run in the potential window of -0.2 V to 1.0 V with a scan rate of 100 mV/s, until the hydrogen sorption peaks reached a maximum. The range was chosen to include the region for reversible hydrogen

adsorption/desorption and a high potential maximum where some red/ox of the metal surface could be observed. The experiment was done identically for alkaline electrolyte, except that the potential window used was -0.8 V to 0.4 V, and 0.1 M potassium hydroxide was used instead.

2.3.2.3 CO-Stripping

The stripping (oxidation) of CO on metal surfaces can be used to analyze composition and faceting based on the voltage position at peak current. The assumption can also be made that CO absorbs in approximately a monolayer on the surface of metals. This makes the reaction an alternative method for the determination of the surface area of a catalyst. The CO-stripping reaction proceeds via a Langmuir-Hinshelwood mechanism on metal surfaces,[110] where CO and OH are first absorbed onto the surface as an intermediates that react (CO is oxidized) and desorb from the surface in the final step:

$$CO_{ads} + OH_{ads} \rightarrow CO_2 + H^+ + e^-$$

For the CO-stripping experiments, blanks scans were first run for the loaded catalysts and then the electrode was put into a three-neck flask containing 0.1 M $HClO_4$. With the electrode submerged, CO gas was then bubbled into the solution for 30 minutes. At the same time, a separate flask with 0.1 M $HClO_4$ was bubbled with N_2 gas. The electrode, now covered with a monolayer of CO was then transferred to this solution for the CO-stripping. The voltammetry was carried out at a scan rate of 10 mV/s with a range of 0 to 1.0 V.

2.3.2.4 Electrochemically Active Surface Area (ECASA)

The surface area is calculated in order to normalize the electrochemistry and catalysis data to obtain specific activities (current density). Alternatively, the nominal loading of the mass of the metals in the catalyst or the surface area could be estimated, however, the nominal loading/surface area is less accurate and reproducible between given catalyst batches because of variations in the synthesis yield and mass lost in centrifugation steps, though it is commonly reported because of the DOE fuel cell targets demanding less use of Pt. There are two ways to calculate the surface area of the catalyst; either from the charge collected in CO-stripping or from the charge collected in hydrogen sorption. Assuming monolayer coverage of CO on a metal surface, it requires 420 $\mu C/cm^2$ to convert the CO to CO_2. The charge is obtained from the current collected by integrating the area under the CO-stripping peak. This charge is then divided by the constant to obtain the surface area. Because some metals (Pt) are poisoned by CO, reducing the effective surface area measured by this method, hydrogen sorption can be used alternatively. Assuming monolayer coverage of hydrogen on metal surfaces, charge can be collected from the hydrogen sorption peaks (adsorption and desorption occur typically in the range of -0.2 to 0 V vs. SCE in acidic electrolyte solution) and the calculation can be done similarly, except that 210 $\mu C/cm^2$ is used as the constant for Pt surfaces. Either the desorption or adsorption peak can be used, as it is a reversible process, but sometimes an average is preferable if there is variation between the two. The assumption of monolayer coverage can deviate from unity significantly, however, it is generally

believed valid for the purpose of normalizing catalyst activity, as it is consistent for the same or similar metal surfaces.

2.3.3 Fuel Cell Electrocatalysis Experiments

There are many proposed fuel cell designs by selection of different fuels for the anode oxidation reaction. Aside from hydrogen, alternative fuels research is directed at formic acid, methanol, and ethanol. Though they are not zero-emission technologies, these carbon-based fuels can be readily obtained from renewable biofuels or converted from fossil fuel sources. They also pose less of a danger as they are liquids at room temperature and do not need to be kept under pressure; additionally, the US already has liquid fuels pipelines in place. The problem with formic acid or methanol fuel cells is that the Pt-based catalysts become poisoned by CO_{ads} on the surface as it is an intermediate in the fuel conversion. Research is aimed at increasing the efficiencies and tolerance to CO for these catalysts.

2.3.3.1 Formic Acid Oxidation Reaction (FOR)

Formic acid oxidation proceeds via two pathways on metal surfaces: it can be converted directly to CO_2, or oxidized through an indirect two-step process involving removal of a CO_{ads} intermediate:

$$HCOOH \rightarrow CO_{ads} + H_2O_{ads} \rightarrow CO_2 + 2H^+ + 2e^-$$

Because of this, CV scans generally show two peaks, the forward scan peak is primarily generated from direct oxidation, whereas the 2nd peak occurs on the reverse scan and can

be attributed to the removal of the unreacted adsorbed intermediate. The preference for the direct or indirect pathway is dependent on the metal identity. Typically, Pt and Rh oxidize formic acid by the both direct and indirect pathway, however, Pd has been found to prefer the direct oxidation. This correlates with the CO tolerance of the different metals, and is generally observed for reaction of other carbon-based fuels, such as methanol and ethanol, that involve the same adsorbed CO intermediate in the mechanism. The formic acid oxidation CV experiments were performed by first preparing a solution which was 0.5 M in both $HClO_4$ and HCOOH, and purging with nitrogen for 30 minutes. The scans were carried out at a rate of 100 mV/s and at a potential range of -0.2 to 1.2 V vs. SCE. The CA curves were obtained by holding the voltage at a constant 0.4 V vs. SCE in the same reaction media.

2.3.3.2 Methanol Oxidation Reaction (MOR)

Methanol oxidation also proceeds via direct and indirect pathways, but the reaction is considerably more complex as it produces six electrons rather than two:

$$CH_3OH \rightarrow HCHO + 2H^+ + 2e^- \rightarrow HCOOH + 4H^+ + 4e^- \rightarrow CO + H_2O \rightarrow CO_2 + 6H^+ + 6e^-$$

We examined catalysts for the reaction in both acidic and alkaline electrolyte solution as the catalysts are generally more active in alkaline conditions. For reaction in acidic electrolyte, a solution that was 0.5 M in both CH_3OH and H_2SO_4 was first prepared, and purged with nitrogen for 30 minutes. The scan rate was 100 mV/s and the potential window was 0 to 1.0 V vs. SCE. For reaction in alkaline media, the reaction was performed similarly, except that a solution of 0.1 M in KOH and 0.05 M in CH_3OH was

prepared, and the range was -0.8 to 0.4 V vs. SCE. The CA curves in basic electrolyte were obtained by holding the voltage constant at -0.1 V vs. SCE.

2.3.3.3 Ethanol Oxidation Reaction (EOR)

The mechanism of ethanol oxidation involves an acetic acid intermediate and the production of 12 electrons, again through dual pathways. Ethanol oxidation was also carried out in both acidic and basic electrolyte solutions. For reaction in acidic electrolyte, a solution that was 0.1 M in both ethanol and $HClO_4$ was prepared. The scan range was -0.3 to 1.0 V vs. SCE done at 5 mV/s. Alkaline ethanol oxidation was done in solutions 1 M in both ethanol and KOH. The scan range was -0.8 to 0.3 V vs. SCE at a scan rate of 50 mV/s.

2.3.3.4 Oxygen Reduction Reaction (ORR) and Rotating Ring Disc Electrode (RRD)

The oxygen reduction reaction was performed on a rotating ring disc electrode. The instrument was an RRDE-3A from BioLogic. The electrode was lowered into a oxygen-saturated solution of 0.1 M $HClO_4$, rotated at a speed of 1600 RPM, and the sweep was carried out from 0.8 to 0 V vs. SCE at 5 mV/s.

2.3.4 Chronoamperometry (CA)

Chronoamperometry experiments measure the current obtained over time as the potential is held at some constant value. These experiments are useful to examine the durability of the catalyst, or how the catalyst activity declines over time at an operative

potential. For CA experiments, blank scans were first performed, and the electrodes were introduced to the same electrolyte solutions as those used for CVs of catalysis. The voltage constant was chosen based on the potential of peak current for the corresponding reaction.

3.0 RESULTS AND DISCUSSION

Results are presented and discussed in this section, beginning with the synthesis and characterization of lattice strained nanoparticles in the monometallic Pd system. The discussion then extends to catalysis studies of differently strained nanoparticles with Pd and Pd alloy surfaces. This is followed by the work with Rh-containing nanoparticles, and by the most recent work with Ni-sandwiched nanoparticles. A portion of the supporting data is not shown here in order to reduce redundancy (blank CV scans, control experiments, etc.); however, this material is available online as a supplementary supporting information file for the respective publications in which it appears.

3.1 Shaped Pd Nanocrystal Synthesis and Catalysis by Pd Surfaces

Many new methods for the shape-controlled synthesis of Pd nanocrystals and nanocrystals with Pd surfaces were developed. The different types of particles studied include Pd cubes, Pd octahedra, Pd icosahedra, Pd cuboctopods, Au-Pd core-shell cubes, Au-Pd core-shell octahedra, PdPt alloy octahedra, and Au-PdPt core-alloy-shell octahedra. Most of these structures can be created at different sizes and the composition can be tuned for the alloy surfaces. The synthesis, characterization, and catalysis of these

Pd-containing nanocrystals is described, beginning with synthesis using an unconventional capping agent, PDADMAC.

3.1.1 Promotion of the Halide Effect via a Hybrid Cationic, Polymeric Stabilizer

The rational design of wet-chemical synthesis routes that allow for complete control of the structure of metal nanoparticles is still challenging, despite the now decades of research in the field. Realizing this goal will ultimately be accomplished by obtaining a better understanding of the thermodynamic and kinetic mechanisms of control that can be established by stabilizing ligands at the NP-solvent interface.[111] The terms surfactant, capping agent, and stabilizer are used interchangeably to describe molecules which modulate interactions at the interface between solutions and growing metal NP surfaces. These stabilizers arguably play the most important role in control of structure during NP nucleation and growth, by dictating the surface energy differences between facets and by their influence on rates of deposition, dissolution, and diffusion on these surfaces.

Stabilizers can be generally classified into two categories: as surfactants or polymers. Two typically chosen stabilizer systems for shaped metal NP syntheses are charged micellar surfactants, such as the cationic cetyltrimethylammonium halides (CTAX, X = halide), and uncharged polymers, such as polyvinylpyrrolidone (PVP), with halide salts.[112-115] Despite differences in molecular and supramolecular structure, their ability to control the growth of shaped metal NPs highly depends on the halide ions.[116] Thus, research into the functions of the halides in guiding NP geometry during growth is of paramount concern. Some previous reports discussed the mechanisms of halide-

dependent morphology,[4,117,118] but it is difficult to fully decouple the functions of halides from stabilizers, and the many other intertwined parameters affecting the complex growth of NP surfaces.[12,119,120] Because shaped metal NPs are generally synthesized using different identities and concentrations of stabilizers, halides, metal precursors, and reducing agents, etc., connecting the knowledge gained from disparate experimental synthesis conditions into a set of overarching guidelines is similarly challenging. Furthermore, research has been focused primarily on systems of Au NPs in this regard, leaving most late transition metals in the dark on this subject.

Here, we used polydiallyldimethylammonium halide (PDADMAX, X = halide), a cationic, polymeric stabilizer, that functions as a hybrid between conventional stabilizers (CTAX and PVP) in the synthesis of shaped metal nanocrystals. Because PDADMAX stabilizers combine both the advantage of polymer stabilizers (PVP) in having higher local concentration on the NP surfaces and the advantage of cationic surfactants (CTAX) in having charge-balancing, shaping halide ions, we hypothesized that by using this cationic polymeric stabilizer, the local concentration of halide ions near the surface will be increased, in effect, increasing their preferential binding of specific facets in the shaped NP synthesis. Therefore, the role of halides could be made more obvious, and the shape of the NPs can be simply changed by the choice of halide (Figure 13). It is worth mentioning that some works utilizing PDADMAX (also abbreviated, PDDA) have recently been reported to make metal NPs,[102,121-132] but effects of halides accompanying this unique stabilizer remains wholly uninvestigated.

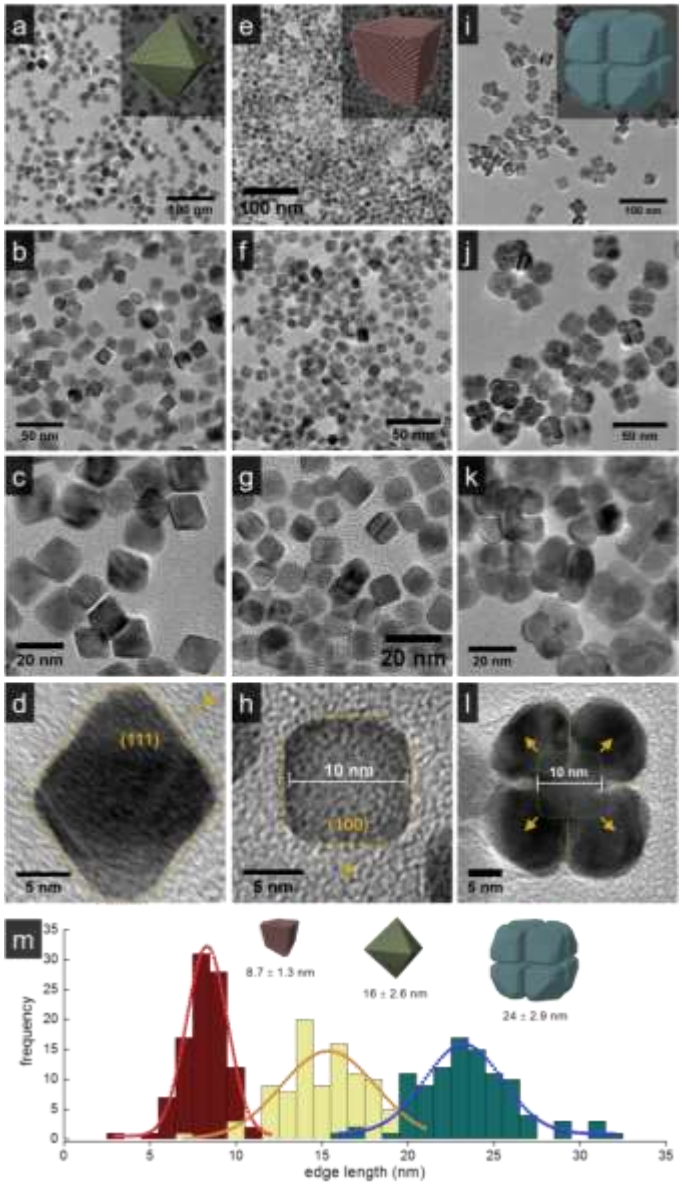

Figure 13. TEM and HRTEM images of (a-d) ~16 nm Pd octahedra, (e-h) ~9 nm Pd cubes, and (i-l) ~24 nm Pd cuboctopods synthesized using PDADMAC as the stabilizer. Inset of (a,e,i) are crystal models, and (m) gives size distribution histograms and average edge lengths of the NPs (red, yellow, and blue for cubes, octahedra, and cuboctopods, respectively).

To first prove the stronger binding of PDADMAX, single-cluster surface-enhanced Raman spectroscopy (SERS) was carried out on the different stabilizers on well-defined and isolated Au NP clusters. (Figure 14) The intrinsic binding affinity of PDADMAC and CTAC on dimer-, trimer-, and tetramer-clusters of Au nanosphere is probed by comparing the δ(CH) of quaternary ammonium group of the respective stabilizers at the Raman shift of 1265 cm^{-1}.[133-135] The two stabilizers both have a quaternary ammonium group, with a chloride ion to balance charge. The hyperspectral SERS imaging of PDADMAC- and CTAC-bound isolated Au nanosphere trimer-clusters are measured and subsequently correlated with SEM imaging to ensure fair comparison. In a typical SERS measurement, 80-nm Au nanospheres are thoroughly washed with piranha solution to obtain Au nanospheres free of surfactants. These "naked" Au nanospheres are added to PDADMAC and CTAC solutions for 4 hours before washed and re-dispersed on Si substrates for SERS measurements. A typical single-cluster SERS spectrum of PDADMAC-bound Au nanosphere trimer-clusters demonstrates 5-fold higher SERS signals at 1265 cm^{-1} Raman shift than their CTAC counterparts (Figure 14a-e). The results are obtained by comparing the SERS response of at least 22 different Au nanosphere trimer-clusters from both stabilizers. We also compare the SERS intensities of Au nanosphere dimer- and tetramer-clusters bound with PDADMAC and CTAC, which demonstrate that the SERS intensities of the δ(CH) of quaternary ammonium groups from PDADMAC are also generally 3 to 5 times higher than the CTAC surfactant (Figure 14f).

These results align with our hypothesis of a stronger interaction of PDADMAX on nanoparticle surfaces, and so we first demonstrate how PDADMAC alone yields ~16 nm Pd octahedra. The Pd nanooctahedra are shown in TEM images in Figure 13. The octahedral shape terminated by {111} is visible from TEM images in Figure 13(a-d). We note here that it is rare to obtain such a high yielding synthesis of uniformly octahedral Pd NPs at this size by a rapid, one-step approach (without requiring seeds).[37,136] Importantly, the aqueous synthesis is carried out with only three components: metal precursor, reducing agent, and PDADMAC stabilizer. The production of Pd nanooctahedra reveals the intrinsic binding trends of the halides, without complications from other shaping agents. We believe that Cl- ions bind the {111} facets resulting in the octahedral shape and that PDADMAC enhances this effect as a cationic polymer stabilizer. This fits with the triangular geometries often observed for the afore mentioned PDADMAC-based Au nanoparticle syntheses. The Cl- promoted octahedra formation cannot be achieved by CTAC or PVP with added Cl- ions, because only the cationic polymeric stabilizer can increase the local concentration of Cl- ions high enough to promote the specific facets in the shaped nanoparticle synthesis; CTAC monomers may be too labile, and PVP can only offer dipole forces, meaning that the interaction is not strong enough to have a significant effect on the surface energy differences between facets. Moreover, the cationic backbone of the PDADMAC polyelectrolyte could adopt a more rigid conformation due to repulsive monomer interactions and so this supramolecular structure could be more conducive toward faceting.

Generally, it is believed that the heavier/softer halides, Br- and I-, bind more favorably to Pd {100}.[12,137] We hypothesized that by adding I-, to PDADMA-mediated syntheses, we could form cubic Pd nanoparticles. Figure 13(e-h) shows transmission electron microscope (TEM) images of sub-10 nm Pd nanocubes synthesized using PDADMAC and I- ions. The resulting nanoparticle sizes are much smaller compared to the analogous CTAB/I- shape-control methods.[12,104] The results again support our hypothesis that the polymeric cationic stabilizer's stronger capping characteristics assist iodide's influence in facet control, increasing the time halides spend near the growing nanoparticle surface.

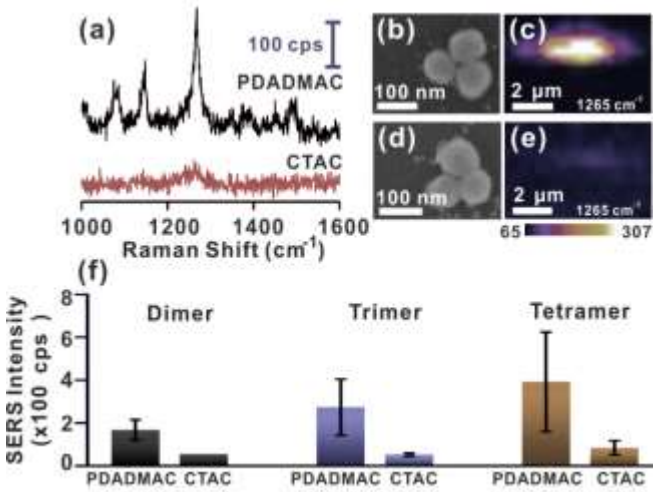

Figure 14. (a) Single-cluster surface-enhanced Raman scattering (SERS) spectra, (b, d) the corresponding SEM images, and (c, e) the corresponding SERS images of PDADMAC- (black curve) and CTAC-bound (red curve) isolated Au nanosphere trimers. (f) The single-cluster SERS intensities of the δ(CH) of quaternary ammonium groups (at 1265 cm-1) on the corresponding isolated PDADMAC- and CTAC-bound Au nanosphere dimers, trimers and tetramers.

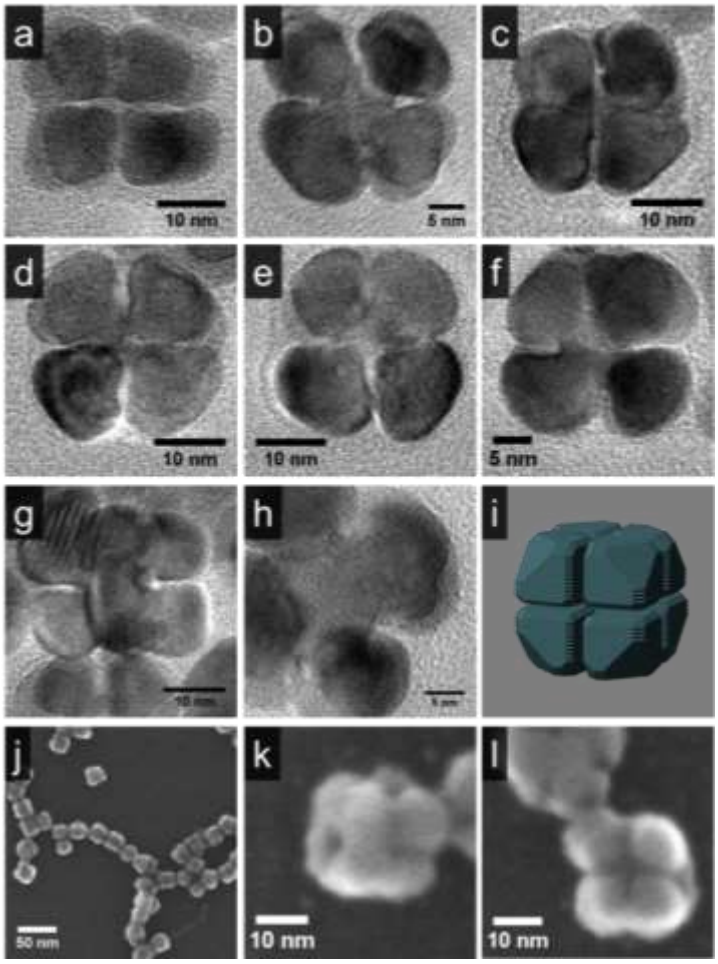

Figure 15. TEM (a-h) and SEM (j-l) images of Pd cuboctopods along with crystal model in (i).

Following this information, we believed that seed-mediated overgrowth of Pd on the PDADMA-stabilized cubic Pd NPs could yield unique structures. We followed a procedure adapted by our group for overgrowth; as-synthesized cubic Pd nanoparticles were added into a growth solution with Pd precursor.[101,102,104,105] The results are shown in

Figure 13(i-l). In this case, ~24 nm Pd octopodal structures were obtained, with cross sections that have a striking resemblance to four-leaf clovers (shamrocks), and are distinguished from the larger bimetallic Au-Pd alloy octopods popularized by DeSantis et al.,[138] among others.[139] The octopodal geometry was determined by observation of the (100) cross-section in conjunction with particles tilted at the 110 zone axis (cube on edge), where six of the eight pods could be viewed (Figure 15). A core of Pd resembling the ~9 nm cubic seeds is established at the center of the eight pods, which appear to be connected at the eight corners of this cubic seed. Figure 3 gives HRTEM lattice images that show the epitaxial relationship between the cube seed and the overgrowth, itself taking on a truncated cubic appearance. Scanning electron microscopy (SEM) was performed to obtain more 3D imaging of the surface structure of the octopods (Figure 15j-l). The 8 lobes can be resolved as well as the gaps in between them in SEM images. The overall structure can alternately be envisioned as a truncated cuboctahedron with excavated channels along the center of {100} faces, hence the apt portmanteau, 'cuboctopod', emerged to describe the structure. The anisotropic epitaxial overgrowth in this monometallic system is unique and can be explained by the enhanced binding affinity of I- on {100} facets of Pd; the truncated {111} corners of cubic seeds will be less populated by I-, and deposition of Pd atoms can still occur. There is a rapid growth outward along the <111> directions (Scheme 1), 'ballooning' into I- passivated {100} and other facets. Smaller CTAX monomers cannot achieve such a structure because of a higher rate of exchange compared to the extended polymer backbone of PDADMAX. Remarkably the cuboctopod morphology was also achieved using Br- instead of I-, and

this information could also be used to generate Pt nanocrystals of the same morphology in a one-pot synthesis. The geometry is usually observed for bimetallic nanoparticles, and is rarely observed for monometallic systems, especially at these small size scales. The PDADMAX interaction may amplify the subtle differences in surface energies of different facets of the same metal, where this feature could then be used to design other novel monometallic anisotropic nanostructures. Figure 16 illustrates the synthesis of the differently shaped Pd NPs by the PDADMA-halide binding effect.

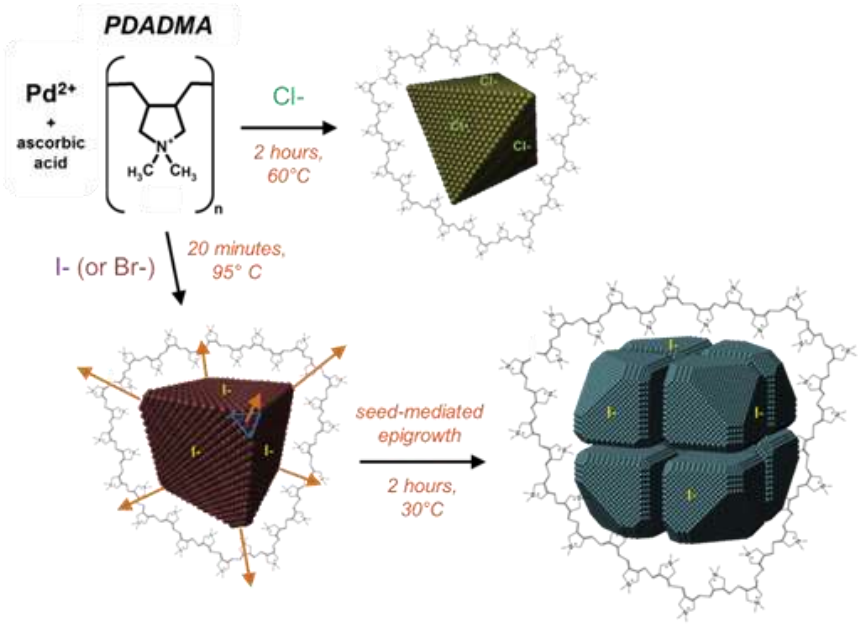

Figure 16. Schematic illustration of the promotion of the halide effect in the formation of shaped nanocrystals and anisotropic epigrowth via the hybrid, cationic polymeric stabilizer, PDADMA.

We believe the evidence provided by SERS, in addition to the control synthesis experiments, support the conclusions of PDADMA promoting halide adsorption such that the labile chloride ion, often excluded from discussions of shaping mechanisms, becomes an important factor in the shape-control of Pd nanocrystals. Future work is directed toward extending the synthesis to other transition metals, investigating differently charged polymers as stabilizers, and the discovery of new materials and methodologies with the structure-directing polyelectrolyte.

3.1.2 Global HRXRD Evidence of Shape-Dependent Anisotropic Strain Gradients in Pd Nanocubes

The following work was done in collaboration with Paolo Scardi, Alberto Leonardi, and Luca Gelisio at the University of Trento, Italy. Most of the modeling and diffraction analysis was done by Luca Gelisio and so some of the material below may also appear in his 2014 Ph.D. thesis: "Structure and Properties of Nanostructured Materials from Atomistic Modeling and Advanced Diffraction Methods," while my own contributions were in the materials synthesis, sample preparation, diffraction experiments, and catalysis discussion. Portions of this section have been reproduced in part with permission from P. Scardi, A. Leonardi, L. Gelisio, B.T. Sneed, M.K. Sheehan, and C-K. Tsung, "Resolution of Anisotropic Atom Displacement in Metal Nanocrystals by XRD Imaging," Physical Review B, as a manuscript accepted for publication. Unpublished work copyright 2015 American Physical Society.

Full resolution of the atomic arrangement within nanocrystals at a global scale will drive progress in fundamental and applied research involving metal nanocrystals. Electron microscopy has made great progress in this direction, supported by the development of aberration-corrected scanning transmission electron microscopy (STEM) and high angle annular dark field imaging (HAADF), combined with X-ray spectroscopy tecniques (EDX, EELS).[55,140-144] While state-of-the-art microscopy delivers the highest spatial resolution of any probe, showing features down to the atomic scale, the statistical basis of microscopy is inherently limited by low sampling. It is typical that only a few "representative" nanoparticles are to be examined in TEM (or SEM), before projecting the ideal morphology on the rest of the batch, which contains several billions of other uncharacterized particles.[6,141] Perfectly modeled polyhedra are often given in support of conclusions, without a real structural basis and similarity. Additionally, the electron beam causes damage (restructuring) of samples and can make *in-situ* measurements difficult.

High-quality information of atomic structure may also be obtained by coherent X-ray diffraction (CXD), a powerful imaging technique that gives information of shape together with a maps of lattice strain, however, the smallest particles that can be analyzed by CXD using the currently available instrumentation is about ~60 nm in diameter. Smaller crystallite sizes still create important and still unsolved challenges in terms of counting statistics for the experimental CXD pattern, due to low sampling, as in electron microscopy.

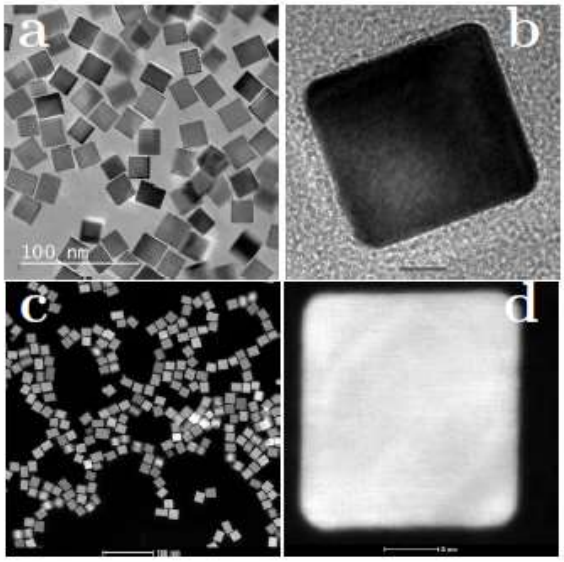

Figure 17. TEM (a,b) and HAADF (c,d) images of Pd nanocrystals. (b,d) A nanocrystal oriented along [00h], showing the truncation of edges and corners responsible for (110) and (111) faceting, respectively.

It may seem bizarre that the conventional technique of X-ray powder diffraction (XRD), should enter the picture. Aside from showing the average phase composition, XRD is often used to determine the size of nanoparticles. Rough measurements can be made from the peak width at half max, by taking advantage of the inverse relationship it has with the crystallite domain size, as detailed in the Scherrer relation, though this calculation goes somewhat misused, often ignoring nanoparticle defects, shape, and strain effects.[55] This characterization method could be significantly enhanced with recent nanoscience trending toward improved atomic-level control of synthesis, aimed at producing nanoparticles with uniform size and shape. Under such conditions, XRD offers

data nearly identical to CXD, but with the added benefits of straightforward analysis rapid global data collection of the ensemble of peaks produced by trillions of nano-domains in the usual sample.

This new model is shown here for catalytic Pd nanocubes.[37,38,107] Exhibited in Figure 17, the highly uniform Pd nanocubes are truncated at edges and corners, resulting in not just (100) facet planes, but also some percentage of (111) corner and (110) edge planes. The HRXRD pattern gives a unique fingerprint for the ensemble. This is shown in the inset of Figure 18, where the 200 reflection shows interference fringes from parallel 100 facets, a feature that is specific to cubic crystal domains, and is observable here for the first time in global XRD because the crystallites are nearly identical in size and shape (approaching roughly ~99% cubes by count and higher by volume percent). The results are similar to the data produced by CXD on much larger cubic crystals, however, the data here is global, collected for perhaps trillions of particles in the sample. Furthermore, the HRXRD pattern gives information along many crystallographic directions, which can be used to model the entire pattern. Specifically, we implement a cube model with truncated edges and corners and refine the level of cube edge and corner truncation, and distribution of sizes. The result in Figure 19 demonstrates the excellent fit between our model and the real data (nanoparticle size and shape determined from XRD modeling agrees with TEM measurements). According to the data, nanocubes have edges of ~15 nm, with a standard deviation of ~2 nm, and an edge/corner truncation of 18%. The counting statistics of a survey of 1000+ particles in TEM resulted in 98.4% being cubic or rectangular shaped particles and ~1.6% non-cubic. This value is higher than ~99%

when factoring in percent by volume, on account of the non-cubic particles mostly presenting themselves as small spheres.

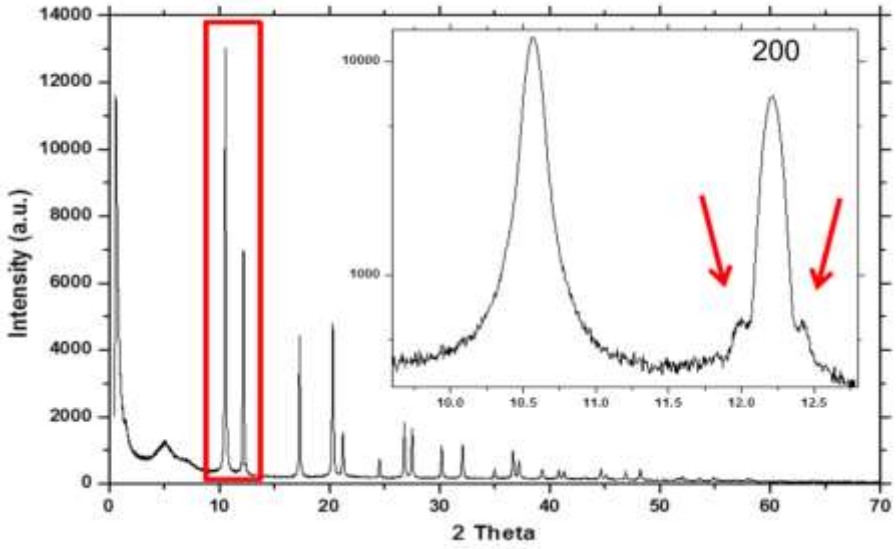

Figure 18. Experimental XRD pattern for Pd nanocubes. The inset magnifies the 200 peak. Arrows indicate the interference fringes from the parallel 100 facets of the nanocrystals.

The XRD modeling done here also includes for strain effects, described according to elastic tensor symmetry, which capitalizes on hkl-dependent line broadening information to probe strain anisotropy. The results are shown in a Warren's diagram, representing the standard deviation of the atomic displacement distribution as a function of the distance L between scattering centers along each given crystallographic orientation. Examples of these diagrams are shown in Figure 20 for three directions, [hhh], [hh0] and [h00], with the first and last corresponding to the extremes of anisotropic elastic behavior. The r.m.s.

displacement is larger along [h00], i.e. perpendicular to the cube faces, than along [hhh], i.e. the body diagonal direction. This is not only a direct consequence of the elastic anisotropy of Pd, but is also related to the morphology of the nanocrystal.

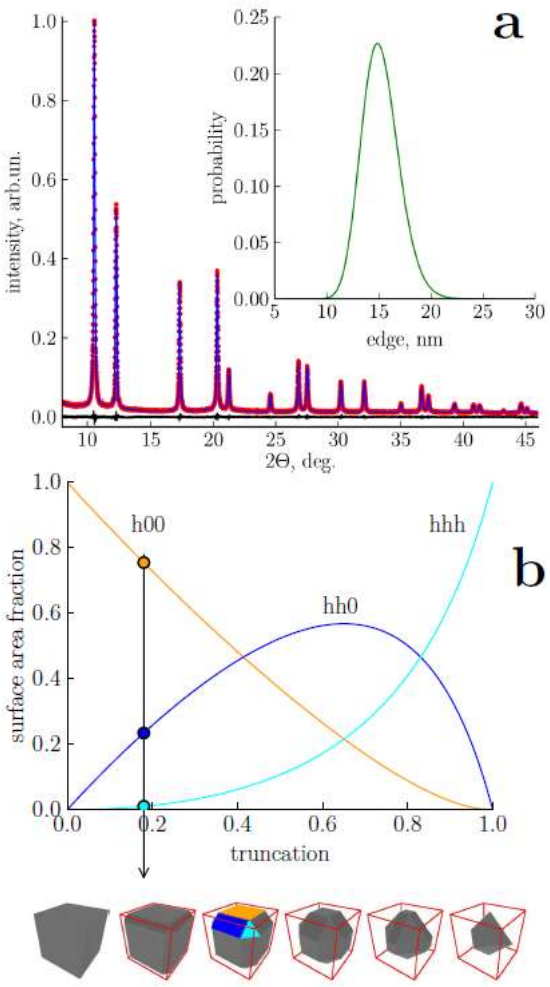

Figure 19. Modeling of the XRD data of Fig 18 together with residual (a). The resulting distribution of cube edges is shown in the inset (a). The value of cube truncation, on a scale ranging from cube (0% truncation) to octahedron (100% truncation) using surface are of different low-index facets is shown in (b).

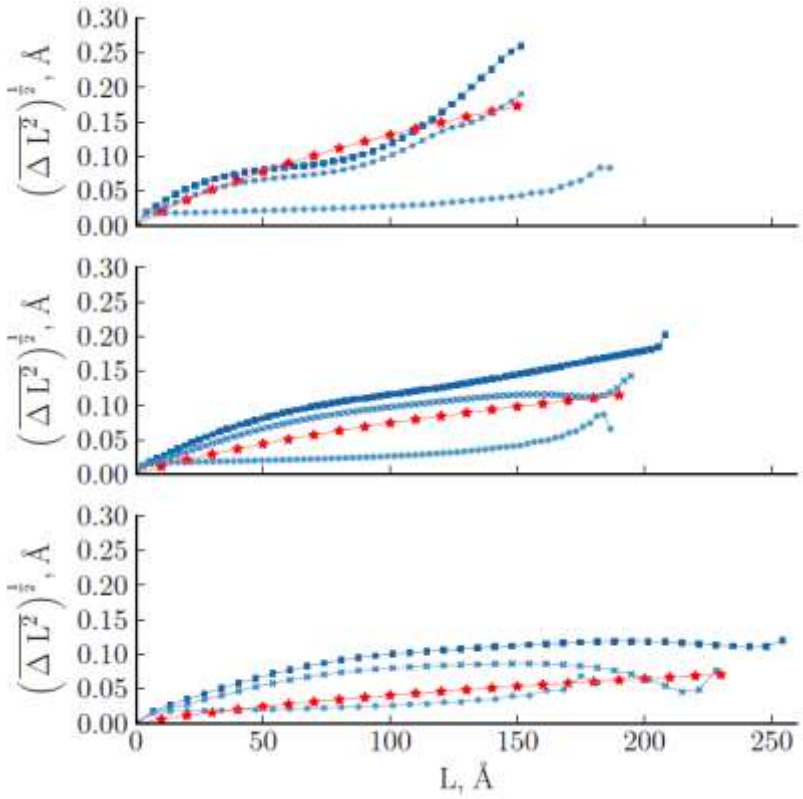

Figure 20. Warren's plot for the system: root-mean-square atomic displacement along the given scattering direction (upper, [h00], center, [hh0], and lower, [hhh]) as a function of the correlation distance L between scattering centers within the crystalline domain. The plots refer to results of the modeled XRD data (red stars) and to MD results for a perfect cube (blue squares), a truncated cube (crosses) (as described in Figure 19), and a sphere (circles), all with the same total number of atoms (constant volume).

To better appraise the significance of these results, the truncated edge/corner cube suggested by Figure 19 was used to create an atomistic model. Molecular dynamics (MD) was used to generate a plausible representation of the Pd nanocrystals at room

temperature. As a result of the MD procedure, driven by the reduction of potential energy of the crystal, atoms are displaced from their reference positions. The effect is especially evident in surface regions. An example of this displacement field, calculated with respect to the corresponding ideal fcc lattice, is shown in Figure 21a for a (100) face and adjacent (110) and (111) facets (defined with respect to the refined truncated cube shape of Figure 19). Corner atoms have the highest tendency to shrink toward the core, with the overall effect that the nanocrystal surface is bulging outward and corners compressed inward as if trying to achieve a more spherical shape.

The atomic-level information provided by MD can be used to calculate Warren's plots along specific crystallographic directions, to compare the trends with those obtained experimentally by XRD. This comparison between a modeled sphere shape, a perfect cube with sharp edges, and a cube with truncated edges and corners suggested by the XRD analysis is shown in Figure 20. The agreement with the XRD result is good despite the modeling enforcing a smooth (linear to square root) trend with L, the correlation length between couples of scattering centers in the crystalline domain. The Warren plot strain profiles calculated by MD display differences associated with each particle shape, and the agreement between the truncated cube model and XRD experimentally derived curve reveals the high sensitivity of this analysis technique to subtle particle shape details such as edge truncation.

To demonstrate the differences in morphology-dependent strain, the same figure shows Warren's plots for a spherical Pd nanocrystal with the same total number of atoms. Atomic displacements in a spherical object are much smaller, and the overall shrinking

effect much more isotropic than in the cubic nanocrystals. The symmetry of the spherical shape tends to cancel out different displacement components arising from the elastic anisotropy of Pd. As an additional valence of the results of Figure 20, the good match with the XRD trends provides a strong experimental validation for the MD simulations, so far hardly available in the literature on this specific subject. MD predictions can then be safely used to further speculate about the nature of strain in metal nanocrystals. With this capability, we are able to generate a more accurate picture of lattice strain, which can be coupled to other property maps. Figure 22 shows a TEM image of representative Pd nanocrystals from a batch, with corresponding displacement maps calculated by MD, based on the shape. The out-of-plane (normal) displacement component (top) is highest in face center regions, pushing atoms outward, and along all edges and corners, with opposite, strong inward displacement. This is responsible for the curvature of atomic facets, which has been experimentally observed in other systems. All displacement components tend to build up from core to surface, a feature visible in the (110) cross-section map (central cube map): inward displacement is highest along body diagonal, whereas a broad, roughly pyramidal region has atoms displaced outward, along the [h00] directions. It is also worth studying the atomic displacement in the plane of each exposed facet (lower cube map). Here one clearly sees the component projected on the surface, which tends to be the highest near corners and edges (dark regions) and is lower in the center of each facets (yellow to white-colored regions): most importantly, the pattern is far from being uniform on each given facet, meaning that there is a significant difference

in the lattice positions of atoms across the entire surface, and so the local surface properties could be different depending on the location of the atoms in question.

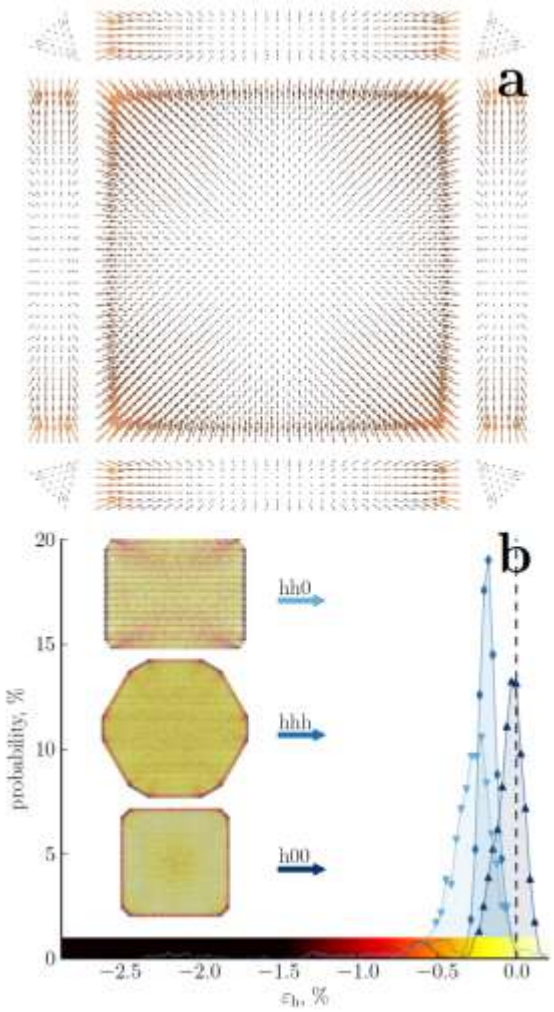

Figure 21. Map of atomic displacement from the starting (ideal) positions to equilibrium after MD on (100), (110) and (111) facets for the cubes (truncation of edges and corners from the XRD); arrows have been amplified 5-fold for graphical clarity (a); histograms of the average local strain on the three low-index cross-sections (hh0), (hhh) and (h00), shown in the inset. The color scale represents the strain distribution (b).

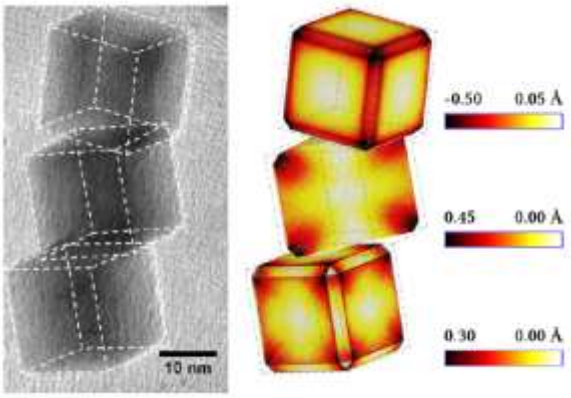

Figure 22. TEM image of Pd nanocubes (left) with corresponding atomic displacement maps (right) for the outlined cubes: normal component of the surface (top), normal of the component projected on the (110) cross-section (middle), and on the surfaces of the nanocrystal (bottom).

Our new observation of anisotropic atomic displacement in shaped nanocrystals can be used to explain and support many unique results in morphology-dependent catalysis previously reported in the literature. The relationship between shape, strain, and catalytic behavior can be invoked for nanocrystal-catalyzed hydrogenations and electrocatalysis relevant to energy conversion chemistry. For example, one representative work reported recently by Laskar et al.[38] studied selective hydrogenation of alkynes on shaped Pd nanocrystals. Similar to many previous reports, their study on Pd cubes of different sizes showed that catalytic activities, when normalized by the surface area, are higher for larger sized nanocrystals. It was reasoned that the increased ratio of face atoms to corner and edge atoms increased the number of active sites available via an ensemble effect.

This conjecture is based on a previous work that suggests the phenomenon has a threshold around 11 nm, beyond which the effect would be non-existent. However, the variation in ratios of face atoms to edge and corner atoms at the larger size ranges encountered by Laskar et al. are quite small (ranging between 98-99% face atoms); and so it is unlikely that such an increase in the catalytic performance is influenced by ensemble effects alone. Both size-dependent anisotropic displacement of constituent atoms within the particle plays a role at these nano size scales (10-40 nm), as well as non-uniform distributions of atomic distances across the exposed facets. Furthermore, the displacement would have a considerable impact on the geometry of the proposed ensemble sites. These two effects, site availability and geometry, could be coupled cooperatively, increasing catalytic activities for larger sizes.

This important feature is shown in Figure 23a, where histograms of the average local strain (ε_b) on the (100) face are compared for different particle sizes. Two main features are clearly shown by the distributions: a peak located approximately at $\varepsilon_b = \sim -1.25\%$ (labeled E) and another one, larger and closer to zero (labeled I). Peak E is related to atoms along the edges of the (100) facet, whereas peak I belongs to atoms sitting inside the face. The inset shows trends of mean ε_b values and standard deviation of peak I: for increasing nanocrystal size, peak I moves toward zero-strain values, i.e., toward the equilibrium bond length (0.389 nm in these simulations). At the same time the standard deviation tends to slightly decrease, as the strain becomes more homogeneous across the (100) surface. This result clearly indicates that the average local strain on (h00) facets is largest in smallest cubes, and increasingly more uniform for larger sizes.

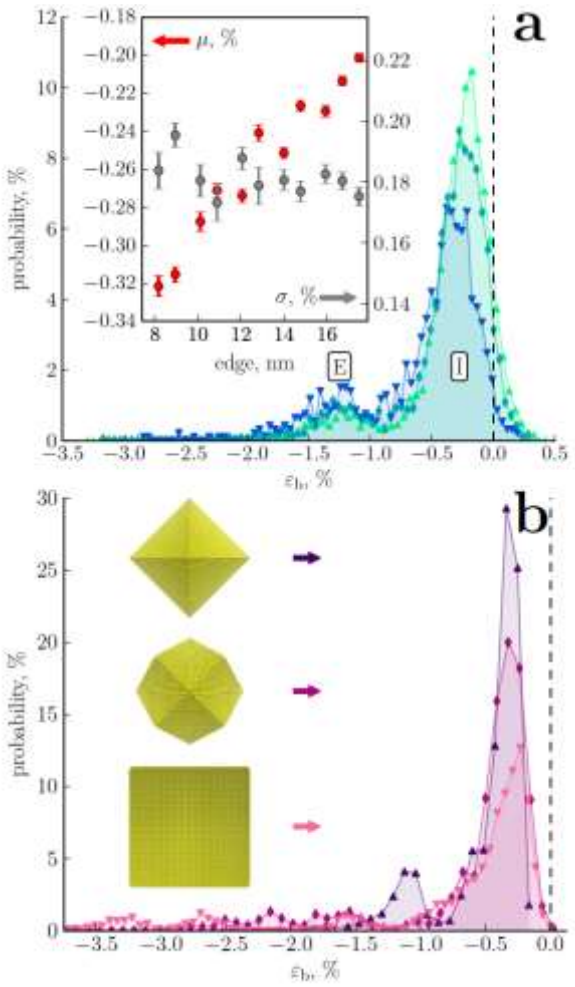

Figure 23. Histogram of the average local strain: (a) on (100) face for three different sizes (using the same truncated cube result from the XRD analysis, and particles 8.2 (downward-pointing, blue triangles), 13.2 (teal diamonds), and 18.3 (upward-pointing, green triangles) nm on edge); the inset shows mean position and width with standard deviation of the main strain component for different sizes. In (b), nanocrystals with same total surface, enclosed by different facets: octahedron (hhh) (upward-pointing, purple triangles), rhombic dodecahedron (hh0) (mangenta diamonds), and cube (h00) (downward-pointing pink triangles).

Besides the size-dependent non-uniformity, nanocrystal shape also has a direct effect on the displacement. This is shown in Figure 23b, where the average local strain histograms refer to nanocrystals with the same total surface area, but enclosed by different facets, respectively, (hhh) for octahedron, (h00) for cube, and (hh0) for rhombic dodecahedron. The cubic shape gives the largest dispersion of strain values, whereas the octahedral shape has more uniform surface strain, and the (hh0) surface enclosed shape is in between. Though the average strain for octahedra is more uniform, they do show the most sizable peak below around -1% ε_b. This shape-dependent atom displacement information was not precisely factored into the analysis of catalytic performance of shaped nanocrystals. While most works cite that the different packing of atomic planes results in changes to catalytic behaviors, the strained surface that exists due to the displacement likely contributes as well.

It is worth considering that even slight adjustments to the d-band structure (sorption characteristics) of a catalyst for a particular reaction, which may involve multiple intermediates and mechanistic pathways, can have a significant impact. Changes in d-band structure from strain can result in unexpected behavior, where both tensile and compressive strain can give similar d-band shifts and activity increases. We believe the surface strain in these (and other) nanostructures could be responsible for both their improved performance and selectivity, and the combination of experiment and simulation presented here allows for a technique to assess and predict this strain influence on catalysis. This critical information, previously unavailable to scientists, can now be

acquired and incorporated into theory to paint a more complete and global picture of catalysis on metal nanoparticle surfaces.

3.1.3 Synthesis and Catalysis by Differently Strained Pd Surfaces

Portions of the following section have been reproduced in part with permission from Kuo, C.-H.; Lamontagne, L. K.; Brodsky, C. N.; Chou, L.-Y.; Zhuang, J.; Sneed, B. T.; Sheehan, M. K.; Tsung, C.-K., The Effect of Lattice Strain on the Catalytic Properties of Pd Nanocrystals. ChemSusChem 2013, 6 (10), 1993-2000., Copyright 2013 Wiley. Some of the work may appear in Momo Yaguchi's 2012 Master's thesis, "The Effect of Lattice Strain in Electrochemical Oxidations Catalyzed by Au-PdPt Core-shell Octahedral Nanoparticles," (available at http://hdl.handle.net/2345/2928), and I thank her for the use of this material as co-author of the unsubmitted manuscript.

3.1.3.1 Strained Pd Surfaces

Palladium plays an important role in industrial chemical reactions including hydrogenations, carbon monoxide oxidation, organic coupling, and more recently in fuel cell applications as anode and cathode electrocatalyst for small alcohol oxidations and the oxygen reduction reaction.[35,110,145] A number of methods for improving the activity of Pd catalysts have been shown.[82] To enhance the catalytic properties, Pd-based bimetallic alloy nanoparticles have been widely studied.[78,146-149] The catalytic properties of Pd monolayers on different metal supports have also been studied. In order to systematically study the lattice strain effect on Pd catalysis, we developed several methods for

synthesizing Pd nanocrystals possessing different degrees of lattice stain. A series of shape-controlled Pd nanocrystals with lattice strain generated from different sources was synthesized: single-crystalline Pd nanocubes and nanooctahedra, twinned Pd icosahedra, and Au-Pd core-shell nanocubes and nanooctahedra. All of the Pd nanoparticles were generated using the ionic surfactant capping agent, cetyltrimethylammonium bromide (CTAB), in the aqueous phase, which allows for the nanoparticles to be easily cleaned and prepared for characterization and catalysis tests. Most syntheses utilize weak reducing agents and low temperatures to facilitate the formation of both twinned and core-shell structures. Twinned boundaries are readily formed when nanoparticles are synthesized at low temperatures[150,151] and the epitaxial core-shell structures are formed preferentially by using seed-mediated syntheses with slow reduction.[152] To study their catalytic properties, carbon monoxide oxidation (CO stripping), formic acid (FA) oxidation, and gas-phase ethylene hydrogenation were carried out over the particles and the results showed lattice-strain-dependent behaviors. [101]

First, we synthesized a series of Pd nanoparticles enclosed by {111} surfaces: single crystalline Pd octahedra, single crystalline Au-Pd core-shell octahedra, and twinned Pd icosahedra. Next we synthesized {100}-terminated particles: single crystalline Pd cubes and single crystalline Au-Pd core-shell cubes. Figure 24 shows TEM images of the different shaped Pd nanoparticles and different shaped Au-Pd core-shell nanoparticles studied, along with their idealized crystal models. The single crystalline Pd nanocubes and nanooctahedra were made by a seed-mediated method using ~8 nm Pd seeds generated from borohydride reduction. Both Pd nanocubes (Figure 24a-b) and Pd

nanooctahedra (Figure 24e-f) have a well-defined shape with slight corner and edge truncation. The twinned Pd nanoparticles (Figure 24i-j) were synthesized using a hydrothermal method at a mild temperature (110 °C) in the presence of CTAB and sodium citrate. The twinned, icosahedra have a narrow size distribution centered at 20 nm. A Pd icosahedron has 20 (111) facets along with 30 twinned edges that meet at 12 corners. The TEM projection of an icosahedron appears hexagonal and shows clear twin boundaries between the 111 lattices of a face-centered cubic crystal. In order to have a uniform and small gold core in the core-shell structures, we have developed a new method for the synthesis of Au seeds. The Au small seeds (cores) (Figure 24k-l) were prepared similarly to Pd seeds used in generating the shaped Pd nanocrystals, excepting for that carbon monoxide gas was introduced to the solution. The structure is determined by TEM at high magnification to be a truncated octahedron and the average edge length is around ~8 nm. Carbon monoxide contributes to the confinement of particle sizes together with CTAB. Much bigger Au octahedra were obtained when the synthesis was conducted without purging the solution with CO gas.[100] Monodisperse Au-Pd core-shell nanoparticles were synthesized via epitaxial growth of Pd on Au after the Au seeds were synthesized. To synthesize Au-Pd core-shell octahedra, larger amounts of the seed solutions were used. (Figure 24g-h) The thickness of the Pd shells is around 1 nm, resulting in approximately 3 to 6 monolayers of Pd (111) facets. For the Au-Pd nanocubes (Figure 24c-d), a smaller amount of Au seeds was used in the synthesis. This led to the formation of thicker cubic Pd shells. This thickness-dependent structural control has been previously reported. It is noteworthy that the residual CO in the Au seed

solution needs to be controlled. CO has been known to adsorb preferably on Pd 111 surfaces and thus to prevent growth along the [111] direction.[145,153,154] Many Au-Pd nanoparticles with rounded, irregular morphology on the Pd shells were formed when the solution of Au seeds containing CO was used for the synthesis of Au-Pd nanocubes.

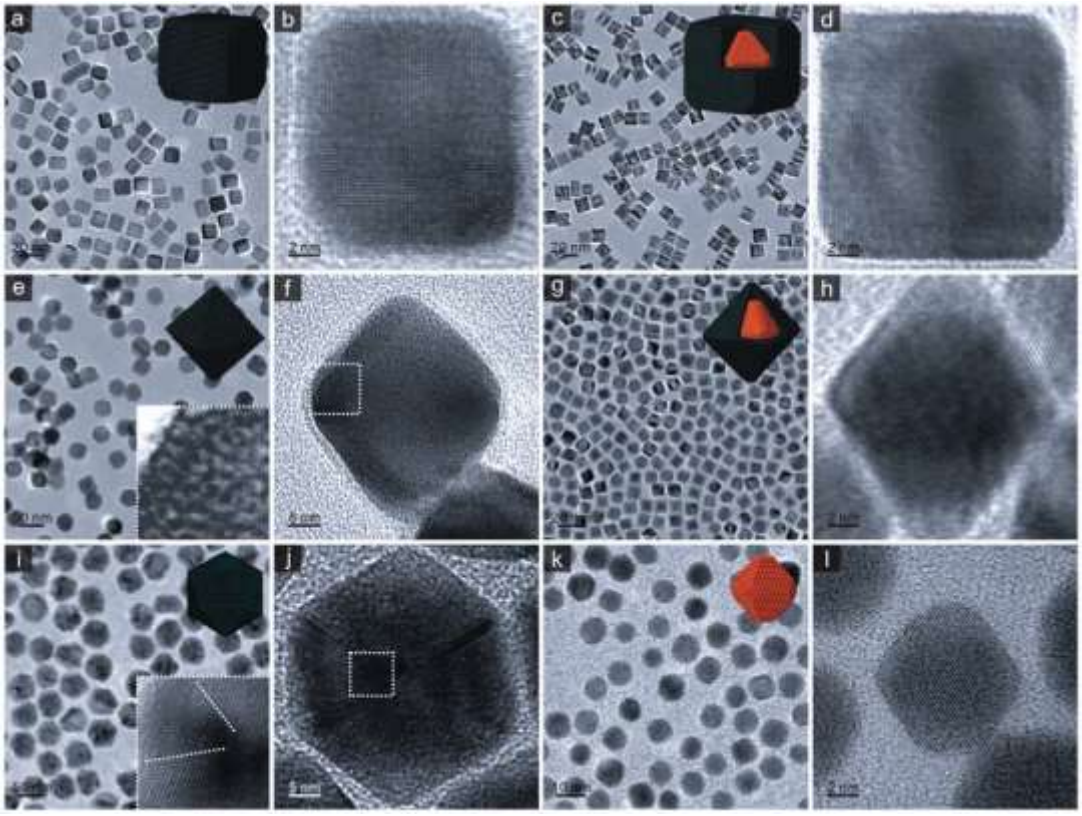

Figure 24. TEM images and models of (a,b) Pd nanocubes, (c,d) Au-Pd core-shell nanocubes, (e,f) Pd nanooctahedra, (g,h) Au-Pd core-shell nanooctahedra, (i,j) twinned Pd icosahedra and (k,l) Au seeds. High resolution images of (d) and (h) clearly show the different contrast of a core and a shell. The Au seeds are confirmed to be truncated octahedral shapes in (l). The darker lines in (j) are the twin boundaries taking place between two sets of Pd (111) crystal faces.

To study the lattice distortion generated by lattice strain in these nanoparticles, XRD was used. Figure 25 shows powder XRD of Pd and Au-Pd nanoparticles. The patterns of single crystalline Pd nanocubes and octahedra (Figure 25a) show no significant difference in their peak positions and align well with the positions of their bulk counterpart. Based on the position of Pd 111 peaks, the lattice constants of Pd nanocubes and octahedra are both approximately 3.891Å, which is near to the bulk database value of Pd. The intensity ratios between 111 and 100 of Pd are different for cubes and octahedra due to the preferred orientation of particles taking place on the sample substrates, which further proves the shape uniformity. Peaks for Pd icosahedra show an obvious left-shift to lower 2-theta degrees compared to those of single crystalline Pd nanoparticles. We believe the distortion is attributed to the lattice expansion strain existing in twin boundaries of a Pd icosahedron.

For Au-Pd core-shell octahedra (Figure 25b), the independent peaks around the bulk Pd position of Pd shells were not indexed because the Pd shell, being relatively thin, was not observable beyond the background, and most likely any Pd signal would appear under the tail of the main Au peaks as highly strained. There is indeed an observable shoulder overlapped with the Au 111 peak. After deconvolution, the 111 peak was deconvoluted to an Au 111 peak and a Pd 111 peak. The position of the Au 111 peak is very close to that of Au seeds.. The position of the Pd 111 peak has a left shift from that of bulk Pd 111 giving the lattice expansion of ~3%. The pattern of the Au-Pd nanocubes, however, shows well-separated Au and Pd peaks, most likely due to larger Pd domains. The peaks from the Au cores again do not show a significant shift compared with those of the Au

seeds (Figure 25c). The Pd 111 peak has a left shift from the bulk Pd 111 position of single crystalline Pd, indicating the lattice expansion of ~0.34%. The lattice strain in Au-Pd core-shell nanostructures has been studied by using aberration-corrected scanning transmission electron microscopy.[98,155] The lattice mismatch of Au and Pd is ~4.7%. It was found that when the Pd atomic layers are few (less than 6 monolayers), many Shockley partial dislocations (SPDs) and stacking faults (SFs) formed in the Pd shell to release strain. In a thick Pd shell (more than 15 atomic monolayers), the dislocations are merely observed in the first three monolayers over the Au-Pd interfaces and few SPDs are seen on the surface of Pd shells. According to this observation, it is reasonable that the lattice distortion of the octahedral Pd shells reaches 3%, very close to the lattice mismatch between Pd and Au, because the number of Pd atomic monolayers is less than six. However, the lattice distortion of Au-Pd nanocubes is only 0.34% due to the relaxation over the long distance from the Au-Pd interface to the Pd surface. We note that XRD of multimetallic nanocrystals (at current stage) cannot be used to decouple and fully surface strain from the core and the interface, being an average of the ensemble. In following we will use these average strain values instead in the comparisons of catalytic activity.

To study the relations between the catalytic properties and the fine differences in lattice structures of these particles, a series of electrochemistry reactions and gas-phase catalysis reactions and were run. CO electrooxidation (CO stripping) is structure sensitive and frequently used to study the surface of metallic catalysts. According to the Langmuir-Hinshelwood mechanism, CO_2 is formed from the reaction between the CO molecule and

the OH molecule generated by water oxidation on the metal surface. The structure sensitivity is ascribed to the preferential formation of OH_{ads} on different sites.[110] We performed CO stripping directly on the Pd and Au-Pd nanoparticles on a glassy carbon working electrode without any binder or support. Figure 26a shows the curves of CO stripping performed with Pd and Au-Pd nanoparticles. The CO oxidation on single crystalline Pd octahedra enclosed by {111} facets and Pd nanocubes enclosed by {100} facets occurred at 0.72 V and 0.65 V, respectively. This result is similar to the observation on previous single crystal studies, in which the close-packed 111 facet has lower activity than the more open 100 facet. The Pd icosahedron is also enclosed by {111} facets but the potential is at 0.69 V, which is in between cubes and octahedra. We believe that this is contributed by lattice strain in the twinned structure. Although the surface of icosahedra is {111} facet dominant, the icosahedron surface is more open than an octahedron surface due to the expansive lattice strain, and the boundary at many edges between individual crystallites. Because of this we would expect the activity of icosahedra to be in between cubes and octahedra. As the average calculated lattice distortion increases from 0.36% for Pd icosahedra, to 3% for Au-Pd octahedra (both enclosed mainly by {111} facets), the CO-stripping potential decreases further to 0.64 V. A similar trend was observed in cubic nanoparticles (mainly enclosed by {100} facets); the potential of Au-Pd nanocubes was shifted to a lower value of 0.61 V compared with 0.65 V for Pd nanocubes, which we attributed to the expansion of Pd's lattice in the core-shell structure. The changes in the oxidation potential can be explained by the d-band center upshift due to expansive strain and opening of the lattice.[156] Looking at the

magnitudes of these structure-dependent activities, the difference between the Pd and Au-Pd octahedra is the largest. The reason might be that in addition to the influence of lattice strain, the ligand effect needs to be considered for Au-Pd octahedral, because of the small number of monolayers. Ligand effects are caused by the atomic vicinity of two dissimilar surface metal atoms that induces charge transfer between the atoms, and thus affects their band structures. Electronic charge will transfer from the metal with the higher Fermi level to the metal with the lower Fermi level, in this case, from Pd to Au. Unlike geometric effects, such as lattice strain, the charge transfer of ligand effects is limited primarily to the first few atomic layers. An Au-Pd octahedron has only 3 to 6 atomic layers of Pd on the surface of Au, so the charge transfer effect between Au and Pd could reach the particle surface. In this case, both expansive strain and ligand effect result in an upshift in Pd's d-band center and enhanced CO stripping activity, which agrees with observed oxidation potentials. In the nanocube case, more Pd atomic layers are on the Au surface because of the geometric structure. The 100 facets of the Pd surfaces are farther away from the Au, so both the effect of lattice strain and the influence of ligand effect are limited. Based on this proposed mechanism, it would be possible to further decrease the CO-oxidation potential by using cubic Au seeds to form Au-Pd core-shell nanocubes with a thin Pd shell.

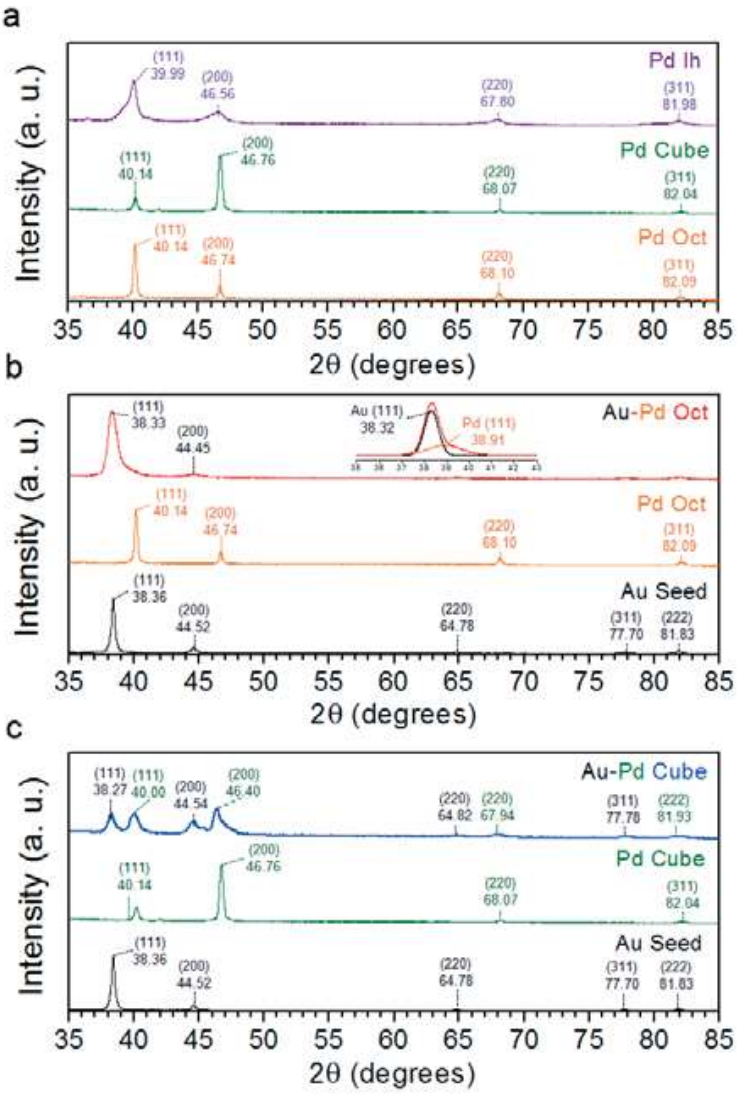

Figure 25. X-ray diffraction patterns of Au seeds, Pd nanoparticles, and Au-Pd core-shell nanoparticles: (a) comparison of spectra for monometallic Pd nanoparticles of different morphologies, (b) comparison of monometallic and core-shell (111)-terminated nanoparticles with Pd surfaces, and (c) comparison of monometallic and core-shell (100)-terminated nanoparticles with Pd surfaces (Au seed spectra are given in b,c for reference).

The electrochemical oxidation of formic acid (FOR) is one of the simplest model systems for the oxidation of a small organic molecule. Also, because FOR is a good candidate for chemical fuel in fuel cells due to its high energy density (1740 Wh/kg) and easy storage, FOR is one of the most well-studied electrochemistry reactions. It is generally believed that the two possible pathways of FOR are direct and indirect.[86,110] In the direct pathway, removal of hydrogen happens either from the C-H bond or the O-H of HCOOH, followed by oxidation on the metal catalyst surface to generate CO_2. It is known that FOR by Pd goes through the direct pathway, due to much weaker CO adsorption on Pd than on Pt (Pt exhibits an indirect pathway).[157] Figure 26b shows the forward scan curves of Pd and Au-Pd nanoparticles toward FOR. Pd icosahedra and Au-Pd octahedra both have current densities of 2.5 mA/cm^2, which is higher than that of Pd octahedra at 1.6 mA/cm^2. Their oxidation potentials are also much lower than that of Pd octahedra. This observation can be explained by the upshift of Pd's d-band center due to lattice expansion. For nanocubes, the Au-Pd core-shell structures have lower potential and higher current density for FOR compared with those of Pd nanocubes, demonstrating that the lattice strain effect is also observable for Pd (100) surfaces. It is important to mention that the FOR behaviors of Pd icosahedra and Au-Pd octahedra are similar, which is different from the trend in CO oxidation.[148] This shows that the ligand effect has less influence on FOR than CO oxidation. Also, it has been reported before that the activity of FOR direct pathway is highly related to the step and defect sites on the surface; therefore, the high number of surface defect sites on Pd icosahedra could compensate for the smaller degree of lattice expansion of Pd icosahedra compared to Au-Pd octahedra.[110]

Figure 27 shows bar charts summarizing the relation between lattice expansion and catalytic activity.

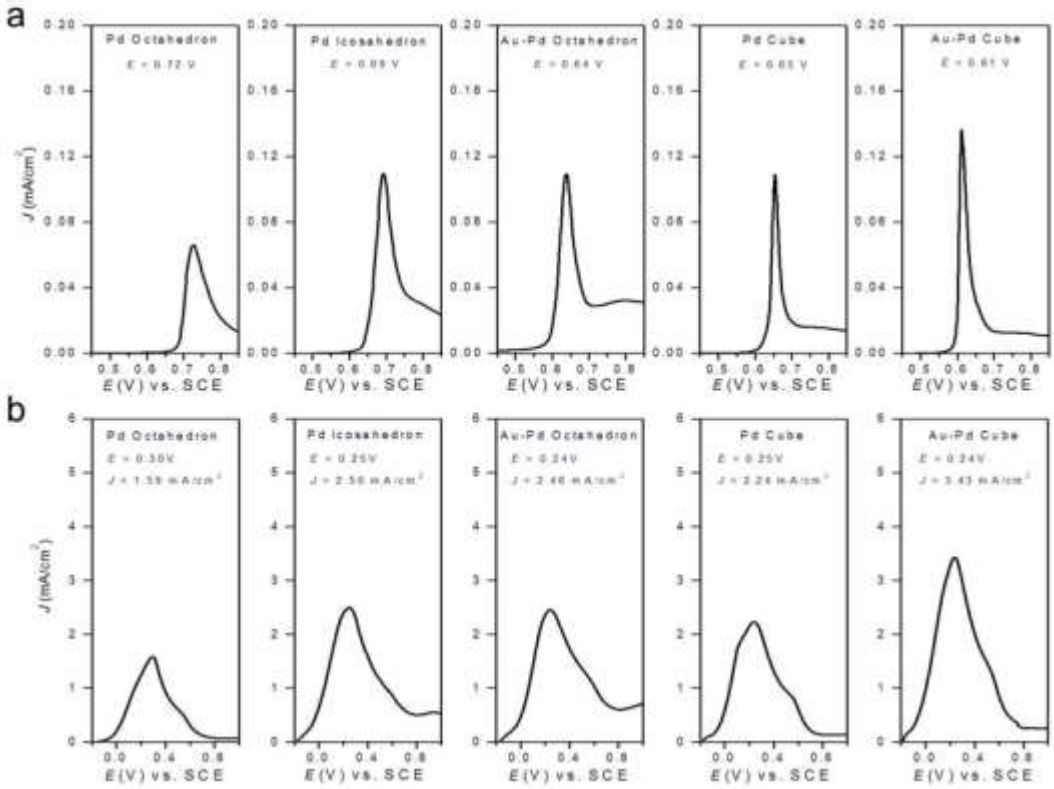

Figure 26. CV curves of Pd and Au-Pd core-shell nanoparticles as catalysts toward a) carbon monoxide and b) formic acid oxidation.

Gas-phase ethylene hydrogenation was also carried out to understand the surfaces of the nanoparticles. Ethylene hydrogenation has been used as an ideal model reaction to study the active site number during gas-phase heterogeneous catalysis.[40,103,158,159] The nanoparticles were used as catalysts directly instead of using calcination pretreatments.

Different from the traditional preparation method for heterogeneous catalysts, we didn't pretreat the nanoparticles with calcination for complete removal of the capping agent because we want to preserve the original surface structure of the nanoparticles. Figure 27d shows a column chart of ethylene hydrogenation activity. Even without calcination, the activities toward ethylene hydrogenation for all of the nanoparticles are appreciable, representing the ease of cleaning the nanoparticle surfaces synthesized with ionic surfactants.[160] Similar activities of ethylene hydrogenation for Pd icosahedra, Au-Pd cube, and Au-Pd octahedra were observed. Similar activities of single crystalline Pd octahedra and Pd cubes were also observed. However, there is a large difference in activities between these two groups of nanoparticles, the single crystalline nanoparticles with lattice expansion and the nanoparticles with no lattice expansion. The activity is mostly related to the number of active sites on the surfaces of the catalysts at the same temperature for this reaction.[161] There are two possible explanations for the observed differences in activity. The first may be due to subtle differences in the synthesis or in cleaning steps. The single crystalline Pd cubes and octahedra were synthesized with varying amounts of different halides and were cleaned using a sacrificial coating method, however the strained particles were cleaned by simple centrifugation and redispersion in DI water. Based on the differences in cleaning, the unstrained particles might have less adsorbed CTAB than the strained particles, which could lead to higher activity. Also the strained surfaces may be capped more strongly by these surfactants. The observed results may be due to some combination of these factors. It is important to note that during electrocatalysis; blanks scans of the nanoparticles in sulfuric acid were performed until

most of the CTAB was removed from the surface and the current density is normalized by CO stripping, so the obtained current densities should reflect intrinsic activity without surface hindrances.

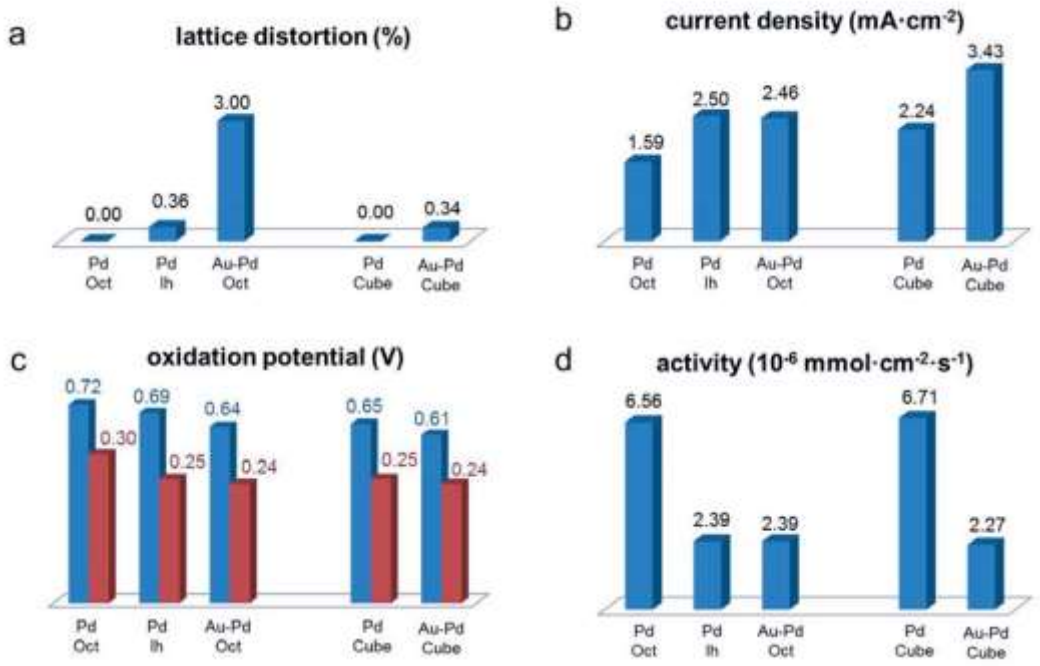

Figure 27. Column charts of (a) lattice distortion, (b) current densities for formic acid oxidation, (c) oxidation potentials of CO (blue) and formic acid (red), and (d) activities for gas phase ethylene hydrogenation at 45°C for Pd and Au-Pd nanoparticles.

3.1.3.2 Strained Pd-Pt Alloy Surfaces

We demonstrated a general strategy for the synthesis of metal core-alloy shell nanostructures with Pd-Pt alloy surfaces, by combining co-reduction and seed-mediated approaches. Octahedral alloy nanoparticles consisting of Pd and Pt were synthesized in a

one-pot hydrothermal method with co-reduction by sodium citrate at a temperature of 110 °C. CTAB was again used as the cationic surfactant, along with citrate as a shape-directing agent to preserve and grow {111} facets. In the synthesis, the composition of the alloy PdPt nanoparticles could be adjusted by mixing different molar ratios of Pd^{2+}/Pt^{2+}, yielding three compositions of Pd_3Pt, PdPt, and $PdPt_3$ for catalysis studies. In addition, octahedral core-shell nanoparticles consisting of Au cores and Pd-Pt alloy shells were synthesized by the addition of Au octahedral seeds before the co-reduction took place. These nanoparticles were characterized using TEM and EDX. The Pt-rich surface composition of the alloy and core-shell nano-particles was proved by STEM/EDX and x-ray photoelectron spectroscopy (XPS). The activity for all nanoparticles was then tested toward the formic acid oxidation reaction (FOR), a model cathode reaction for fuel cells. Significant differences in activity were observed between alloy and core-shell particles and are attributed to lattice strain. To quantify the lattice strain, the highest performing, Au-$PdPt_3$ core-shell nanoparticles, were synthesized with different thickness of alloy shells, and analyzed with synchrotron-based high resolution powder x-ray diffraction (HRXRD). The best performance in formic acid oxidation occurred for 2.3 nm shell thicknesses of PdPt, revealing the extent of lattice strain toward the surface.

Our method utilizes the hydro-thermal reaction in aqueous solution at 110°C, and successfully yields octahedral alloy nanoparticles with {111}-dominant crystal faces. In these conditions, cetyltrimethylammonium bromide (CTAB) in conjunction with citrate, is the used for the control of size and shape. Slow reaction rates plays a key role for particles growing with {111}-terminated crystal faces. Because oxygen could etch

particles or new-born nuclei to slow down the growth rate, a reference experiment bubbled with oxygen gas was carried out for comparison. When the reaction was run with oxygen gas in the solution, larger {111} crystal face dominant alloy octahedra and nanoprisms came out, which proves the influence of the slower reaction rate.

By adjusting the molar ratio between Pt^{2+} and Pd^{2+} ions mixed in the reaction, different compositions of alloy with the size of sub-13 nm could be made. To make core-shell structures for lattice strain studying, Au seeds of 8.2 nm were added to the growth solution (DI water, Pt, Pd, and sodium citrate) before the reduction occured in the oven. These Au seeds are single crystalline and monodisperse truncated octahedral. After reaction, Au-PdPt core-shell nanoparticles formed with the size ranging from ~14 nm to ~16 nm while Pd/Pt ratio changed. In Figure 28, TEM images show uniform PdPt alloy and Au-PdPt core-shell octahedral nanoparticles with three different Pd/Pt ratios, including Pd_3Pt, PdPt, and $PdPt_3$. In figure 28(b,f,j) are 2D HRTEM lattice images showing the atomic plane, where d-spacings of both {111} and {001} lattices from the [110] zone axis can are measured (octahedra sitting on a (110) edge). According to these images, there is a single-crystalline domain in each nanoparticle and {111} crystal faces are exposed on the alloy surfaces of all three compositions. HRTEM images in Figure 28(d,h,l) display lattices of both Au core and PdPt alloy shell metal phases. These images provide strong evidence of the conformal epitaxial overgrowth of the shells despite the instrinsic lattice mismatch of ~5% (maximum theoretical distortion). The lattice spacings of the Au phase (dashed outline) are larger than in the PdPt shell region, which is likely

due to the larger lattice parameters of Au compared to both Pd and Pt (a_{Au} = 4.087 Å, a_{Pd} = 3.867 Å, and a_{Pt} = 3.920 Å).

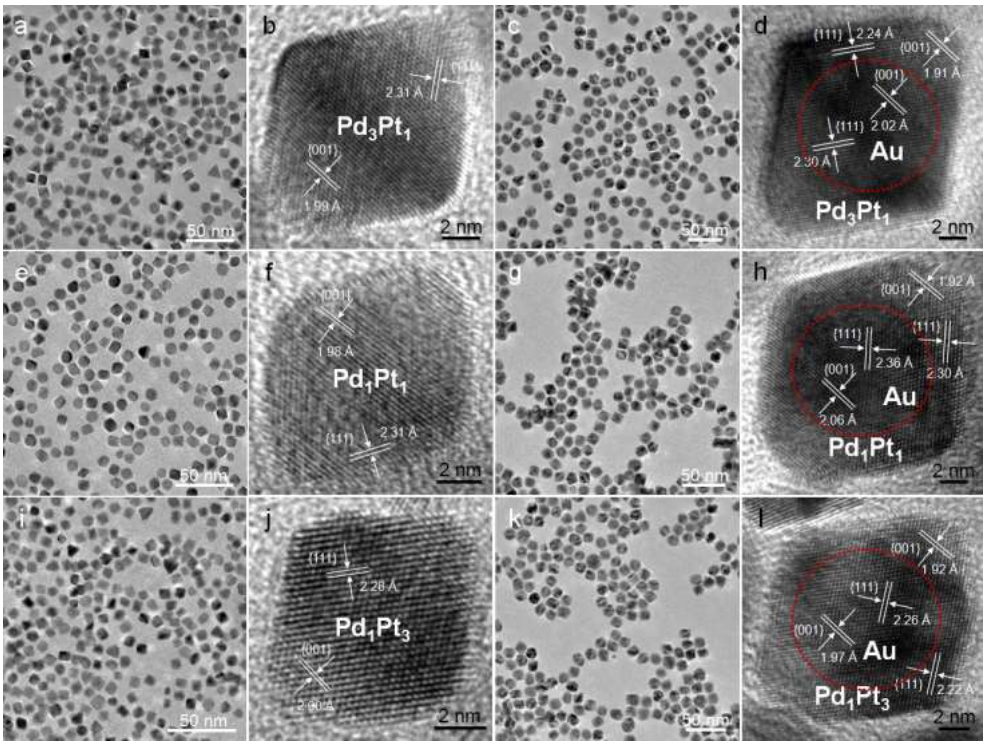

Figure 28. TEM images of a, e, i) PdPt alloy octahedral nanoparticles and c, g, k) Au-PdPt core-shell octahedral nanoparticles. The synthetic conditions change from a, c) richer amount of H_2PdCl_4 (Pd^{2+}/Pt^{2+} = 3 in molar ratio), e, g) equal amount between H_2PdCl_4 and K_2PtCl_4, and i, k) richer amount of K_2PtCl_4 (Pd^{2+}/Pt^{2+} = $^1/_3$ in molar ratio). The Au cores are used in the same amount for different core-shell conditions. High-resolution TEM images show the clear {111} and {001} lattice fringes of b, f, j) PdPt d, h, l) Au-PdPt with different Pd/Pt compositions. The dashed red line area represents location of a Au core in which lattice spacing is larger than that on shell due to the larger lattice parameter of Au than Pd and Pt.

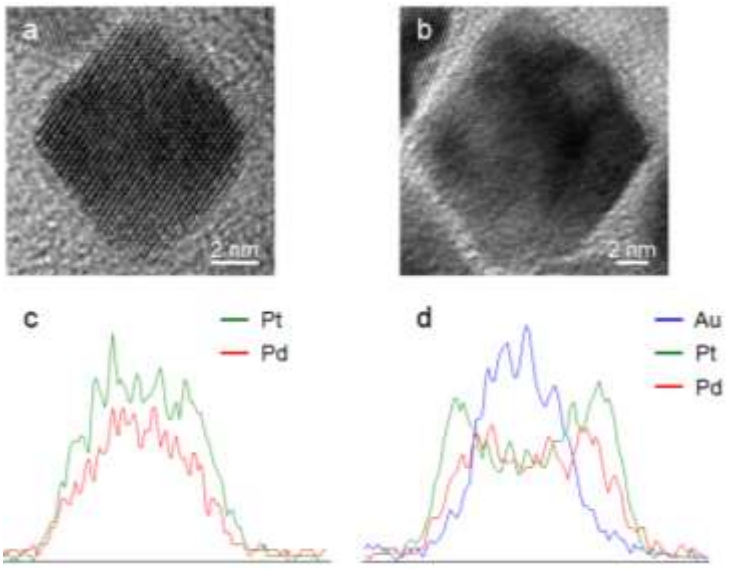

Figure 29. TEM images and TEM-EDX line-scanning analysis on (a,c) an octahedral $PdPt_3$ alloy and (b,d) Au-$PdPt_3$ core-shell nanoparticles. Both PdPt alloy particle and shell indicate Pt signal is richer on the surface.

To know the compositions of Pd and Pt, EDX was carried out. In TEM/EDX analysis, the shell composition was obtained to confirm the atomic ratio of Pd and Pt. Compositions of octahedral PdPt alloy nanoparticles were $Pd_{2.6}Pt_{1.0}$, $Pd_{1.0}Pt_{1.0}$, and $Pd_{1.0}Pt_{2.4}$ and those of PdPt alloy shells were $Pd_{2.7}Pt_{1.0}$, $Pd_{1.3}Pt_{1.0}$, and $Pd_{1.0}Pt_{2.5}$. Alloy nanoparticles and alloy shells have similar Pd/Pt ratios despite the seeded-growth difference, representing our mild strategy could coat PdPt alloy without having to overcome a substrate influence, and with tunable compositions. In TEM images, it is difficult to distinguish the core and shell structures for metals with similar masses. Hence, elemental analysis of STEM/EDX with line-scanning mode was done for

validation of Au-PdPt core-shell structures. Figure 29 exhibits these results for $PdPt_3$ and Au-$PdPt_3$ single particles in which the distribution of all elements shows their corresponding locations. Noticeably, the signal of Pt is slightly higher than that of Pd at the edges of the particles of both alloy and core-alloy-shell nanoparticles. This likely suggests that a thin Pt-'skin' might exist due to surface segregation.

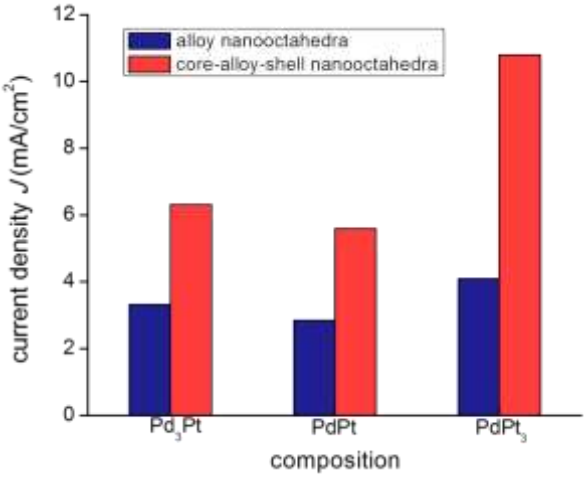

Figure 30. Current density of PdPt alloy and Au-PdPt core-shell octahedral nanoparticles in different Pd/Pt compositions.

Carbon monoxide (CO) oxidation (stripping) has been known to be sensitive to the surface structure of the catalysts since the experiments on CO electrooxidation at Pt single-crystal electrodes.[162] On the metal surface, CO absorbs on a free site and is oxidized by reacting with surface-bonded hydroxyl group OH, according to Langmuir-Hinshelwood. The OH_{ads} is generated by the oxidation of water in either acidic or alkaline media. Therefore, the structure sensitivity is ascribed to the preferential

formation of OH_{ads}. Some studies declared that PdPt alloy nanoparticles manifests different behaviors in CO electrooxidation compared with Pd and Pt.[78,163] Their potentials are located in-between Pt (0.75 V) and Pd (0.97 V) versus RHE because of different electronic surface structures changing with alloy compositions.[163] Plots of CO stripping curves on PdPt alloy and Au-PdPt core-shell nanoparticles were done in sulfuric acid electrolyte. The CO oxidation peak of Pd_3Pt (111) shows up at 0.59 V versus SCE. With increasing Pt content, the potentials of CO oxidation shift to 0.52 V (PdPt) and 0.54 V ($PdPt_3$) due to the change of electronic structures on their surfaces.[146,164] Some of the curves exhibited shoulders, which could be due to variations in composition. For core-shell nanoparticles, the peaks of CO oxidation are sharp without obvious shoulders accompanying, indicating better uniformity due to the Au template directing the mild overgrowth. There is no significant shift in the peak position between alloy and core-shell nanoparticles in the same PdPt composition. This validates that the atomic distribution of Pt and Pd on the surface of an alloy can be preserved by our method in both one-pot and seed-mediated conditions.

Formic acid is a good choice for chemical fuel in fuel cells due to its high energy density (1740 Wh/kg) and easy storage.[110] The oxidation of formic acid (FOR) is one of the simplest model systems for the oxidation of a small organic molecule. There are believed to be two possible pathways of FOR: direct and indirect.[81,148] In the direct pathway, the removal of hydrogen happens either from C-H bond or O-H of HCOOH followed by oxidation on the surface of the catalysts to generate CO_2. Indirect pathway is known as non-Faradaic (no electron flow) dehydrogenation of formic acid, in which CO

is produced first and competes with formic acid in occupying free sites on the surface of catalysts. The CO adsorbed on catalysts has to be removed by oxidation so as to retrieve free sites, which is the step of CO stripping. Pt is usually the material of the electrode extensively studied in direct formic acid fuel cells (DFAFCs). However, Pt is expensive and strongly poisoned by CO adsorption, prohibiting reaction rate and efficiency. Current elecrocatalysts for FOR have been improved by the use of modified Pt-based alloy for efficient energy generation.[81,82] FOR was tested by running CV experiments on a potentiostat. The FOR by the alloy and core-alloy-shell nanoparticles followed mainly indirect pathway. On the positive scan, there are weak peaks between 0.6 and 0.8 V. This peak is ascribed to CO_{ads} oxidation on the surface of nanoparticles. In the reverse negative scan, the strong and broad peak between 0.0 V and 0.6 V is attributed to the oxidation of formate. The peak can also be observed in positive scan but much weaker because of the competitive adsorption between formate and CO. One phenomenon is worth noticing. Both CO and formate oxidation peaks of Au-PdPt core-shell nanoparticles are stronger than those of the PdPt alloy nanoparticles. Figure 30 gives a bar chart summarizing current densities (activity) of PdPt alloy and Au-PdPt core-shell nanoparticles for FOR. The results reveal the importance of the Au cores. We know that alloys with different compositions could cause the differences in activity due to variation of the d-band center, caused by ligand and strain effects, as well as by ensemble effects. However, the difference is not obvious among these three PdPt alloy nanoparticles, and the small changes could be due to competition of these effects for different atomic distributions of Pd and Pt on and just beneath the surface. Conversely, the Au core has a

significant influence on the surface of the shell which we believe originates from lattice strain caused by lattice mismatch between Au core and PdPt shell, because the shell thicknesses are beyond the limits for significant charge transfer and ligand effects. On strained sites, the adsorbed OH groups are likely able to react faster with CO to form CO_2. In order to further understand the relationship between lattice strain and catalytic activity, we have prepared Au-$PdPt_3$ nanoparticles with thinner and thicker shells by adjusting the total mole number of Pd^{2+} and Pt^{2+}. Three different sizes of Au-$PdPt_3$ core-shell nanoparticles including 10.8 nm, 12.8 nm, and 15.2 nm were synthesized (Figure 31). Based on their sizes, the thickness, *t*, is 1.3 nm, 2.3 nm, and 3.5 nm after subtracting the average size of the Au cores (8.2 nm). The exact compositions for each thickness from EDX analysis are: Au-$Pd_{1.0}Pt_{2.9}$ (t = 1.3 nm), Au-$Pd_{1.0}Pt_{2.5}$ (t = 2.3 nm), and Au-$Pd_{1.0}Pt_{2.5}$ (t = 3.5 nm), respectively. The Au-$PdPt_3$ nanoparticles maintain their {111} crystal face dominant structures regardless of shell thickness. Cyclic voltammagrams of FOR on Au-$PdPt_3$ nanoparticles were obtained. For comparison, we also included the $PdPt_3$ alloy nanoparticles of approximate equal thickness, sizes of 7.8 nm. Interestingly, current density J changes from 5.65, 10.08, 4.11, to 4.09 mA/cm^2 as the thickness increases. This non-linear curve reveals the important relationship between activity and lattice strain in which the best activity occurs at a specific value for the shell thickness, in a volcano-type relation.

It has already been noted that the Au-PdPt particles have higher FOR activity than PdPt particles due to lattice strain, so this explains the lower current density value for $PdPt_3$ alloy nanoparticles. The lower activity of the Au-$PdPt_3$ particles with the thinnest

shell thickness of 1.3 nm can be explained by the ligand effect. Due to ligand effect, mainly caused by charge transfer, electron density is transferred from the metal with a higher Fermi level to a metal with a lower Fermi level.[165] The Fermi levels of Au, Pd, and Pt are 7.25, 7.69, and 4.2 eV, respectively. Electron density, therefore, is transferred from Pd to Pt, from Au to Pt, as well as from Pd to Pt through Au. Because the shells of the Au-$PdPt_3$ particles are Pt-rich, the overall effect is charge transfer from the core to the shell, increasing the shell's d-band filling. This increased filling results in a lowering of the shell's d-band center and a decrease in FOR activity. Lattice strain imparted by Au, on the other hand, raises the d-band center, increasing FOR activity. For sufficiently thick $PdPt_3$ shells (t = 2.3 nm) the strain effect is dominates, resulting in high activity; whereas for thin $PdPt_3$ shells the ligand effect is dominant, resulting in low activity. When the shell is very thick (t = 3.5 nm), neither effect is strong and the particles show similar activity to the bimetallic alloy $PdPt_3$ with no core.

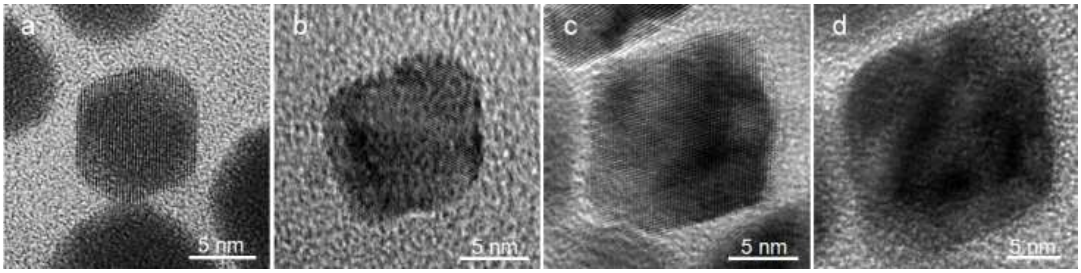

Figure 31. TEM images show different thickness of PdPt shells, b) 1.3 nm, c) 2.3 nm, and d) 3.5 nm, coating on a) Au cores.

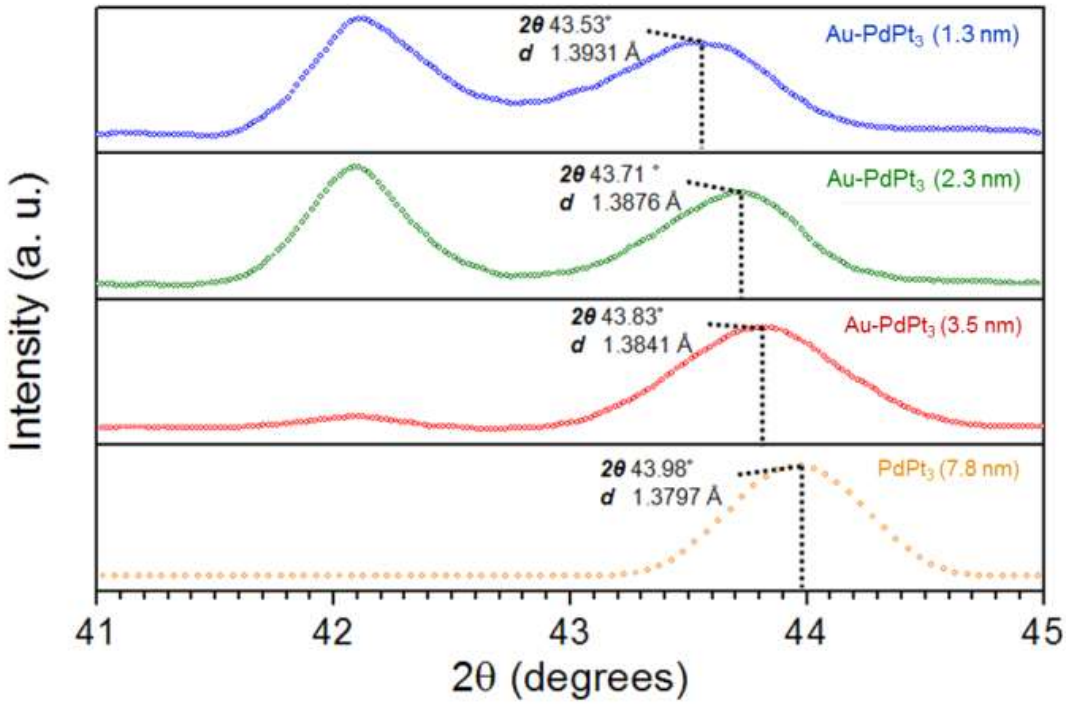

Figure 32. Synchrotron-based XRD patterns of (220) peaks of $PdPt_3$ alloy and Au-$PdPt_3$ core-shell nanoparticles with three different shell thickness. The wavelength of synchrotron x-ray incident on samples is 1.0332 Å. These broad peaks in-between 43°-44° represents the (220) peak of $PdPt_3$ alloy (shell) shifts to the left as the thickness of shell decreases.

To estimate lattice strain, synchrotron-based HRXRD with x-ray wavelength of 1.0332 Å was performed. Figure 32 includes the (220) peaks of XRD patterns of $PdPt_3$ alloy and Au-$PdPt_3$ core-shell nanoparticles within the range from 41° to 45°. In these patterns, there are two peaks for Au-$PdPt_3$ core-shell nanoparticles but only one for $PdPt_3$ alloy nanoaprticles. It is believed that peaks located at 42.11° are contributed by Au

cores. There is no significant shift occuring on these peaks as thickness varying. Broad peaks located in-between 43° and 44° correspond to that of $PdPt_3$, indicating they are contributed by alloy shells. There is an obvious trend of peaks shifting from 43.49° to 43.98°. According to Bragg's law, the (220) d-spacing of alloy exhibits lattice expansion from 1.3797 to 1.3943 Å with thickness decreasing. The lattice parameter $a°_{PdPt}$ is the estimated lattice parameter obtained from Vegard's law in which lattice parameter $a°_{AB}$ of a homogeneous alloy A_xB_{1-x} is the sum of $xa°_A$ and $(1-x)a°_B$. The value of a_{PdPt} is the experimental value of lattice parameter obtained from the equation $d_{hkl} = (h^2 + k^2 + l^2)/a^2$, where d_{hkl} is the lattice spacing of {hkl} crystal faces. Lattice strain δ_s is the difference between $a°_{PdPt}$ and a_{PdPt}, representing the atomic arrangement on the surface varied due to the strain force. It is important to note, that for $PdPt_3$ alloy nanoparticles where composition is similar, there is very little difference between $a°_{PdPt}$ and a_{PdPt} that we believe it should be induced by inhomogeneous distribution of Pd an Pt atoms, and so strain due to alloying can be negated. For Au-$PdPt_3$, the thinner the shell, the larger is the lattice strain δ_s. Based on their {111} crystal face dominant structures, the estimated number of atomic layers Au-$PdPt_3$ samples is about 5 (t = 1.3 nm), 10 (t = 2.3 nm), and 15 (t = 3.5 nm) layers. Fewer atomic layers on the shell are more easily influenced by lattice mismatch over the interface with the Au core. However, strain would shrink when atomic layers increase because the surface becomes further and further away from the source of the lattice strain. Figure 33 gives a plot summarizing the relationships between lattice strain, current density, and thickness. Current density J is 4.11 mA/cm^2 for Au-$PdPt_3$ (t = 1.3 nm), which is near to 4.09 mA/cm^2 of the $PdPt_3$ alloy. Noticeably, J peaks

at 10.08 mA/cm^2 and then drops to 5.65 mA/cm^2, following the thinning of the alloy shells. The volcano curve suggests that a peak in activity exists when the shell thickness begins to shrink to thinner values, and then the effect is canceled out by either over-straining in thin layers and/or competition from increasing ligand effects. This is an exciting and significant finding which provides not only a good way to efficiently tune and utilize lattice strain, but also a new route in making better-performing catalysts, where a 'multi-faceted' optimization of important factors that dictate catalysis behavior can take place, independent of the other variables.

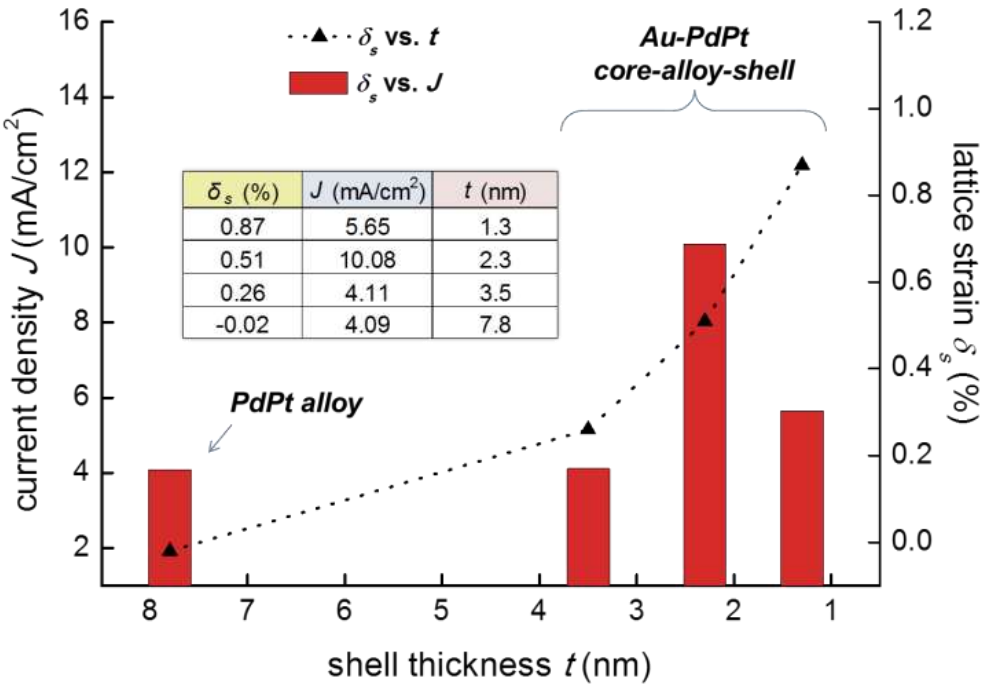

Figure 33. The relation of lattice strain, current density, and thickness of PdPt alloy domains.

3.2 Rh-Containing Bimetallic Nanoparticles

Portions of the following section have been reproduced in part with permission from Sneed, B. T.; Kuo, C.-H.; Brodsky, C. N.; Tsung, C.-K., "Iodide-Mediated Control of Rhodium Epitaxial Growth on Well-Defined Noble Metal Nanocrystals: Synthesis, Characterization, and Structure-Dependent Catalytic Properties." J. Am. Chem. Soc. 2012, 134 (44), 18417-18426., and from Sneed, B. T.; Brodsky, C. N.; Kuo, C.-H.; Lamontagne, L. K.; Jiang, Y.; Wang, Y.; Tao, F.; Huang, W.; Tsung, C.-K., "Nanoscale-Phase-Separated Pd–Rh Boxes Synthesized via Metal Migration: An Archetype for Studying Lattice Strain and Composition Effects in Electrocatalysis." J. Am. Chem. Soc. 2013, 135 (39), 14691-14700. Copyrights 2012 and 2013 American Chemical Society.

Rh is a choice metal for study because of its versatility, activity, and selectivity over so many chemical transformations, such as NO-reduction, CO-oxidation, electro-oxidations, hydrogenations, and hydroformylations.[166-170] Rhodium is another platinum group metal that has been investigated as an electrocatalytic material.[51,104,168,171-179] The chemical stability of rhodium films is greatly increased compared to other platinum group metals (PGM) and has been utilized in micro-electronics.[180,181] Controlling the size, shape, and composition of Rh overgrowth in a core-shell structure could allow for similar advancements in the metal's application towards enhanced heterogeneous catalysis, electrocatalysis, hydrogen storage, and plasmon-enhanced catalysis.[124,167-170,174,175,177,179,182-188]

The synthesis of nanoparticles with control of Rh surface, however, remains challenging because of its propensity towards forming disordered nanostructures.[6] The

lack of structural control for Rh could be attributed to the small number of suitable surfactants or adsorbate additives which can stabilize the growing Rh surface in such a way as to expose specific facets. Halide or pseudo-halide anions have been extensively used as additives for shape-control of Au, Pd, and Pt nanoparticles,[12,13] but so far this strategy has not been successfully utilized with Rh nanoparticle synthetic methods.

Many works have exhibited dendritic,[189] horned,[179] aggregated,[190] or networked[175,179] nanostructures of Rh which are either polycrystalline, exposing random crystal facets, or are otherwise without much long-range order. The dendritic morphology has been reported using other noble metals such as Pt.[76] Pioneering examples demonstrate the synthesis of Rh cubic, octahedral, and other shaped structures,[167,187,190-199] but these examples show that there is still ample room for improvement of nanoscale control of particles comprising Rh, as roughness and particle irregularity remain problems to be overcome and the surface facets have not been well studied. The strategy of introducing shaped metal seeds during the synthesis has been developed as an alternative route to achieve morphological control. The use of a structure-controlled crystal substrate to direct overgrowth has been reported as an effective method for control of the surface structure and metal-metal interface in bimetallic systems.[152,200,201]

3.2.1 Synthesis and Evolution of Rh-Containing Bimetallic Nanoparticles

Figure 34 illustrates how the monodisperse and shape-controlled NCs of Pd and Au were used as substrates to generate the Rh island epigrowth with the assistance of iodide adsorbate ions. Ascorbic acid was used as reducing agent in the aqueous

cetyltrimethylammonium bromide (CTAB) solution. The tunable size of the Rh overgrowth and the variety of sizes, metal types, and morphologies of the substrate nanoparticles employed demonstrate that this is a general method which offers a new level of control of Rh. Directing the Rh epigrowth at the atomic-level on these metal substrate nanoparticles offers advantages to catalytic performance through both modification of the surface electronic and geometric structure, and through the introduction of a controlled metal interface.[202-205] We demonstrate that the substrate NCs impart their morphology to the Rh growth which influences its activity towards CO-stripping and formic acid oxidation electrocatalysis.

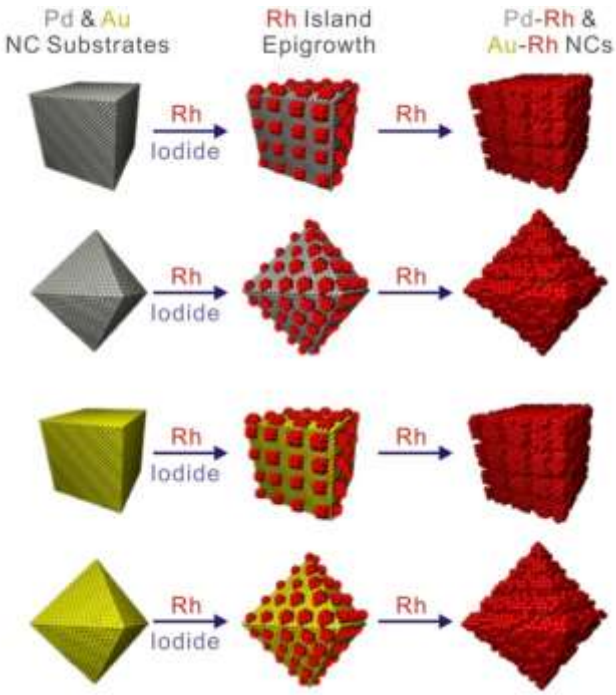

Figure 34. Synthetic strategy for controlled rhodium epigrowth on noble metal nanocrystals.

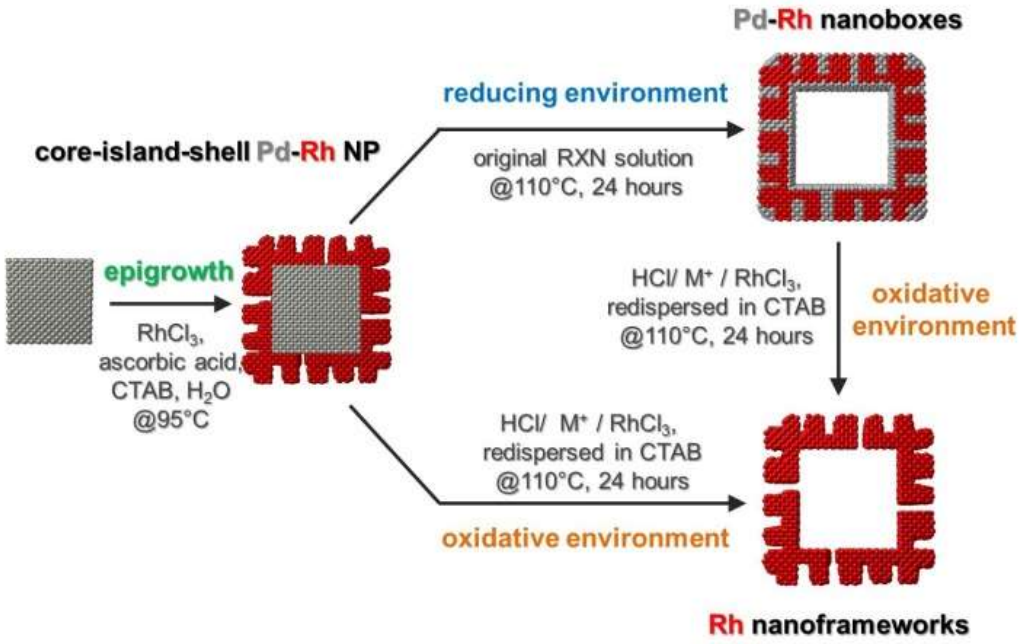

Figure 35. Illustration of the synthesis of Pd-Rh nanoboxes and Rh cubic nanoframeworks from core-island-shell NCs with heating under different red/ox environments.

We then show a synthesis of shape-controlled Pd-Rh nanoboxes, and Rh nanoframeworks by controlling metal migration at the atomic level, and we describe in detail their characterization, mechanisms for formation, and catalytic behaviors. Utilizing metal migration in a nanoparticle has been demonstrated as a way to achieve atomic level structural control.[206-208] In recent years, this concept has been used to control Rh structures. Zhang et al. demonstrated the sacrificial re-placement of Rh by Pd to generate hollow Pd cubes with Rh cubes in the interior.[77] Xie et al. have shown that removal of cubic Pd cores from Pd-Rh core-nanoframes can produce pure Rh nanoframes with high

surface area and a degree of facet control.[189,209] This was achieved by oxidative etching with the addition of HCl/$FeCl_3$ and accelerated by the formation of halide complexes. Relatedly, a surface detachment-readhesion mechanism promoted by metal-halide complexes has also been proposed and studied in the synthesis of monometallic Rh nanocubes.[210]

Using this information, we take advantage of the Pd-Rh heterostructures to evolve new structures. Instead of directly influencing the Rh during nucleation and growth, we are able to control the migration of the Pd in bimetallic particles post-synthesis (Figure 35). The migration treatment of the core-island-shell nanoparticles at raised temperatures without the addition of an etchant or reducing agent generated hollow bimetallic Pd-Rh nanoboxes with smooth faceting, while the addition of an etchant generated hollow Rh nanostructures consisting of a fused-island frame-work. The Pd nanoparticles, Pd-Rh core-island-shell nanostructures, Pd-Rh nanoboxes, and Rh nanoframeworks structure were then examined and compared for activity in CO-stripping, formic acid oxidation (FOR), ethanol oxidation (EOR), and oxygen reduction (ORR) electrocatalysis. The activity for these model fuel cell reactions is then used to link the factors of lattice strain and composition in the nanostructures to their catalytic behaviors.

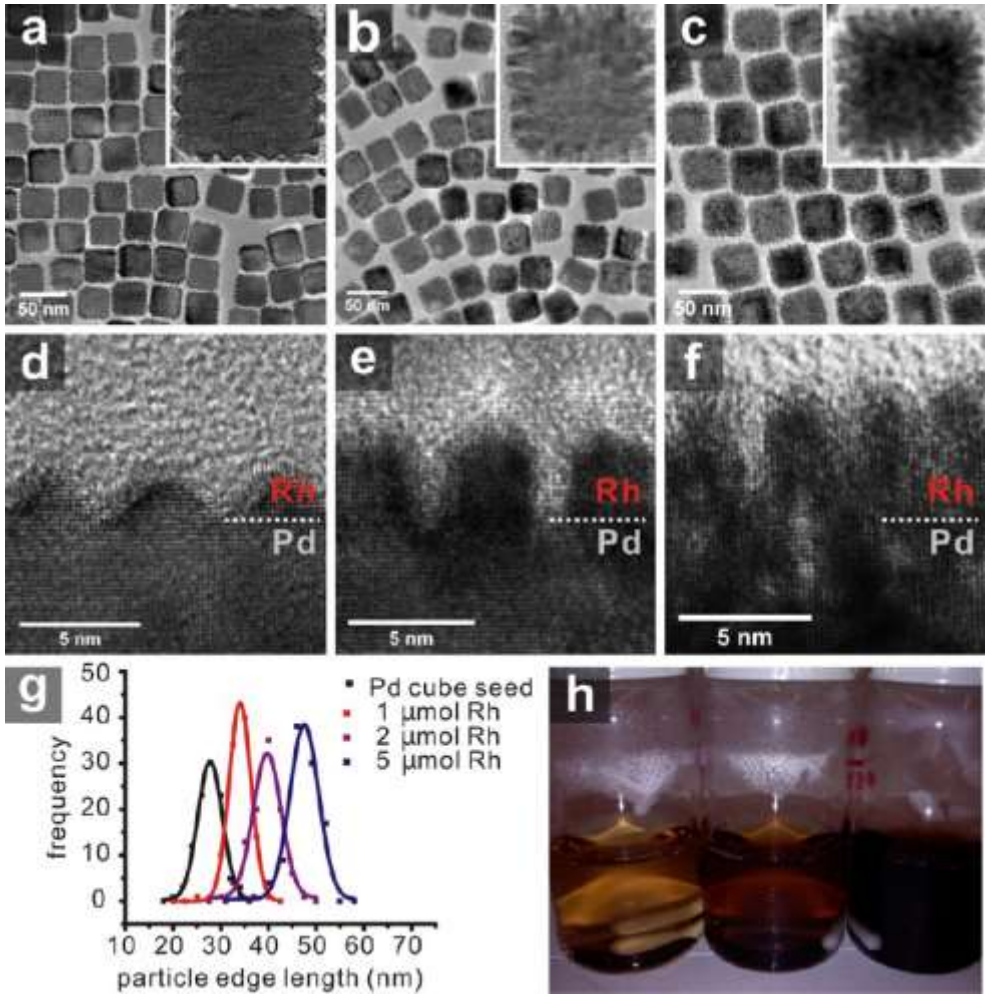

Figure 36. The overgrowth of Rh. TEM images of the Pd-Rh NCs are shown in with a) 1, b) 2, and c) 5 µmol of Rh in the growth solution. Insets are high magnification images of single particles. In (d-f) are HRTEM images of the resulting Rh on Pd particles for each solution: d) 1, e) 2, and f) 5 µmol of Rh in the growth solution. Size distributions and a Gaussi-an fit are given in g) for the substrates and bimetallic parti-cles (100 individual particle measurements per sample), as well as a photo (h) of each of the growth solutions post-synthesis (1, 2, and 5 µmol of Rh left to right).

The progression of Rh overgrowth on substrates was first examined by changing the amount of Rh overgrowth on the Pd cubes shown in Figure 36. It was observed that the Rh overgrowth begins by reduction onto the Pd surface in the form of small islands (Figures 36a,d) at low concentration of Rh in the growth solution. These islands are around ~3 nm in diameter, and arrange on the cube faces in grid-like patterns. A small amount of Pd surface may still be exposed. Subsequent growth appears to have preference for these just-formed islands, rather than filling spaces in between (Figures 36b,e). This type of growth mode (Volmer-Weber island growth)[3,211] has been observed previously with the noble metals.[76,189,200,212] Further growth of the islands produces small Rh columns of similar diameter to the islands extending from the Pd cores. Additional growth, shown in Figures 36c,f, results in a dense 'forest' of single crystal Rh columns. The overgrowth can be tuned by the addition of Rh to give ~2-3 nm islands, ~5-6 nm columns, and ~8-10 nm long single-crystal columns of Rh (Figure 36g). The structure appears open and with channels observed between the columns. The overgrowth still retains the original crystal lattice orientation at even higher amounts of Rh because of the epitaxial overgrowth for the fcc metal. Though a limit for the overgrowth was not observed, small free Rh particles start to form in solution with higher precursor amounts, but the growth on substrates remains single-crystalline. This information gives insight into the mechanism of growth observed and demonstrates our ability to control the overgrowth thickness by simply increasing or decreasing the amount of Rh in the growth solution.

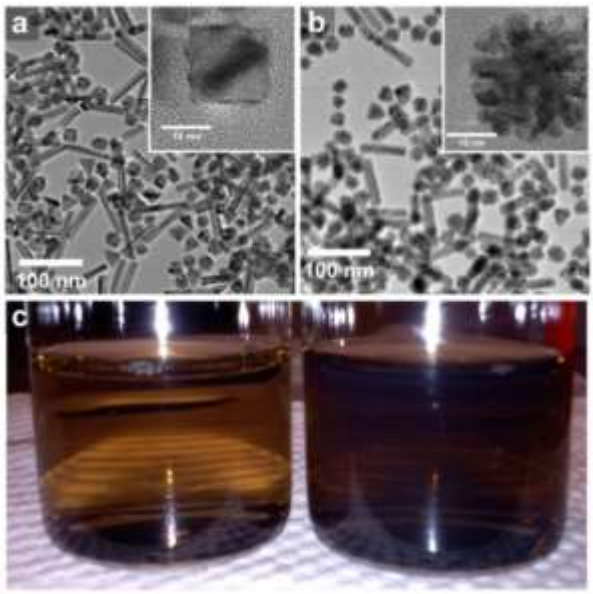

Figure 37. The critical role of iodide in the epitaxial overgrowth. Low magnification TEM and HRTEM (insets) images of particles obtained without iodide (a) and with iodide (b) in the growth solutions for intermediate amounts of Rh (2 μmol). A different degree of color change resulting from the growth can be seen in c) a photo of growth solutions without iodide (left) and with iodide (right) for comparison.

Upon investigation of how the method presented could generate more control for Rh, we found that iodide ions play the most important role in the overgrowth. Figure 37 displays TEM images and a photo which reveal that Rh overgrowth occurs in a much higher yield when the growth solution contains iodide ions. Figure 37a shows the overgrowth without any iodide ions, while Figure 37b show those with iodide ions. (The irregularity of the Pd substrate particles used for overgrowth is due to their synthesis without the use of iodide in order to control the I- amount in the growth solution; the high

yield of uniform cubic substrates shown previously was achieved by adding iodide ions). A stark contrast is observed regarding the amount of Rh overgrowth with and without iodide ions. With the same amount of precursor, substrate NCs, and otherwise identical conditions, only solutions with iodide yielded significant overgrowth. The photo in Figure 37c is for solutions with I- (right) and without I- (left). The difference in the darkness of the solution confirms what is seen under TEM. The much darker solutions contain larger particles from more Rh overgrowth. The color transformation or darkening of the growth solution is more rapid for the growth solutions which contain iodide. The color change for iodide solutions occurs in ~2 minutes, while a more gradual slight darkening is observed for solutions without iodide. For solutions without iodide, a small amount of nanoparticles < 1 nm were observed under TEM and are likely small Rh NCs that have formed in solution away from the substrate surface. This is evidence of the importance of iodide ions in the incorporation of Rh onto the Pd substrate surface. The critical roles of iodide ions are proposed and discussed here.

Iodide ions may serve multiple functions to facilitate the epitaxial overgrowth. First, iodide ions decrease the reduction potential of the Rh ions by complexation, which decreases the formation of free Rh nuclei. Second, the iodide ions draw the Rh ions to the surfaces of sub-strate crystals due to their strong interaction with Pd. The Pd surfaces lower the barrier of reduction by introducing a substrate as a seed for the growth. Others have similarly invoked anion coordination as a powerful tool in drawing the precursor metal ions nearer to the seed crystal surface to accelerate the growth process.[213] Third, iodide itself could serve as a reducing or oxidizing agent as the I^-/I_2 red/ox pair, which

would activate the Pd surface for Rh overgrowth.[214,215] Overall, the iodide ions inhibit the free nucleation of Rh in the solution, draw the Rh ions to the Pd surfaces, and promote the Rh reduction on the Pd surface.

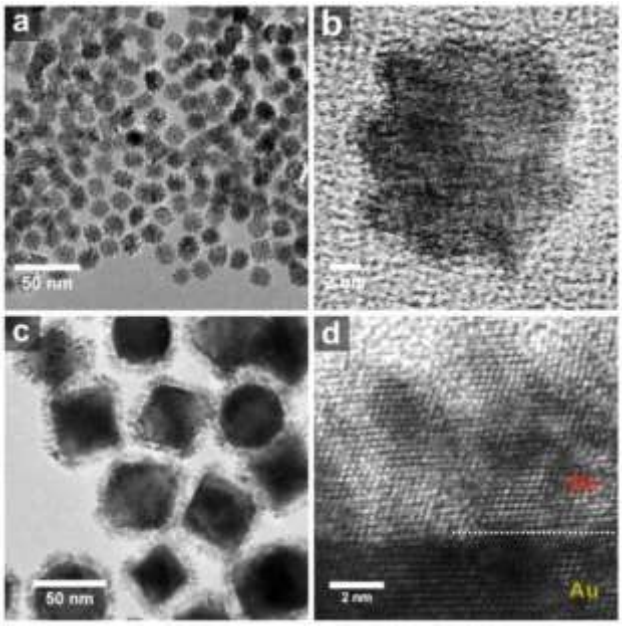

Figure 38. TEM (a, c) and HRTEM (b, d) images are shown for Rh-overgrowth after changing the size, shape, and metal type of the substrates. For comparison, (a, b) 12 nm Pd cubes and (c, d) 60 nm Au octahedrons were used.

In order to support this hypothesis and demonstrate the versatility of this method, smaller Pd cubes as well as Au octahedrons and Au cubes were used as substrates for overgrowth (Figures 38 and 39). Iodide ions were added to promote the Rh overgrowth. The size of the Rh islands and columns remains around ~2-3 nm in width, regardless of crystal seed size and type. Using a gold substrate, a similar type of growth can be seen.

Epitaxy was observed for the gold particles as well, despite the rather large lattice mismatch of ~7%, compared to ~2% for Pd-Rh. Observation of cubic Au-Rh nanocrystals under TEM displays the Rh epigrowth also occurs on gold cubes under similar conditions.

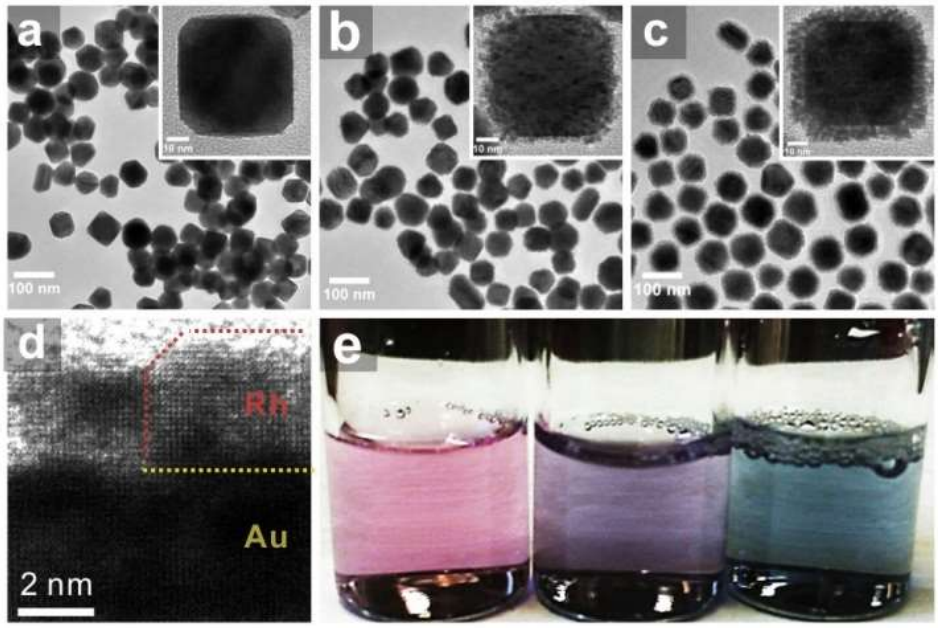

Figure 39. TEM images (a-c) are shown above for Rh-overgrowth on Au nanocubes with increasing Rh amounts of a) 1, b) 2, and c) 5 μmol Rh. In d), HRTEM of a selected particle shows the epitaxy between phases. A photo of each of the solutions is included in e) to show the effect of overgrowth on the SPR of the Au-Rh NCs.

Figure 39 shows overgrowth on Au cubes with 1, 2, and 5 μmol Rh in the growth solution. The same trend in epitaxial growth progression (island growth into columns) is observed in TEM and under HRTEM in Figure 39d despite the large lattice mismatch

(~7%). A photo of the respective growth solutions in Figure 39e displays the effect of Rh overgrowth on the gold core's visible surface plasmon resonance (SPR) band. The nanoparticle solutions become progressively bluer in appearance as more Rh is added to the substrate surface, because of the absorption and scattering due to the SPR. The effect of Rh overgrowth on the SPR band of the Au substrates was investigated using UV-visible spectroscopy. Extinction spectra shown in Figures 40a and 40c were obtained for cubic Au-Rh NCs with serial amounts of Rh in the growth solutions. A red-shift of the absorbance peak at ~530 nm is observed for the larger amounts of Rh precursor added to the solution. This peak not only shifts but broadens after more overgrowth, demonstrating the effect of additional Rh epigrowth on the surface plasmon resonance of Au NCs. Recently, H. Chen *et al* used Au-Pd overgrowth to elucidate the cause for this shift.[216] They have shown that the shift is due to percolation of the plasmon as the in-homogeneous growth perturbs the transition of the dielectric to the metal. In our system, we observe the same peak shift and broadening as what would be expected for a non-continuous overgrowth. In this way we monitor the overgrowth of Rh on gold. Figure 40 clearly demonstrates the difference between the overgrowth with and without iodide ions. Solutions containing iodide in Figure 40c,d (larger Rh overgrowth) show a much more dramatic shift in the SPR band. The Au-Rh nanostructures that can be generated by this method offer potential towards plasmon-enhanced catalysis.[188]

Next, the post-synthesis evolution to Pd-Rh nanoboxes (NBs) and Rh nanoframeworks (NFWs) by manipulation of Pd migration in Pd-Rh core-island-shell nanocubes (NCs) is depicted in Figure 41. First, Pd-Rh core-island-shell nanocubes were synthesized as

described. Then, the core-island-shell nanocubes undergo transformation to either Pd-Rh NBs or Rh NFWs through alternate pathways involving migration and oxidative etching of the Pd cubic core. Under migration treatment by moving the original core-island-shell reaction solution to a pressure vessel at a raised temperature, Pd atoms relocated from the core to the gaps between surfaces of the Rh framework overgrowth. The process recapitulated a cubic outer surface and resulted in the Pd-Rh NBs. In the formation of Rh NFWs from core-shell NPs, the Pd can then be selectively removed from the NBs by addition of an etchant such as dilute hydrochloric acid or metal ions to rinsed nanoparticles that have been resdispersed in solutions of CTAB. Both NBs and core-island-shell particles produce Rh NFWs, devoid of Pd, when etchant is added. The Rh nanoframework can be observed intact after etching of NBs, suggesting that the NB metal phases are separate in the structure.

The pure Pd, core-shell Pd-Rh, hollow Pd-Rh, and hollow Rh nanoparticles are uniform in size and shape after observation of many particles under TEM. Representative TEM images are shown in Figure 42(a-h): substrate Pd NCs, core-island-shell NCs, NBs, and hollow NFWs in 42(a,e), 42(b,f), 42(c,g), and 42(d,h), respectively. Ideal crystal model cross-sections showing the proposed evolution from Pd cubes to Rh cubic frameworks are given in Figure 42(i). It can be seen that the Rh cubic framework is left intact and the crystal domains are aligned. The fused regions are formed during the initial overgrowth. As the islands grew in size in the formation of the core-shell particles, they were epitaxial and made contact to form a porous yet, interconnected network of islands on the cube facets.

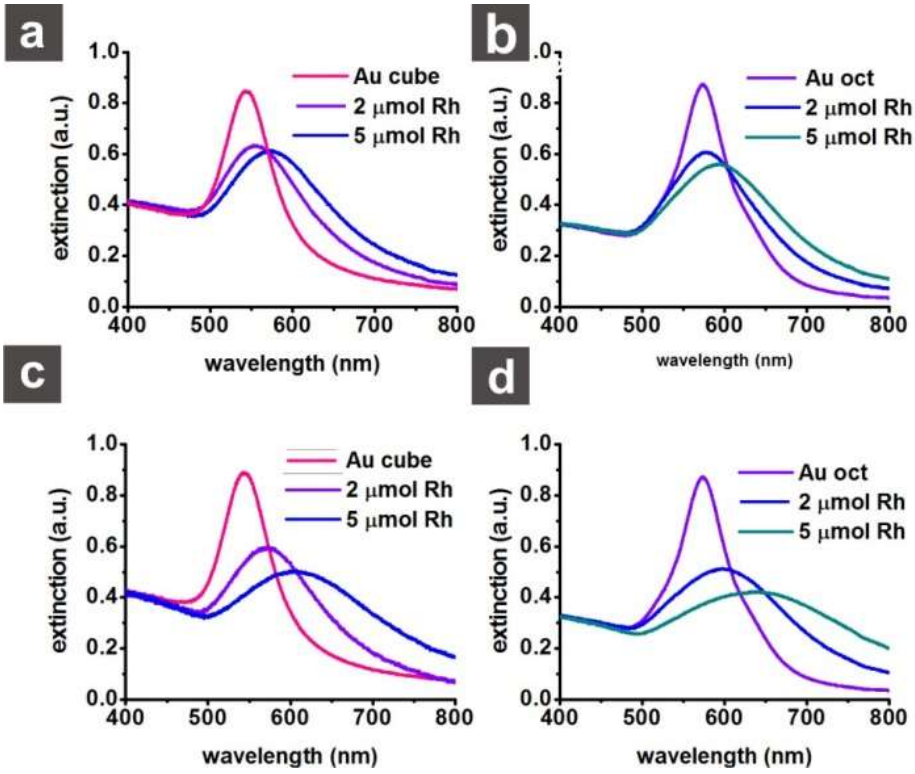

Figure 40. UV-Vis spectra for cubic and octahedral Au-Rh nanoparticle solutions with different amounts of Rh overgrowth: a) cubic and b) octahedral NPs synthesized without iodide in the growth solution for 0, 2, and 5 μmol of Rh in the growth solution. Extinction spectra for c) and d) are for cubic and octahedral NPs, respectively, synthesized with iodide added to the growth solution.

Moreover, this actually demonstrates that our previous speculation of the Volmer-Weber island growth mode was not entirely accurate. Rather, the fused framework strongly suggests that a mixed Stranski-Krastanov island-film growth mode could also be occurring, which favors the result of the island frameworks being more ordered than the

dendrites of previous work. Likely this is primarily due to the self-assembly of cationic CTAB surfactant (CTAB being the major difference between methodologies) in combination with iodide additive, and different solvent/particle interfacial properties assisting in an ordered self-assembly of the initial nucleation and growth events.

Figure 42(a-c) show additional TEM and HRTEM images of Pd-Rh NBs. The morphology is truncated-cubic with a hollow cubic interior. The shell is mostly filled and single crystalline. The migration was terminated at the outer edges of Rh island columns, corresponding with the known thickness (~4-5 nm) of the original Rh epigrowth. The cubic morphology indicates that the outer surfaces of these particles are dominated by {100} facets. Some {100}-terraces (along with steps in between) can be observed in the cross section of the HRTEM image of the shell in Figure 42(c). This was the case across the majority of particles. A contrast variation throughout the TEM cross-sections of the cube faces can be observed in the images. It could be contributed by the phase-segregation of Pd and Rh. Nanoboxes of different sizes and morphologies can also be synthesized by this route.

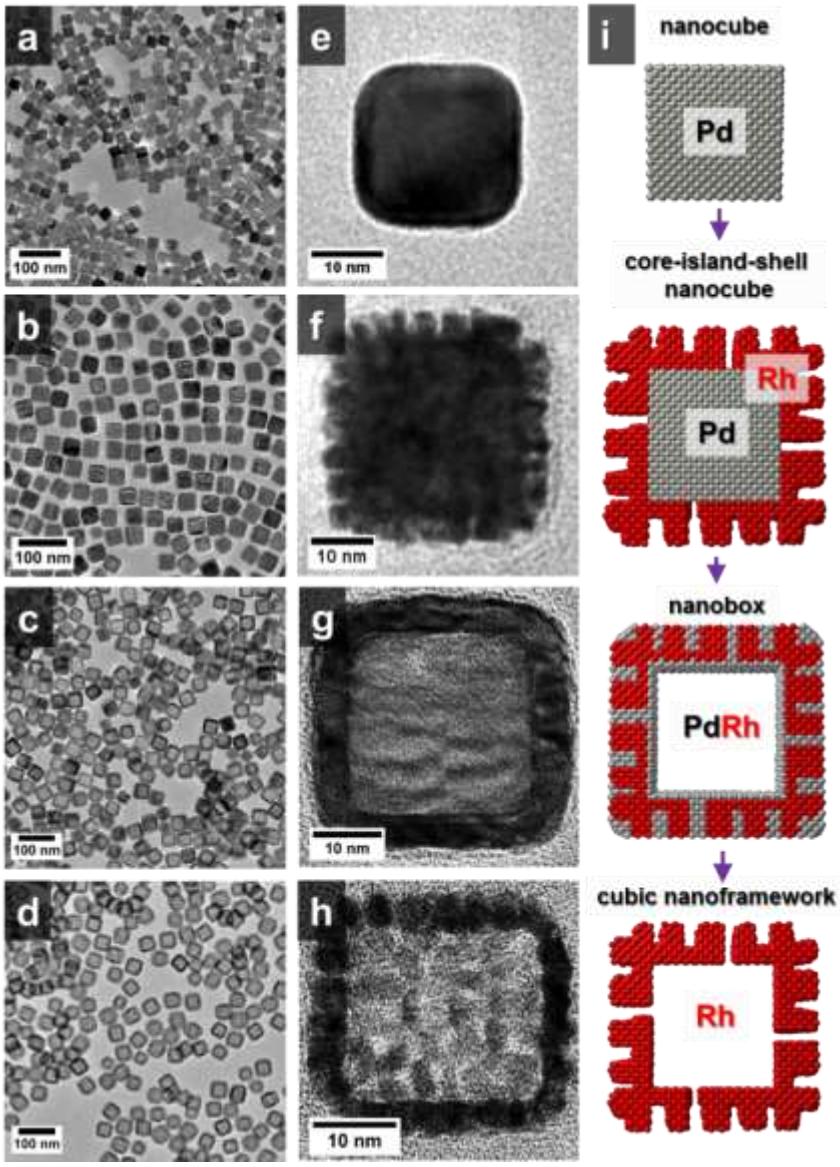

Figure 41. TEM images of (a,e) Pd nanocubes, (b,f) Pd-Rh core-island-shell nanocubes, (c,g) Pd-Rh NBs, and (d,h) Rh cubic NFWs. A scheme in (i) shows models for the structural evolution from Pd nanocube to Rh cubic NFW. The image in Figure 1(g) contains a single Pd-Rh NB where contrast in the shell reveals the underlying Rh island framework in the structures.

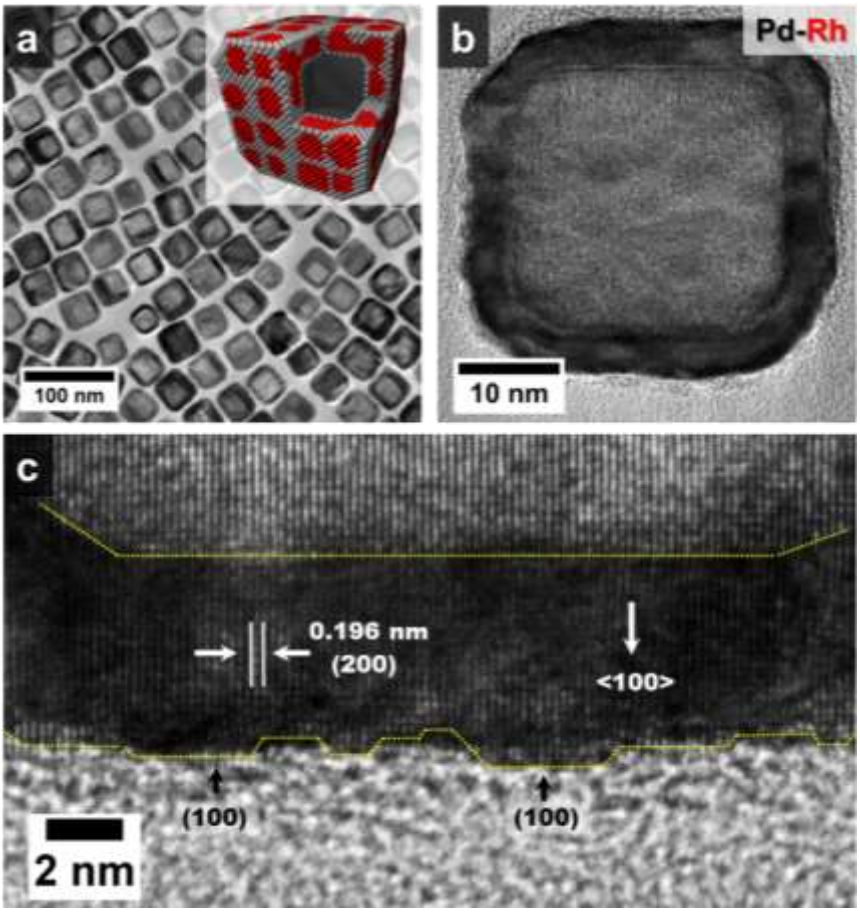

Figure 42. TEM and HRTEM images of Pd-Rh nanoboxes. In (a) is a low magnification image of Pd-Rh NBs with a crystal model inset, (b) high magnification image of a single Pd-Rh NB, and (c) HRTEM image of the single-crystalline shell of the nanobox which exhibits {100}-dominant faceting.

Controlling the migration of atoms in nanoparticles is a common feature to nanoparticle syntheses. Galvanic replacement, the Kirkendall effect, Ostwald ripening, oxidative etching, and surface detachment and readhesion mechanisms have all been used

to control the atom migration in nanoparticles.[79,208,210,217-220] Preferential migration of one element to the particle surface under reducing or oxidizing environments has also been reported. This occurs because of fundamental differences in metal-metal bonding, metal surface free energy, and heats of formation of the corresponding surface metal-oxide.[16,17,20] In our study, the mechanism of migration is unique. First, the Rh islands provide a framework matrix for Pd migration. This does not occur via galvanic replacement because of Pd's higher potential for reduction. Following, it is important to discuss the reason for the Rh nanoframeworks being left intact, both during the migration and after adding etchants. This is essentially a result of Rh's higher chemical and kinetic stability. It is known that Pd dissolves in HCl at elevated temperatures, whereas Rh is resilient to the same treatment. The fundamental explanation for the better chemical stability of Rh under such conditions can be explained by the higher Rh-Rh bond energy com-pared to Pd-Pd[221] and by the slower kinetics of halide complexation for Rh (kinetic stability of Rh). The halide ions have a preference for Pd because of a better 'soft-soft' interaction as compared to Rh.[180,181] In our synthesis, the Pd atoms or ions migrate from the particle cores via small gaps between the Rh islands in the shell and this is accelerated by bromide ions supplied by CTAB present in the solution. Previously, Xie et al. have also invoked metal ion complexes in the explanation for oxidative etching of Pd in their recent work on the synthesis of Rh nanoframes.[209]

The chemical stability of Rh and Pd is understood, yet it is clear the formation of the Pd-Rh NBs involves more than oxidative etching of the Pd core. The Pd atoms or ions must diffuse along the surface and deposit between Rh islands in order to recapitulate a

cubic particle with {100} facets. Recently, Yao et al. have suggested detachment-readhesion as a plausible theory for the relocation of metal atoms in single metal nanoparticle solutions.[210] Their study suggests that halide-complexation is an important step in the mechanism. Tao et al. have, from another standpoint, discussed the preferential enrichment of the surface by one metal over the other depending on the red/ox environment above Pd-Rh bimetallic particles at high temperatures in gas phase.[20] They found that Rh prefers the surface in oxidative environments because of a lower heat of formation of the surface metal-oxide (stability under oxidative gas environments). Pd only migrated to the surface when there was a reducing environment. This has been attributed to Pd's lower surface energy. We believe a combination of these processes dictates the formation of the Pd-Rh NBs. Since the solution of migration treatment to form NBs is the original reaction solution, the combination of reducing environment (ascorbic acid in excess) and CTAB serves as a driving force for the Pd migration at raised temperature due to surface energy. The migration of Pd to the outer surfaces results in a box-like appearance which is the result of both the initial substrate morphology and the affinity of halides for the Pd and Rh {100} facets. Under oxidative conditions (when etchant is added), the Pd is not stable enough to remain in the nanostructure and is dissolved to yield pure Rh NFWs, which are chemically resistant to the treatment. The red/ox environment of the solution, the kinetic stability of Rh, and detachment-readhesion of Pd atoms mediated by bromide ions, all play a role in the formation of the Pd-Rh NBs. The halides' occupation of {100} facets and the initial substrate's orientation both serve the important role of regenerating the cubic

morphology.[209,210] Additionally, the diagonal relation of the periodic table supports Rh having similar properties to Pt, which is also known to be more resistant to etching than Pd (nobility).

Control experiments were performed to confirm this mechanism for Pd migration and removal from the core-island-shell nanoparticles. Trimetallic particles containing Au were synthesized to discover whether or not more noble metals were unstable enough to be removed by the method. First, a layer of Pd was overgrown on Au seeds. These bimetallic nanoparticles were then used to overgrow Rh to create Au-Pd-Rh core-shell-island-shell trimetallic nanoparticles. The Au-Pd-Rh nanoparticles were washed and redispersed in CTAB solution and subjected to the identical oxidative conditions for generating the Rh cubic NFWs. It was assumed that Au would be resilient to the etching treatment. This was confirmed by the resulting yolk-shell Au-Rh nanoparticles shown in Figure 43(a,b) along with the synthetic scheme in 43(c). Pd was selectively removed from the inner shell layer of these particles, leaving the Au seed intact in the porous Rh shell. This process generated the Au-Rh yolk-shell type nanostruc-tures. EDX measurements of the samples confirmed that the particles did not contain a significant amount of Pd after etching. The experiments led to the conclusion that Pd is, again, unstable under the oxidative environment of these conditions. Gold, like rhodium, is resilient to the oxidation treatment, and so the red/ox environment and the metal stability are important factors in the synthesis of NBs and NFWs. Additional control experiments involving the choice of etchant, other noble metals such as Pt, and those with particles

formed with the addition of excess halides and reducing agent to the washed nanoparticles instead of etchant, provided more evidence in support of the conclusions.

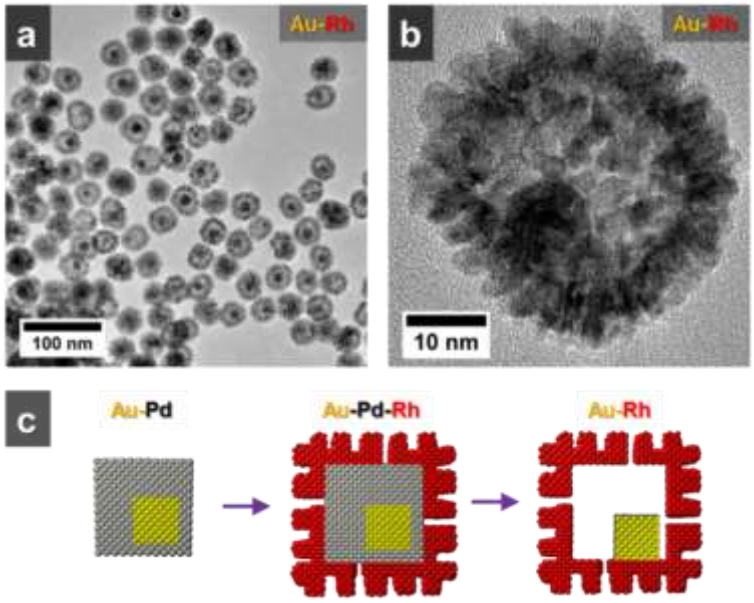

Figure 43. (a,b) TEM images of Au-Rh yolk-shell nanoparti-cles. A scheme is given in 3(c) for yolk-shell formation by selectively etching the Pd layer.

3.2.2 Characterization of Rh Bimetallic Nanoparticles

Electron microscopy was used to characterize the nanoparticles that were synthesized. Figure 44 displays the highly uniform Pd nanocubes and nanooctahedrons synthesized and used as substrates for the overgrowth of Rh. The relatively large size of the shaped crystals (~30 and ~60 nm on edge for cubes and octahedrons, respectively) allows us to systematically study the growth on different crystal facets as their surface facets are well defined in this size range. The overgrowth is observed to take on a grid-like arrangement

of islands extending from the palladium surface. Rhodium's preference for island epitaxy is explained using bond dissociation energy and surface energy. Since the bond dissociation energy between atoms is higher with Rh, atoms prefer to deposit on preformed islands rather than on the Pd surface so that the interfacial strain is reduced. Since ascorbic acid is a weaker reducing agent, already deposited Rh will auto-catalyze further reduction preferably at the surface of the growing islands.

Rhodium overgrowth on Pd and Au nanocrystals has been studied previously,[189,222] but closer inspection reveals important characteristics of our nanoparticles that set it apart from previous examples. The Pd-Rh nanoparticless retain the overall shape of their substrate and the Rh islands are observed to take on a distinct shape themselves. The size distribution of islands is highly uniform and their appearance is identical across hundreds of observed NCs. The epitaxial, single-crystalline nature of the Pd-Rh nanoparticles is revealed by selected area electron diffraction (SAED) and high-resolution TEM (HRTEM). The size of the overgrowth islands can be tuned by changing the amount of Rh added. To confirm the crystalline structure of the overgrowth islands, the HRTEM images in conjunction with SAED patterns were obtained for a higher amount of Rh overgrowth on the different Pd substrate morphologies. Figure 45 shows the respective TEM, SAED, and HRTEM images for a single a-c) Pd cube, d-f) Pd-Rh cubic nanoparticle, h-i) Pd octahedron, and j-l) Pd-Rh octahedral nanoparticle. Despite some branching structures with higher amounts of Rh, the growth was still found to be single-crystalline; that is, occurring epitaxially from the substrate rather than by particle attachment from the solution. Cubic nanoparticles are viewed from the [100] zone axis

and octahedral nanoparticles are viewed from the [111] zone axis in the images. The single-diffraction-patterns of the Pd-Rh NCs clearly reveal the single-crystalline, epitaxial nature of the overgrowth. The d-spacings obtained from SAED patterns of the nanoparticles with Rh epigrowth are smaller in comparison to those for the pure Pd crystals (Figures 45b,e,h,k) because of Rh's smaller lattice parameters (lattice mismatch of ~2%).

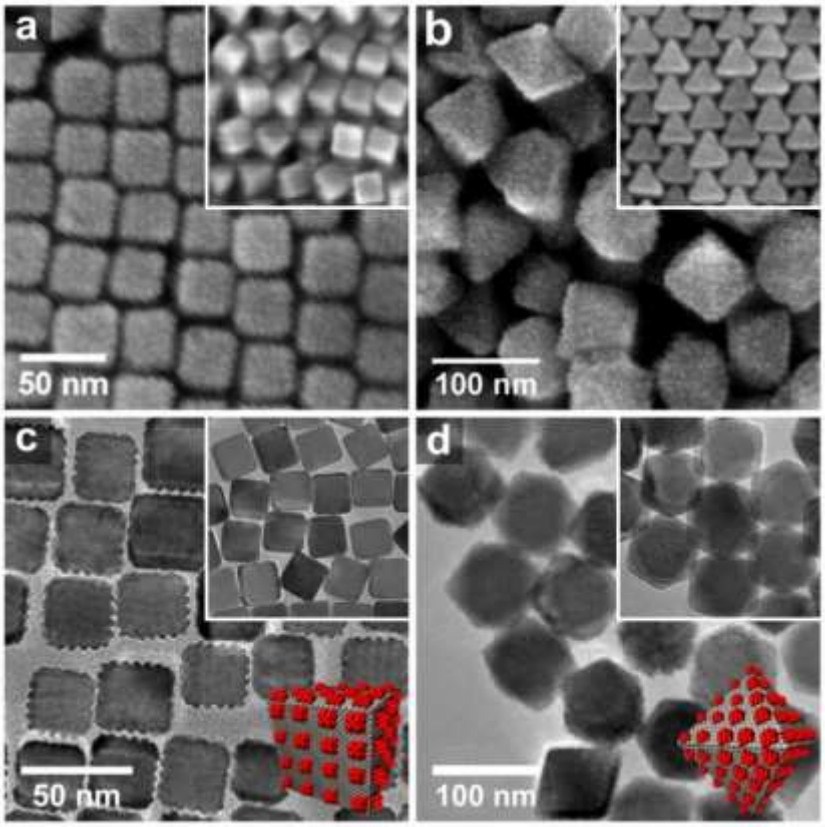

Figure 44. Electron microscope images. SEM (a,b) and TEM (c,d) images were taken for palladium nanocubes (a,c) and nanooctahedrons (b,d) with Rh overgrowth. Insets show the corresponding uniform substrate crystals before the Rh overgrowth.

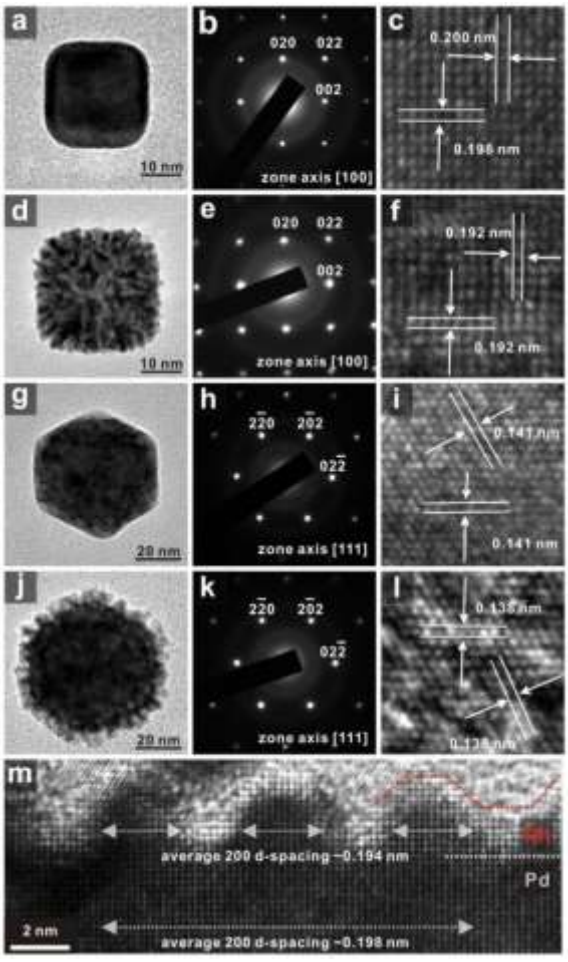

Figure 45. Structures of the Pd-Rd nanoparticles. Above are (a, d, g, and j) transmission electron microscope (TEM) images, (b, e, h, and k) selected area electron diffraction (SAED) patterns, and (c, f, i, and l) high resolution TEM (HRTEM) images for rows (a-c) Pd cubic nanoparticle substrates, (d-f) Pd-Rh cubic nanoparticles, (g-i) Pd octahedral nanoparticle substrates, and (j-l) Pd-Rh octahedral nanoparticles. HRTEM in m) shows the different average d-spacings obtained for {200} planes at locations in the interface of Pd core and Rh island overgrowth.

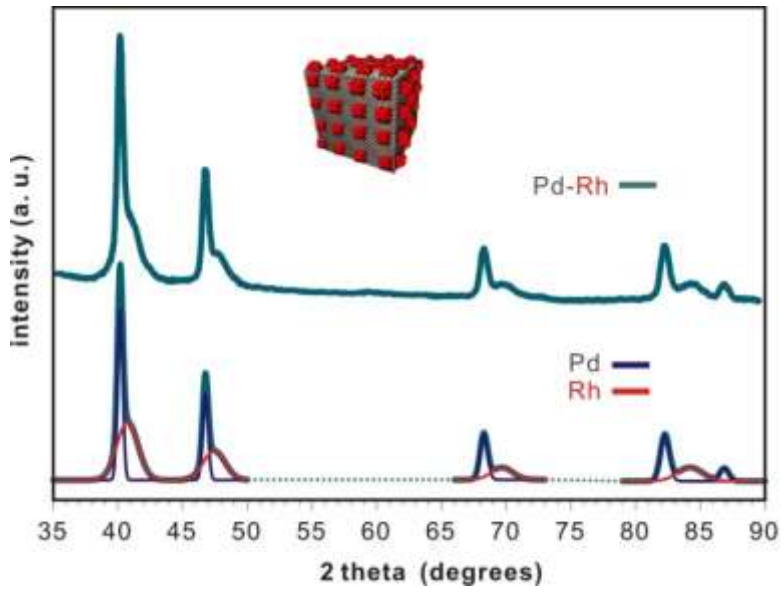

Figure 46. Powder X-ray diffraction (XRD) spectra for Pd-Rh nanoparticles with 5 μmoles of Rh added for growth. The spectrum is deconvoluted to give the respective Pd and Rh contributions in the spectrum below.

The HRTEM images further verify the epitaxy of Rh on Pd substrates. The square 2D lattice observed for cubic nanoparticles shows the {100} planes for fcc metals, as does the hexagonal lattice of the {111} planes observed for octahedral nanoparticles. Note that for Pd-Rh lattice images the beam was focused on the Rh overgrowth portion of the nanoparticles, where Rh d-spacings were measured. For cubic Pd substrates, d-spacings for the {200} planes were around 0.200 nm and for the cubic Pd-Rh nanoparticles, the d-spacing of {200} is 0.192 nm. For octahedral Pd substrates, the {220} d-spacing is 0.141 nm, while the Pd-Rh octahedral nanoparticles d-spacing is 0.138 nm. The d-spacings agree with those obtained for pure Pd and Rh from crystallographic databases for the

respective metal's lattice planes. Figure 45m clearly displays the interface between Pd and Rh. Different average d-spacings are obtained for planes in the same direction but for different regions close to the interface (interior Pd cubic core and exterior Rh overgrowth). The average spacing is about 0.194 nm for the Rh overgrowth whereas for the Pd core location, the spacing is 0.198 nm. The difference reveals the transition between the Pd and Rh metal phases. Hundreds of the Pd-Rh nanoparticles were surveyed, but fewcould be found containing misaligned lattice fringes. This indicates all of the resulting island overgrowth is epitaxial. Particle formation and attachment from the solution has been observed with alternate methods for synthesizing Pd-Rh nanoparticles, but this was not observed in our case.[189] The latter is significant as our method can generate Rh overgrowth with complete epitaxy and a higher degree of control over the island growth's uniformity in terms of both size and shape.

Powder X-ray diffraction (XRD) was performed to understand the overgrowth (Figures 46). The spectra for Pd-Rh nanoparticles show clear Pd diffraction patterns, which closely resemble that of the pure Pd nanoparticles. A distinct Rh shoulder can be observed to the right of all of the Pd peaks. The centers of these shoulders lie at the expected position for Rh for all of the peaks. For example, the 111 peak max for Pd lies at ~40.2° while the shoulder's center is at ~40.7°. The difference in the peak position for Pd and Rh is more pronounced at larger angles. Deconvolution of the spectrum reveals the contributions of Pd and Rh to the spectrum (Figure 46). The separation of the metallic phases indicates that the composition of the growth should be mainly pure Rh rather than Pd-Rh alloy. The broad Rh peaks are due to the smaller domain size relative to Pd. The

crystal domain size calculated from the Rh deconvoluted peaks is ~6.0 nm, which is comparable to the average between the length and diameter of an individual Rh column.

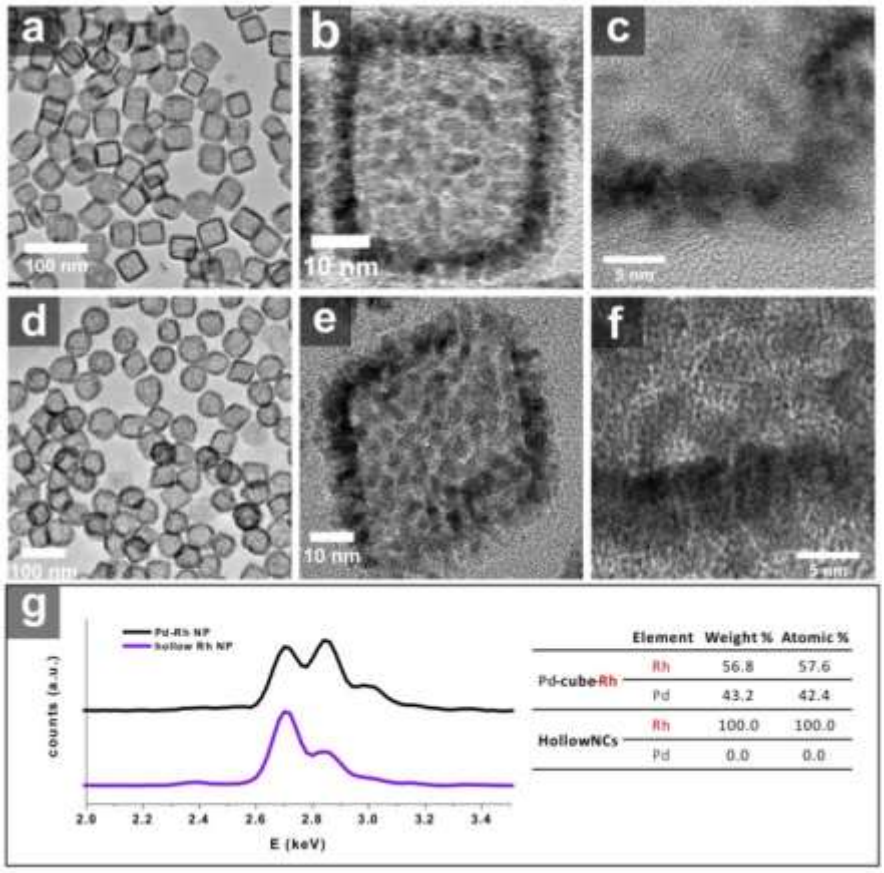

Figure 47. Hollow Rh nanoparticles after selective etching of the Pd cores. TEM images of hollow (a-c) cubic and (d-f) octahedral Rh nanoparticles. In Figure 4g are EDX spectra of Pd-Rh NCs and the resulting hollow Rh nanoparticles after etching.

Energy-dispersive X-ray spectroscopy confirms the ability to control the metal ratio between the core and shell. The Pd substrate cores could be selectively etched away by diluted hydrochloric acid. The resulting hollow nanocrystals retain their overall

morphologies and well-aligned crystal domains (Figures 47a-f), despite the island structure. EDX spectroscopy shown in Figure 47g confirms that the Pd had been etched away and the hollow nanocrystals are composed of Rh. The corresponding spectrum of particles before etching is used for comparison above the spectrum for the hollow particles. There is disappearance of the signal for the Pd L-lines for hollow particles, and quantitatively no Pd could be detected. To the best of our knowledge, this was the first example of well-defined hollow Rh nanostructures, and led to the study of metal migration in the system. It also demonstrates the ability to generate Rh NCs with more complex nanostructures with high surface area, stability, and defined morphology.

The surface structures of the Rh islands were studied by HRTEM and electrochemistry. It was observed that the islands grown at lower Rh amounts appear to take on a specific, truncated pyramidal shape (Figure 48). Different structures for the Rh islands were proposed by comparing the HRTEM images and the crystal models. In the case where the Pd substrates are cubic, a majority of these Rh truncated pyramids should expose {100} facets at the upmost surfaces, and a combination of {111}, {100}, and {110} facets on the sides of the islands. It is difficult to rule out the possibility of a small degree of high-index facets. A model and images for the cubic Pd-Rh islands are shown in Figures 48(a-c). An angle of ~45° can be measured between the 100 direction (normal to the Pd cube surface) and the side of the pyramidal shaped islands. The normal to this plane should be the <110> direction based on the angle measurement. From this cross-section, we might conclude a (110) side surface or a (110) edge formed by two (111) planes (Figure 48c). The latter is more ideal since the (111) surface is more

thermodynamically stable than (110). A similar shape for Rh islands was observed by P. Nolte et al.[223] They described a truncated Rh pyramid formed on a metal oxide substrate which was terminated by {100} and {111} surfaces. For the Pd substrates that are octahedral, a majority of the Rh pyramids likely expose {111} facets (Figures 48g-i) although again there is the likelihood for the presence of others. The angles measured from the cross-section lead us to believe that they are truncated tetrahedrons completely enclosed by {111} surfaces. The two distinct angles, ~35° and ~20°, measured between the side surface against the direction normal to the substrate surface correspond to the angles between a (100) edge [formed by two (111) planes] and a (111) plane, measured respectively, with the <111> direction. The proposed structures in the model shown in Figure 48i should give the observed lattice cross-section from the HRTEM images. Given this structural information, we speculate that the cubic nanoparticles are dominantly enclosed by both {100} and {111} Rh facets while there should be a majority of {111} Rh facets on the octahedral nanoparticles. Furthermore, the difference between the two shapes is more distinguishable at higher amounts of overgrowth because the cubic nanoparticles are dominantly enclosed by mainly {100} (Figures 48d-f). The images in Figures 48(d-f) show how more overgrowth on cubic substrates generate more {100} surfaces due to the lengthening of islands into columns which should introduce sides that expose {100} facets. This conjecture is verified upon examination of the distinct electrocatalytic properties of the two Pd-Rh nanoparticles with different morphologies. The results of this study are discussed below.

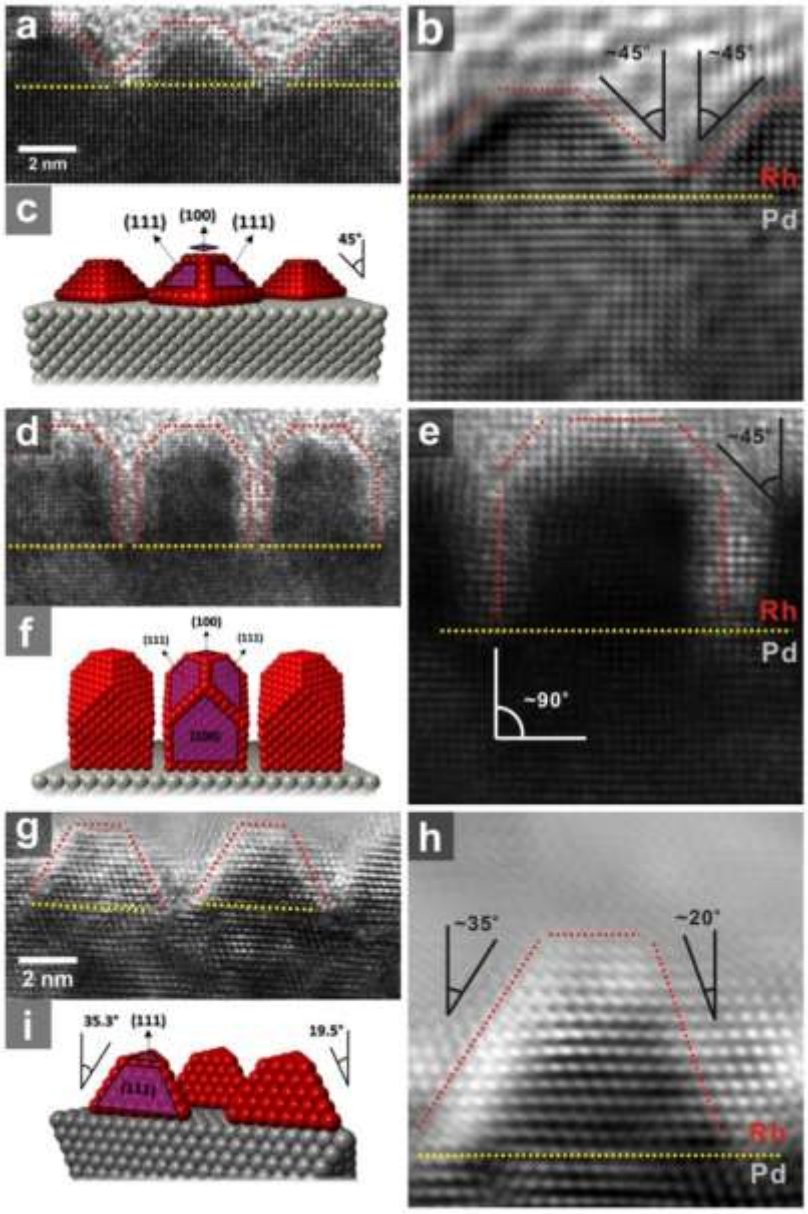

Figure 48. Surface structures of the Rh overgrowth. HRTEM images (a, d, g), FFT-enhanced images (b, e, h), crystal models (c, f, i) for island overgrowth on Pd nanocubes (a-c), col-umn growth on Pd nanocubes (d-f), and island growth on nanooctahedrons (g-i).

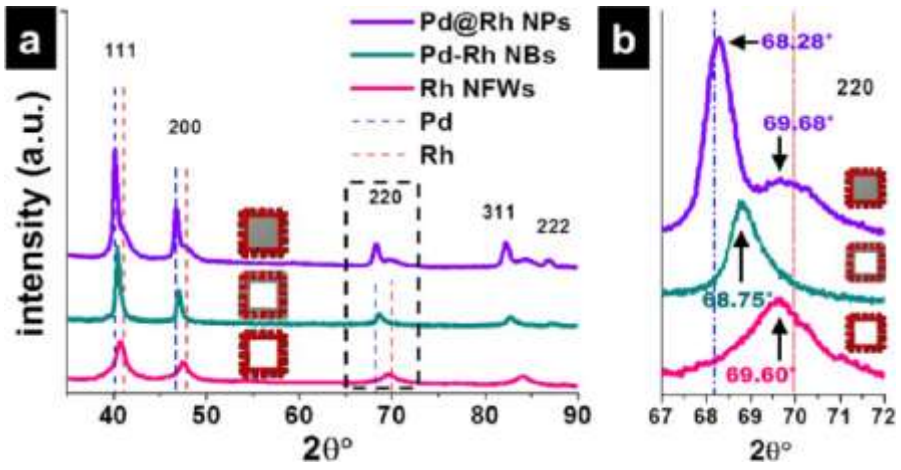

Figure 49. Powder XRD spectra of the Pd-Rh nanoparticles. Shown in (a) are spectra for Pd-Rh NPs, Pd-Rh nanoboxes, and Rh cubic nanoframeworks with monometallic bulk spec-trum peak positions of both metals given for comparison. The 220 peak region is magnified and shown to the right in (b).

To determine the crystal structures and degree of lattice strain on these structures, powder X-ray diffraction spectra were obtained for nanoparticle samples. The spectra obtained for Pd-Rh NBs and Rh NFWs are shown in Figure 49(a) along with peak positions of the pure metals from the structural database and a spectrum of the precursor core-island-shell structures. The peak positions do not overlay on the bulk angle positions. Even the Rh NFW peaks are shifted to lower-angle positions compared to the bulk, most likely due to expansive lattice strain of Rh. It has been noted, however, that the 4d noble metals tend to relax away from their bulk positions at these size scales to a greater extent than their 5d counterparts.[6] A closer look at the spectra for the 220 peaks is given in 49(b). The single 220 peak at 69.60° for the Rh NFWs agrees with the EDX

analysis that most of Pd is removed the structure, and so peaks at the Pd position do not show up in the spectrum for these single metal frameworks. The peak position of Rh NFWs actually aligns well with the shoul-der position (69.68°) from analysis of the core-island-shell nanoparticles. The Rh shoulder for the core-island-shell spectrum is broader than the Rh peak from NFWs indicating that there may be more variation in lattice parameters in the core-shell structure. This could be attributed to declining strain and influence of Pd at further distances from the core. Interestingly, only a single peak at 68.75° was observed for the Pd-Rh NBs.

The single 220 peak could suggest a homogeneous alloying of the metals in the shell which was conflicting with our expectation for segregation of the metal phases, so HAADF/STEM/EDX elemental mapping was used to gather more information. A clear distribution of Rh islands intact in the nanobox structure would confirm the proposed phase segregation. HAADF/STEM/EDX images and elemental maps were obtained for a single Pd-Rh nanobox and are provided in Figure 50(a-e). It is clear from the elemental mapping that there is indeed phase-segregation in the shell and that Pd is dispersed alternately between local Rh islands. This is evidenced by the nanoframework's appearance in the Rh map in Figure 50(c) and the overlay of Pd and Rh signals (shown in red and green, respectively) in Figure 50(b) that shows the alternating arrangement of metal phases. Note that the images in Figure 50(a-e) are of a single NB viewed from the [110] zone axis. The proposed orientation of the particle is shown in models in Figure 50(f,g) and was achieved by tilting the sample in TEM. Best resolution of the alternating metal phases was obtained when the cube edge was viewed at this orientation of [110]

zone axis. Interference from structure above and below the cross-section occured when the NBs were oriented and viewed along the cube faces ([100] zone axis) and so the contrast of phases is best at these thinner, exposed edges of the cube. The size of the Rh phases matches the size from the initial overgrowth structure of 4-5 nm. This information reaffirms the proposed structure and mechanism of Pd migration through gaps and channels left open from the initial Rh overgrowth and relocation at the external surface. The diffuse Pd map in 50(d) shows that Pd has filled in the Rh island framework to regenerate the cube shape. The combined maps further validate our findings that the filling terminates with the Rh columns. This is important for catalysis studies as it suggests that both Pd and Rh {100} surfaces should be exposed on the NBs. Additionally, since HAADF/STEM/EDX, TEM, and HRTEM all show that the Rh framework is intact, we argue that either our lab-based powder XRD instrument (non-synchrotron source) is not sensitive enough to resolve segregation for phases at less than 5 nm, or that both phases are strained so that they give a single peak in XRD as what would be expected for a more homogeneous alloy. It is clear that the definitions here begin to get 'fuzzy' due to the nanoscale sizes.

Additional images of the Pd-Rh NB shell are shown in Figure 51(a-c) to elucidate the lattice parameters of the shell and to identify any strained features in the structure. Measurements of the d-spacing between {200} planes were obtained in Figure 51(d) from an FFT contrast-enhanced HRTEM image shown in Figure 51(c). The FFT-enhanced image was generated from the HRTEM image in Figure 51(b). Measurements in Figure 51(d) were made by averaging the d-spacing every 5 atomic planes for a total of

70 atomic planes (roughly ~ 14 nm). This resulted in 14 averaged d-spacings along the shell. This was then repeated in a similar fashion until five rows of measurements were tabulated (from the interior to the exterior portion of the nanobox shell). While the d-spacing did vary along the shell, no noticeable trend could be observed. However, a significant difference in the lattice spacing for the {200} planes could be distinguished when each of the 14 columns' and 5 rows' measurements were averaged (plotted in Figure 51(e) and 51(f), respectively). The curve of lattice spacing traveling along the shell tends to oscillate, whereas, the spacing is somewhat constant going from the inner shell wall to the outer surface of the nanobox. The variation in lattice spacing results from the small mismatch (~2%) of the two metal phases as they meet at several interfaces along the shell. This could be expected for an alternating arrangement of metal phases and is in line with the results of the previous analysis. Note, the relaxation of the lattice parameters for these metals at the nanoscale (d-spacings above the bulk values) has been experimentally observed and explained elsewhere.[6]

In addition to the lattice variation caused by alternating phases, defects or dislocations could be found in what appear to be channels utilized by Pd to fill the shell during diffusion to the exterior surface. This is shown in Figure 52(a-d). FFT contrast-enhanced images of the shell shown in Figure 52(b,d) more clearly show a defect site. The edge dislocation highlighted is one of a few that could be observed from particle to particle and is likely due to the need to release lattice strain built up between the separate phases or any incomplete filling of the framework during Pd migration. Strain-releasing mechanisms in bimetallic NPs have been discussed in detail recently by Bhattari et al.[224]

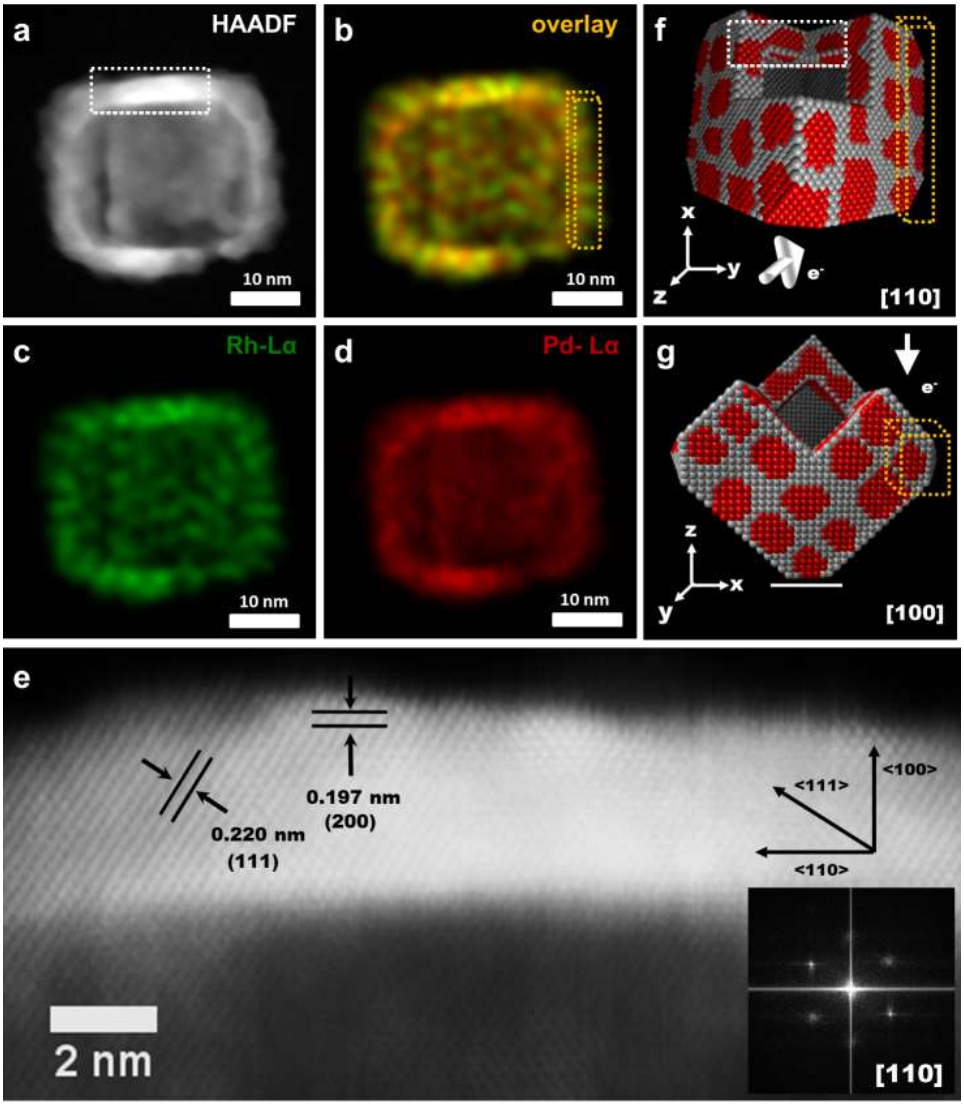

Figure 50. HAADF/STEM images and STEM/EDX elemental maps. Shown are (a) high angle annular dark-field image of a single Pd-Rh NB, (b) overlayed maps of Pd and Rh signals, (c) Rh contribution, (d) Pd contribution, and (e) is a magnification of the section highlighted by the white, dashed box in (a). Inset of (e) is FFT of the magnified image to show the crystal orientation. (f,g) show nanocrystal models with the proposed orientation of the particle observed for STEM/EDX mapping.

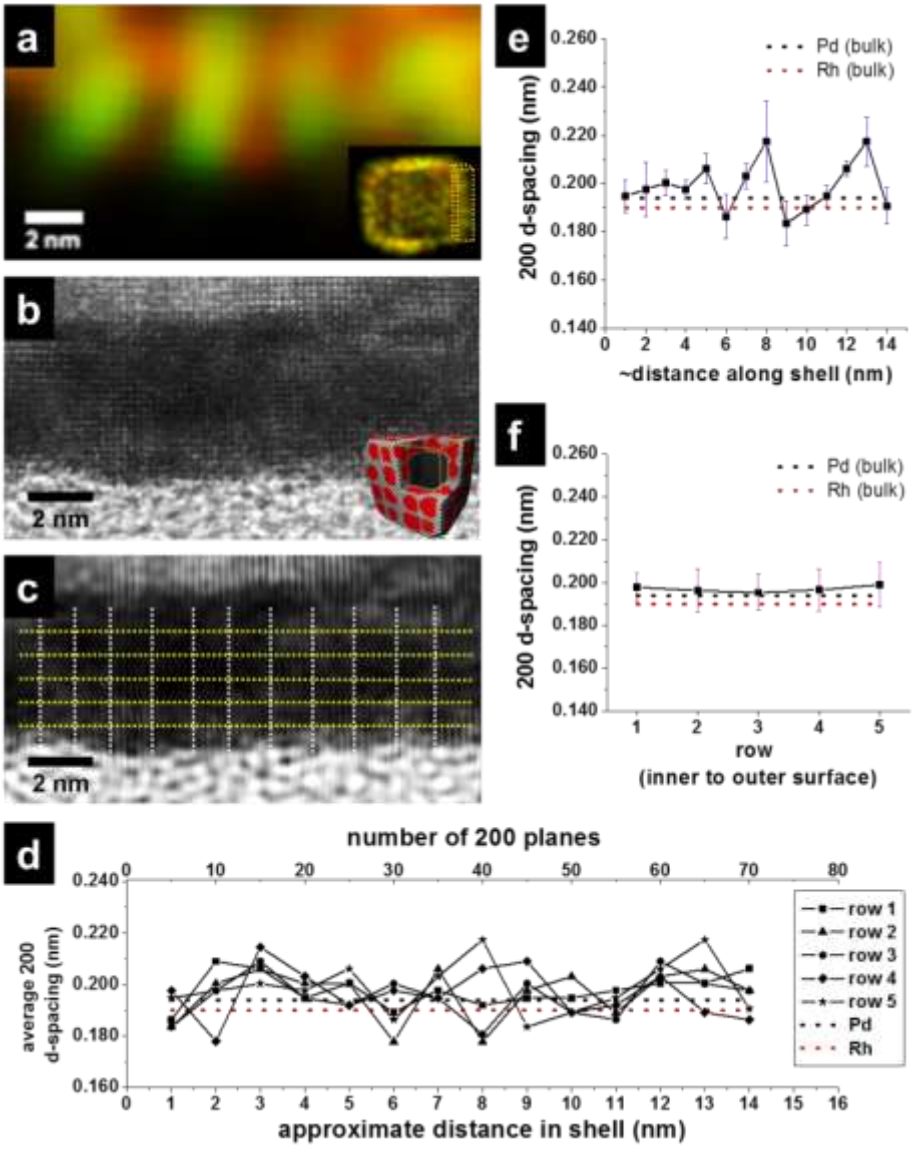

Figure 51. In (a) is a magnified STEM/EDX image of the shell region. In (b) is an HRTEM image of the shell of a single Pd-Rh nanobox. (c) gives an FFT contrast-enhanced HRTEM image of the shell showing curvature of {200} planes with grid overlayed of the set of d-spacing measurements which are plotted in (d). Averaged d-spacing along and across the shell are given in (e) and (f), respectively.

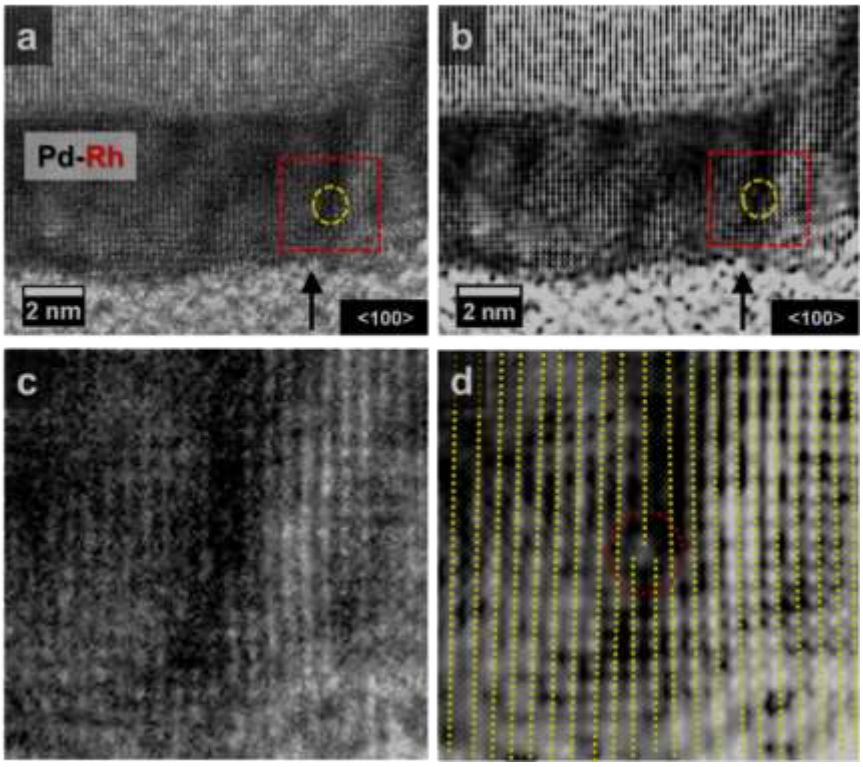

Figure 52. HRTEM image of (a) Pd-Rh hollow alloy nanocube shell and (c) magnified region showing a lattice dislocation. FFT contrast-enhanced HRTEM image of (a) is given in (b) and (d) is the selected area of the image magnified to isolate the dislocation.

3.2.3 Electrocatalysis by Rh-Containing Bimetallic Nanoparticles

Electrocatalysis can be used as a powerful tool to probe the surface structure of metal NCs.[110] Many electrochemical reactions, including carbon monoxide stripping and formic acid oxidation, are surface-structure sensitive, meaning both the potential required for the reaction and the current produced in the reaction depend on the surface structure of the catalyst used. As a result, these reactions can be used to determine or confirm

characteristics about the surface structure of metal NCs. Here, carbon monoxide oxidation and formic acid oxidation were performed on the Pd-Rh NCs to investigate the surface structures. Carbon monoxide oxidation or "CO-stripping" occurs when a positive potential scan is applied to oxidize a monolayer of CO present on the surface of the metal NCs, yielding a characteristic peak for specific crystal facets of metal NCs. CO and OH adsorb on the surface of the metal and then react via a Langmuir-Hinshelwood reaction. Based on this mechanism, CO stripping is more favorable on Rh surfaces with more open crystal facets, which have lower-coordinated metal atoms. Thus the {100} crystal facet requires less energy to catalyze CO stripping than the {111} facet, and the CO stripping peak occurs at a lower potential on the {100} facet than the {111}.[225,226] CO-stripping experiments were performed using cubic and octahedral Pd-Rh NCs, after running fifty blank scans in sulfuric acid. The resulting voltammograms are shown in Figure 53a. The cubic NCs exhibit a CO-stripping peak at a lower potential than the octahedral NCs. The CO-stripping experiment, therefore, confirms that the surfaces of synthesized Pd-Rh cubic NCs are different from that of Pd-Rh octahedral NCs. The difference could be mainly attributed to the {100} crystal facets at the surface of the cubes and the {111} crystal facets at the surface of the octahedrons. This is in good agreement with our finding that the Rh overgrowth has a certain degree of facet-control imparted by the structures of the crystal substrates. It is important to note that some of the surface Rh atoms can be oxidized at a relatively low potential (0.5 – 0.7 V vs. RHE, depending on the facet).[225] The repeated oxidation and reduction of surface Rh atoms results in the formation of defect sites distributed evenly over the surface. As CO oxidation takes place

preferentially at defect sites, this surface roughening step increases the particles' catalytic activity. Because the surface structure of the cubic Pd-Rh NCs is different from that of the octahedral Pd-Rh NCs, the morphologies exhibit characteristic CO stripping peak potentials, even after surface roughening.

Formic acid oxidation experiments were also carried out for both cubic and octahedral Pd-Rh NCs, and the voltammograms are shown in Figure 53b. For both morphologies, the voltammogram exhibits two peaks, one near 0.1 V and one near 0.6 V. This two-peak graph is characteristic of an indirect formic acid oxidation path-way, in which the mechanism involves a CO-poisoning intermediate. It is known that formic acid oxidation follows an indirect pathway on Rh,[227] whereas it follows a direct pathway through an adsorbed formate intermediate on Pd.[157] According to the obtained voltammograms, the synthesized Rh-Pd NCs are indeed enclosed by Rh surfaces as the curves do not follow a direct pathway. The main formic acid oxidation peak, in which CO is oxidized to CO_2, near 0.1 V, occurs at a similar potential for both the cubic and octahedral NCs. The current density (normalized by electrochemically active surface area) for the cubic NCs is approximately twice the current density for the octahedral NCs, showing that the cubic NCs have a higher intrinsic activity for formic acid oxidation than the octahedral NCs. It has been reported previously that the {100} crystal facet is more active than the {111} for formic acid oxidation on a Pt surface, because formic acid oxidation takes place preferentially on more open metal surfaces.[149] As it is known that formic acid oxidation follows the same mechanism on Rh as on Pt,[227] it is probable that Rh follows the same trend in crystal facet activity. We have shown that our Pd-Rh cubic NCs have a more

open surface than the octahedral NCs, and the formic acid oxidation exper-iment confirms this expected trend.

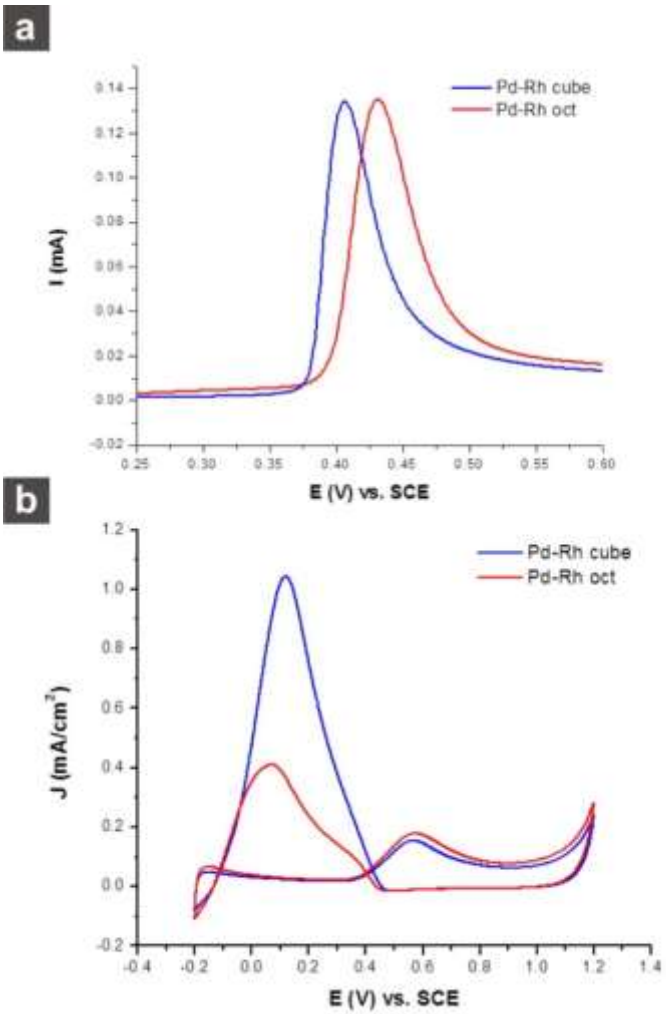

Figure 53. Cyclic voltammetry curves obtained for (a) CO-stripping and (b) formic acid electro-oxidation. Integration of the CO-stripping current was used to calculate the electrochemically active surface area to normalize the activity of the catalysts for formic acid oxidation.

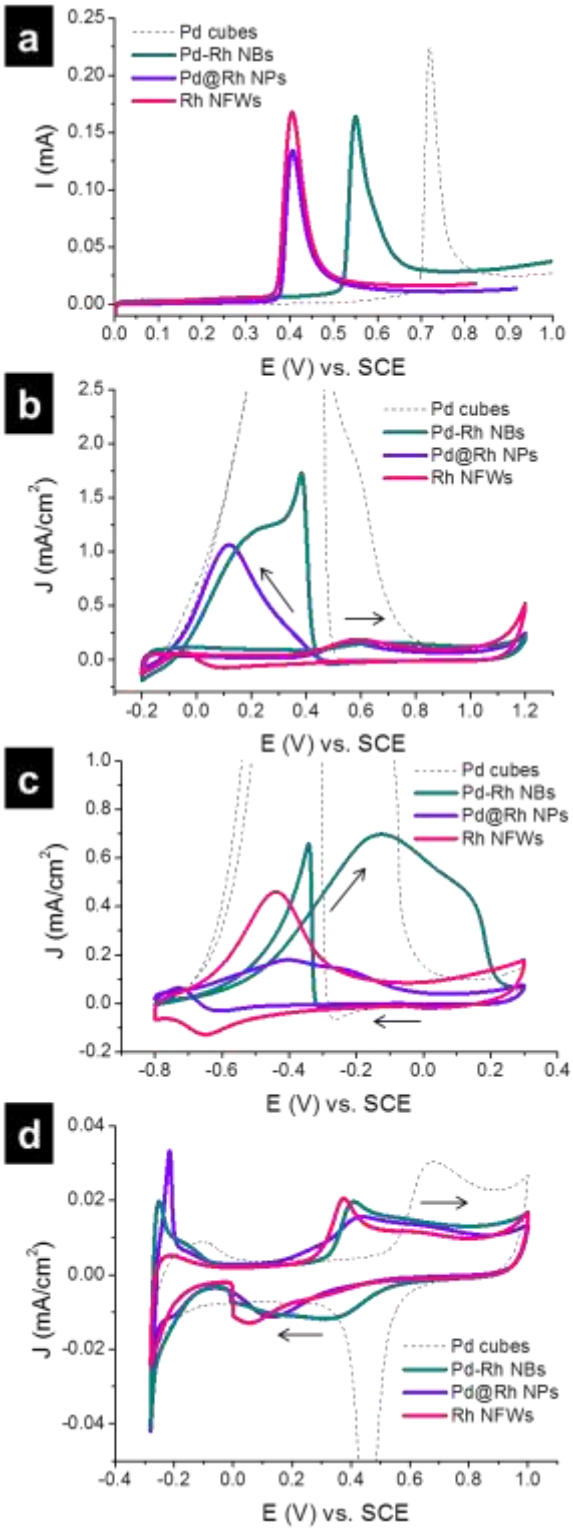
a
Pd cubes
Pd-Rh NBs
Pd@Rh NPs
Rh NFWs
I (mA)
E (V) vs. SCE
b
J (mA/cm^2)
E (V) vs. SCE
c
J (mA/cm^2)
E (V) vs. SCE
d
J (mA/cm^2)
E (V) vs. SCE

Figure 54. Cyclic voltammetry curves for electrochemical catalysis by Pd-Rh nanoparticles: (a) CO-stripping, (b) formic acid oxidation, (c) alkaline ethanol oxidation, and (d) acidic ethanol oxidation for Pd cubes, Rh nanoframeworks, Pd-Rh core-island-shell nanocubes, and Pd-Rh alloy nanoboxes.

Electrochemistry was also used to test the catalytic behavior of the more sophisticated Pd-Rh materials and to study effects of composition and lattice strain on catalysis arising from this archetype. A number of studies have been conducted recently on the effect of lattice strain for Pd,[228] Pt,[229] Pd-Pt alloy,[78,82] and Ru[230] as electrocatalysts but to our knowledge there has been no similar study for Rh. These studies cite the shift in d-band center due to lattice strain as the reason for enhanced or lessened catalytic activity. Expansion of the outer lattice shifts the d-band center upward, increasing the strength of chemisorption bonds, while compressing the outer lattice shifts the d-band center downward, in general weakening chemisorption bonds.[230] X-ray photoelectron spectroscopy (XPS) was carried out for the nanoparticle samples to probe the changes in Pd and Rh electronic structure due to lattice strain. The Pd and Rh 3d binding energies showed shifts for both bimetallic structures compared to the pure Rh NFWs. Other groups have correlated these core-level shifts to a shift in the d-band center, [94,231] though we have not ruled out differences in oxidation states for these different structure. Incorporating a second metal into a metal nanostructure affects the catalytic activity via ensemble, ligand, and geometric strain effects, but strain is the only effect that can influence activity past a few atomic layers.[229] The impact of strain on the electrocatalytic

activity of Rh NFWs and Pd-Rh NBs was studied alongside pure Pd nanocubes and Pd-Rh core-island-shell NPs for comparison.

Figure 54(a) shows results of CO stripping on the different nanoparticles, performed in a CO-saturated 0.1 M HClO4 electrolyte solution. Core-island-shell Pd-Rh cubic NPs and pure Rh NFWs exhibit a nearly identical CO oxidation potential near 0.40 V vs. SCE, pure Pd cubes reach peak oxidation potential at 0.72 V, and Pd-Rh NBs appear in-between, near 0.55 V. These results suggest that the lattice strain of Rh has low impact on CO stripping activity, and that the trend arises from composition. The core-shell particles should have a higher degree of lattice strain than the Rh NFWs, because the Pd core actively expands the Rh lattice. Both particle types exhibit the same CO stripping activity, however, indicating that lattice strain plays no significant role in this reaction. This result also indicates that the surface of the Pd-Rh core-island-shell NPs is mainly composed of Rh, with almost no Pd exposed. The Pd-Rh NB peak is between pure Pd and pure Rh, most likely due to a mixed composition at the surface.

Curves for the formic acid oxidation reaction (FOR) are given in Figure 54(b). From lowest to highest activity (reverse scan current density) the particle types are: Rh NFWs, Pd-Rh core-island-shell NPs, Pd-Rh NBs, and Pd nanocubes. This trend may be caused by the composition (amount of Pd), lattice strain, metal-metal interface, or a combination of the three. As stated earlier, Rh NFWs and Pd-Rh core-shell nanoparticles have the same CO stripping activity, indicating that the surface composition is the same – the Rh fused column layer is thick enough for Pd-Rh core-shell NPs that there is no Pd surface exposed. These two particle types, however, show vastly different activity for FOR. The

Rh cubic NFWs have fractional current density while Pd-Rh core-shell structures show a peak close to 1 mA/cm^2. The CO stripping result eliminates Pd composition as a factor for FOR in this case, because the oxidation peaks had almost identical positions. Lattice strain can be invoked to explain the enhancement for Rh's FOR catalytic activity rather than composition or synergy. There are sequentially large increases in current density when considering Pd-Rh core-shell NPs, NBs, and pure Pd nanocubes. This trend matches an increasing degree of Pd composition and also follows the trend of increasing lattice parameter. All of the particles comprising Rh surface exhibit an indirect reaction pathway versus Pd's direct pathway. Rh typically follows an indirect pathway for FOR while Pd follows a direct pathway, so in the case of Pd-Rh NBs the FOR reaction is either occurring on the Rh surface or on a combination of Pd and Rh surfaces but is exhibiting predominantly Rh character. The absence of direct pathway in the NBs could be explained by the modification of the Pd's lattice by Rh phases. Lattice strain likely affects FOR activity by increasing the adsorption of formic acid. On Rh, FOR proceeds by an indirect pathway. In the first step, HCOOH is adsorbed as CO, and in the second step CO is oxidized to CO_2. The adsorption of HCOOH has been shown to be the rate-limiting step in FOR.[232] The upward shift in the d-band center due to lattice expansion increases the catalyst's ability to bind adsorbates. Norskov et al. showed that a higher d-band center leads to stronger chemisorption bonds,[230] and it has been shown that on a Pd (111) surface lattice expansion led to higher FOR activity due to stronger adsorption of HCOOH.[228] Unfortunately, because the adsorption step does not involve electron transfer we cannot see a CV peak corresponding to HCOOH adsorption step. Thus we can only

infer an increased rate of adsorption by a higher peak on the reverse scan; the more HCOOH is adsorbed as CO the more CO molecules are oxidized to CO_2, and a higher current is obtained. Accordingly we see that the particles with more strain have a higher oxidation peak on the reverse scan.

Ethanol oxidation reaction (EOR) was performed in both acidic and alkaline solutions. The EOR in an alkaline electrolyte tends to have higher activity than acidic EOR,[233,234] so we focus the discussion on the EOR in a solution of 1 M KOH and 1 M EtOH in order to determine the effect of lattice strain on EOR activity. The CV curves are shown in Figure 54(c). The lowest current density is shown by the Pd-Rh core-shell NPs. The curve shows two adjacent peaks in the forward scan and a very small reverse scan peak. These characteristics are typical of a Rh alkaline EOR CV. The pure Rh NFWs have a higher current density and a lower peak onset potential than core-shell NPs, and do not exhibit the identifying Rh characteristics. The next highest current density is shown by Pd-Rh NBs, which have equally high forward and reverse scans, similar to Pd. EOR proceeds by a dual-pathway mechanism, either producing acetic acid and releasing only 4 electrons, or producing carbon dioxide and releasing 12 electrons.[234] Often, not all of the ethanol is completely oxidized to CO_2 on the forward scan, and the leftover incompletely oxidized products are oxidized further on the backward scan.[176] Thus, the ratio of the forward to backward current densities (j_f/j_b) can be used to compare the selectivity of the catalysts for the complete oxidation pathway, with a higher jf/jb value indicating a more selective catalyst. The j_f/j_b values for Pd NPs, Pd-Rh NBs, Pd-Rh core-shell NPs, and Rh NFWs are 0.809, 1.05, 2.55, and ∞, respectively (Rh NFWs have zero backward scan). These

values indicate that the particles with more Rh have higher selectivity for the complete oxidation pathway. Looking at both the onset potentials and the j_f/j_b ratios, the less-strained particles with smaller surface lattices are better alkaline EOR catalysts. This trend is interestingly the opposite of the trend for FOR, demonstrating that these electrochemical reactions are uniquely sensitive to surface lattice strain and electronic structure. Even though the trend also correlates with decreasing Pd composition, composition alone cannot explain the trend. We can see by the different activities of Rh NFWs and Pd-Rh core-shell NPs, which have the same Rh surface composition as determined by CO stripping, that lattice strain must play a role in altering the kinetics of the reaction.

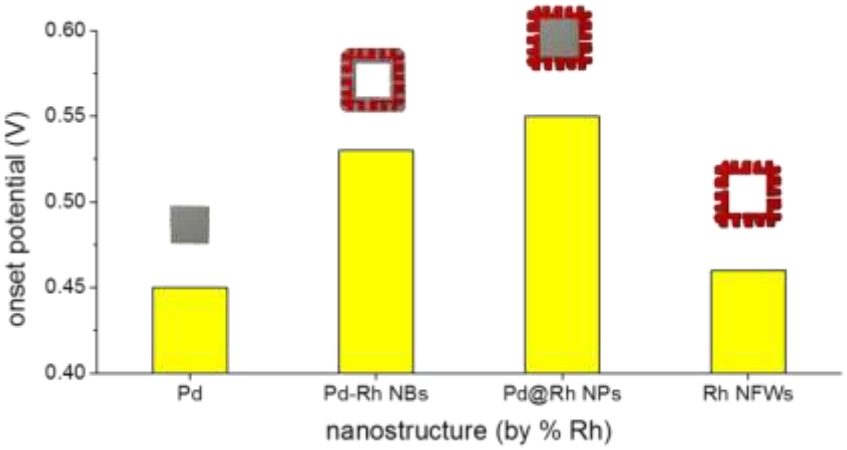

Figure 55. The onset potentials of the oxygen reduction reac-tion catalyzed by Pd-Rh nanoparticles.

EOR was also performed in a perchloric acid electro-lyte. There has been little research done on EOR in acidic media on Rh. One study compared EOR activity for Rh nanocubes, dendrites, and horned particles,[179] obtaining CVs similar to ours, shown in Figure 54(d). Our results show similar current densities for Rh NFWs, Pd-Rh NBs, and core-shell NPs, with Pd cubes at a higher current density. According to Pd's higher intrinsic activity, we would expect to see higher activity for Pd-Rh NBs, which have some Pd exposed on the surface, but these particles have approximately the same current density as the other Rh-exposing structures, suggesting some degree of modification of Pd's lattice.

The oxygen reduction reaction (ORR) was the last electrochemical reaction tested and the onset potentials are shown in Figure 55. This reaction interestingly does not follow the same trends in activity as for FOR or EOR. In the ORR, onset potential is used as the measure for catalytic performance. The Pd-Rh core-island-shell NPs are the most active at 0.55 V, followed by Pd-Rh NBs at 0.53 V, Rh NFWs at 0.46 V, and lastly Pd cubes at 0.45 V. For the ORR, pure Pd typically has low activity,[235] and our results show that by combining Pd with Rh to form bimetallic NPs, we can increase Pd's ORR activity. The Pd-Rh NBs have a higher onset potential than the Pd cubes, but a similar shaped curve indicating some Pd character in the reaction. The core-island-shell NPs, on the other hand, have a very different curve, with a large dip around 0.15 V that is characteristic of Rh due to the reduction of surface hydroxyls.[172] This dip shows that the core-shell NPs exhibit predominantly Rh character for this reaction, indicating that the surface is Rh and exposes little to no Pd. The pure Rh NFWs, however, show a lower onset potential.

Because the surface composition for these two particle types is the same (as determined by CO stripping) but the activity is different, the differing factor could be lattice strain. It has been shown that ORR activity can be altered by compressing the lattices of metal NPs.[88,229,236] The rate-limiting step for oxygen reduction is the desorption of O and OH from the metal surface, so a smaller lattice with a lower d-band center is ideal because it weakens chemisorption bonds, allowing O and OH to dissociate. A volcano relation was obtained for the onset potentials in the ORR for the different catalysts where the bimetallic structures display activity at higher voltage.

3.3 Pd-Ni-Pt Core-Sandwich-Shell Nanoparticles

Portions of the following section have been reproduced with permission from Sneed, B. T.; Young, A. P.; Jalalpoor, D.; Golden, M. C.; Mao, S.; Jiang, Y.; Wang, Y.; Tsung, C.-K., Shaped Pd–Ni–Pt Core-Sandwich-Shell Nanoparticles: Influence of Ni Sandwich Layers on Catalytic Electrooxidations. ACS Nano 2014, 8 (7), 7239-7250. Copyright 2014 American Chemical Society.

Despite the advancement of M-Pt NP electrocatalysts, such as Ni, there are few established methods for creating core-shell M-Pt NPs with well-defined shape control. Current strategies for producing Ni-Pt alloy NPs with shape control require Ni and Pt ions to be co-reduced.[54] Usually this is accompanied by a variety of capping/shaping agents.[55,237,238] Wu et al. have recently contributed a shape-controlled synthesis for Ni octahedra,[239] and others have demonstrated control of shape for bimetallic systems with core-shell Pd-Cu and Ag-Ni nanocubes.[240,241] While these works are excellent examples

of the power in colloidal synthesis, the synthesis with rational structural control remains a challenge. Also, various cleaning methods are required due to the strong bonding capping agents used in these organic phase syntheses.

An aqueous,[112] layer-by-layer epitaxial overgrowth approach[240,242] to shape-controlled M-Pt core-shell NPs would be desirable for the exploration of strained nanoarchitectures, as well as for the opportunity to study strain effects on catalysis by multishelled structures. Direct control of the size, over-all shape, and the thickness of each layer in a core-sandwich-shell nanostructure would provide a platform to gain better understanding of lattice strain effects on catalytic activity and perhaps elucidate the limits for these effects experimentally. Previous works show tuning the shell thickness and NP size as a way to increase catalytic activity.[58,88] The activity changes observed with expansive or compressive lattice strain (from the lattice mismatch at metal-metal interfaces) have been attributed to subtle altering of the binding energies of adsorbates, by way of perturbation of the surface d-band.[43,63] The d-band model offers a straightforward design principle to fine-tune Pt-based electrocatalysts,[57] yet there is still much debate over its validity as a general descriptor and predictor of cata-lytic activity.[95,96]

3.3.1 Synthesis of Shaped Pd-Ni-Pt Sandwich Nanoparticles

We presented an aqueous, low temperature route to shape-controlled Pd-Ni-Pt core-sandwich-shell nanoparticles using cetyltrimethylammonium bromide (CTAB) as the capping agent and hydrazine as the reducing agent. Figure 56 demonstrates how Pd cubes function as shaped crystal substrates which catalyze and direct the oriented overgrowth of

Ni. Pt ions are added after the Ni overgrowth to 'trap' the metallic Ni phase and complete the layer-by-layer synthesis of the shaped ternary metal nanoparticles. This method allows for control of the overall size, shape, and layer thickness by the choice of substrate and amount of precursor salts added in the growth solution.

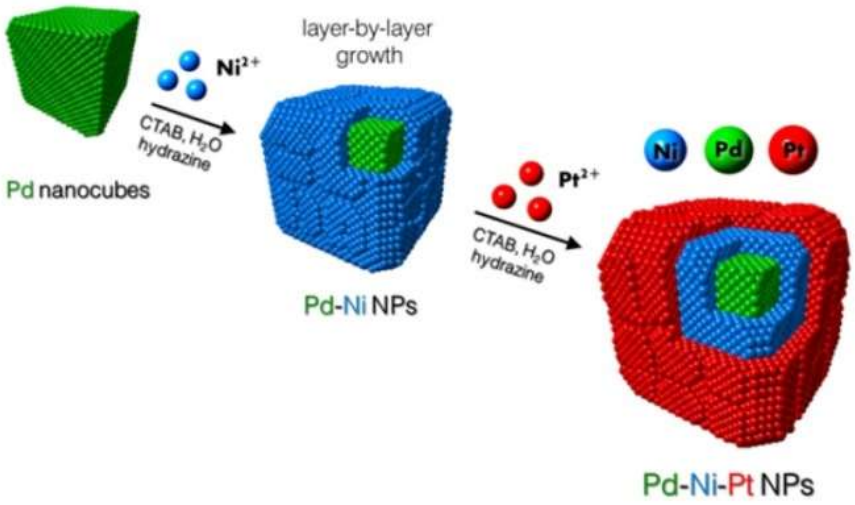

Figure 56. Synthesis of cubic Pd-Ni-Pt core-sandwich-shell nanoparticles.

The strategy presented here is attractive toward the end goal of understanding the impact of lattice strain on the catalytic performance of core-shell nanoparticles. The cubic Pd-Ni-Pt struc-tures are investigated as formic acid oxidation (FOR) and methanol oxidation (MOR) electrocatalysts, for which the Pt(100) facets are expected to have higher activity.[110] We discuss the findings of increased specific activity of the catalysts with a Ni-sandwich layer as being due to strain on Pt by the Ni layers beneath the surface.

The durability of the different catalysts is assessed, and the smaller trimetallic Pd-Ni-Pt nanoparticles retain the highest activity over time over both the larger ternary NPs and the Pd-Pt control NPs for MOR in alkaline solutions. The trends in activity are similar in acidic conditions; however, because of dealloying and restructuring from potential cycling in acid, their behavior may be more a result of a composition change at the surface, rather than from strain. We further show that an octahedral morphology can be produced by substituting Pd octahedra for the Pd nanocubes in the synthesis. These NPs could be the subject of future studies in oxygen reduction catalysis. Finally, we use the strategy to create quaternary, core-triple-shelled Au-Pd-Ni-Pt nanoparticles with a cubic shape at a size of ~20 nm. To our knowledge, the novel, shaped multi-shelled nanoparticles shown here are unprecedented in the literature.

In attempting to synthesize shaped Pd-Ni-Pt multilayered NPs by a wet chemical route, insights were gained from earlier works that successfully demonstrated control of Ni at this size scale. Grzelczak et al. were able to produce Ni nanoparticles of different sizes by adjusting the Ni^{2+} to reducing agent ratio in the growth solution and observed size-dependent magnetic properties.[243] Their synthesis was accomplished in water at low temperatures using hydrazine as the reducing agent and CTAB surfactant. The authors confirmed metallic Ni in their work using X-ray structural analysis; however, it was speculated that the surface remained passivated by several oxide layers. Moreover, no control of faceting was reported. This general strategy was utilized to make Ni nanostructures in several of their works,[244-246] while others have since published variations of the Ni-reduction method.[247-249] Recent syntheses yield more complex Ni

nanostructures[250,251] and theoretical work proposes and describes the faceting of Ni crystals.[252]

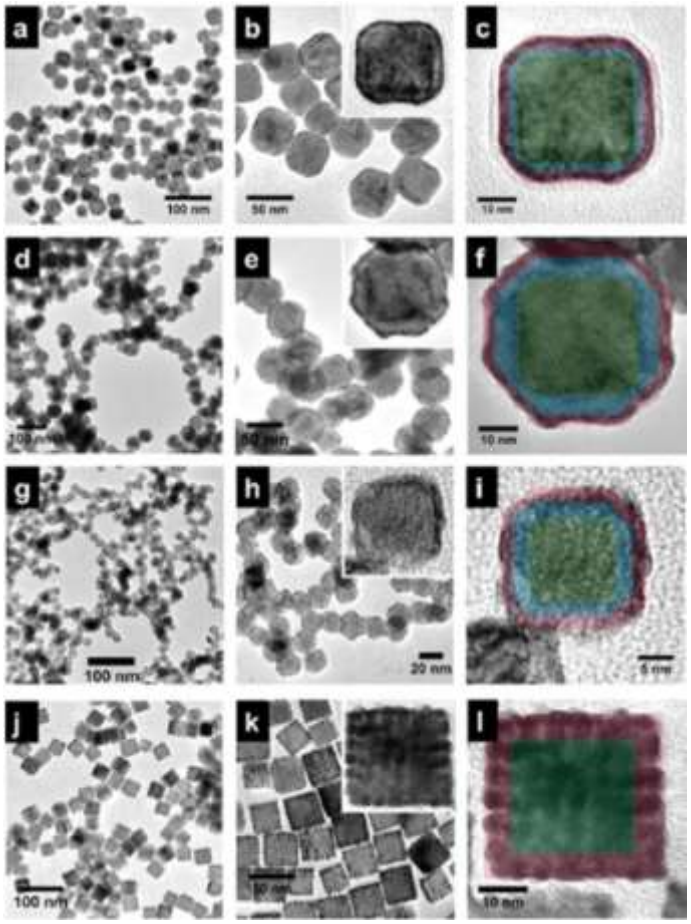

Figure 57. TEM and recolored TEM images of cubic Pd-Ni-Pt and Pd-Pt nanoparticles. In (a-c) are Pd-Ni-Pt nanoparticles synthesized with ~2.5 nm Ni sandwich, (d-f) NPs synthesized with ~4.1 nm Ni sandwich, (g-i) smaller ~20 nm Pd-Ni-Pt nanoparticles, and (j-l) Pd-Pt core-shell nanoparticles. The original TEM images that were recolored are shown as insets in the upper right of images in the middle column. The Pd, Ni, and Pt regions are shown under green, blue, and red transparencies, respectively, in the recolored images.

Liz-Marzán's group showed that the Ni nanoparticles could only be formed in this synthesis system under certain conditions: 1) catalytic Pt nanoparticle seeds must be introduced for the overgrowth of Ni, 2) the growth solution must be sealed to trap the H_2 gas evolved during the synthesis, which promotes Ni reduction and limits surface oxidation, and 3) the growth must occur without magnetic pertubations, such as a stir bar in the growth solution, otherwise the particles may collect and precipitate prematurely, or fuse into chains or wires. We hypothesized that we could make use of this approach, by reducing Ni on shaped Pd substrates instead of small Pt seeds. Their use of mild conditions with ionic surfactants resembled the conditions used for seed-mediated growth of other metal nanoparticles from our previous work with Au, Pd, and Rh. It was feasible that combining the strategies would lead to a greater control of Ni faceting in the overgrowth, which has not been attempted before.

In a typical synthesis of Pd-Ni-Pt nanoparticles, shaped Pd substrates (nanocubes) were prepared, and dispersed into an aqueous solution of CTAB in a small glass vial. Nickel ions were then added in the form of nickel(II)chloride hexahydrate ($NiCl_2 \cdot 6H_2O$), and an amount of hydrazine monohydrate solution was added last. The vial was sealed and maintained in a water bath at 50°C for ~2 hours (without stirring) until a color change occurred indicating the Ni overgrowth. Pt ions were then injected in the form of K_2PtCl_4, and heating continued in the water bath for ~1 hour. The ternary metal particles were then removed from heat and collected by centrifugation at 4000 RPM, redispersed, and washed for characterization. In other works, the problem of surface oxidation was avoided by alloying (co-reduction) or by working in organic solvent; however, it is

shown that oxides can still form on the surface of such structures in these conditions, especially in aqueous solutions.[240,253] Accordingly, we attempted to prevent oxide formation by 'capping' of the Ni layer with overgrowth of Pt in the same 'pot'. This simul-taneously addresses the issue of surface oxidation and creates the desired shaped M-Pt core-shell motif desired for catalysis.

The 'trapped' metallic Ni phase in the Pd-Ni-Pt nanoparticles can be observed by contrast in transmission electron micro-scope (TEM) images shown in Figure 57(a-l). Three types of nanoparticles with different sizes and Ni layer thicknesses were synthe-sized. The nanoparticles in 57(a-c) were synthesized by introducing 100 and 50 μL of the Ni and Pt precursors, respectively, to growth solutions containing ~30 nm Pd nanocubes. This resulted in ~2.5 nm of Ni and 1.6 nm of Pt layers. Particles in 57(d-f) were synthesized similarly, excepting for a doubling of the amounts of the Ni and Pt metal precursors. This led to 4.1 nm of Ni and 1.6 nm of Pt overgrowth. The nanoparticless shown in 57(g-i) were created using smaller, ~12 nm Pd nanocubes in place of the larger substrates, resulting in nanoparticles approximately ~20 nm in size. Nickel is observed in the TEM images as a lighter phase 'sandwiched' between a dark Pd core and a darker Pt surface layer. The difference in contrast is due to the increased electron scattering of the heavier 4d and 5d metals. Recolored TEM images in Figure 57 highlight the different metal phases in the structure. The final truncated cubic morphology is a result of the well-defined cubic shape of the Pd substrates and the layer-by-layer overgrowth. The roughened appearance of the surface is likely due to the lattice mismatch (~10-11% for these metals) and high degree of strain and defects imparted by having the Ni

'sandwiched' between the Pd and Pt layers. Core-shell Pd-Pt NPs also shown in Figure 57(j-l) lack the Ni layer and are used for comparison as a control in x-ray diffraction and electrochemical catalysis studies presented later in this work; such structures have also shown enhanced performance in the literature as electrocatalysts.[76]

We demonstrate the synthesis affords differently shaped and more sophisticated layered nanostructures, in addition to those studied in catalysis. It was found that the Ni and Pt overgrowth could be replicated on ~30 nm Pd octahedra and on cubic Au-Pd core-shell sub-strates. This was accomplished by replacing the Pd nanocubes with Pd octahedra or Au-Pd core-shell nanocubes in the growth solution. The resulting nanoparticles TEM images are shown in Figure 58(a-h). The octahedral ternary metal nanoparticles appear in 58(a-d) and the cubic quaternary metal nanoparticles appear in 8(e-h). The octahedral Pd-Ni-Pt nanoparticles are expected to be the subject of future work as promising candidates for oxygen reduction catalysis (ORR) for fuel cell cathodes. In the high magnification TEM image in Figure 58(g), the four metal phases in one of the quaternary cubic nanoparticles can be resolved. A gold cuboctahedral seed is established in the core as the darkest contrast, with a slightly brighter, distinct cubic Pd shell encasing it. As before with the cubic ternary metal nanoparticles, a thin layer of lighter contrast Ni phase surrounds the Au-Pd cube followed by a thin, dark band of Pt at the surface. This shows our method could be used to create nanoparticles with as many as four different and distinguishable metal layers while holding the particle size at or below ~20 nm. The shaped multi-shelled metal nanoparticles displayed in this work are rare in

the literature, to our knowledge, though there is an excellent example of hollow ternary layered noble metal nanoparticles from Gonzalez et al.[217]

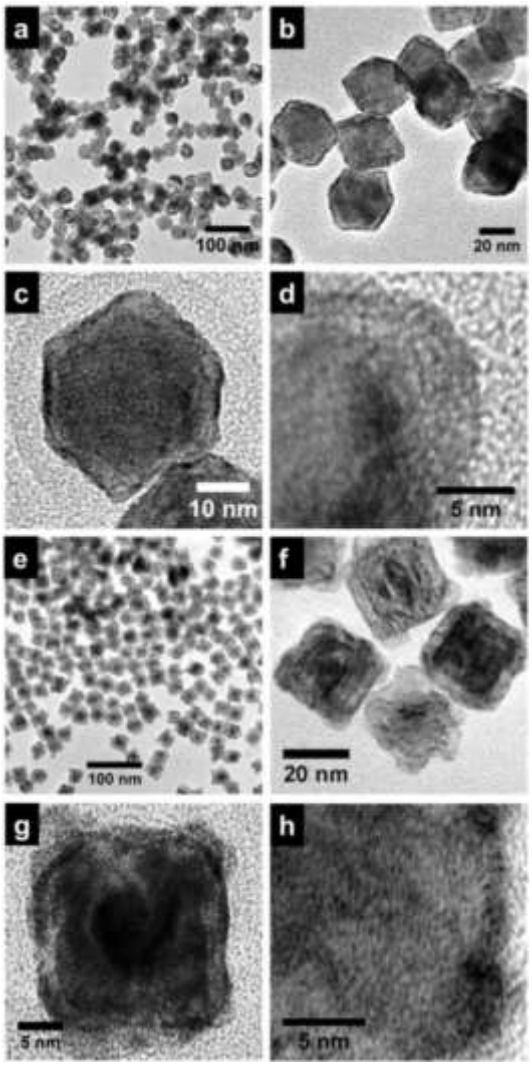

Figure 58. In (a-d) are TEM and HRTEM images of ~30 nm Pd-Ni-Pt nanooctahedra and in (e-h) are images of cubic multishelled Au-Pd-Ni-Pt quaternary metal nanoparticles. In (c,g) TEM images of single particles are shown where each of the multiple metal phases can be resolved by contrast, and HRTEM images of the respective nanoparticles are given in (d,h).

3.3.2 Characterization of Pd-Ni-Pt Sandwich Nanoparticles

To investigate the composition, conformal overgrowth, and to confirm the core-sandwich-shell structure of the Pd-Ni-Pt nanoparticles, X-ray elemental analysis was carried out. Element maps from scanning trans-mission electron microscopy with energy dispersive X-ray spectroscopy (STEM/EDX) and high angle annular dark field images (HAADF) are given for the nanoparticles in Figure 59(a-f). There is a clear distinction between the lower mass Ni phase and heavier Pd and Pt phases in the HAADF images in Figure 59(a,b) as was observed in TEM. Here the Ni appears as a dark band between bright Pt and Pd regions. The STEM/EDX maps for each metal are given in 59(c-e) with the overlayed map in 59(f) confirming the double-shelled structure of the Pd-Ni-Pt nanoparticles. The HRTEM image in 59(g) shows continuous epitaxy from the Pd core through the Ni phase to the Pt shell. The size of the Ni-Pt shells is around ~4 nm, and this is composed by a ~2.5 nm layer of Ni. Measurements of the d-spacings in the HRTEM image in 59(g) agree with the proposed core-sandwich-shell structure in that the (200) d-spacing becomes smaller traveling away from the Pd core from ~0.199 nm to ~0.193 nm in the Ni layer, but then increases near the Pt surface back to ~0.200 nm. This suggests the Pt atoms at the surface experience compression, and we speculate that thicker Ni layers could impart more strain to the Pt surface, by increasing influence of Ni's smaller lattice parameters. We also note that none of the measured d-spacings approach the larger bulk NiO (200) d-spacing of 0.208 nm, which indicates a metallic Ni layer. This is discussed in more detail following the surface characterization by TEM.

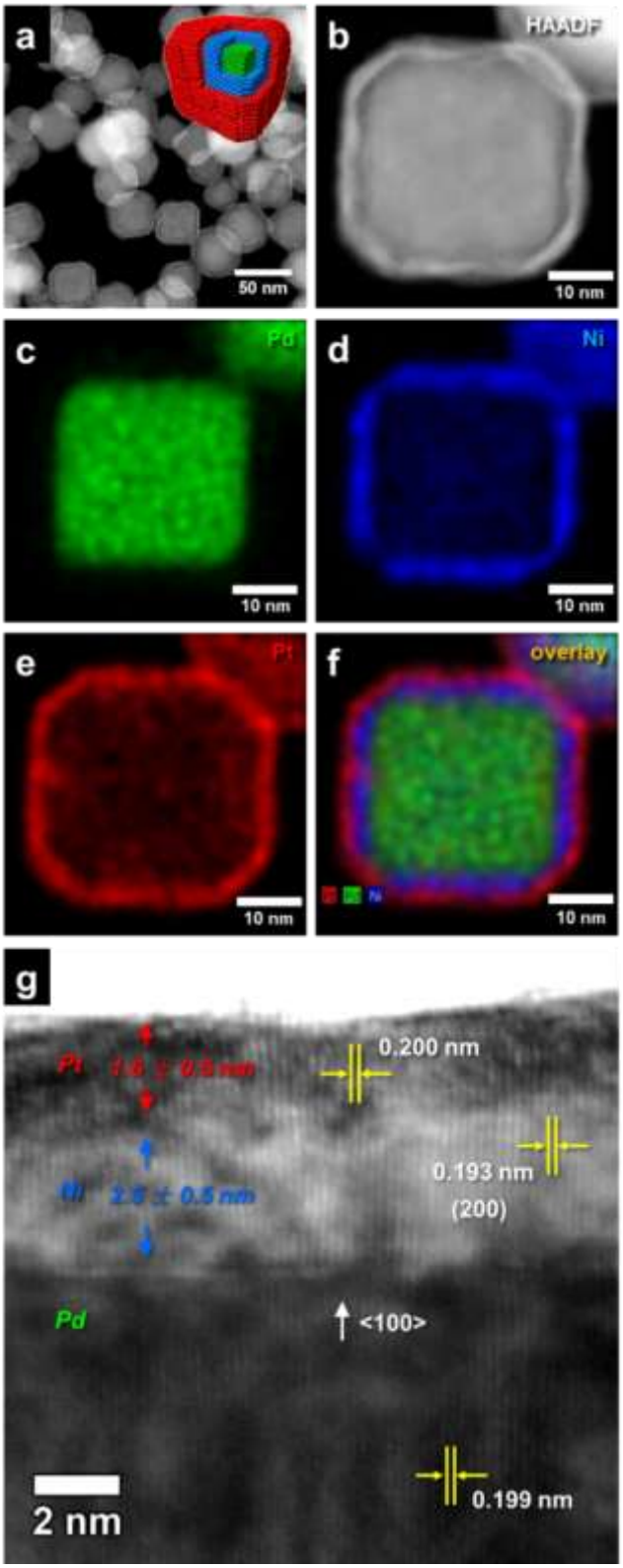
a
50 nm
b
HAADF
10 nm
c
Pd
10 nm
d
Ni
10 nm
e
Pt
10 nm
f
overlay
10 nm
g
Pt 1.6 ± 0.5 nm
Ni 2.6 ± 0.5 nm
Pd
0.200 nm
0.193 nm
(200)
<100>
0.199 nm
2 nm

Figure 59. HAADF images, STEM/EDX elemental maps, and an HRTEM image of Pd-Ni-Pt nanoparticless with a ~2.5 nm Ni layer. In (a,b) are HAADF images, (c,d,e) are STEM/EDX element maps for Pd, Ni, and Pt, respectively, taken for the NP in (b), (f) the image containing the overlayed maps, and (g) HRTEM cross-section of a NP showing the layer thickness and measured 200 d-spacings. A structural model is given in the inset of (a).

The surface structure was probed by high resolution TEM (HRTEM) for individual particles and orientations shown in Figure 60(a-e). The overall truncated cubic morphology is apparent in 60(a,b) with a model of the double-shelled particles inset of (a). In Figure 60(c) square lattice patterns can be observed for nanoparticles lying on the cube face ([100] zone axis). Figure 60(d) shows the rhombic (distorted hexagonal) lattice images for nanoparticles lying on the cube edge ([110] zone axis). Both sets of images allow for examination of the proposed Pt(100) surface planes and epitaxy through the Ni and Pt shells. From these images and observation of several other nanoparticles we can conclude they are primarily (100)-dominant in faceting, and that the Ni and Pt overgrowth occurs epitaxially, with some 'lifted' terraces and steps at the surface, and edge dislocations in the shell produced by defects from the lattice misfit. In a lattice image of the corner of a Pd-Ni-Pt NP on edge in Figure 60(e), an approximately ~25° curvature is observed in the atomic planes extending at different angles toward the surface, which we believe is also a result of the highly strained interfaces meeting at the

vertex of the cubes. A similar observation of strain in Ni nanostructures has been described by Wang et al.[97] They show a nearly ~40° reversible 'flip' in the unit cell of Ni nanowires induced by bending of the nanostructure.

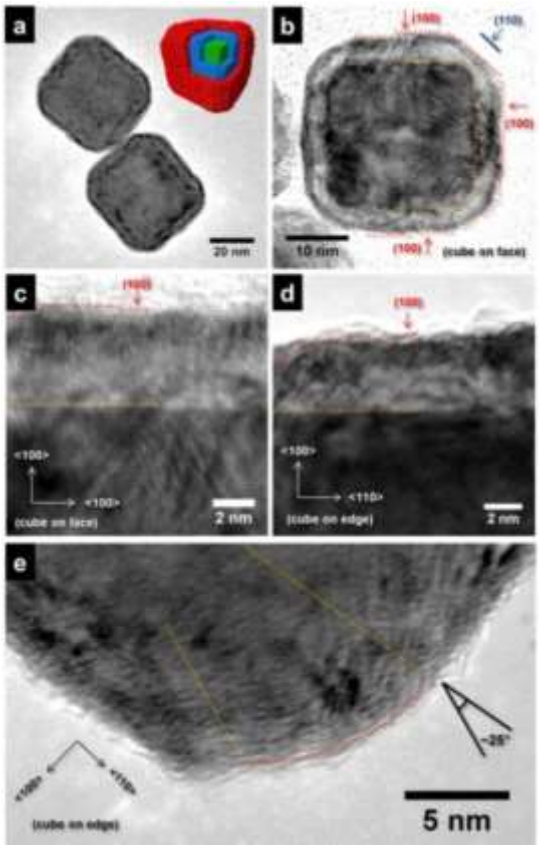

Figure 60. TEM and HRTEM images of Pd-Ni-Pt nanoparticles. In (a,b) are TEM images showing the truncated cubic morphology with crystal model inset in (a). In (c-e) are HRTEM lattice images showing the epitaxy and surface structure. For the image in (c), square 2D lattices are obtained from viewing a nanoparticle down the 100 axis (cube lying on face), and for (d,e) the lattices come from viewing in the 110 direction (cube lying on edge). The image in (e) shows the lattice distortion in the shell brought about by the high interfacial mismatch for the metal layers (~10-11%) meeting at a corner.

The questions of oxide content and strain within the Ni phase are addressed by analysis of powder X-ray diffraction (XRD) of the Pd-Ni-Pt nanoparticles and this is shown in Figure 61(a,b). It is first noted that no diffraction peaks corresponding to the bulk NiO positions can be observed for the samples. The spectrum for nanoparticles with a ~2.5 nm Ni sandwich layer shows a single fcc diffraction pattern similar to the bulk Pd reference. Peaks were observed for the thicker nanoparticles with a ~4.1 nm Ni sandwich layer close to the metallic Ni position. This global information shows that little to no oxide is forming during or after the synthesis and that metallic Ni resides within the sandwich layer. The pattern also suggests that the Ni lattice parameters may come closer to the bulk values with increasing thickness of the Ni sandwich layer (with decreasing influence of core and shell lattices).

XRD is a good qualitative tool to indicate the existence of lattice strain. However, we note that quantitatively determining strain on the surface in this complex system, even average strain from peak positions, does not reflect the actual surface strain with much certainty, and so this was not attempted (though our collaborators are developing the modeling techniques that could assist with this in the future). Both XRD spectra for the different shell thicknesses of Pd-Ni-Pt have peak 'tails' in the direction of higher 2θ degrees. The magnification of the 111 region is dis-played in Figure 61(b). The tailing is a result of strain in the Ni layer, whereby the Ni lattice expands and Pd and Pt lattices compress. This tailing feature does not appear in the Pd-Pt control, and so corroborates with strain emanating from the introduction of the Ni sandwich layer. There is a lack of the tailing feature in the smaller Pd-Ni-Pt nanoparticles because of the smaller domain

size and broadening in the distribution. The maximum peak positions of all of the Pd-Ni-Pt nanoparticles are shifted to the right of the bulk Pd 2θ degrees and little area under the peaks lie at the bulk Pt diffraction lines, especially for the higher angle 200 and 220 peaks. Again, the exact amount of surface strain is not straightforward to assess from these shifts because of the complexity in three metal phases, the differences between the spectra regarding the presence of broadening, the tailing feature, and the appearance of the "Ni" peak in the larger-sized, thicker-shelled nanoparticles.

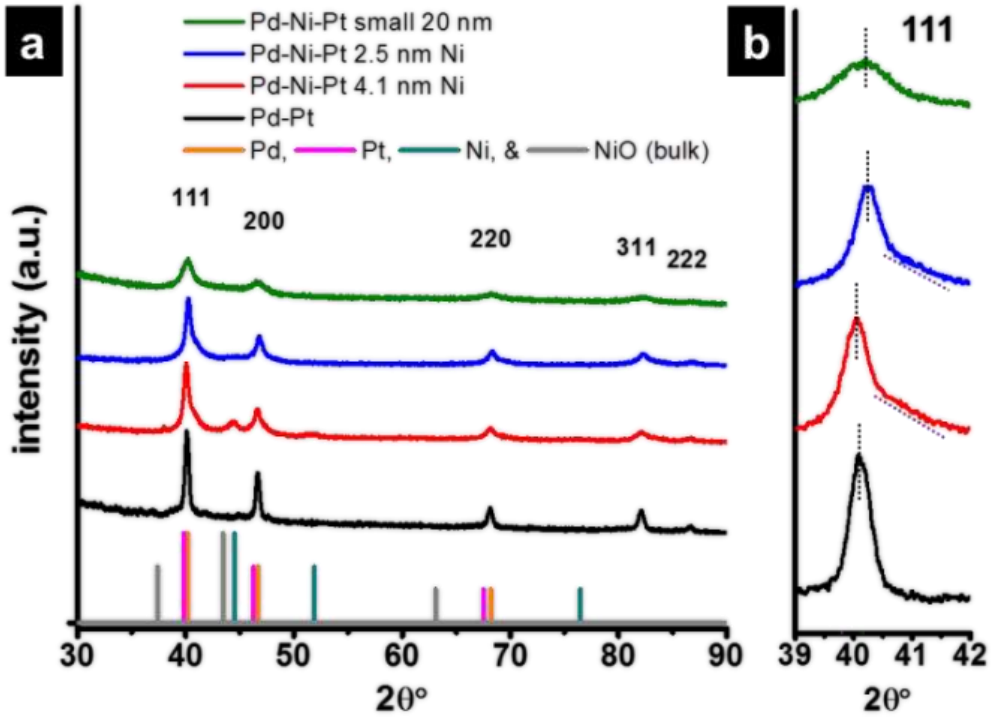

Figure 61. In (a) are the powder XRD spectra of the different Pd-Ni-Pt and Pd-Pt nanoparticles with peak positions of bulk Pd, Ni, Pt, and NiO for reference. Plot (b) magnifies the 111 region to show the peak shift and tailing of the Pd-Ni-Pt nanoparticles as compared to the Pd-Pt nanoparticles.

3.3.3 Electrocatalysis by Pd-Ni-Pt Sandwich Nanoparticles

The catalytic properties of the cubic Pd-Ni-Pt nanoparticles of different sizes and shell thicknesses were studied in the electrooxidation of methanol and formic acid. It is generally believed that both of these catalytic reactions readily occur on more open (100) and (110) surfaces of Pt as opposed to the close-packed (111) facets.[225] Significant improvements have been made to Pd and Pt MOR catalysts by addition of a transition metal to the structure, including alloyed and core-shell structures.[80,254-258] In our work different shell thicknesses and sizes of Pd-Ni-Pt nanoparticles are compared alongside the Pd-Pt core-shell nanoparticle control. Cyclic voltammetric (CV) and chronoamperometric curves (CA) were obtained for the catalysts of different sizes and Ni thicknesses to show both activity and stability. Typical blank scans were carried out in acidic and alkaline electrolyte solutions. Integration of the current collected from the hydrogen desorption peak was used to determine the electrochemical surface area of the different catalysts. This surface area was then used to normalize the catalytic activity for the electrooxidation reactions. The CV plots of initial activity, bar plot summaries, and CA curves for alkaline MOR, and for MOR and FOR in acidic conditions, are shown in Figures 62 and 63, respectively.

FOR and MOR on Pt surfaces proceed by formation of intermediates which are oxidized and removed on the forward and reverse scans.[110] We use the forward and reverse scan peak current densities to discuss the initial activity of the various catalysts for FOR and MOR in acidic and basic solutions. It has been reasoned that a sandwich layer consisting of a single atomic monolayer of mismatching non-precious metal would

impart little to no strain to a Pt monolayer surface in Pt-M-Pt structures; therefore, any changes in catalytic behavior are predicted to arise primarily through ligand effects.[57] In contrast, for the case of multiple sandwich layers and more than one monolayer of Pt surface atoms (the case here), ligand effects are expected to be minimalized, and the influence of lattice strain is expected to be the major contributor to catalysis, assuming restructuring due to dealloying or leaching of the non-precious component does not occur to a significant extent because of the relatively thick Pt surface layer.[63] As the Ni layer thickness increases for the Pd-Ni-Pt nanoparticles, we would expect the influence of the mismatch to become greater, and so the perturbation to Pt surface atoms may be increased, resulting in changes to catalytic activity.

To test the hypothesis of a strain influence on catalysis, CV scans were carried out for MOR in alkaline solutions shown in Figure 62(a). It was observed that the larger, thicker Ni-layered nanoparticles showed current density at ~0.8 mA/cm2. The catalysts with thinner Ni layers and the Pd-Pt control showed similar peak activities around ~0.4 mA/cm2, at best, roughly half the activity of the Pd-Ni-Pt nanoparticles with thicker shells. This confirms a diminished strain effect for thin Ni sandwich layers and increasing strain from larger Ni amounts. In addition, the ratio of the forward to reverse scan peak currents is much higher with the sandwich catalysts compared to the control, which shows more efficient oxidation and CO-tolerance for these catalysts.[80,257] A bar plot summary in 62(b) for MOR in base demonstrates the average activity across different catalyst batches to be consistent. Smaller Pd-Ni-Pt nanoparticles had a much higher current density compared to the other catalysts at ~1.6 mA/cm2, showing that the design

could be extended down to size ranges that are more relevant for industrial applications. Figure 62(c) gives CA curves for MOR in alkaline solution generated by holding the voltage at -0.1 V vs. SCE. This value was chosen because it overlapped with the position of the forward oxidation peak. These transient current density curves follow similar trends in activity, as for the CV experiments, with the Ni-sandwiched catalysts holding the highest activity over time.

Improvement of FOR and MOR electrocatalysis in acidic conditions was also observed. For FOR catalysis shown in Figure 63(a), it can be seen that the larger Pd-Ni-Pt nanoparticles again outperform the Pd-Pt control. Catalysts with thicker Ni layers show higher current densities (nearly double) compared to the thinner-shelled NPs. The low forward scan peak for each of the catalysts is indicative of the Pt indirect pathway, confirming the surface composition. The smaller sized Pd-Ni-Pt nanoparticles have the highest specific activity at ~7 mA/cm^2. These trends follow suit in MOR in acidic electrolyte shown in Figure 63(b), with the large Pd-Ni-Pt nanoparticles with thicker Ni layers achieving ~0.4 mA/cm^2. Again the smaller sized Pd-Ni-Pt cubic nanoparticles attained the highest activity at ~0.8 mA/cm^2. The similar trends in reactivity observed between the different catalytic oxidations could be expected based on the similarity of the reaction pathways on Pt, following direct oxidation to CO_2, and indirect oxidation through adsorbed carbonaceous intermediates, such as CO and formate.[110] In fact, all of the Pd-Ni-Pt ternary metal nanoparticle structures outperform the Pd-Pt control. A summary of the specific activities for both reactions in acid electrolyte is given in the bar plot in Figure 63(c), where initial activity for different batches of each of the four

catalysts were again averaged to show the consistency. We note the higher activity for MOR catalysis in base is generally ascribed to adsorbed hydroxyls assisting in the oxidation reaction.[258]

The CA studies given in Figure 63(d) show the catalyst du-rability for FOR at constant 0.4 V; chosen due to the location of the oxidation peak. The catalysts retain their activity trends following Ni amounts in the sandwich layer and size of the Pd-Ni-Pt nanoparticles. Recent reports show that larger sized particles are more sensitive toward non-precious metal leaching in acidic conditions, making them unstable and less active over time.[22] Since the particle size here is above the limit proposed, we would expect to see activity changes over time due to this effect. The transient current density plot over an extended time frame shows an increase in the activity is observed for the Ni-containing catalysts after the initial drop from 0 s, where they rise to reach a plateau before they finally begin to decay. Markovic et al. have discussed a similar feature for Pt-Ru alloy surfaces as being due to poisoning and removal of CO adsorbed after an initial period of time by Ru sites, however this feature on the Pd-Ni-Pt catalysts is unexpected given the conformal Pt-coating, unless dealloying is occurring.[258] The reason for this and the variation in activity for reaction in acidic media would become clear upon examination of the catalyst structure after electrochemical experiments.

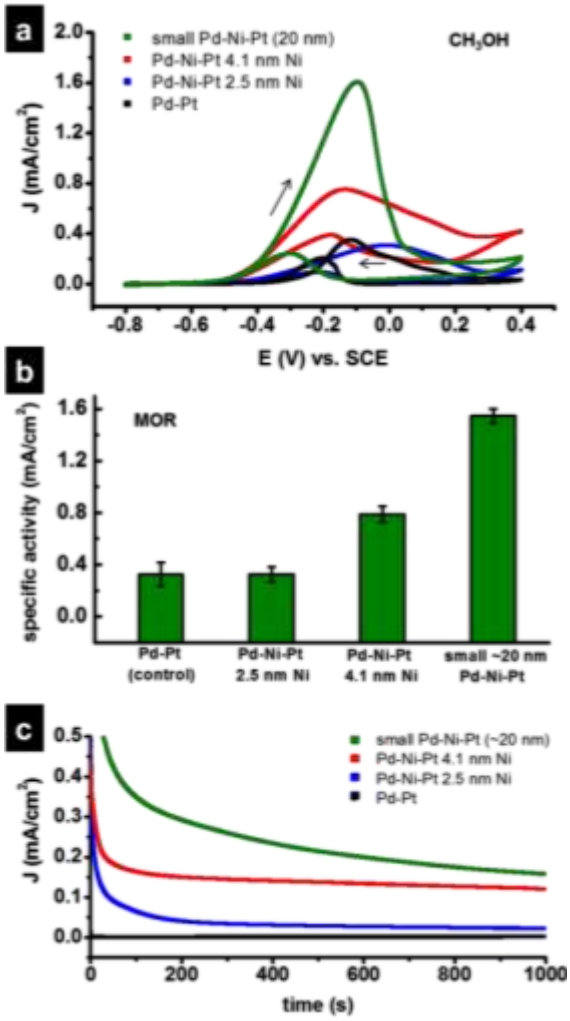

Figure 62. Cyclic voltammetry and chronoamperometry of multi-layered Ni nanoparticles showing the catalytic activity for methanol electrooxidation in alkaline conditions. In (a) are CV cycles obtained in solutions which were 0.1 M in KOH and 0.05 M in CH_3OH, and (b) bar graph of trends in catalyst specific activity showing the average peak current densities for multiple batches of each catalyst. In (c) are CA curves for the different nanoparticle catalysts for MOR at -0.1 V vs. SCE to show the transient current density.

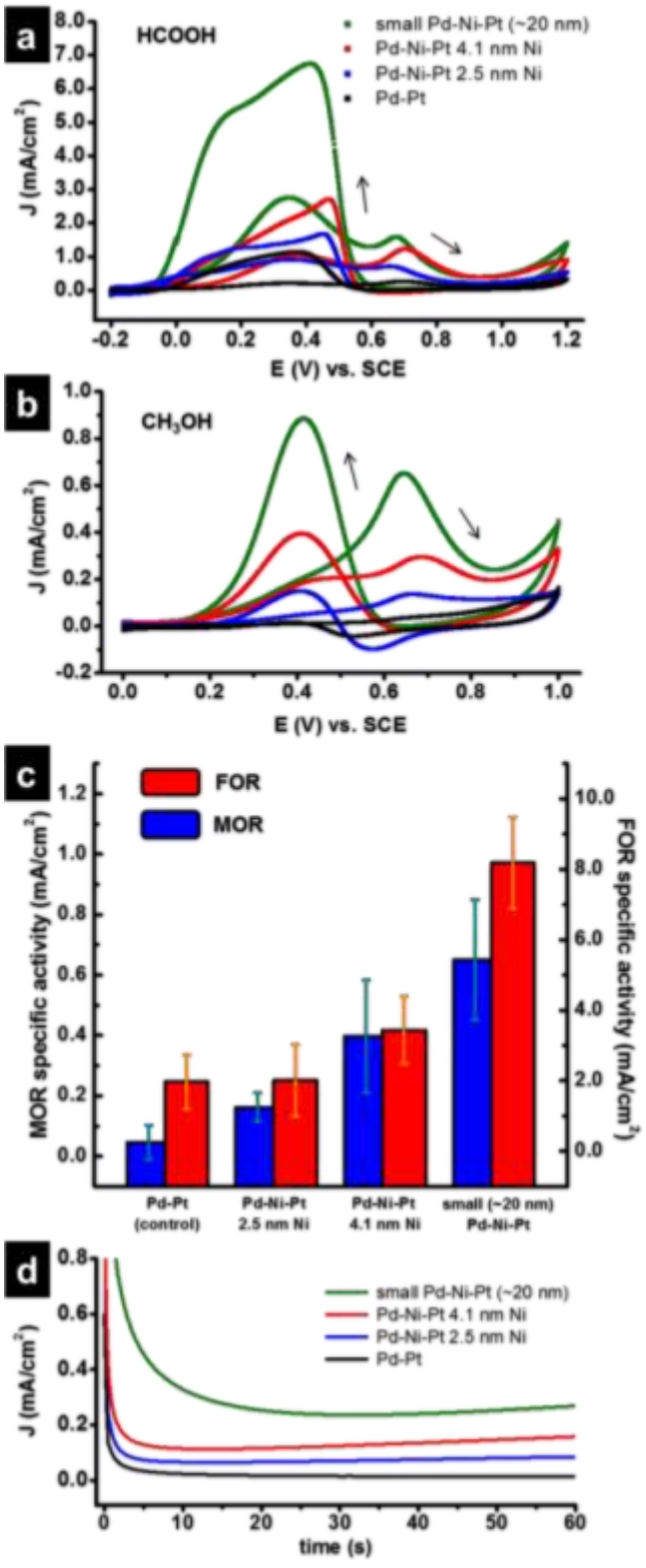
a
HCOOH
small Pd-Ni-Pt (~20 nm)
Pd-Ni-Pt 4.1 nm Ni
Pd-Ni-Pt 2.5 nm Ni
Pd-Pt
J (mA/cm²)
E (V) vs. SCE
b
CH₃OH
J (mA/cm²)
E (V) vs. SCE
c
FOR
MOR
MOR specific activity (mA/cm²)
FOR specific activity (mA/cm²)
Pd-Pt (control)
Pd-Ni-Pt 2.5 nm Ni
Pd-Ni-Pt 4.1 nm Ni
small (~20 nm) Pd-Ni-Pt
d
small Pd-Ni-Pt (~20 nm)
Pd-Ni-Pt 4.1 nm Ni
Pd-Ni-Pt 2.5 nm Ni
Pd-Pt
J (mA/cm²)
time (s)

Figure 63. Cyclic voltammetry and chronoamperometry of multi-layered Ni nanoparticles showing the catalytic activity for electro-oxidations in acidic conditions. In (a) are CV cycles obtained in solutions which were 0.5 M in both HCOOH and $HClO_4$, (b) CV curves obtained in solutions which were 0.5 M in both CH_3OH and H_2SO_4, and (c) bar graph of trends in specific activity for each reaction. Multiple batches of each catalyst were synthesized and their peak current densities averaged. In (d) are CA curves for the different nanoparticle catalysts for FOR at 0.4 V vs. SCE.

We initially assumed that the improved performance of the small Pd-Ni-Pt catalysts and the difference in activity for higher Ni amounts in the sandwich layer were lattice strain-related based on the catalytic trends, XRD peak shifts and tailing, and HRTEM of the catalysts before the reactions; however, this assumes the nanoparticle surfaces underwent no changes during the potential cycling in acid and base electrolyte. The catalysts were re-examined in TEM after the electrochemical experiments were carried out to confirm whether or not the layered nanoparticle structure remained intact. The images of the highest-performing catalysts (small and large Pd-Ni-Pt nanoparticles with the thickest Ni layer) on the carbon support after CA experiments in acidic FOR and basic MOR are shown in Figure 64(a-h). A stark difference is apparent in the NP catalysts after reaction in acidic conditions in 64(e-h), whereas after reaction in base in 64(a-d), the structure resembles that before electrochemistry is carried out. For FOR in perchloric acid and blank scans in sulfuric acid, the core of the Pd-Ni-Pt nanoparticles appears void, despite the Pt coating. The Pd and Ni signals remaining in EDX of the

sample indicate the metals are not completely removed, however, and this suggests Pd and Ni sites remain in the frameworks.

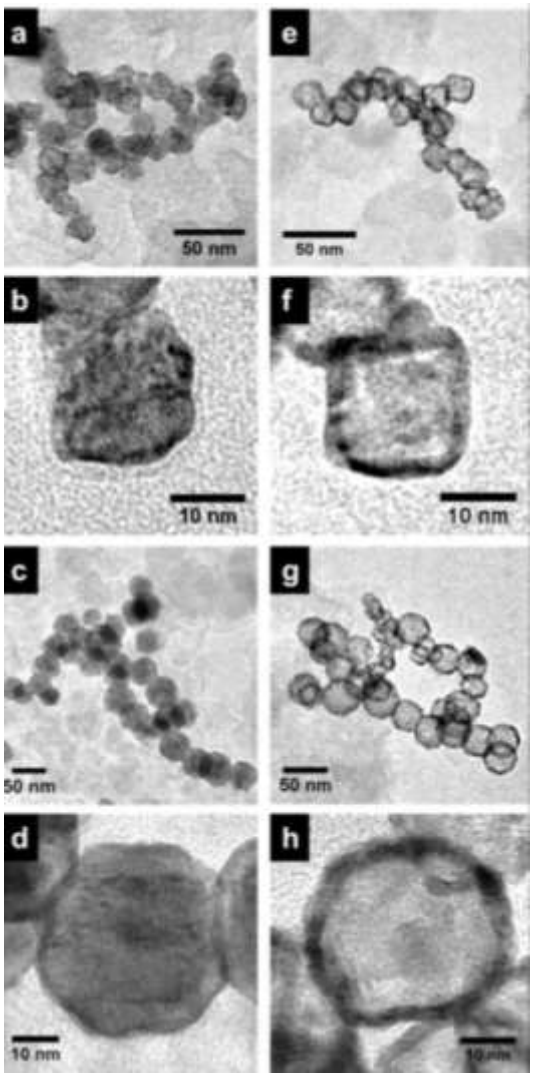

Figure 64. TEM images of cubic Pd-Ni-Pt nanoparticles on the carbon support after the electrochemical experiments in acid and base electrolyte. Images of small Pd-Ni-Pt nanoparticles are given after reaction in basic conditions in (a,b) and acidic conditions in (e,f). In (c,d) and (g,h) are the large Pd-Ni-Pt nanoparticles after reaction in basic and acidic media, respectively.

Following from the TEM results, the case of MOR in KOH solution where catalyst stability is higher, strain governs reactivity, whereas in acidic FOR and MOR conditions, the nanoparticles restructure so that a combination of strain, ligand, and ensemble effects govern the reactivity trends. Before reaction, we believe the compressive strain on the Pt surface may be highest in the small Pd-Ni-Pt nanoparticles, due to the combined strain effects from Ni sandwich layers and smaller size, followed by the larger NPs with ~4.1 nm Ni, the nanoparticles with ~2.5 nm Ni, and the Pd-Pt control nanoparticles. This would explain the enhanced catalytic performance in basic MOR. The higher activity with increasing amounts of Ni and decreasing overall nanoparticle size for both FOR and MOR in acidic conditions is more likely a result of a combination of this effect and composition changes from dealloying and restructuring. Notably, the hollow structures observed after cycling in acid resemble recent displays of electrocatalysts with stable porous M-Pt nanosheets and nanoframeworks, although formed by a different route.[56,259] The Pt-Ni nanoframeworks produced by C. Chen, Y. Kang et al., were formed from oxidative aging of the particles in solution after the synthesis and still showed considerable enhancement and stability for oxygen reduction catalysis. These examples support the finding of increased activity of the catalysts after leaching of Pd and Ni. The post-cycling TEM also suggest that even Pd in a core–shell configuration is susceptible to leaching effects from potential cycling in acid, and examination of such Pd-containing electrocatalysts after reaction should not be excluded from future studies.

4.0 PROPOSAL FOR FUTURE WORK

One of the greatest challenges of the 21st century is to develop better catalysts for sustainable energy technologies. At the present stage, these processes require new and advanced solid-state heterogeneous catalysts. The lack of highly efficient catalysts is currently restricting the widespread implementation of many energy conversion and storage technologies, and calls for new catalyst design principles which can lead to better fundamental understanding of nanomaterials and surface chemistry, and ultimately, higher-performing catalytic materials for this important reaction. The broad impact of the proposed future research will be to help contribute to a sustainable energy future, and so we aim to further develop the new archetypes shown previously to push the boundary of knowledge in regard to fuel cell electrocatalysts.

The state-of-the-art ORR electrocatalysts show similarities in the design of the nanostructures which yield certain advantageous structural motifs: 1) facet matters: a specific Pt (111) surface remains the best catalytic surface for the ORR reaction because of its position of the d-band relative to the Fermi level and geometric packing, 2) size matters: catalyst sizes approaching ~10 nm find better conversions, due to its geometric and electronic structures, 3) composition matters: non-precious metals, such as Ni and Co, have been incorporated to lower catalyst cost, while simultaneously, improving activity and stability of the catalysts, and finally 4) structure changes matter: metal migration and restructuring of the catalysts during reaction conditions results in a complex multilayered nanoparticle structure; a shaped core-sandwich-shell nanostructure was found to be an ideal structure for catalysis and the enhanced catalytic performance

highly depends on the lattice stain in this sandwich structure. According to this, we hypothesize that the shaped core-sandwich-shell structure is ideal in providing stable lattice strain in nanoparticles. Also, it will be an excellent platform for simultaneously adjusting the degree of lattice strain in shaped nanoparticles, while retaining the capability to tune the other important parameters independently. It is important to note that the sandwich structures in the previous studies were arrived at indirectly, through leaching processes that can vary based on the particle size, shape, composition, surface segregation energies, and potential cycling conditions. Our synthesized core-sandwich-shell design offers a higher degree of control of the structures, so there is much more that can be learned and taken away from these guiding principles that could lead to fundamental understanding of the relationship between surface chemistry, structure, and performance.

Our proposed future work will take on more detailed studies of different core-sandwich-shell nanoparticle materials. The size, shape, and facet of the core nanocrystals in the core-sandwich-shell will first be controlled to provide well-defined substrates for the epitaxial overgrowth of the sandwich layers of non-precious metals, such as Fe, Co, Ni, Cu, and their alloys, which in general are challenging to be structurally controlled. The sandwich layers provide the source of lattice stain for the surface shells, which are composed by catalytically active metals such as Pt, Pd, Rh, Ir, and their alloys. The direct use of non-precious metal nanocrystals as core substrates is an alternative route and it benefits the design of inexpensive catalysts; however, the well-defined shape and size of

the substrates is sacrificed, which could delay development of a well-defined platform for the fundamental understanding of lattice strain in nanoparticles.

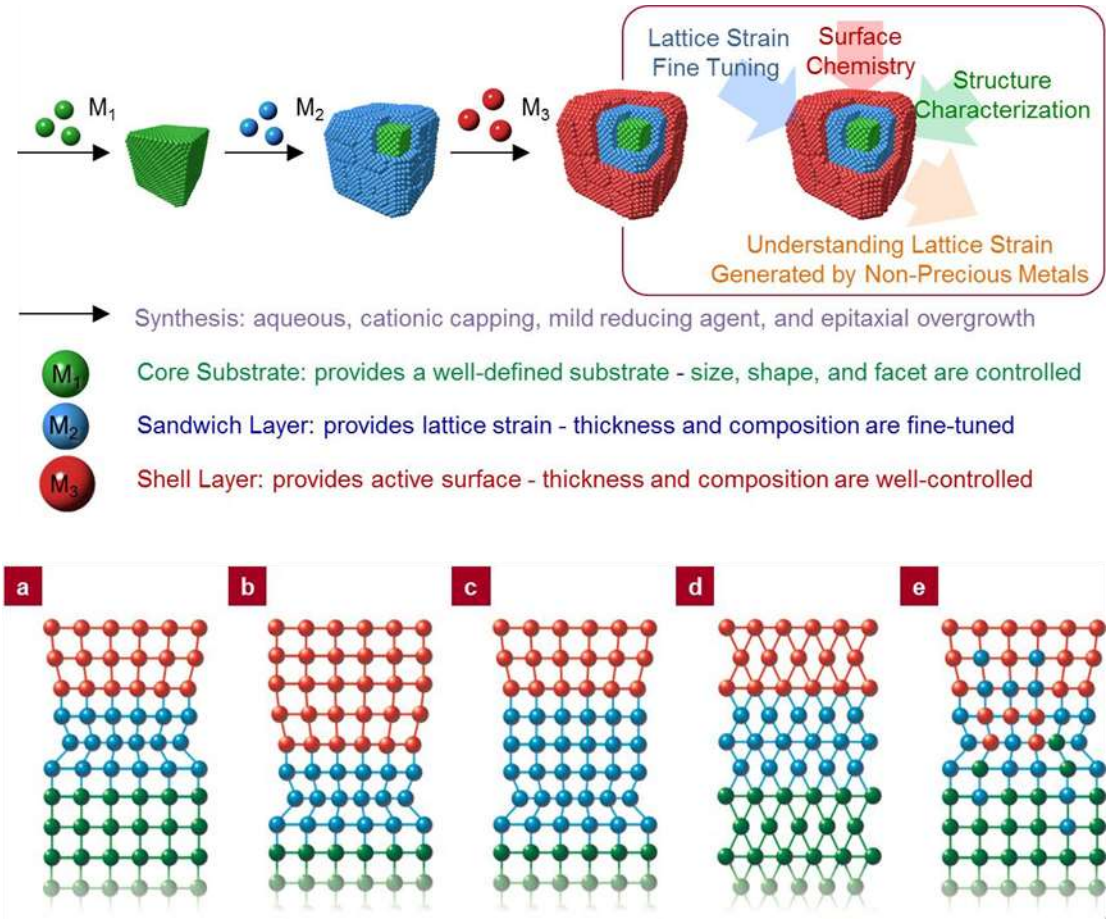

Figure 65. Schematic for proposed study of lattice strain, surface chemistry, and characterization through the sandwich nanoparticle archetype. Below are models depicting the different scenarios for fundamental studies: a,b) strain-tuning of electronic surface structure and elucidation of limits of the lattice strain effect in catalysis by control of shell thickness, a,c) strain-tuning of electronic surface structure by control of sandwich layer thickness, a,d) relation of strain to morphology, and a,e) metal migration through restructuring or alloying at the multiple interfaces.

Relying on the ability of independently adjusting each structural parameter in our approach, we propose to systematically tune and characterize all parameters of the core-sandwich-shell archetype, and use model catalytic reactions as a surface characterization tool to couple the relationship between surface electronic structures and lattice strain of nanoparticles. We first aim at diversifying the synthetic strategy for the sandwich archetype and increasing our ability to fine-tune the structures: size and shape of the core substrate, thickness and composition of the sandwich layer, and thickness and composition of the surface shell. We will mainly focus on thicker surface shells (> 1 nm) in order to decouple lattice strain and ligand effects. All of the structures will be characterized by a series of microscopic, spectroscopic, and diffraction-based techniques as described above. Parallel structure comparisons will be used to obtain initial understanding (Figure 65). For example, comparing the core-sandwich-shell nanoparticles with the same core substrate and sandwich layer, but different thickness of the shell layer will provide information on the effective range of lattice strain (a, b). Comparing the nanoparticles with the same core substrate and shell layer but with different thickness of the sandwich layer will provide information on the strength of strain provided by non-precious metal layers (a, c). Comparing the nanoparticles with the same sandwich layer and shell layer but different shape of the core substrate will provide information on the facet-dependence of lattice strain (a, d). Comparing the nanoparticles before and after the reactions will provide information on metal migration (a, e). After optimizing the synthesis and acquiring the fundamental understanding of the structures, well-studied model electrochemistry and gas-phase catalytic reactions will be used as

tools to interrogate the metal surfaces. Reactions of interest include electrochemical small molecule oxidations and oxygen reduction, as well as gas-phase CO oxidation and alkene hydrogenations. We understand that metal migration and reconstruction during the reactions will influence the lattice strain effect over time, as well as other electronic, geometric, and ensemble effects. Therefore, we will carefully monitor metal migration and reconstruction induced by reaction conditions. The long-term objective for this research is to use the new platform to gain a fundamental understanding of nanoparticle lattice strain introduced by non-precious metal layers.

Furthermore, we hypothesize that a similar strategy could be used to create metal-oxide, metal-sulfide, and even metal-carbide sandwich layers. There has recently been an influx of research in the area of these materials due to their important optical, catalytic, electrical, and magnetic properties (and their respective applications).[260-262] Sandwiching oxide, sulfide, and carbide layers between two metals is fundamentally of interest in studying migration and stability of the interfaces at the nanoscale. Specifically, cobalt sulfide and tungsten carbide possess the ability to act in a similar fashion as many of the platinum and platinum group metal catalysts due to the shifts in the d-band.[263-265] By having similar catalytic activity as platinum, these materials can also be used as a replacement for expensive platinum in several reactions. CuO_x, CoS_x, and WC_x, sandwich layers will be considered first. Controlled growth of Cu_2O and Co_3S_4 in an aqueous system has been demonstrated before and our group has successfully overgrown these materials on the surface of Pd cores via the same aqueous system mentioned in the

previous section.[266] A direct aqueous synthesis of WC_x will be challenging, and answering this challenge might require calcination at higher temperatures.[267]

Many recently published nanoparticle catalysis studies only consider the initial activity of a reaction and the original structure of the nanoparticles, and then draw conclusions about the particles' intrinsic catalytic activity. It has even become an accepted norm for many multi-metallic nanoparticle electrocatalytic studies to consider only the first few cycles of a reaction. These previous studies might provide some fundamental understanding; however, it is known that nanoparticles undergo metal migration and restructuring under different chemical environments, so the structure and activity vary during a reaction. Because the final target is to develop a more active and stable nanoparticle catalyst, it is vital to determine the degree of migration and restructuring on nanoparticles under different physical conditions. We aim to study the physical transformations of the core-sandwich-shell nanostructures under exposure to different chemical environments. The multiple interfaces present in the core-sandwich-shell design will allow us to study multiple possible migration and restructuring pathways. Though it could seem somewhat complicated with more interfaces, it will allow us to design experiments in which we expect to see mixing and segregation occur, and then modify the conditions to find ways to prevent or stabilize certain configurations. The results of the studies of metal migration that includes diffusion and segregation behaviors between different phases, e.g. monometallic shells and sandwiches, intermetallic alloy shells and sandwiches, and heterogeneous alloy shells and sandwiches, will all give a set of rules for predicting structural transformations based on the reactive

environment type. Many works have begun to address this computationally, but of course this needs to be confirmed experimentally, and for beyond simpler bimetallic systems. We will first synthesize a library of possible core-sandwich-shell configurations, and systematically subject them to different conditions. Some expected results are the formation of oxides in O_2 gas environments, etching in acidic media, metal migration due to surface energies, and restructuring due to the high strain built up from a lattice mismatch. These transformations can also be used as to a tool to fine tune the nano-architectures after nanoparticles were synthesized in the colloidal system.

We expect challenges, and so we propose contingencies for these problems: 1) the lattice strain mechanism is not as efficient as we expected; by reducing the thickness of the M_3 shell to sub-nm scale, our structure is at an excellent position to study ligand effects as well, and to elucidate the real limits to the lattice strain effect as an alternative, 2) oxidation of non-precious metals poses certain challenges to our design; we can carry out the entire synthesis under the inert atmosphere of a glove box in organic solvents, 3) it is possible that we might face the problem of low level of control of other materials including Fe, Co, Cu, oxides, sulfides, and carbides; poly-ol syntheses and organic solvent–hydrophobic surfactant syntheses will be utilized instead, 4) identification of lattice strain could be challenging; additional techniques could be carried out, such as X-ray absorption spectroscopy.

Figure 66. A 2.5 cm 3D-printed colored sandstone model of the core-sandwich-shell Pd-Ni-Pt nanocube.

Currently, we have also been utilizing crystal modeling and 3D-printing software to create macro-sized models of the nanostructures we are designing and creating (Figure 66). We are in the process of recruiting students with computer science, graphic design, and art majors (or minors) to help develop this end of our research. We believe the slogan, "nanotechnology - in the palm of your hand", will help both attract future scientists, and promote future investigations in the science of nanomaterials, while at the same time, these models allow our research concepts to be more easily communicated to the general community.

In summary, the goals of future research in this direction are 1) to develop a wet chemical method for synthesizing a library of binary and ternary metal core-sandwich-shell nanoparticles, with the ability to simultaneously tune size, composition, layer thickness, and morphology, independent of other parameters, 2) to resolve lattice strain

by new and advanced imaging, diffraction, and simulation techniques, 3) to examine and isolate the effect of the lattice strain mechanism from ligand, ensemble, and other effects, and 4) to investigate the migration of metals in this novel structural archetype. This research will allow fundamental understanding of the concepts of lattice strain, its relationship to size and shape, and the limitations of the lattice strain effect on catalysis. The understanding could be used in a variety of potential applications e.g. catalysis, electronics, plasmonics, and for new techniques for the characterization of surface lattice strain in nanomaterials. Our preliminary works highlight the delicate interplay between lattice strain and the traditional factors invoked to explain catalytic reactivity of multi-metallic surfaces and metal-metal interfaces. We ultimately expect that this information, combined with lattice strain and composition maps correlating the change in surface electronic structure (surface d-band) of nanocrystals, is expected to reveal the true structure and location of active sites in heterogeneous and electrochemical catalysis, where conflicting explanations for the source of improvement exist in the literature. The information can then be used to generate 3D volcano plots and maps relating catalytic activity to composition, strain, and other factors.[268] This will have broad implications in the future for the field of catalyst design, and in the development of more efficient and sustainable chemistry.

5.0 CONCLUSION AND OUTLOOK

To promote the effect of halide ions in the growth of shaped Pd nanocrystals, we utilized polydiallyldimethylammonium halides (PDADMAX, X = halide), a hybrid cationic, polymeric stabilizer. Surface enhanced Raman spectroscopy and synthesis experiments provide evidence supporting the high concentration of PDADMA on metal surfaces likely promotes the local surface adsorption of halides. By utilizing the preferences of Cl-, Br-, and I-, in binding of Pd {111} and {100} in this system, we confirm the role of halides and demonstrate the creation of Pd cubes, Pd octahedra, and novel Pd cuboctopods by simply tuning the halides.

Nearly identical Pd nanocubes have been synthesized in high yield and X-ray powder diffraction patterns were obtained with interference fringes affording access to unprecedented structural details of nanocrystal size, shape, and complex anistropic atomic displacement for a population of trillions of nanoparticles. The excellent agreement between diffraction data and molecular dynamics (MD) provides strong experimental validation of MD simulations and the proposed data-interpretation paradigm. These results show that individual atomic displacements within the nanocubes are not only a function of disrupted bonds and the crystallographic planes of the adjacent surface; but rather complex strain gradients extending across all surfaces of the particle strongly influence the atomic displacements. This observation of non-uniform surface strain and the manner in which it is affected by different sizes, shapes, and locations

within each facet could be the key to understand many surface related properties of shaped nanocrystals, including those associated with important catalysis applications.

We have studied the lattice strain enhancement of electrocatalytic properties on differently strained Pd nanocrystal surfaces. Different extents of lattice strain are evident due to the intrinsic twinning in the Pd icosahedra and the lattice mismatch between the Au seeds and the Pd and PdPt shells in the core-shell particles. During electrocatalysis, decreased potentials of CO stripping and increased current densities of FOR oxidation were observed for the strained nanoparticles, likely due to perturbation of the d-band center. For gas phase ethylene hydrogenation, the activities of the strained nanoparticles are lower than those of the single crystalline Pd nanoparticles, which was most likely due to the presence of CTAB that could not be removed completely from the surface. A method for preparing Au-PdPt nanoparticles with multifaceted control over the factors which dictate catalytic activity was presented. The activity of the catalysts were tuned by control and optimization of composition and lattice strain in the shaped core-shell nanoparticles, to give a more active formic acid oxidation electrocatalyst. This resulted in a volcano plot comparing strain from shell thickness versus the specific activity, where an optimum intermediate thickness was discovered.

Additionally, a novel method for synthesizing controlled Rh island film overgrowth on metallic nanocrystal substrates has been developed. Iodide in conjunction with a shape-controlled nanocrystal substrate directs the epitaxial overgrowth of rhodium, which results in the formation of single-crystalline island shells. The new role of iodide in the overgrowth is unprecedented in the literature. The observed epitaxy in the case of

rhodium is accomplished here despite large lattice mismatches (~7% for Au-Rh), higher bond dissociation energies in the shell metal (Pd-Rh, Au-Rh), and higher electronegativity in the shell metal (Pd-Rh). The distinct surfaces were studied and confirmed by HRTEM and electrocatalysis. The model catalysts synthesized here might not be practical as industrial catalysts due to the relatively large size; however, we provide a powerful new tool for the high level control of metal nanostructures, which could enrich the fundamental understanding of structure-dependent heterogeneous catalysis.

The evolution and mechanism for the formation of Pd-Rh nanoboxes and Rh nanoframeworks from the Pd-Rh core-island-shell nanoparticles was presented. The two different sets of cubic particles are generated by the heating of core-island-shell nanocubes under either reductive or oxidative environments. Detachment-readhesion mediated by bromide ions was discussed as a plausible mechanism for the formation of the Pd-Rh NBs, with the chemical stability of each metal playing a major role in their formation. The synthesis utilizes the Rh island-film growth, and Pd's rapid ligand exchange kinetics in combination with etchants to generate semi-ordered grid-like, alternating metal phases in a shape-controlled hollow structure, which is a novel and fundamentally curious archetype, unprecedented in the literature, and only accessed through our route. The migration of Pd between Rh columns in the shell creates a phase-separated and strained heterostructure, driven by Pd's lower surface energy. The phases observed here (< 5 nm phases) could only be resolved by advanced microscopy techniques, and demand new definitions for what constitutes an 'alloy' at this size scale.

Extending this strategy yielded additional heterostructures, such as yolk-shell Au-Rh nanoparticles. Finally, the cubic nanoparticles' catalytic activities were investigated in model fuel cell reactions. It was discovered that lattice strain and composition at the surface were the most important factors influencing their catalytic behaviors, most notably in increasing Pd's performance as an ORR catalyst. For the purpose of studying the effects of lattice strain on catalysis, the grid-like nanobox architecture is of great interest. Future efforts are being directed toward other PGM and non-precious metal systems where the migration mechanism could be utilized to create and study strain in nanocrystals that take on this new structural archetype.

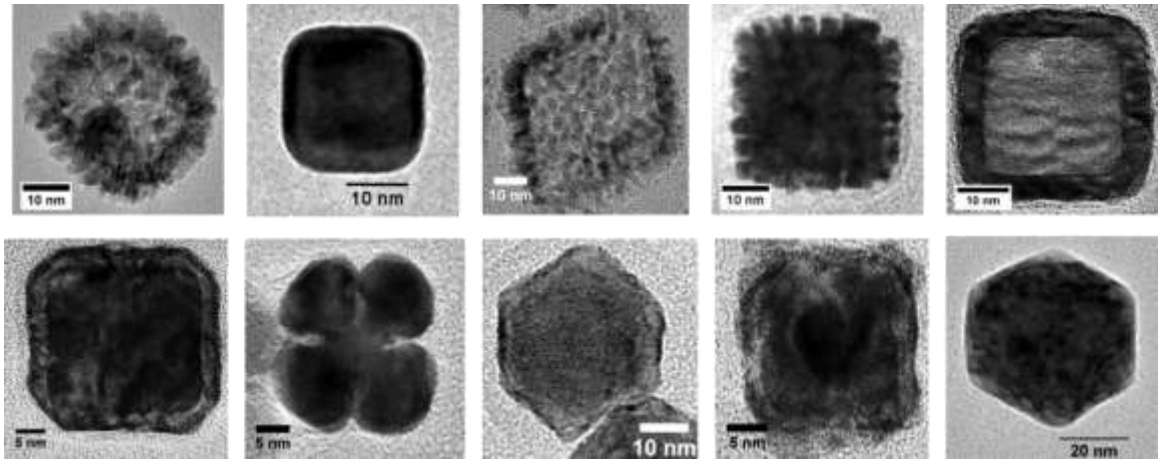

Figure 67. Collage of TEM images of the new architectures accessed by the methods developed.

Finally, shaped Pd-Ni-Pt core-sandwich-shell nanoparticles were synthesized using cubic and octahedral Pd substrates in the aqueous phase at low temperature with cationic surfactant and hydrazine as the reducing agent. It has been demonstrated that the method

produces ternary and quaternary multilayered metal nanoparticles comprising Ni with control of shape, size, and Ni layer thickness. Importantly, the one-pot, layer-by-layer overgrowth strategy allows for 'trapping' of the pristine, metallic Ni layer before surface oxidation occurs. These novel nanoparticle structures were characterized and served as a platform to study the activity of the catalysts in the electrocatalytic oxidation of methanol and formic acid. Their stability is also assessed via chronoamperometry. The improved performance of the Pd-Ni-Pt particles over the Pd-Pt control results from increased compressive strain on the Pt surface. It was found that the smaller sized particles and larger Ni sandwich layers are more active and stable over a longer period of time, suggesting a potentially effective catalyst design in future work. Further investigations are aimed at a systematic study of the impact of different shapes and different Ni and Pt layer thicknesses on electrocatalysis by the multi-shelled structures; in particular, the tuning of the Ni and Pt shell thickness of octahedral Pd-Ni-Pt nanoparticles to obtain a better-performing ORR catalyst.

The work culminates in many new, well-defined, and more sophisticated nanocrystal archetypes (Figure 67), through green, low temperature, mild reduction, aqueous routes, whilst addressing several different synthesis and characterization challenges along the way. We have shown the importance of these structures, not only as potentially effective design strategies for industry, but also as ideal platforms for the fundamental study of lattice strain, the related factors of shape, size, and composition, and how this impacts the catalytic behaviour of the nanoscale materials. The future is promising for this research direction, especially with regard to the number of new and different materials in these

families that can now be accessed and studied. We believe many new insights can be gained by systematically controlling lattice strain, and decoupling it from the other conventional parameters of nanocrystal structure. Unforeseen applications in nano-plasmonics, sensors, and batteries could also present themselves, due to the versatility of these late transition metals; however, the broader impact of this work will be in advance toward a more sustainable energy future with renewable and zero-emission technologies, in particular, toward the fabrication of better-performing automotive fuel cell electrocatalysts.

REFERENCES

(1) LaMer, V. K.; Dinegar, R. H. *J. Am. Chem. Soc.* **1950**, *72*, 4847.
(2) Oxtoby, D. W. *Acc. Chem. Res.* **1998**, *31*, 91.
(3) Venables, J. A.; Spiller, G. D. T.; Hanbucken, M. *Reports on Progress in Physics* **1984**, *47*, 399.
(4) Almora-Barrios, N.; Novell-Leruth, G.; Whiting, P.; Liz-Marzán, L. M.; López, N. *Nano Lett.* **2014**, *14*, 871.
(5) Kawasaki, H. *Nanotechnology Reviews* **2013**, *2*, 5.
(6) Sanchez, S. I.; Small, M. W.; Bozin, E. S.; Wen, J.-G.; Zuo, J.-M.; Nuzzo, R. G. *ACS Nano* **2012**, *7*, 1542.
(7) Cui, C.; Gan, L.; Neumann, M.; Heggen, M.; Roldan Cuenya, B.; Strasser, P. *J. Am. Chem. Soc.* **2014**, *136*, 4813.
(8) Zhang, J.; Yang, H.; Fang, J.; Zou, S. *Nano Lett.* **2010**, *10*, 638.
(9) Guo, S.; Li, D.; Zhu, H.; Zhang, S.; Markovic, N. M.; Stamenkovic, V. R.; Sun, S. *Angewandte Chemie International Edition* **2013**, *52*, 3465.
(10) Ahmadi, T. S.; Wang, Z. L.; Green, T. C.; Henglein, A.; El-Sayed, M. A. *Science* **1996**, *272*, 1924.
(11) Wu, H.-L.; Kuo, C.-H.; Huang, M. H. *Langmuir* **2010**, *26*, 12307.
(12) Niu, W.; Zhang, L.; Xu, G. *ACS Nano* **2010**, *4*, 1987.
(13) Chen, M.; Wu, B.; Yang, J.; Zheng, N. *Adv. Mater. (Weinheim, Ger.)* **2012**, *24*, 862.
(14) Sau, T. K.; Rogach, A. L. *Adv. Mater. (Weinheim, Ger.)* **2010**, *22*, 1781.

(15) Buck, M. R.; Schaak, R. E. *Angewandte Chemie International Edition* **2013**, *52*, 6154.
(16) Ruban, A. V.; Skriver, H. L.; Nørskov, J. K. *Physical Review B* **1999**, *59*, 15990.
(17) Wang, L.-L.; Johnson, D. D. *J. Am. Chem. Soc.* **2009**, *131*, 14023.
(18) Froemming, N. S.; Henkelman, G. *The Journal of Chemical Physics* **2009**, *131*, 234103.
(19) Andriotis, A. N.; Mpourmpakis, G.; Broderick, S.; Rajan, K.; Datta, S.; Sunkara, M.; Menon, M. *The Journal of Chemical Physics* **2014**, *140*, 094705.
(20) Tao, F.; Grass, M. E.; Zhang, Y.; Butcher, D. R.; Renzas, J. R.; Liu, Z.; Chung, J. Y.; Mun, B. S.; Salmeron, M.; Somorjai, G. A. *Science* **2008**, *322*, 932.
(21) Holton, O. T.; Stevenson, J. W. *Platinum Metals Review* **2013**, *57*, 259.
(22) Gan, L.; Heggen, M.; O'Malley, R.; Theobald, B.; Strasser, P. *Nano Lett.* **2013**, *13*, 1131.
(23) Debe, M. K. *Nature* **2012**, *486*, 43.
(24) Sau, T. K.; Rogach, A. L.; Jäckel, F.; Klar, T. A.; Feldmann, J. *Adv. Mater. (Weinheim, Ger.)* **2010**, *22*, 1805.
(25) Neumann, O.; Feronti, C.; Neumann, A. D.; Dong, A.; Schell, K.; Lu, B.; Kim, E.; Quinn, M.; Thompson, S.; Grady, N.; Nordlander, P.; Oden, M.; Halas, N. J. *Proceedings of the National Academy of Sciences* **2013**, *110*, 11677.
(26) Brongersma, M. L.; Halas, N. J.; Nordlander, P. *Nat Nano* **2015**, *10*, 25.
(27) Sheng, W.; Alhasan, A. H.; DiBernardo, G.; Almutairi, K. M.; Rubin, J. P.; DiBernardo, B. E.; Almutairi, A. *Plastic and Reconstructive Surgery Global Open* **2014**, *2*, e283.
(28) Wilker, M. B.; Schnitzenbaumer, K. J.; Dukovic, G. *Isr. J. Chem.* **2012**, *52*, 1002.
(29) Clavero, C. *Nat Photon* **2014**, *8*, 95.
(30) Baffou, G.; Quidant, R. *Chem. Soc. Rev.* **2014**, *43*, 3898.
(31) Ha, J. W.; Ruberu, T. P. A.; Han, R.; Dong, B.; Vela, J.; Fang, N. *J. Am. Chem. Soc.* **2014**, *136*, 1398.
(32) Zaera, F. *Catal. Lett.* **2012**, *142*, 501.
(33) Knözinger, H.; Kochloefl, K. In *Ullmann's Encyclopedia of Industrial Chemistry*; Wiley-VCH Verlag GmbH & Co. KGaA: 2000.
(34) Lee, H.; Habas, S. E.; Kweskin, S.; Butcher, D.; Somorjai, G. A.; Yang, P. *Angew. Chem.* **2006**, *118*, 7988.
(35) Tian, N.; Zhou, Z.-Y.; Sun, S.-G.; Ding, Y.; Wang, Z. L. *Science* **2007**, *316*, 732.
(36) Lee, I.; Delbecq, F.; Morales, R.; Albiter, M. A.; Zaera, F. *Nat Mater* **2009**, *8*, 132.
(37) Jin, M.; Zhang, H.; Xie, Z.; Xia, Y. *Energy & Environmental Science* **2012**, *5*, 6352.
(38) Laskar, M.; Skrabalak, S. E. *ACS Catalysis* **2014**, *4*, 1120.
(39) Bratlie, K. M.; Lee, H.; Komvopoulos, K.; Yang, P.; Somorjai, G. A. *Nano Lett.* **2007**, *7*, 3097.
(40) Tsung, C.-K.; Kuhn, J. N.; Huang, W.; Aliaga, C.; Hung, L.-I.; Somorjai, G. A.; Yang, P. *J. Am. Chem. Soc.* **2009**, *131*, 5816.

(41) Norskov, J. K.; Bligaard, T.; Rossmeisl, J.; Christensen, C. H. *Nature Chemistry* **2009**, *1*, 37.
(42) Nilsson, A.; Pettersson, L. G. M.; Hammer, B.; Bligaard, T.; Christensen, C. H.; Nørskov, J. K. *Catal. Lett.* **2005**, *100*, 111.
(43) Hwang, S. J.; Kim, S.-K.; Lee, J.-G.; Lee, S.-C.; Jang, J. H.; Kim, P.; Lim, T.-H.; Sung, Y.-E.; Yoo, S. J. *J. Am. Chem. Soc.* **2012**, *134*, 19508.
(44) Xin, H.; Linic, S. *The Journal of Chemical Physics* **2010**, *132*, 221101.
(45) Yu, T. H.; Hofmann, T.; Sha, Y.; Merinov, B. V.; Myers, D. J.; Heske, C.; Goddard, W. A. *The Journal of Physical Chemistry C* **2013**, *117*, 26598.
(46) Bandarenka, A. S.; Koper, M. T. M. *J. Catal.* **2013**, *308*, 11.
(47) Guo, S.; Zhang, S.; Sun, S. *Angewandte Chemie International Edition* **2013**, *52*, 8526.
(48) Long, N. V.; Thi, C. M.; Yong, Y.; Nogami, M.; Ohtaki, M. *J. Nanosci. Nanotechnol.* **2013**, *13*, 4799.
(49) Mayrhofer, K. J. J.; Arenz, M. *Nat Chem* **2009**, *1*, 518.
(50) Norskov, J. K.; Bligaard, T.; Rossmeisl, J.; Christensen, C. H. *Nat Chem* **2009**, *1*, 37.
(51) Singh, A. K.; Xu, Q. *ChemCatChem* **2013**, *5*, 652.
(52) Stephens, I. E. L.; Bondarenko, A. S.; Gronbjerg, U.; Rossmeisl, J.; Chorkendorff, I. *Energy & Environmental Science* **2012**, *5*, 6744.
(53) Oezaslan, M.; Hasché, F.; Strasser, P. *The Journal of Physical Chemistry Letters* **2013**, *4*, 3273.
(54) Cui, C.; Gan, L.; Li, H.-H.; Yu, S.-H.; Heggen, M.; Strasser, P. *Nano Lett.* **2012**, *12*, 5885.
(55) Choi, S.-I.; Xie, S.; Shao, M.; Odell, J. H.; Lu, N.; Peng, H.-C.; Protsailo, L.; Guerrero, S.; Park, J.; Xia, X.; Wang, J.; Kim, M. J.; Xia, Y. *Nano Lett.* **2013**, *13*, 3420.
(56) Chen, C.; Kang, Y.; Huo, Z.; Zhu, Z.; Huang, W.; Xin, H. L.; Snyder, J. D.; Li, D.; Herron, J. A.; Mavrikakis, M.; Chi, M.; More, K. L.; Li, Y.; Markovic, N. M.; Somorjai, G. A.; Yang, P.; Stamenkovic, V. R. *Science* **2014**, *343*, 1339.
(57) Kaya, S.; Friebel, D.; Ogasawara, H.; Anniyev, T.; Nilsson, A. *J. Electron Spectrosc. Relat. Phenom.* **2013**, *190, Part A*, 113.
(58) Zhang, X.; Lu, G. *The Journal of Physical Chemistry Letters* **2013**, *5*, 292.
(59) Menning, C. A.; Hwu, H. H.; Chen, J. G. *The Journal of Physical Chemistry B* **2006**, *110*, 15471.
(60) Wang, C.; Chi, M.; Li, D.; Strmcnik, D.; van der Vliet, D.; Wang, G.; Komanicky, V.; Chang, K.-C.; Paulikas, A. P.; Tripkovic, D.; Pearson, J.; More, K. L.; Markovic, N. M.; Stamenkovic, V. R. *J. Am. Chem. Soc.* **2011**, *133*, 14396.
(61) Wang, G.; Van Hove, M. A.; Ross, P. N.; Baskes, M. I. *The Journal of Chemical Physics* **2005**, *122*.
(62) Cui, C.; Gan, L.; Heggen, M.; Rudi, S.; Strasser, P. *Nat. Mater.* **2013**, *12*, 765.
(63) Strasser, P.; Koh, S.; Anniyev, T.; Greeley, J.; More, K.; Yu, C.; Liu, Z.; Kaya, S.; Nordlund, D.; Ogasawara, H.; Toney, M. F.; Nilsson, A. *Nat Chem* **2010**, *2*, 454.

(64) Wu, J.; Li, P.; Pan, Y.-T.; Warren, S.; Yin, X.; Yang, H. *Chem. Soc. Rev.* **2012**, *41*, 8066.
(65) Beyerlein, K. R.; Snyder, R. L.; Li, M.; Scardi, P. *J. Nanosci. Nanotechnol.* **2012**, *12*, 8554.
(66) Wasserman, H. J.; Vermaak, J. S. *Surf. Sci.* **1972**, *32*, 168.
(67) Ishikawa, K.; Uemori, T. *Physical Review B* **1999**, *60*, 11841.
(68) Qi, W. H.; Wang, M. P. *Journal of Nanoparticle Research* **2005**, *7*, 51.
(69) Fukuhara, M. *Phys. Lett. A* **2003**, *313*, 427.
(70) Patala, S.; Marks, L. D.; Olvera de la Cruz, M. *The Journal of Physical Chemistry C* **2013**, *117*, 1485.
(71) Wu, J.; Qi, L.; You, H.; Gross, A.; Li, J.; Yang, H. *J. Am. Chem. Soc.* **2012**, *134*, 11880.
(72) Lv, T.; Wang, Y.; Choi, S.-I.; Chi, M.; Tao, J.; Pan, L.; Huang, C. Z.; Zhu, Y.; Xia, Y. *ChemSusChem* **2013**, *6*, 1923.
(73) Wang, D.; Xin, H. L.; Hovden, R.; Wang, H.; Yu, Y.; Muller, D. A.; DiSalvo, F. J.; Abruña, H. D. *Nat. Mater.* **2013**, *12*, 81.
(74) Alayoglu, S.; Nilekar, A. U.; Mavrikakis, M.; Eichhorn, B. *Nat. Mater.* **2008**, *7*, 333.
(75) Bauer, J. C.; Chen, X.; Liu, Q.; Phan, T.-H.; Schaak, R. E. *J. Mater. Chem.* **2008**, *18*, 275.
(76) Lim, B.; Jiang, M.; Camargo, P. H. C.; Cho, E. C.; Tao, J.; Lu, X.; Zhu, Y.; Xia, Y. *Science* **2009**, *324*, 1302.
(77) Zhang, H.; Jin, M.; Liu, H.; Wang, J.; Kim, M. J.; Yang, D.; Xie, Z.; Liu, J.; Xia, Y. *ACS Nano* **2011**, *5*, 8212.
(78) Deng, Y.-J.; Tian, N.; Zhou, Z.-Y.; Huang, R.; Liu, Z.-L.; Xiao, J.; Sun, S.-G. *Chemical Science* **2012**, *3*, 1157.
(79) Hong, J. W.; Kang, S. W.; Choi, B.-S.; Kim, D.; Lee, S. B.; Han, S. W. *ACS Nano* **2012**, *6*, 2410.
(80) Kang, Y.; Pyo, J. B.; Ye, X.; Gordon, T. R.; Murray, C. B. *ACS Nano* **2012**, *6*, 5642.
(81) Kang, Y.; Qi, L.; Li, M.; Diaz, R. E.; Su, D.; Adzic, R. R.; Stach, E.; Li, J.; Murray, C. B. *ACS Nano* **2012**, *6*, 2818.
(82) Zhang, H.; Jin, M.; Xia, Y. *Chem. Soc. Rev.* **2012**, *41*, 8035.
(83) Gan, L.; Yu, R.; Luo, J.; Cheng, Z.; Zhu, J. *The Journal of Physical Chemistry Letters* **2012**, *3*, 934.
(84) Wang, X.; Orikasa, Y.; Takesue, Y.; Inoue, H.; Nakamura, M.; Minato, T.; Hoshi, N.; Uchimoto, Y. *J. Am. Chem. Soc.* **2013**, *135*, 5938.
(85) Montes de Oca, M. G.; Plana, D.; Celorrio, V.; Lazaro, M. J.; Fermín, D. J. *The Journal of Physical Chemistry C* **2012**, *116*, 692.
(86) Yang, J.; Yang, J.; Ying, J. Y. *ACS Nano* **2012**, *6*, 9373.
(87) Yang, J.; Chen, X.; Yang, X.; Ying, J. Y. *Energy & Environmental Science* **2012**, *5*, 8976.

(88) Wang, J. X.; Inada, H.; Wu, L.; Zhu, Y.; Choi, Y.; Liu, P.; Zhou, W.-P.; Adzic, R. R. *J. Am. Chem. Soc.* **2009**, *131*, 17298.
(89) Schnur, S.; Groß, A. *Physical Review B* **2010**, *81*, 033402.
(90) Shiihara, Y.; Kohyama, M.; Ishibashi, S. *Physical Review B* **2013**, *87*, 125430.
(91) Kitchin, J. R.; Nørskov, J. K.; Barteau, M. A.; Chen, J. G. *Phys. Rev. Lett.* **2004**, *93*, 156801.
(92) Kitchin, J. R.; Nørskov, J. K.; Barteau, M. A.; Chen, J. G. *The Journal of Chemical Physics* **2004**, *120*, 10240.
(93) Bagus, P. S.; Wieckowski, A.; Freund, H. *Computational and Theoretical Chemistry* **2012**, *987*, 22.
(94) Richter, B.; Kuhlenbeck, H.; Freund, H. J.; Bagus, P. S. *Phys. Rev. Lett.* **2004**, *93*, 026805.
(95) Xin, H.; Linic, S. *The Journal of Chemical Physics* **2010**, *132*.
(96) Yu, T. H.; Hofmann, T.; Sha, Y.; Merinov, B. V.; Myers, D. J.; Heske, C.; Goddard, W. A. *The Journal of Physical Chemistry C* **2013**.
(97) Wang, L.; Liu, P.; Guan, P.; Yang, M.; Sun, J.; Cheng, Y.; Hirata, A.; Zhang, Z.; Ma, E.; Chen, M.; Han, X. *Nat Commun* **2013**, *4*.
(98) Bhattarai, N.; Casillas, G.; Ponce, A.; Jose-Yacaman, M. *Surf. Sci.* **2013**, *609*, 161.
(99) Kwon, S. G.; Krylova, G.; Phillips, P. J.; Klie, R. F.; Chattopadhyay, S.; Shibata, T.; Bunel, E. E.; Liu, Y.; Prakapenka, V. B.; Lee, B.; Shevchenko, E. V. *Nat. Mater.* **2015**, *14*, 215.
(100) Chang, C.-C.; Wu, H.-L.; Kuo, C.-H.; Huang, M. H. *Chem. Mater.* **2008**, *20*, 7570.
(101) Kuo, C.-H.; Lamontagne, L. K.; Brodsky, C. N.; Chou, L.-Y.; Zhuang, J.; Sneed, B. T.; Sheehan, M. K.; Tsung, C.-K. *ChemSusChem* **2013**, *6*, 1993.
(102) Sneed, B. T.; Brodsky, C. N.; Kuo, C.-H.; Lamontagne, L. K.; Jiang, Y.; Wang, Y.; Tao, F.; Huang, W.; Tsung, C.-K. *J. Am. Chem. Soc.* **2013**, *135*, 14691.
(103) Kuo, C.-H.; Tang, Y.; Chou, L.-Y.; Sneed, B. T.; Brodsky, C. N.; Zhao, Z.; Tsung, C.-K. *J. Am. Chem. Soc.* **2012**, *134*, 14345.
(104) Sneed, B. T.; Kuo, C.-H.; Brodsky, C. N.; Tsung, C.-K. *J. Am. Chem. Soc.* **2012**, *134*, 18417.
(105) Sneed, B. T.; Young, A. P.; Jalalpoor, D.; Golden, M. C.; Mao, S.; Jiang, Y.; Wang, Y.; Tsung, C.-K. *ACS Nano* **2014**, *8*, 7239.
(106) Hu, P.; Zhuang, J.; Chou, L.-Y.; Lee, H. K.; Ling, X. Y.; Chuang, Y.-C.; Tsung, C.-K. *Journal of the American Chemical Society* **2014**, *136*, 10561.
(107) Jin, M.; Liu, H.; Zhang, H.; Xie, Z.; Liu, J.; Xia, Y. *Nano Research* **2011**, *4*, 83.
(108) Gao, C.; Vuong, J.; Zhang, Q.; Liu, Y.; Yin, Y. *Nanoscale* **2012**, *4*, 2875.
(109) Kuo, C.-H.; Hua, T.-E.; Huang, M. H. *J. Am. Chem. Soc.* **2009**, *131*, 17871.
(110) Koper, M. T. M. *Nanoscale* **2011**, *3*, 2054.
(111) Wang, Y.; He, J.; Liu, C.; Chong, W. H.; Chen, H. *Angewandte Chemie International Edition* **2015**, *54*, 2022.
(112) Sau, T. K.; Rogach, A. L. *Advanced Materials (Weinheim, Germany)* **2010**, *22*, 1781.

(113) Murphy, C. J.; Sau, T. K.; Gole, A. M.; Orendorff, C. J.; Gao, J.; Gou, L.; Hunyadi, S. E.; Li, T. *The Journal of Physical Chemistry B* **2005**, *109*, 13857.
(114) Xia, Y.; Xiong, Y.; Lim, B.; Skrabalak, S. E. *Angewandte Chemie International Edition* **2009**, *48*, 60.
(115) Tao, A. R.; Habas, S.; Yang, P. *Small* **2008**, *4*, 310.
(116) Ortiz, N.; Skrabalak, S. E. *Langmuir* **2014**, *30*, 6649.
(117) Ha, T. H.; Koo, H.-J.; Chung, B. H. *The Journal of Physical Chemistry C* **2006**, *111*, 1123.
(118) Bower, M. M.; DeSantis, C. J.; Skrabalak, S. E. *The Journal of Physical Chemistry C* **2014**, *118*, 18762.
(119) Gilroy, K. D.; Hughes, R. A.; Neretina, S. *J. Am. Chem. Soc.* **2014**, *136*, 15337.
(120) Hu, D.; Chou, K. C. *J. Am. Chem. Soc.* **2014**, *136*, 15114.
(121) Li, C.; Shuford, K. L.; Chen, M.; Lee, E. J.; Cho, S. O. *ACS Nano* **2008**, *2*, 1760.
(122) Tran, T. T.; Lu, X. *The Journal of Physical Chemistry C* **2011**, *115*, 3638.
(123) Gwo, S.; Lin, M.-H.; He, C.-L.; Chen, H.-Y.; Teranishi, T. *Langmuir* **2012**, *28*, 8902.
(124) Cappillino, P. J.; Sugar, J. D.; Hekmaty, M. A.; Jacobs, B. W.; Stavila, V.; Kotula, P. G.; Chames, J. M.; Yang, N. Y.; Robinson, D. B. *J. Mater. Chem.* **2012**, *22*, 14013.
(125) Lee, Y.-J.; Schade, N. B.; Sun, L.; Fan, J. A.; Bae, D. R.; Mariscal, M. M.; Lee, G.; Capasso, F.; Sacanna, S.; Manoharan, V. N.; Yi, G.-R. *ACS Nano* **2013**, *7*, 11064.
(126) Zhou, G.; Yang, Y.; Han, S.; Chen, W.; Fu, Y.; Zou, C.; Zhang, L.; Huang, S. *ACS Appl. Mater. Interfaces* **2013**, *5*, 13340.
(127) Chen, H.; Wang, Y.; Dong, S. *Inorg. Chem.* **2007**, *46*, 10587.
(128) Lu, B.; Zhang, Z.; Hao, J.; Tang, J. *RSC Advances* **2014**, *4*, 21909.
(129) Zhang, S.; Shao, Y.; Liao, H.; Engelhard, M. H.; Yin, G.; Lin, Y. *ACS Nano* **2011**, *5*, 1785.
(130) Zhang, S.; Shao, Y.; Yin, G.; Lin, Y. *J. Mater. Chem.* **2009**, *19*, 7995.
(131) Wang, L.; Wang, Y.; Li, A.; Yang, Y.; Tang, Q.; Cao, H.; Qi, T.; Li, C. *J. Power Sources* **2014**, *257*, 138.
(132) Shen, J.; Li, T.; Huang, W.; Long, Y.; Li, N.; Ye, M. *Electrochim. Acta* **2013**, *95*, 155.
(133) Huang, X.; El-Sayed, I. H.; Qian, W.; El-Sayed, M. A. *Nano Lett.* **2007**, *7*, 1591.
(134) Nikoobakht, B.; Wang, J.; El-Sayed, M. A. *Chem. Phys. Lett.* **2002**, *366*, 17.
(135) Oyelere, A. K.; Chen, P. C.; Huang, X.; El-Sayed, I. H.; El-Sayed, M. A. *Bioconjugate Chem.* **2007**, *18*, 1490.
(136) Lim, B.; Jiang, M.; Tao, J.; Camargo, P. H. C.; Zhu, Y.; Xia, Y. *Adv. Funct. Mater.* **2009**, *19*, 189.
(137) Peng, H.-C.; Xie, S.; Park, J.; Xia, X.; Xia, Y. *J. Am. Chem. Soc.* **2013**, *135*, 3780.
(138) DeSantis, C. J.; Skrabalak, S. E. *J. Am. Chem. Soc.* **2012**, *135*, 10.

(139) Wang, L.-B.; Wang, Y.-C.; Guo, H.-Y.; Huang, J.-L.; Zhao, Y.-L.; Liu, Q.-Y.; Wu, X.; Zeng, J. *Particle & Particle Systems Characterization* **2014**, n/a.
(140) Urban, K. W. *Science* **2008**, *321*, 506.
(141) Billinge, S. J. L.; Levin, I. *Science* **2007**, *316*, 561.
(142) Chen, C.-C.; Zhu, C.; White, E. R.; Chiu, C.-Y.; Scott, M. C.; Regan, B. C.; Marks, L. D.; Huang, Y.; Miao, J. *Nature* **2013**, *496*, 74.
(143) Ortalan, V.; Uzun, A.; Gates, B. C.; Browning, N. D. *Nat Nano* **2010**, *5*, 843.
(144) Shibata, N.; Pennycook, S. J.; Gosnell, T. R.; Painter, G. S.; Shelton, W. A.; Becher, P. F. *Nature* **2004**, *428*, 730.
(145) Huang, X.; Tang, S.; Mu, X.; Dai, Y.; Chen, G.; Zhou, Z.; Ruan, F.; Yang, Z.; Zheng, N. *Nat Nano* **2011**, *6*, 28.
(146) He, W.; Liu, J.; Qiao, Y.; Zou, Z.; Zhang, X.; Akins, D. L.; Yang, H. *J. Power Sources* **2010**, *195*, 1046.
(147) Sourov, G.; Ranjan, K. S.; Raj, C. R. *Nanotechnology* **2012**, *23*, 385602.
(148) Brummer, S. B.; Makrides, A. C. *The Journal of Physical Chemistry* **1964**, *68*, 1448.
(149) Grozovski, V.; Solla-Gullón, J.; Climent, V.; Herrero, E.; Feliu, J. M. *The Journal of Physical Chemistry C* **2010**, *114*, 13802.
(150) Pauling, L. *Proc. Natl. Acad. Sci. U. S. A.* **1989**, *86*, 9637.
(151) Henning, A. M.; Watt, J.; Miedziak, P. J.; Cheong, S.; Santonastaso, M.; Song, M.; Takeda, Y.; Kirkland, A. I.; Taylor, S. H.; Tilley, R. D. *Angewandte Chemie International Edition* **2013**, *52*, 1477.
(152) Habas, S. E.; Lee, H.; Radmilovic, V.; Somorjai, G. A.; Yang, P. *Nat. Mater.* **2007**, *6*, 692.
(153) Huang, X.; Zhao, Z.; Fan, J.; Tan, Y.; Zheng, N. *J. Am. Chem. Soc.* **2011**, *133*, 4718.
(154) Dai, Y.; Mu, X.; Tan, Y.; Lin, K.; Yang, Z.; Zheng, N.; Fu, G. *J. Am. Chem. Soc.* **2012**, *134*, 7073.
(155) Ding, Y.; Fan, F.; Tian, Z.; Wang, Z. L. *J. Am. Chem. Soc.* **2010**, *132*, 12480.
(156) Celorrio, V.; Montes de Oca, M. G.; Plana, D.; Moliner, R.; Lázaro, M. J.; Fermín, D. J. *The Journal of Physical Chemistry C* **2012**, *116*, 6275.
(157) Rice, C.; Ha, S.; Masel, R. I.; Wieckowski, A. *J. Power Sources* **2003**, *115*, 229.
(158) Aliaga, C.; Tsung, C.-K.; Alayoglu, S.; Komvopoulos, K.; Yang, P.; Somorjai, G. A. *The Journal of Physical Chemistry C* **2011**, *115*, 8104.
(159) Kuhn, J. N.; Tsung, C.-K.; Huang, W.; Somorjai, G. A. *J. Catal.* **2009**, *265*, 209.
(160) Lee, H.; Habas, S. E.; Kweskin, S.; Butcher, D.; Somorjai, G. A.; Yang, P. *Angewandte Chemie International Edition* **2006**, *45*, 7824.
(161) Cremer, P. S.; Somorjai, G. A. *J. Chem. Soc., Faraday Trans.* **1995**, *91*, 3671.
(162) Leger, J.-M.; Beden, B.; Lamy, C.; Bilmes, S. *Journal of Electroanalytical Chemistry and Interfacial Electrochemistry* **1984**, *170*, 305.
(163) Cho, Y.-H.; Cho, Y.-H.; Lim, J. W.; Park, H.-Y.; Jung, N.; Ahn, M.; Choe, H.; Sung, Y.-E. *Int. J. Hydrogen Energy* **2012**, *37*, 5884.

(164) Stamenkovic, V. R.; Fowler, B.; Mun, B. S.; Wang, G.; Ross, P. N.; Lucas, C. A.; Marković, N. M. *Science* **2007**, *315*, 493.
(165) Tang, W.; Henkelman, G. *The Journal of Chemical Physics* **2009**, *130*, 194504.
(166) Gandhi, H. S.; Graham, G. W.; McCabe, R. W. *J. Catal.* **2003**, *216*, 433.
(167) Zhang, Y.; Grass, M. E.; Huang, W.; Somorjai, G. A. *Langmuir* **2010**, *26*, 16463.
(168) Zhang, Y.; Janyasupab, M.; Liu, C.-W.; Li, X.; Xu, J.; Liu, C.-C. *Adv. Funct. Mater.* **2012**, 22 (17) 3570.
(169) Breit, B. **2007**, *24*, 145.
(170) Yuan, Y.; Yan, N.; Dyson, P. J. *ACS Catalysis* **2012**, *2*, 1057.
(171) Balan, B. K.; Sathe, B. R. *J. Nanosci. Nanotechnol.* **2012**, *12*, 8994.
(172) Cao, D.; Wieckowski, A.; Inukai, J.; Alonso-Vante, N. *J. Electrochem. Soc.* **2006**, *153*, A869.
(173) Kiran, V.; Ravikumar, T.; Kalyanasundaram, N. T.; Krishnamurty, S.; Shukla, A. K.; Sampath, S. *J. Electrochem. Soc.* **2010**, *157*, B1201.
(174) Park, K.-W.; Han, D.-S.; Sung, Y.-E. *J. Power Sources* **2006**, *163*, 82.
(175) Sathe, B. R.; Balan, B. K.; Pillai, V. K. *Energy & Environmental Science* **2011**, *4*, 1029.
(176) Shen, S.; Zhao, T. *Journal of Materials Chemistry A* **2013**, *1*, 906.
(177) Suo, Y.; Hsing, I. M. *J. Power Sources* **2011**, *196*, 7945.
(178) Tedsree, K.; Chan, C. W. A.; Jones, S.; Cuan, Q.; Li, W.-K.; Gong, X.-Q.; Tsang, S. C. E. *Science* **2011**, *332*, 224.
(179) Yuan, Q.; Zhou, Z.; Zhuang, J.; Wang, X. *Inorg. Chem.* **2010**, *49*, 5515.
(180) Bernardis, F. L.; Grant, R. A.; Sherrington, D. C. *Reactive and Functional Polymers* **2005**, *65*, 205.
(181) Renner, H.; Schlamp, G.; Kleinwächter, I.; Drost, E.; Lüschow, H. M.; Tews, P.; Panster, P.; Diehl, M.; Lang, J.; Kreuzer, T.; Knödler, A.; Starz, K. A.; Dermann, K.; Rothaut, J.; Drieselmann, R.; Peter, C.; Schiele, R. In *Ullmann's Encyclopedia of Industrial Chemistry*; Wiley-VCH Verlag GmbH & Co. KGaA: 2000.
(182) Bergamaski, K.; Gonzalez, E. R.; Nart, F. C. *Electrochim. Acta* **2008**, *53*, 4396.
(183) Friebel, D.; Viswanathan, V.; Miller, D. J.; Anniyev, T.; Ogasawara, H.; Larsen, A. H.; O'Grady, C. P.; Nørskov, J. K.; Nilsson, A. *J. Am. Chem. Soc.* **2012**.
(184) Gustafson, J.; Westerström, R.; Mikkelsen, A.; Torrelles, X.; Balmes, O.; Bovet, N.; Andersen, J. N.; Baddeley, C. J.; Lundgren, E. *Physical Review B* **2008**, *78*, 045423.
(185) Jacinto, M. J.; Kiyohara, P. K.; Masunaga, S. H.; Jardim, R. F.; Rossi, L. M. *Applied Catalysis A: General* **2008**, *338*, 52.
(186) Sathe, B. R.; Shinde, D. B.; Pillai, V. K. *The Journal of Physical Chemistry C* **2009**, *113*, 9616.
(187) Zhang, Y.; Grass, M. E.; Kuhn, J. N.; Tao, F.; Habas, S. E.; Huang, W.; Yang, P.; Somorjai, G. A. *J. Am. Chem. Soc.* **2008**, *130*, 5868.
(188) Adleman, J. R.; Boyd, D. A.; Goodwin, D. G.; Psaltis, D. *Nano Lett.* **2009**, *9*, 4417.

(189) Kobayashi, H.; Lim, B.; Wang, J.; Camargo, P. H. C.; Yu, T.; Kim, M. J.; Xia, Y. *Chem. Phys. Lett.* **2010**, *494*, 249.
(190) Ewers, T. D.; Sra, A. K.; Norris, B. C.; Cable, R. E.; Cheng, C.-H.; Shantz, D. F.; Schaak, R. E. *Chem. Mater.* **2005**, *17*, 514.
(191) Biacchi, A. J.; Schaak, R. E. *ACS Nano* **2011**, *5*, 8089.
(192) Hoefelmeyer, J. D.; Niesz, K.; Somorjai, G. A.; Tilley, T. D. *Nano Lett.* **2005**, *5*, 435.
(193) Long, N. V.; Chien, N. D.; Hirata, H.; Matsubara, T.; Ohtaki, M.; Nogami, M. *J. Cryst. Growth* **2011**, *320*, 78.
(194) Bi, Y.; Lu, G. *Chem. Commun. (Cambridge, U. K.)* **2008**, 6402.
(195) Biacchi, A. J.; Schaak, R. E. *ACS Nano* **2011**.
(196) Humphrey, S. M.; Grass, M. E.; Habas, S. E.; Niesz, K.; Somorjai, G. A.; Tilley, T. D. *Nano Lett.* **2007**, *7*, 785.
(197) Zhang, H.; Li, W.; Jin, M.; Zeng, J.; Yu, T.; Yang, D.; Xia, Y. *Nano Lett.* **2010**, *11*, 898.
(198) Zhang, H.; Xia, X.; Li, W.; Zeng, J.; Dai, Y.; Yang, D.; Xia, Y. *Angewandte Chemie International Edition* **2010**, *49*, 5296.
(199) Zhang, Y.; Grass, M. E.; Habas, S. E.; Tao, F.; Zhang, T.; Yang, P.; Somorjai, G. A. *The Journal of Physical Chemistry C* **2007**, *111*, 12243.
(200) Fan, F.-R.; Liu, D.-Y.; Wu, Y.-F.; Duan, S.; Xie, Z.-X.; Jiang, Z.-Y.; Tian, Z.-Q. *J. Am. Chem. Soc.* **2008**, *130*, 6949.
(201) Jiang, M.; Lim, B.; Tao, J.; Camargo, P. H. C.; Ma, C.; Zhu, Y.; Xia, Y. *Nanoscale* **2010**, *2*, 2406.
(202) Alayoglu, S.; Eichhorn, B. *J. Am. Chem. Soc.* **2008**, *130*, 17479.
(203) Li, Y.; Liu, Q.; Shen, W. *Dalton Trans.* **2011**, *40*, 5811.
(204) Valden, M.; Lai, X.; Goodman, D. W. *Science* **1998**, *281*, 1647.
(205) Zhou, X.; Xu, W.; Liu, G.; Panda, D.; Chen, P. *J. Am. Chem. Soc.* **2009**, *132*, 138.
(206) Suntivich, J.; Xu, Z.; Carlton, C. E.; Kim, J.; Han, B.; Lee, S. W.; Bonnet, N.; Marzari, N.; Allard, L. F.; Gasteiger, H. A.; Hamad-Schifferli, K.; Shao-Horn, Y. *J. Am. Chem. Soc.* **2013**, DOI:10.1021/ja402072r.
(207) Tao, F.; Dag, S.; Wang, L. W.; Liu, Z.; Butcher, D. R.; Bluhm, H.; Salmeron, M.; Somorjai, G. A. *Science* **2010**, *327*, 850.
(208) Tao, F.; Grass, M. E.; Zhang, Y.; Butcher, D. R.; Aksoy, F.; Aloni, S.; Altoe, V.; Alayoglu, S.; Renzas, J. R.; Tsung, C.-K.; Zhu, Z.; Liu, Z.; Salmeron, M.; Somorjai, G. A. *J. Am. Chem. Soc.* **2010**, *132*, 8697.
(209) Xie, S.; Lu, N.; Xie, Z.; Wang, J.; Kim, M. J.; Xia, Y. *Angewandte Chemie International Edition* **2012**, *51*, 10266.
(210) Yao, S.; Yuan, Y.; Xiao, C.; Li, W.; Kou, Y.; Dyson, P. J.; Yan, N.; Asakura, H.; Teramura, K.; Tanaka, T. *The Journal of Physical Chemistry C* **2012**, *116*, 15076.
(211) Koch, R. *J. Phys.: Condens. Matter* **1994**, *6*, 9519.
(212) Colombi Ciacchi, L.; Pompe, W.; De Vita, A. *The Journal of Physical Chemistry B* **2003**, *107*, 1755.

(213) Serpell, C. J.; Cookson, J.; Ozkaya, D.; Beer, P. D. *Nat Chem* **2011**, *3*, 478.
(214) Fan, N.; Yang, Y.; Wang, W.; Zhang, L.; Chen, W.; Zou, C.; Huang, S. *ACS Nano* **2012**, *6*, 4072.
(215) Wang, D.; Li, Y. *J. Am. Chem. Soc.* **2010**, *132*, 6280.
(216) Chen, H.; Wang, F.; Li, K.; Woo, K. C.; Wang, J.; Li, Q.; Sun, L.-D.; Zhang, X.; Lin, H.-Q.; Yan, C.-H. *ACS Nano* **2012**.
(217) González, E.; Arbiol, J.; Puntes, V. F. *Science* **2011**, *334*, 1377.
(218) Liu, J.; Qiao, S. Z.; Chen, J. S.; Lou, X. W.; Xing, X.; Lu, G. Q. *Chemical Communications* **2011**, *47*, 12578.
(219) Schaak, R. E.; Sra, A. K.; Leonard, B. M.; Cable, R. E.; Bauer, J. C.; Han, Y.-F.; Means, J.; Teizer, W.; Vasquez, Y.; Funck, E. S. *J. Am. Chem. Soc.* **2005**, *127*, 3506.
(220) Vasquez, Y.; Henkes, A. E.; Chris Bauer, J.; Schaak, R. E. *J. Solid State Chem.* **2008**, *181*, 1509.
(221) Harada, M.; Asakura, K.; Ueki, Y.; Toshima, N. *The Journal of Physical Chemistry* **1993**, *97*, 10742.
(222) Chantry, R. L.; Siriwatcharapiboon, W.; Horswell, S. L.; Logsdail, A. J.; Johnston, R. L.; Li, Z. Y. *The Journal of Physical Chemistry C* **2012**, *116*, 10312.
(223) Nolte, P.; Stierle, A.; Jin-Phillipp, N. Y.; Kasper, N.; Schulli, T. U.; Dosch, H. *Science* **2008**, *321*, 1654.
(224) Bhattarai, N.; Casillas, G.; Ponce, A.; Jose-Yacaman, M. *Surf. Sci.* **2013**, *609*, 161.
(225) Housmans, T. H. M.; Feliu, J. M.; Koper, M. T. M. *J. Electroanal. Chem.* **2004**, *572*, 79.
(226) Xu, Q.; Linke, U.; Bujak, R.; Wandlowski, T. *Electrochim. Acta* **2009**, *54*, 5509.
(227) Adić, R. R.; Tripković, A. V. *Journal of Electroanalytical Chemistry and Interfacial Electrochemistry* **1979**, *99*, 43.
(228) Kibler, L. A.; El-Aziz, A. M.; Hoyer, R.; Kolb, D. M. *Angewandte Chemie International Edition* **2005**, *44*, 2080.
(229) Strasser, P.; Koh, S.; Anniyev, T.; Greeley, J.; More, K.; Yu, C.; Liu, Z.; Kaya, S.; Nordlund, D.; Ogasawara, H.; Toney, M. F.; Nilsson, A. *Nature Chemistry* **2010**, *2*, 454.
(230) Mavrikakis, M.; Hammer, B.; Nørskov, J. K. *Phys. Rev. Lett.* **1998**, *81*, 2819.
(231) Zhou, W. P.; Lewera, A.; Larsen, R.; Masel, R. I.; Bagus, P. S.; Wieckowski, A. *The Journal of Physical Chemistry B* **2006**, *110*, 13393.
(232) Xiang, J.; Wu, B.-L.; Chen, S.-L. *J. Electroanal. Chem.* **2001**, *517*, 95.
(233) Lai, S. C. S.; Kleijn, S. E. F.; Öztürk, F. T. Z.; van Rees Vellinga, V. C.; Koning, J.; Rodriguez, P.; Koper, M. T. M. *Catal. Today* **2010**, *154*, 92.
(234) Lai, S. C. S.; Koper, M. T. M. *Phys. Chem. Chem. Phys.* **2009**, *11*, 10446.
(235) Savadogo, O.; Lee, K.; Oishi, K.; Mitsushima, S.; Kamiya, N.; Ota, K. I. *Electrochem. Commun.* **2004**, *6*, 105.
(236) Zhang, J.; Vukmirovic, M. B.; Xu, Y.; Mavrikakis, M.; Adzic, R. R. *Angew. Chem.* **2005**, *117*, 2170.

(237) Porter, N. S.; Wu, H.; Quan, Z.; Fang, J. *Acc. Chem. Res.* **2013**, *46*, 1867.
(238) Wu, J.; Gross, A.; Yang, H. *Nano Lett.* **2011**, *11*, 798.
(239) Wu, Y.; Cai, S.; Wang, D.; He, W.; Li, Y. *J. Am. Chem. Soc.* **2012**, *134*, 8975.
(240) Jin, M.; Zhang, H.; Wang, J.; Zhong, X.; Lu, N.; Li, Z.; Xie, Z.; Kim, M. J.; Xia, Y. *ACS Nano* **2012**, *6*, 2566.
(241) Ping, H.; Chen, Y.; Guo, H.; Wang, Z.; Zeng, D.; Wang, L.; Peng, D.-L. *Mater. Lett.* **2014**, *116*, 239.
(242) Habas, S. E.; Lee, H.; Radmilovic, V.; Somorjai, G. A.; Yang, P. *Nat. Mater.* **2007**, *6*, 692.
(243) Grzelczak, M.; P rez- uste, .; Rodr guez-González, B.; Spasova, M.; Barsukov, I.; Farle, M.; Liz-Marzán, L. M. *Chem. Mater.* **2008**, *20*, 5399.
(244) Grzelczak, M.; Rodríguez-González, B.; Pérez-Juste, J.; Liz-Marzán, L. M. *Adv. Mater. (Weinheim, Ger.)* **2007**, *19*, 2262.
(245) Sánchez-Iglesias, A.; Grzelczak, M.; Rodr guez-González, B.; Guardia-Gir s, P.; Pastoriza-Santos, I.; P rez- uste, .; Prato, M.; Liz-Marzán, L. M. *ACS Nano* **2009**, *3*, 3184.
(246) Sanles-Sobrido, M.; Banobre-Lopez, M.; Salgueirino, V.; Correa-Duarte, M. A.; Rodriguez-Gonzalez, B.; Rivas, J.; Liz-Marzan, L. M. *J. Mater. Chem.* **2010**, *20*, 7360.
(247) Sarkar, S.; Sinha, A. K.; Pradhan, M.; Basu, M.; Negishi, Y.; Pal, T. *The Journal of Physical Chemistry C* **2010**, *115*, 1659.
(248) Senapati, S.; Srivastava, S. K.; Singh, S. B.; Biswas, K. *Cryst. Growth Des.* **2010**, *10*, 4068.
(249) Wu, Z. G.; Munoz, M.; Montero, O. *Advanced Powder Technology* **2010**, *21*, 165.
(250) Jana, S.; Chang, J. W.; Rioux, R. M. *Nano Lett.* **2013**, *13*, 3618.
(251) Nelson, N. C.; Ruberu, T. P. A.; Reichert, M. D.; Vela, J. *The Journal of Physical Chemistry C* **2013**, *117*, 25826.
(252) Zhang, W.-B.; Chen, C.; Zhang, S.-Y. *The Journal of Physical Chemistry C* **2013**, *117*, 21274.
(253) Zhang, B.; Wu, J.; Li, X.; Liu, H.; Yadian, B.; Ramanujan, R. V.; Zhou, K.; Wu, R.; Hao, S.; Huang, Y. *The Journal of Physical Chemistry C* **2014**.
(254) Abdel Rahim, M. A.; Hassan, H. B.; Abdel Hameed, R. M. *Fuel Cells* **2007**, *7*, 298.
(255) Deivaraj, T. C.; Chen, W.; Lee, J. Y. *J. Mater. Chem.* **2003**, *13*, 2555.
(256) Liu, X.-J.; Cui, C.-H.; Gong, M.; Li, H.-H.; Xue, Y.; Fan, F.-J.; Yu, S.-H. *Chem. Commun. (Cambridge, U. K.)* **2013**, *49*, 8704.
(257) Prabhuram, J.; Manoharan, R. *J. Power Sources* **1998**, *74*, 54.
(258) Tripković, A. V.; Popović, K. D.; Grgur, B. N.; Blizanac, B.; Ross, P. N.; Marković, N. M. *Electrochim. Acta* **2002**, *47*, 3707.
(259) Jia, Y.; Jiang, Y.; Zhang, J.; Zhang, L.; Chen, Q.; Xie, Z.; Zheng, L. *J. Am. Chem. Soc.* **2014**, *136*, 3748.
(260) Gao, M.-R.; Xu, Y.-F.; Jiang, J.; Yu, S.-H. *Chem. Soc. Rev.* **2013**, *42*, 2986.

(261) Giordano, C.; Erpen, C.; Yao, W.; Antoniett, M. *Nano Lett.* **2008**, *8*, 4659.
(262) Kuo, C.-H.; Huang, M. H. *Nano Today* **2010**, *5*, 106.
(263) Chen, Z.; Higgins, D.; Yu, A.; Zhang, L.; Zhang, J. *Energy & Environmental Science* **2011**, *4*, 3167.
(264) Wang, R. H.; Xie, Y.; Shi, K. Y.; Wang, J. Q.; Tian, C. G.; Shen, P. K.; Fu, H. G. *Chemistry-a European Journal* **2012**, *18*, 7443.
(265) Zhang, L.; Zhang, J.; Wilkinson, D. P.; Wang, H. *J. Power Sources* **2006**, *156*, 171.
(266) Dance, I. G.; Choy, A.; Scudder, M. L. *J. Am. Chem. Soc.* **1984**, *106*, 6285.
(267) Hunt, S. T.; Nimmanwudipong, T.; Roman-Leshkov, Y. *Angewandte Chemie-International Edition* **2014**, *53*, 5131.
(268) Cheng, J.; Hu, P. *J. Am. Chem. Soc.* **2008**, *130*, 10868.